

Targeting ROS metabolism and hypoxia signaling sensitizes castration-resistant prostate cancer to androgen receptor signaling inhibition

Adrián Martínez Tébar

ADVERTIMENT. La consulta d'aquesta tesi queda condicionada a l'acceptació de les següents condicions d'ús: La difusió d'aquesta tesi per mitjà del servei TDX (www.tdx.cat) i a través del Dipòsit Digital de la UB (diposit.ub.edu) ha estat autoritzada pels titulars dels drets de propietat intel·lectual únicament per a usos privats emmarcats en activitats d'investigació i docència. No s'autoritza la seva reproducció amb finalitats de lucre ni la seva difusió i posada a disposició des d'un lloc aliè al servei TDX ni al Dipòsit Digital de la UB. No s'autoritza la presentació del seu contingut en una finestra o marc aliè a TDX o al Dipòsit Digital de la UB (framing). Aquesta reserva de drets afecta tant al resum de presentació de la tesi com als seus continguts. En la utilització o cita de parts de la tesi és obligat indicar el nom de la persona autora.

ADVERTENCIA. La consulta de esta tesis queda condicionada a la aceptación de las siguientes condiciones de uso: La difusión de esta tesis por medio del servicio TDR (www.tdx.cat) y a través del Repositorio Digital de la UB (diposit.ub.edu) ha sido autorizada por los titulares de los derechos de propiedad intelectual únicamente para usos privados enmarcados en actividades de investigación y docencia. No se autoriza su reproducción con finalidades de lucro ni su difusión y puesta a disposición desde un sitio ajeno al servicio TDR o al Repositorio Digital de la UB. No se autoriza la presentación de su contenido en una ventana o marco ajeno a TDR o al Repositorio Digital de la UB (framing). Esta reserva de derechos afecta tanto al resumen de presentación de la tesis como a sus contenidos. En la utilización o cita de partes de la tesis es obligado indicar el nombre de la persona autora.

WARNING. On having consulted this thesis you're accepting the following use conditions: Spreading this thesis by the TDX (**www.tdx.cat**) service and by the UB Digital Repository (**diposit.ub.edu**) has been authorized by the titular of the intellectual property rights only for private uses placed in investigation and teaching activities. Reproduction with lucrative aims is not authorized nor its spreading and availability from a site foreign to the TDX service or to the UB Digital Repository. Introducing its content in a window or frame foreign to the TDX service or to the UB Digital Repository is not authorized (framing). Those rights affect to the presentation summary of the thesis as well as to its contents. In the using or citation of parts of the thesis it's obliged to indicate the name of the author.

UNIVERSITAT DE BARCELONA

FACULTAT DE MEDICINA I CIÈNCIES DE LA SALUT PROGRAMA DE DOCTORAT EN BIOMEDICINA

TARGETING ROS METABOLISM AND HYPOXIA SIGNALING SENSITIZES CASTRATION-RESISTANT PROSTATE CANCER TO ANDROGEN RECEPTOR SIGNALING INHIBITION

ADRIÁN MARTÍNEZ TÉBAR 2023









UNIVERSITAT DE BARCELONA

FACULTAT DE MEDICINA I CIÈNCIES DE LA SALUT

PROGRAMA DE DOCTORAT EN BIOMEDICINA

TARGETING ROS METABOLISM AND HYPOXIA SIGNALING SENSITIZES CASTRATION-RESISTANT PROSTATE CANCER TO ANDROGEN RECEPTOR SIGNALING INHIBITION

ADRIÁN MARTÍNEZ TÉBAR

2023

Memòria presentada per Adrián Martínez Tébar per optar al grau de

Doctor per la Universitat de Barcelona

Dr. Álvaro Aytés Meneses

Dr. Francesc Viñals Canals

Adrián Martínez Tébar

Director Tutor Autor

TABLE OF CONTENT

	1
LIST OF ABBREVIATIONS	9
LIST OF FIGURES	14
LIST OF TABLES	16
SUMMARY	17
RESUMEN	21
INTRODUCTION	25
1. PROSTATE BIOLOGY	26
1.1. HUMAN PROSTATE	26
1.2. MOUSE PROSTATE	27
1.3. CELLULAR ORGANIZATION IN THE PROSTATE	28
1.4. ANDROGEN RECEPTOR: STRUCTURE AND FUNCTION	30
2. PROSTATE CANCER	32
2.1. PROSTATE CANCER INCIDENCE AND ETIOLOGIC FACTORS	32
2.1.1. INICIATION AND PROGRESSION OF PROSTATE CANCER	33
2.1.2. GENETIC AND MOLECULAR MECHANISMS OF PROSTATE CANCER INITIATION AND PROGRESSION	34
2.2. DIAGNOSIS OF PROSTATE CANCER	36
2.2.1. PROSTATE SPECIFIC ANTIGEN (PSA) SCREENING	36
2.2.2. GRADING OF BIOPSIES AND STAGING	36
2.2.3. INDOLENT VS AGGRESSIVE DISEASE	37
2.3. MANAGEMENT OF PROSTATE CANCER	38
2.3.1. ACTIVE SURVEILLANCE AND WATCHFUL WAITING	38
2.3.2. SURGERY	38

2.3.3. RADIOTHERAPY	39
2.3.4. Androgen Deprivation Therapy (ADT)	39
2.3.5. CHEMOTHERAPY	39
3. ANDROGEN RECEPTOR AND CASTRATION-RESISTANT PR	OSTATE
CANCER (CRPC)	40
3.1. RETENTION OF AR SIGNALING IN CRPC	40
3.2. TREATMENTS OF CRPC	42
3.3. METASTATIC PROSTATE CANCER	44
4. PROSTATE CANCER MODELS	45
4.1. PROSTATE CANCER CELL LINES	45
4.2. XENOGRAFT MODELS	46
4.3. GENETICALLY ENGINEERED MICE MODELS (GEMM)	46
4.4. A GEMM MODEL TO RECAPITULATE CRPC	47
5. CRISPR/CAS9 IN BIOMEDICAL RESEARCH	49
5.1. CRISPR/Cas9 FUNCTION	50
5.2. CRISPR/CAS9 FOR GENOME EDITING IN EUKARYOTES	51
5.3. ACTIVATION OR REPRESSION OF TARGET GENES USING CRISPR	51
5.4. CRISPR SCREENINGS	52
5.4.1. SCREENINGS FOR SYNTHETIC LETHAL INTERACTIONS	52
6. ROS METABOLISM AND HYPOXIA	54
6.1. ROS AND CELLULAR DAMAGE	54
6.1.1. Free radicals and ROS	54
6.1.2. Oxidative stress and cancer	56
6.1.2.1. Sources of ROS contributing to oxidative stress	57
6.1.2.2. Targeting ROS for cancer treatment	57
6.2. NADPH OXIDASES AND CANCER	58
6.2.1. NOX FAMILY	58

6.2.2. DUOX ENZYMES AND CANCER	61
6.3. ROS METABOLISM IN PROSTATE CANCER	62
6.3.1. REDOX-DEPENDENT SIGNALING IN PROSTATE CANCER CELLS	62
6.3.2. MITOCHONDRIAL ACTIVITY AND ROS	63
6.3.3. NOX FAMILY IN PROSTATE CANCER	64
6.4. ROS AND HYPOXIA	65
6.4.1. Hypoxia in tumors	65
6.4.2. HYPOXIA-INDUCIBLE FACTORS (HIFS)	66
6.4.3. HIF-dependent genes and mechanisms	67
6.4.4. HIF ACTIVITY ON TUMOR CELL METABOLISM	69
6.4.5. Hypoxia-induced ROS	70
HYPOTHESIS AND OBJECTIVES	74
OBJECTIVES	76
MATERIALS AND METHODS	78
1. CELL CULTURE	79
1.1. CELL LINES MAINTEINANCE	79
1.1.1. CELL LINES	79
1.1.2. MYCOPLASMA TEST	81
1.1.3. CELL COUNTING	81
1.1.4. CELL FREEZING AND CRYOPRESERVATION	81
1.2. LENTIVIRAL PRODUCTION AND INFECTION	82
1.2.1. 293FT TRANSFECTION FOR LENTIVIRAL PRODUCTION	82
1.2.2. CELL LINE TRANSDUCTION WITH LENTIVIRUS	83
2. MOLECULAR ANALYSES	84
2.1. PROTEIN DETECTION	84
2.1.1. PROTEIN LYSATES PREPARATION FROM CELL CULTURE	84
2.1.2. PROTEIN LYSATES QUANTIFICATION	84
2.1.3. PROTEIN ANALYSIS BY WESTERN BLOTTING	85

2.1.3.1. SDS-PAGE electrophoresis	85
2.1.3.2. Protein transfer	86
2.1.3.3. Immunoblotting	86
2.2. RNA DETECTION	87
2.2.1. RNA EXTRACTION OF CELLS	87
2.2.2. RNA RETRO-TRANSCRIPTION INTO CDNA	88
2.2.3. REAL-TIME QUANTITATIVE PCR	88
3. BACTERIA AND CLONING	90
3.1. HANDLING OF BACTERIA	90
3.1.1. GLYCEROL STOCK	90
3.1.2. BACTERIAL CHEMICAL TRANSFORMATION OF COMPETENT CELLS	90
3.1.3. OBTAINING PLASMIDIC DNA FROM BACTERIA CULTURES	91
3.1.4. LARGE SCALE DNA PREPARATIONS	9:
3.1.5. CHARACTERIZATION OF THE PLASMID DNA BY RESTRICTION DIGEST	9:
4. CRISPRI SCREENING	92
4.1. CRISPRI OPTIMIZATION	92
4.1.1. CLONING OF SGRNA SEQUENCES INTO PCRISPRIA-V2 VECTOR	92
4.1.2. LIBRARY AMPLIFICATION	96
4.2. SCREENING PERFORMANCE	97
4.3. SAMPLE PREPARATION FOR SEQUENCING	98
4.3.1. gDNA isolation	98
4.3.2. Size fractionation of genomic DNA	98
4.3.3. PCR FOR SEQUENCING	99
4.4. CRISPRI SCREENING BIOINFORMATIC ANALYSIS	101
4.4.1. QUALITY CONTROL	101
4.4.2. CRISPRI SCREENING	10:
4.4.2.1. Hits calling	102
4.4.2.2. Functional analysis	102
4.5. BIOINFORMATIC ANALYSIS FROM SU2C PROSTATE CANCER DATASET	102

5. FUNCTIONAL ASSAYS	103
5.1. CELL VIABILITY ASSAY	103
5.2. COLONY FORMATION ASSAY	103
5.3. SYNERGY OF DRUGS	104
5.4. AR TRANSCRIPTIONAL ACTIVITY REPORTER	104
5.5. TOTAL ROS QUANTIFICATION	105
5.6. RNA-seq	105
5.6.1. RNA-SEQ BIOINFORMATIC ANALYIS	106
5.7. METABOLIC ASSAYS	106
5.7.1. ATP RATE ASSAY CALCULATIONS	109
5.7.1.1. Glycolytic ATP production rate calculation	109
5.7.1.2. Mitochondrial ATP production rate calculation	109
5.7.1.3. Total ATP Production Rate calculation	110
5.7.2. MITO STRESS ASSAY CALCULATIONS	110
5.8. ETICHS AND HOUSING	111
5.9. ORTOTHOPIC ENGRAFTMENT	111
5.10. DRUG TREATMENT	112
6. GRAPHIC REPRESENTATION AND STATISTICAL ANALYSIS	113
RESULTS	116
1. GENOME-WIDE CRISPRI SCREENING	117
1.1. PREMISES	117
1.2. SCREENING OPTIMIZATION	117
1.2.1. LIBRARY PREPARATION AND QUALITY CONTROL	117
1.2.2. ENGINEERING OF CRISPRI FUNCTIONAL CELLS	118
1.2.3. DRUG CONCENTRATION OPTIMIZATION	120
1.2.4. GENOME-WIDE SCREEN	122
1.3. SCREENING RESULTS ANALYSIS	123
2. CLINICAL CORRELATES	126

2.1. CORRELATIONS BETWEEN DUOX MEMBERS AND AR	126
2.2. DUOX2 AND ROS SIGNALING PREDICT PATIENT SURVIVAL	128
3. DUOX2 REGULATES ANTIANDROGEN RESPONSE	129
3.1. EFFECT OF DUOX2 KD IN ABIRATERONE RESISTANCE	129
3.2. NOX/DUOX INHIBITION SENSITIZES PCA CELLS TO ABIRATERONE	131
4. CROSS-TALK BETWEEN AR TARGETING AND ROS METABOLISM	133
4.1. ABIRATERONE INFLUENCING TOTAL ROS LEVELS	134
5. MECHANISMS OF ABIRATERONE RESISTANCE VIA DUOX2	136
6. ANTIANDROGENS REGULATION ON HIF-1A AND HYPOXIA SIGNALING	141
6.1. ABIRATERONE AND HIF-1A STABILIZATION	141
6.2. HIF-1A ACTIVITY ON TRANSCRIPTIONAL TARGETS	145
6.3. METABOLIC CHANGES INDUCED BY ABIRATERONE-INDUCED PSEUDOHYPOXIA	147
6.3.1. ATP RATE ASSAY	147
6.3.2. MITO STRESS TEST	149
7. CO-TARGETING HIF AND AR SIGNALING	154
7.1. IN VITRO SYNERGY BETWEEN HIF-1A INHIBITION AND ANTIANDROGENS	154
7.2. <i>IN VIVO</i> VALIDATION OF THE SYNERGY	157
DISCUSSION	162
1. CRIPRI SCREENING AND NOX FAMILY	163
2. DUOX AND ROS METABOLISM MODULATING ANTIANDROGEN RESPONSE	167
2.1. DUOX2 AND ANTIANDROGEN RESISTANCE	167

2.2. ANDROGENS, ANTIANDROGENS AND ROS	169
2.3. ABIRATERONE-INDUCED ROS: MECHANISMS OF RESISTANCE	174
	_
3. PSEUDOHYPOXIA IN PROSTATE CANCER	176
3.1. HIF-1A AND PSEUDOHYPOXIA RESPONSE TO ABIRATERONE	176
3.2. HYPOXIA-ASSOCIATED GENES AND RESPONSE	179
3.3. ABIRATERONE-INDUCED METABOLIC CHANGES	182
3.4. CO-TARGETING PSEUDOHYPOXIA WITH ANTIANDROGENS	185
CONCLUSIONS	191
REFERENCES	195

LIST OF ABBREVIATIONS

Microgram
Microliter
Micrometer
Micromolar
2-oxoglutarate
3-bromopyruvate
Abiraterone
Androgen-dependent
Androgen deprivation therapy
Androgen-independent
Ammonium persulfate
Androgen receptor
Androgen-responsive element
Androgen receptor variant
AR splice variant-7
Adenosine triphosphate
Bipolar androgen therapy
Bicinchoninic acid
Blue-fluorescent protein
Base pair
Benign prostate hyperplasia
Bovine serum albumin
Cyclin-dependent kinase
Complementary DNA
Colony formation assay
cytokeratin
Centimeter
Control
Carbon dioxide
Cobalt chloride
Cytochrome oxidase
Clustered regularly interspaced short
palindromic repeats
CRISPR activation
CRISPR inhibition
Castration-Resistant Prostate Cancer
Cancer stem cell
Threshold cycle
DNA-binding region

dCas9	Dead Cas9
ddH₂O	Bi-distilled water
DDR	DNA damage response
DEG	Differentially-expressed gene
DFO	Desferrioxamine
dH ₂ O	Distilled water
DHE	Dihydroethidium
DHE	Dihydroethidium
DHEA	Dihydroepiandrostenedione
DHT	Dihydrotestosterone
DL	Dorsal lobe
DMEM	Dulbecco's Modified Eagle's Medium
DMSO	Dimethyl sulfoxide
DNA	Deoxyribonucleic acid
DPI	Diphenylene iodonium
DRE	Digital rectal exam
DSB	Double strand break
DUOX	Dual oxidase
ECAR	Extracellular acidification rate
EDTA	Ethylenediaminetetraacetic acid
EMT	Epithelial-to-mesenchymal transition
Enza	Enzalutamide
ETC	Electron transport chain
FA	Fatty acid
FACS	Fluorescence-activated cell sorting
FAD	Flavin adenine dinucleotide
FBL	FAD Binding Lobe
FBS	Fetal Bovine Serum
FC	Fold change
FCCP	Carbonyl cyanide 4-
	(trifluoromethoxy)phenylhydrazone
FDA	Food and Drug Administration
FDR	False discovery rate
FL	Full-length
g	Gram
GEM	Genetically engineered mice
GFP	Green-fluorescent protein
GnRH	Gonadotropin releasing hormone
GO	Gene ontology
GSEA	Gene set enrichment analysis
GSH	Glutathione

h	Hour
H&E	Hematoxylin and eosin
H ₂ O ₂	Hydrogen peroxide
HBSS	Hanks' Balanced Salt Solution
HCl	Chloridric acid
HEPES	4-(2-hydroxyethyl)-1- piperazineethanesulfonic acid
HIF	Hypoxia-inducible factor
HMAs	Hypoxia mimetic agents
HR	Homologous recombination
HRE	Hypoxia-response element
HRP	Horseradish peroxidase
HSP90	heat shock protein-90
IC	Inhibitory concentration
Kb	Kilobase
KD	Knock-down
KD	Knock-down
KDa	Kilodalton
Kg	Kilogram
КО	Knock-out
L	Liter
LB	Lysogeny broth
LBD	Ligand-binding domain
LHRH	Luteinizing hormone-releasing hormone
mCRPC	metastatic CRPC
mg	Milligram
min	Minute
ml	Milliliter
mm	Millimeter
mM	Millimolar
mm ²	Square millimeter
mm³	Cubic millimeter
MOI	Multiplicity of infection
MSigDB	Molecular Signatures Database
mtDNA	Mitochondrial DNA
MTT	Thiazolyl Blue Tetrazolium Bromide
NAC	N-Acetyl-L-cysteine
NaCl	Sodium chloride
NAD	Nicotinamide riboside
NE	Neuroendocrine
NEPC	Neuroendocrine-prostate cancer

ng	Nanogram
NHEJ	Non-homologous end joining
nm	Nanometer
NO	Nitric oxide
NOX	NADPH oxidase
NP	Nkx3.1 ^{CreERT2/+} ; Pten ^{flox/flox} mouse
NPp53	Nkx3.1 ^{CreERT2/+} ; Pten ^{flox/flox} ; Trp53 ^{flox/flox} mouse
NRF2	NF-E2-related factor 2
NSCLC	Non-small cell lung cancer
nt	nucleotide
NTD	Amino-terminal transregulation domain
O/N	Over night
OCR	Oxygen consumption rate
ORF	Open-reading frame
OXPHOS	Oxidative phosphorylation
PAM	Proto-spacer Adjacent Motif
PARP	(Poly) ADP-ribose polymerase
PBS	Phosphate buffered saline
PCa	Prostate cancer
PCA	Principal Component Analysis
PCR	Polymerase chain reaction
PDH	Pyruvate dehydrogenase
PDX	Patient-derived xenografts
PEI	Polyethylenimine
PES	Polyethersulfone
PFA	Paraformaldehyide
pg	Picogram
PHD	Peroxidase homology domain
PHDs	Prolyl Hydroxylases
PHLD	Pleckstrin homology-like domain
PIN	Prostatic intraepithelial neoplasia
PSA	Prostate-specific antigen
PTEN	Phosphatase and tensin homolog
Puro	Puromycin
QOL	Quality of life
qPCR	Quantitative PCR
RIPA	Radioimmunoprecipitation assay buffer
RNA	Ribonucleic acid
RNAi	RNA interference
RNAseq	Ribonucleic acid sequencing

RNP	Ribonucleoprotein
RNS	Reactive nitrogen species
ROS	Reactive oxygen species
rpm	Revolutions per minute
RQ	Relative quantity
RT	Room temperature
RT-qPCR	Real-time quantitative PCR
S	Second
SCR	Spare respiratoy capacity
SD	Standard deviation
SDS	Sodium dodecyl sulfate
sgRNA	Small-guide RNA
siRNA	small interference RNA
SOC	Super optimal broth
SOD	Superoxide dismutase
SpCas9	Streptococcus pyogenes Cas9
SPF	Specific pathogen free
SU2C	Stand Up To Cancer
TAE	Tris-acetate-EDTA
TBS	Tris-buffered Saline
TCA	Tricarboxylic acid
TCGA	The Cancer Genome Atlas
TEMED	Tetramethylethylenediamine
TMA	Tissue microarray
t-NEPC	treatment-related NEPC
TNM	Tumor-node-metastasis
TP53	Tumor protein p53
Tris	Tris(hydroxymethyl)aminomethane
UV	Ultraviolet
VEGF	Vascular endothelial growth factor
Δ	Delta

LIST OF FIGURES

Figure 1. Human and mouse prostate's representation	26
Figure 2. Lineage markers and cellular compartments of a normal human prostate gland	28
Figure 3. The human androgen receptor gene and the AR-LBD dimer interface	31
Figure 4. Prostate cancer progression	34
Figure 5. Grading of prostate cancer biopsies	37
Figure 6. Biosynthesis of dihydrotestosterone (DHT) and the subsequent signaling via the An	drogen
Receptor	43
Figure 7. Schematic representation of NPp53 GEMM generation	48
Figure 8. Primary sequence of the NOX family and DUOXA maturation factors	59
Figure 9. Structures of DUOX and DUOXA proteins as a schematic representation	60
Figure 10. Regulation of hypoxia-inducible factors	67
Figure 11. Schematic representation of oxidative phosphorylation, anerobic glycolysis and a	naerobic
glycolysis	69
Figure 12. Schematic representation of the PCR design used for sgRNA cloning	94
Figure 13. Cloning strategy for a particular sgRNA into the pCRISPRia2 vector, involved the u	se of PCR,
restriction enzymes and ligation	95
Figure 14. Analysis of sequencing results to assess quality control of the CRISPRi library prep	aration 118
Figure 15. CRISPRi system functionality	119
Figure 16. Abiraterone dose selection	121
Figure 17. Schematic representation of the CRISPRi screening performance	122
Figure 18. CRISPRi screening results	123
Figure 19. DUOX genes in the CRISPRi screening	125
Figure 20. Correlation of Duox gene expression with AR score from SU2C dataset	126
Figure 21. Correlation of Duox gene expression with relevant ROS signatures extracted from	SU2C dataset
	127
Figure 22. Survival analysis from SU2C database based on Duox2 signature	129
Figure 23. Validation of Duox2 as a candidate to be targeted to improve antiandrogen thera	py130
Figure 24. DPI synergizes with Abiraterone in NPp53 cells	131
Figure 25. DPI synergizes with Abiraterone in 22Rv1 and LNCaP cells	133
Figure 26. Total ROS quantification by CM-H2DCFA probe	135
Figure 27. GSEA data comparing gene expression profiles from Hallmarks of Molecular Signa	tures Database
(MSigDB)	136
Figure 28. GSEA enrichment plots for androgen response pathway.	137
Figure 29. GSEA enrichment plots for key oncogenic pathways	138
Figure 30. GSEA enrichment plots for interferon and hypoxia response pathways	140

Figure 31. HIF-1 α accumulation and abiraterone sensitivity in response to hypoxia in NPp53 cells, control	οl
and Duox2 KD	142
Figure 32. Pseudohypoxia induced by CoCl ₂ increases abiraterone resistance in CRPC cells	144
Figure 33. qPCR of HIF-1 α and its transcriptional targets	146
Figure 34. Real-Time ATP Rate Assay allows to distinguish between ATP production from OXPHOS and	
glycolysis	148
Figure 35. XF Cell Mito Stress deciphers the OXPHOS metabolism by mitochondria	150
Figure 36. Key parameters of mitochondrial OXPHOS metabolism obtained from XF Cell Mito Stress,	
including A) Basal respiration levels for each condition	153
Figure 37. PX-478 synergizes with antiandrogens in NPp53 cells	155
Figure 38. PX-478 synergizes with antiandrogens in castration-resistant 22Rv1 cells, but not in hormone	ı
sensitive LNCaP cells	156
Figure 39. In vivo combination of enzalutamide and PX-478 results in tumor growth inhibition and survivo	val
improvement	158
Figure 40. Total tumor regression from a mouse treated with the proposed drug combination	160
Figure 41. Role of hypoxia in the clinical course of PCa	188

LIST OF TABLES

Table 1. Most commonly used PCa cell lines for research45
Table 2. List of ROS produced during cellular metabolism. Adapted from Phaniendra, A., Jestadi, D. B., &
Periyasamy, L. (2015) [165]55
Table 3. Media used for cell culture79
Table 4. Cell lines80
Table 5. Oligonucleotides used for the detection of mycoplasma contamination81
Table 6. Primary antibodies used for the Western blot detections87
Table 7. Secondary antibodies used for the Western blot detections87
Table 8. Primers used for RT-qPCR89
Table 9. Restriction enzymes used to confirm correct plasmid genomes92
$ Table 10. Forward and reverse sequences for the oligonucleotides used in the PCR step of sgRNA\ cloning\ for the oligonucleotides and the PCR step of sgRNA\ cloning\ for the oligonucleotides are also becomes a sequence of the oligonucleotides. The possible of the pcR step of sgRNA\ cloning\ for the oligonucleotides are also becomes a sequence of the oligonucleotides. The pcR step of the pcR step of the oligonucleotides are also becomes a sequence of the pcR step of the pcR step of the pcR step of the oligonucleotides are also becomes a sequence of the pcR step of$
CRISPRi. The specific 20-nt sgRNA sequence is highlighted in red93
Table 11. Components of PCR reaction mix and program conditions for generating the product that will be
sequenced for screening analysis99
Table 12. Illumina Hiseq2500 compatible Primers (for PCR and sequencing)100
Table 13. Preparation of the ETC inhibitors used in the ATP Rate Assay and Mitostress Assay kits, indicating
stock and final concentrations107
Table 14. Port positions used for each Seahorse kit, along with the respective compound and volume
loaded in each position108
Table 15. Calculations of the various parameters associated with the OXPHOS metabolism that can be
derived from the ATP Mito Stress Assay110

SUMMARY

Most prostate cancer (PCa) patients who undergo Androgen Deprivation Therapy (ADT) exhibit clinical progression, resulting in the development of castration-resistant prostate cancer (CRPC), which is highly metastatic and frequently lethal. The androgen receptor (AR) is expressed at high levels in CRPC. However, clinical trials in CRPC patients have shown that treatment with abiraterone or enzalutamide, AR signaling inhibitors, can improve survival rates. Unfortunately, these antiandrogens, only provide a temporary delay in disease progression, and resistance almost invariably arises.

The molecular mechanisms that underlie resistance to antiandrogens remain elusive, hindering the development of effective therapies. To obtain candidate genes (hits) that are responsible for the acquisition of resistance or sensibility to abiraterone, we conducted a genome-wide CRISPR inhibition (CRISPRi) screening utilizing a tumor cell line derived from a genetically engineered mouse model (GEMM) carrying the combined inactivation of p53 and Pten, namely de NPp53 model.

We identified that targeting the NOX family of NAPDH oxidases, particularly Duox2, has synthetic lethal interaction with abiraterone exposure. Duox2 is known to play a role in the production of reactive oxygen species (ROS) and has been found to be overexpressed in various types of tumors, including PCa. Mechanistically, we demonstrate that abiraterone treatment leads to ROS generation, which can be prevented by Duox2 knock-down (KD). Through our in vitro studies, we have shown that targeting abiraterone-induced ROS either through silencing of Duox2 or inhibiting the NOX family, restores antiandrogens sensitivity.

To further understand the mechanisms involved in abiraterone-induced ROS and the role of Duox2 in this regulation, we conducted RNA-seq analysis to find that hypoxia-signaling was upregulated by abiraterone in normoxic conditions (pseudohypoxia). However, we observed that Duox2 abrogation prevented this pseudohypoxia activation, indicating that this signaling pathway could potentially be activated as a resistance mechanism to abiraterone.

In particular, we demonstrated that abiraterone treatment in NPp53 cells increases HIF- 1α stabilization, leading to its accumulation at the protein level and subsequent activation of the associated transcriptional program. Furthermore, we found that the accumulation of HIF- 1α upon exposure to antiandrogen was reduced by N-acetyl-L-cysteine, an antioxidant,

or by Duox2 silencing, thus highlighting the central role for NAPDH oxidases as triggers of pseudohypoxia in abiraterone-induced ROS.

Based on the established and widely accepted effect of hypoxia signaling activation on regulating glucose metabolism, we observed that abiraterone induces a metabolic shift towards glycolysis, as evidenced by the decreased contribution of oxidative phosphorylation to ATP production upon abiraterone treatment. Consequently, we propose that the activation of glycolysis is a pseudohypoxia-induced mechanism to sustain ATP levels and promote proliferation.

Therefore, we propose a combination treatment to co-target AR and pseudohypoxia activation using inhibitors of AR signaling and HIF- 1α , respectively. Remarkably, we found that whereas single treatments were ineffective, combining enzalutamide with PX-478 resulted in a significant reduction in tumor growth and increased survival in an orthotopic CRPC in vivo model.

In summary, we have uncovered and validated an actionable mechanism of resistance to AR signaling inhibition based on the activation of hypoxia-signaling mediated by antiandrogen-induced ROS that can be targeted with HIF- 1α inhibitors, thus highlighting the potential of this combined therapeutic approach for CRPC patients.

RESUMEN

La mayoría de paciente de cáncer de próstata (PCa) que reciben la terapia de privación androgénica (ADT) muestran una progresión de la enfermedad, lo que resulta en el desarrollo del cáncer de próstata resistente a la castración (CRPC), que altamente metastático y frecuentemente letal. El receptor de andrógenos (AR) se expresa en niveles altos en CRPC. Sin embargo, los ensayos clínicos realizados en pacientes con CRPC han demostrado que el tratamiento con abiraterona o enzalutamida, inhibidores de la señalización del AR, puede mejorar las tasas de supervivencia. Desafortunadamente, estos antiandrógenos solo proporcionan un retraso temporal en la progresión de la enfermedad, por lo que la resistencia a estos fármacos aparece invariablemente.

Los mecanismos moleculares que subyacen en la resistencia a los antiandrógenos siguen siendo desconocidos, lo que dificulta el desarrollo de terapias efectivas. Para obtener genes candidatos ("hits") responsables de la adquisición de resistencia o sensibilidad a la abiraterona, llevamos a cabo un cribado a nivel genómico basado en la tecnología de inhibición por CRISPR (CRISPRi), utilizando una línea celular tumoral derivada de un modelo de ratón modificado genéticamente (GEMM) con la inactivación combinada de los genes p53 y *Pten*, conocido como modelo NPp53.

Identificamos que la inhibición de la familia de las NADPH oxidasas NOX, particularmente *Duox2*, mostró una interacción de letalidad sintética con el tratamiento con abiraterona. Se sabe que *Duox2* está implicado en la producción de especies reactivas de oxígenos (ROS) y se ha encontrado que está sobreexpresado en varios tipos de tumores, incluyendo el de próstata. A nivel de mecanismo, hemos demostrado que la abiraterona conduce a la generación de ROS, los cual puede prevenirse mediante la supresión de *Duox2*. Mediante nuestros ensayos *in vitro* hemos podido verificar que suprimiendo los ROS inducidos por abiraterona, ya sea mediante el silenciamiento de Duox2 o por la inhibición de la familia NOX, se puede restaurar la sensibilidad a los antiandrógenos.

Para obtener una mayor comprensión de los mecanismos involucrados en la generación de ROS inducidos por la abiraterona, así como del papel de *Duox2* en dicha regulación, realizamos un análisis de RNA-seq, lo que nos llevó a descubrir que la ruta de

señalización asociada a hipoxia se activó por la abiraterona en condiciones normóxicas (pseudohipoxia). No obstante, también pudimos comprobar que la supresión de *Duox2* evitó esta activación de la pseudohipoxia, lo que indica que esta vía de señalización podría activarse como un mecanismo de resistencia a la abiraterona.

En particular, demostramos que el tratamiento con abiraterona en células NPp53 aumenta la estabilización de HIF- 1α , lo que conduce a su acumulación a nivel de proteína y a la posterior activación del programa de transcripción asociado. Además, encontramos que la acumulación de HIF- 1α inducida por la exposición a dicho antiandrógeno se redujo mediante el tratamiento antioxidante con N-acetil-L-cisteína o mediante el silenciamiento de Duox2. Este hecho resalta el papel central de las NADPH oxidasas como desencadenantes de la pseudohipoxia como respuesta a los ROS producidos por la acción de la abiraterona.

Basándonos en el efecto establecido y ampliamente aceptado en cuanto a la activación de la señalización asociada a hipoxia en la regulación del metabolismo de la glucosa, observamos la abiraterona induce un cambio metabólico en favor de la glucólisis, tal y como lo demuestra la disminución de la contribución de la fosforilación oxidativa a la producción de ATP durante el tratamiento con este antiandrógeno. En consecuencia, proponemos que la activación de la glucólisis es un mecanismo inducido por la pseudohipoxia para mantener los niveles de ATP y promover la proliferación.

Por lo tanto, proponemos un tratamiento combinado, dirigido de manera conjunta al AR y a la activación de la pseudohipoxia, utilizando para ello inhibidores de la señalización del AR y de HIF- 1α , respectivamente. Mientras que los tratamientos individuales resultaron ineficaces, la combinación de enzalutamida con PX-478 resultó en una reducción significativa del crecimiento tumoral y un aumento en la supervivencia en un modelo *in vivo* de CRPC ortotópico.

En resumen, hemos descubierto y validado un mecanismo de resistencia a la inhibición de la señalización del AR basado en la activación de la señalización asociada a hipoxia, mediada por los ROS producidos por los antiandrógenos. Este mecanismo puede servir como objetivo terapéutico mediante inhibidores de HIF- 1α , destacando así el potencial de este enfoque terapéutico combinado para paciente con CRPC.

INTRODUCTION

<u>Introduction</u>

1. PROSTATE BIOLOGY

1.1. HUMAN PROSTATE

The **human prostate** is a small walnut-sized accessory gland (the largest in men) located below the urinary bladder, surrounding urethra as it exits from the bladder. The prostate is part of the **male accessory sex glands**, producing important components of the seminal fluid and playing a role in ejaculation. Both **benign prostatic hyperplasia** (BPH) and **prostate cancer** (PCa) are closely associated with this organ as a site of origin, contributing to morbidity and mortality in aging male population [1].

This organ is composed of **glandular and stromal elements**, fused with a pseudocapsule. The prostate can be divided into three distinct zones: central zone (CZ), transition zone (TZ), and peripheral zone (PZ). These zones vary in histology, anatomic features, biological functions, and susceptibility to specific pathologies [1-3] (**Figure 1**).

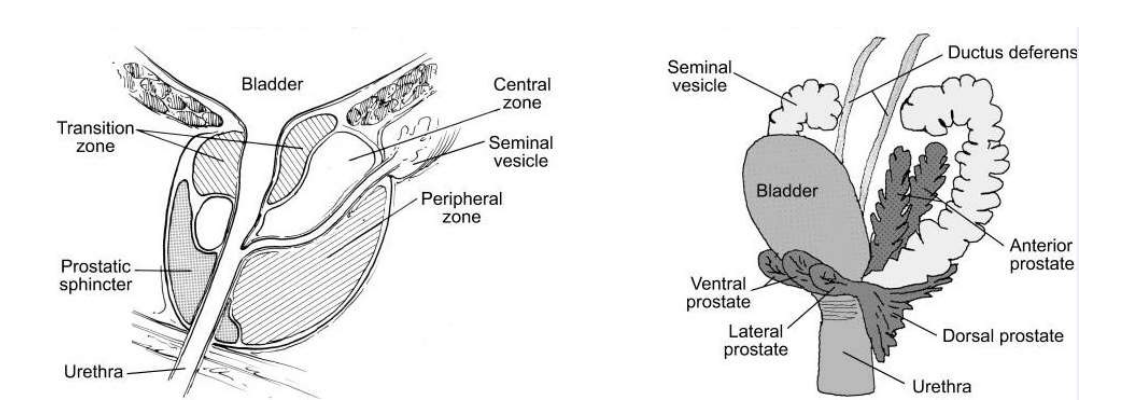


Figure 1. Human and mouse prostate's representation. Schematic structure of human **(A)** and mouse **(B)** prostate, indicating the different components of this organ as well as the surrounding structures [4].

The **peripheral zone**, constituting approximately 70% of the gland, is the **most frequent site of PCa**, accounting for approximately 70-75% of malignancy cases [1, 3, 5]. It originates from the urogenital sinus and surrounds the distal urethra.

Conversely, PCa incidence in the **central zone** is very low, similar to other male secondary sexual tissues as seminal vesicles [4, 6]. This zone is located at the base of the prostate, between the other two zones and surrounding the ejaculatory ducts.

On the other hand, the **transition zone** is the principal site **associated with BPH pathogenesis** [5, 7]. It consists in two small lobules of glandular tissue surrounding the proximal urethra, comprising only 5% of the total prostate volume Although sharing a similar embryologic origin with the peripheral zone, the transitional zone exhibits a lower percentage (approximately 20-25%) of PCa cases. This discrepancy can be attributed to the more fibromuscular nature of the transitional zone stroma, as BPH primarily affects the fibromuscular stroma [1].

Prior to the implementation of PSA (prostate specific antigen) screening, this information highly valuable in classifying the risk of cancer lesions based on the affected site detected through ultrasonography.

Furthermore, there are neurovascular bundles located adjacent to the prostate within the fascia, which allows to surgically remove the prostate (prostatectomy) while preserving the nerve integrity [8, 9].

1.2. MOUSE PROSTATE

The **mouse prostate** is not fused compact structure; insetad, it is divided into **four distinct lobes**: the **anterior lobe** (AL), the **dorsal lobe** (DL), **ventral lobe** (VL), and lateral lobe (LL). These lobes display differences in ductal branching, histological appearance, gene expression and secretory protein profile [6, 10].

The **homology** between certain lobes and zones in the human and mouse prostate has been suggested by several authors [11, 12]. The dorsal and lateral lobes of mice are often combined for analysis and referred to as the "**dorsolateral lobe**". It has been proposed that this combined lobe corresponds to the human peripheral zone of the prostate [12, 13]. However, the Bar Harbor Consensus meeting in 2004 concluded that there is insufficient strong evidence to support this idea [14]. In contrast, analysis of gene expression profiles

Introduction

supports the similarity between the mouse dorsolateral lobe and the human peripheral zone [15]. Nevertheless, more recent data from single-cell studies on the mouse prostate have revealed significant molecular differences between the dorsal and lateral lobes, indicating that the mouse lateral prostate is most similar to the human peripheral zone[16].

In addition, it is noteworthy that mice very rarely develop spontaneous PCa [17]. This aspect remains a subject of controversy when considering rodents as an appropriate model system for research purposes.

1.3. CELLULAR ORGANIZATION IN THE PROSTATE

A **pseudostratified epithelium** composed of various cell types is present in the prostate of both humans and mice. These cells are arranged to form glandular acini that secrete into the luminal space, which ultimately converges upon a duct and into the urethra [18]. Luminal and basal cells have different morphology, functions, and cytokeratin expression (**Figure 2**).

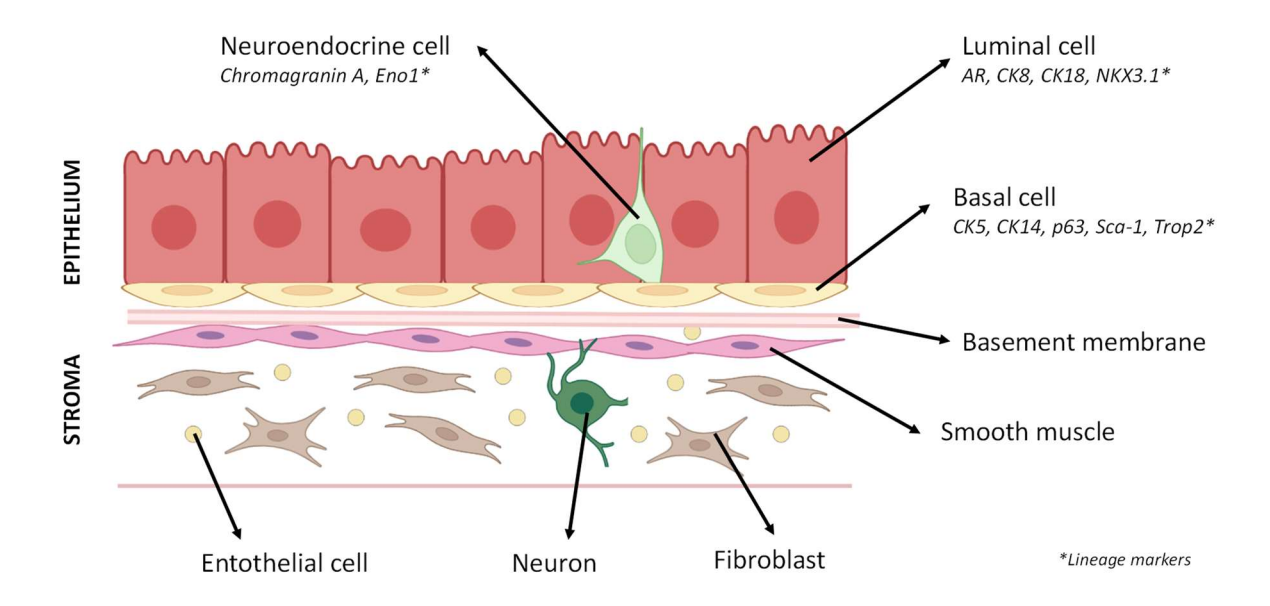


Figure 2. Lineage markers and cellular compartments of a normal human prostate gland. Luminal cells exhibit cytokeratin 8 (CK8) and CK18 expression, as well as and androgen receptor (AR) presence. Basal cells. on the other hand, demonstrate high levels of CK5, CK14 and p63, while displaying very low levels of AR. Neuroendocrine (NE) cells express NE markers such as synaptophysin and chromogranin A, lacking AR expression [19].

- Luminal cells are tall columnar epithelial cells forming a continuous layer. They
 express cytokeratins 8 and 18, as well as AR. These cells have also a secretory
 function, secreting proteins such as PSA.
- 2) <u>Basal cells</u> reside beneath the luminal layer and are non-secretory in nature. They express cytokeratins 5 and 14 [20-22]. While androgen receptor (AR) is expressed at high levels in luminal cells, basal cells exhibit low or undetectable levels of this receptor [23].

Lastly, within the prostate, there exist small subpopulations of cells that show neuroendocrine (NE) differentiation and are located attached to the basal lamina. These NE cells are associated with poor prognosis, tumor progression, and the development of androgen independence. Notably, malignant NE cells lack AR expression and consequently acquire resistance to androgens [24].

Furthermore, within the mesenchymal compartment of the prostate, various types of differentiated cells can be found, collectively forming a fibromuscular stroma situated on the opposing side of the basal lamina [18]. These distinct cell types encompass: 1) **smooth muscle cells**, which establish contact with the epithelium and enable contractile functionality to facilitate the expulsion of prostatic fluid during ejaculation [25], 2) **mature fibroblasts**, which contributes to the formation of an extracellular matrix characterized by abundant collagen fibers [18] and 3) **endothelial cells**, **nerves**, **lymphatic cells**, and **immune cells** residing within the stroma, collectively orchestrating stem cell state and tumorigenesis [18].

Hence, in each prostate gland, a diverse array of cells collaborates to fulfill the secretory function. However, the normal prostate function is compromised when cancer arises, leading to the malignant transformation of prostate cells.

Cancer, a broad category of diseases, can affect nearly any organ or tissue, characterized by the abnormal growth and uncontrolled proliferation of cells. This is often accompanied by the ability to spread throughout other parts of the body (metastasize).

Therefore, comprehending the unique characteristics and underlying mechanisms of PCa is of utmost importance.

PCa represents a particular type of **hormone-dependent cancer**, particularly in its initial stages, in which androgens and AR assume a pivotal role. it becomes imperative to gain a comprehensive understanding of the regulatory mechanisms involved in androgen signaling and identify potential targets for therapeutic interventions.

1.4. ANDROGEN RECEPTOR: STRUCTURE AND FUNCTION

Under physiological conditions, circulating androgens are essential for normal prostate development. The **AR** is **primarily activated by androgens**, both in physiological and pathological conditions.

AR is a **transcriptional regulatory protein** which belongs to the **steroid nuclear receptor** family, which includes other members such as the glucocorticoid receptor (GR), estrogen receptor (ER), progesterone receptor (PR) and mineralocorticoid receptor (MR).

The human AR gene (90 kb) encodes a protein consisting of 918 amino acids, organized into four distinct functional regions: 1) the amino-terminal transregulation domain (NTD), 2) the DNA-binding domain (DBD), 3) the hinge region (H), and 4) the ligand-binding domain (LBD) (Figure 3A) [26].

When androgens bind to the AR, they cause conformational changes in this receptor (Figure 3B,C). As a result, the AR dissociates from the heat shock protein-90 (HSP90) complex, undergoes phosphorylation, engages in homodimerization, and translocates to the nucleus. Within the nucleus, the AR, in association with coregulatory factors, interacts with androgen-responsive elements (AREs) located in the promoter regions of androgen-regulated genes. Examples of such genes include KLK3, TMPRSS2, FKBP5 and PSA [27].

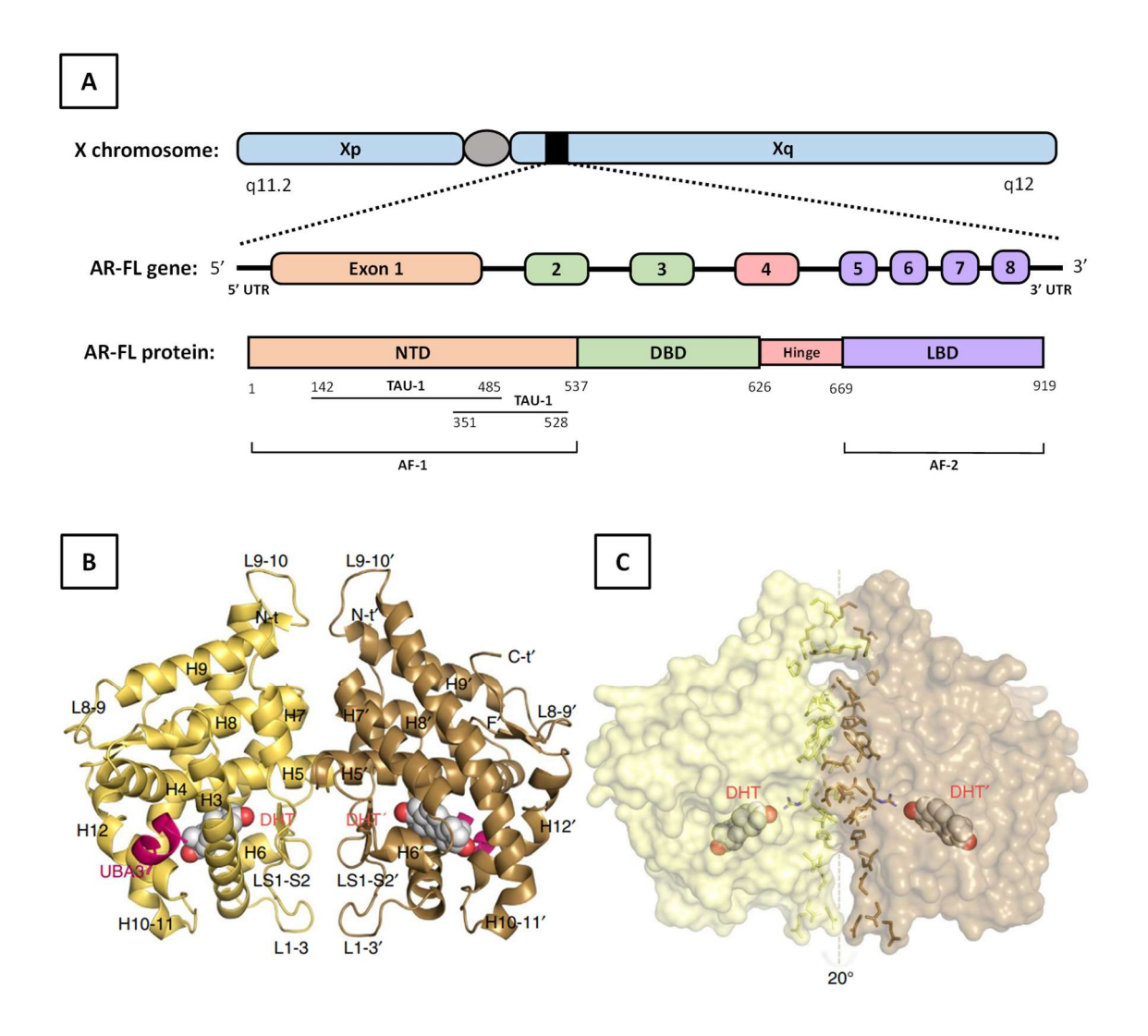


Figure 3. The human androgen receptor gene and the AR-LBD dimer interface. A) Schematic gene and protein structure for the full-length AR (AR-FL). The AR gene, located on the X chromosome (Xq11.2), consist of 8 exons. The correspondence between exons and each protein domain is illustrated by color identity; NTD, DBD and LBD. The NTD contains the AF-1 transactivation domain, which is responsible for strong transcriptional activity and comprises two major transactivation units, TAU-1 and TAU-5. The LBD contains the weaker AF-2. B) Overall structure of the AR-LBD core dimer, with two monomers shown in yellow and brown as cartoons. Dihydrotestosterone (DHT) is represented and highlighted as a cartoon. (C) Surface representation of the AR-LBD homodimer, oriented and colored as B. A was adapted from Ehsani M, David FO, Baniahmad A. (2021) [28]. B and C were extracted from Nadal, M., Prekovic, S., Gallastegui, N. et al. (2017) [29].

In a concurrent research project within this thesis, we have examined the significance of mutations affecting the dimer interface of the AR ligand-binding domain (AR-LBD) and their impact on the structure, protein interactions, and drug response. Our findings demonstrate that these selected mutations have the ability to modulate AR-dependent transcription and the response to antiandrogens by triggering an allosteric switch in the AR-LBD. This switch leads to increased exposure of a critical methylation target, Arg761 [30].

In addition, an extensive list of over 300 potential **AR coregulators** have been identified [31]. These coregulators serve diverse functional roles as either coactivators or corepressors of AR activity. At the molecular level, these coregulators can encompass transcription factors, kinases, molecular chaperones, epigenetic proteins, and more [32]. The levels of AR coregulators can be altered during the progression of PCa, and their presence can induce changes in the ligand specificity of AR [33, 34].

2. PROSTATE CANCER

2.1. PROSTATE CANCER INCIDENCE AND ETIOLOGIC FACTORS

PCa is predicted to be the **most commonly diagnosed cancer in men** and the second leading cause of cancer-related deaths among men, as reported by American Cancer Society. It is estimated that approximately 1 in 7 men will be diagnosed with this cancer during their lifetime, and that 1 in 39 men will die of the disease [35]. Within the past years, PCa mortality has decreased in most of the developed countries, as a consequence of advances in treatment and early detection [36].

Age is considered the primary contributing factor to PCa, with approximately 75% of patients being diagnosed after the age of 65 in Europe [37]. However, other factors such as family history, racial disparities, lifestyle choices (particularly smoking), and certain physical conditions like obesity also play a significant role in the incidence of PCa [38].

2.1.1. Iniciation and progression of prostate cancer

PCa tumors are generally multifocal, meaning that **multiple tumor foci** arise independently within the same prostate [39]. This phenomenon explains why palpable cancers often consist of multiple Gleason grades [40]. In fact, multifocal tumors are also associated with **genotypic heterogeneity** [41].

Therefore, the prostate can undergo **multiple neoplastic transformation events**. However, most of them remain latent and do not progress (subclinical stage). The activation or suppression of critical events or pathogenic programs determines whether the latent disease progresses to a clinical stage.

This malignant transformation as a multistep process is initiated through a condition known as **Prostatic Intraepithelial Neoplasia** (PIN), in which clumps of cancer cells remain confined into the prostate glands. PIN lesions are widely recognized as precursor lesions of PCa (**Figure 4**). At this stage, basal cells are present but reduced in number compared to PCa, as the proliferation primarily occurs in luminal epithelial cells, leading to **luminal hyperplasia**.

There is a strong correlation between PCa progression and aging, making it predominantly a disease affecting older men. However, the presence of histologic foci of PCa in healthy men of between the ages of 20 and 40 suggests that **cancer initiation occurs** at an early age, albeit in a latent form (known as latent carcinoma) [42, 43].

During progression, these cancer cells acquire enhanced proliferative capacity and aggressive properties, eventually infiltrating the stromal tissue surrounding the prostate gland. Eventually, the accumulation of multiple gene mutations within the tumor cells enables them to **invade adjacent organs** and **metastasize** once reached the bloodstream and lymphatic system (**Figure 4**).

Although human PCa exhibits significant heterogeneity, more than 95% of cases are classified as **adenocarcinomas** (luminal phenotype). Nevertheless, the origin of PCa cells

Introduction

remains a subject of debate, with evidence suggesting that both luminal [44-47] and basal [45, 46, 48-50] cells can serve as the initiating cells for cancer development.

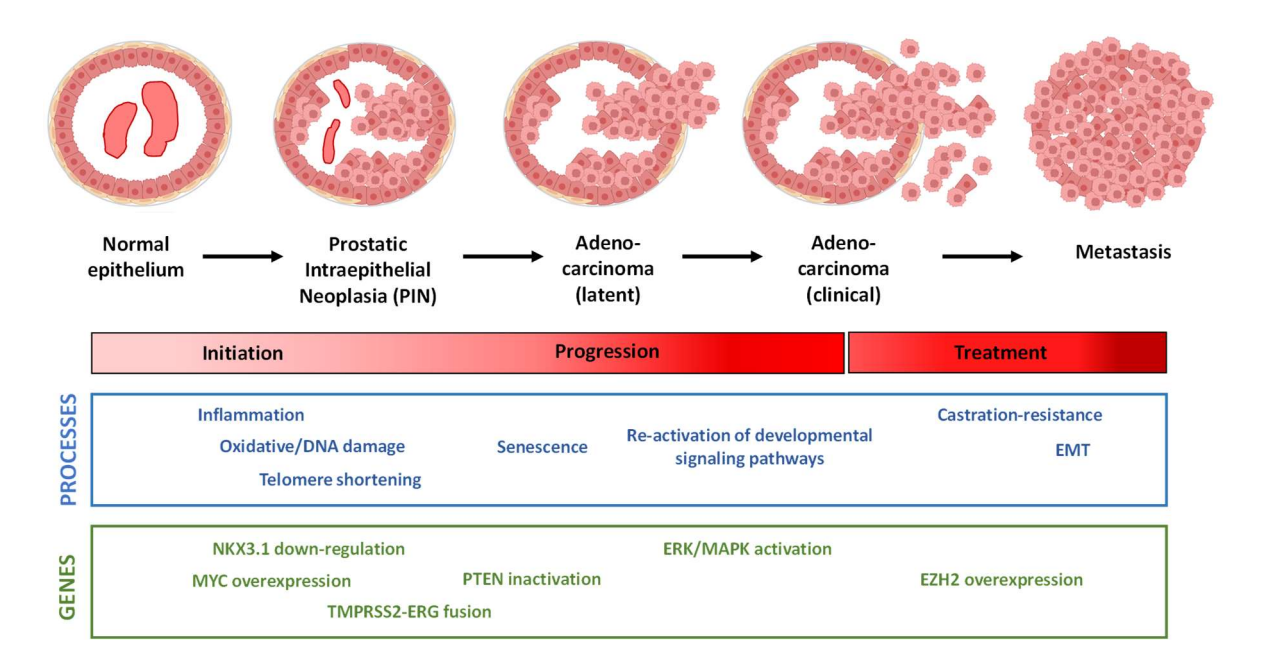


Figure 4. Prostate cancer progression. This figure depicts the progression stages of PCa, along with the corresponding processes or genetic modifications associated with each stage (adapted from Shen et al. 2010).

PCa arising from many mice models also exhibits a relatively predominant **luminal phenotype**, although it may differ in certain histological features from human prostate adenocarcinoma [12].

2.1.2. Genetic and molecular mechanisms of prostate cancer initiation and progression

Several key molecular events have been identified that can initiate or promote PCa. These events include:

NKX3.1 downregulation. NKX3.1 is a PSA-regulated homeobox gene whose loss-of-heterozygosity is a key event in PCa initiation (loss of chromosome 8p21). NKX3.1 haploinsufficiency occurs in most of high-grade PIN lesions and adenocarcinomas [51-53].

- 2) TMPRSS2-ERG translocations. The gene fusion of the 5' untranslated region of TMPRSS2 to ERG (TMPRSS2:ERG) has been found in approximately 50% of localized PCa [54]. This fusion results in the expression of a N-terminally truncated ERG protein, whose expression is then regulated by the TMPRSS2 promoter (androgen-responsive).
- 3) MYC up-regulation. Copy number of MYC oncogene is frequently increased (by the somatic amplification of 8q24 chromosomal region) in advanced prostate tumors [55, 56]. Therefore, this event has been associated with disease progression and is considered a marker of poor prognosis and recurrence. Furthermore, MYC overexpression has been also proposed as a critical oncogenic event driving the initiation of human PCa. This proposal is based on the observation of nuclear MYC up-regulation in PIN lesions and carcinomas that lack of gene amplification [57].
- 4) Epigenetic regulation. The utilization of massive parallel sequencing in tumor specimens from PCa patients has facilitated the identification of genetic alterations that affect genes involved in epigenetic processes, such as DNA modification, histone modification or nucleosome remodeling. Such processes can drive tumorigenesis in PCa, which has been extensively reviewed by our research group in a parallel paper conducted during the duration of this thesis project [58].
- 5) PTEN and PI3K pathway. PTEN acts as a negative regulator of the Phosphoinositide 3-kinase (PI3K) that suppresses the PI3K-AKT-mTOR pathway, which is involved in cell survival, proliferation, and energy metabolism. Loss of tumor suppressor PTEN has been observed in approximately 40% of human PCa specimens [59]. PTEN copy number loss is an early event in prostate carcinogenesis and is correlated with progression to aggressive and castration-resistance disease [60-62].

Despite the significance of these molecular features, they are not currently utilized for the regular diagnosis of PCa, as explained in the subsequent section.

2.2. DIAGNOSIS OF PROSTATE CANCER

Most prostate cancers are initially detected through screening methods such as a **PSA blood test** or a **digital rectal exam** (DRE). Early detection is essential to increase survival rates, as the risk of mortality increases when cancer cells metastasize from the prostate to distant tissues [63].

2.2.1. Prostate Specific Antigen (PSA) screening

PSA is a serine protease belonging to the kallikrein family, which is typically produced in normal prostate secretions. When the normal architecture of the prostate is disrupted or compromised, PSA is released into the bloodstream [64].

In 1991, the use PSA testing was proposed to be used as a first-line screening tool for PCa in individuals with negative DRE findings [65]. The adoption of **PSA screening** was adopted and led to the identification of previously undetected cases of PCa. Consequently, the combination of PSA screening benefits and advancements in the treatment of recurrent and progressive disease contributed to a **decrease in PCa mortality rates** [66].

The widespread implementation of routine PSA screening has encountered challenges due to concerns regarding the potential unnecessary biopsies and the associated **risks of over-diagnosis**, leading to ineffective treatments and significant adverse effects [67, 68].

2.2.2. Grading of biopsies and staging

Following PSA and DRE assessments, the diagnosis of PCa is confirmed (in men with elevated PSA levels) through the analysis of prostate biopsies. **Histopathological grading**, based on the Gleason system, is then conducted, serving as a pivotal prognostic indicator in PCa [69].

This grading and scoring system developed in 1966 [70] is based on the histologic pattern of PCa cell arrangement, glandular differentiation state, and growth pattern in the stroma [71]. This system employs five grade patterns to generate a histologic score ranging

from 2 to 10. These patterns are depicted in a reference drawing used as a guide for recognizing different Gleason grades [69]. A **Modified Gleason Scoring Classification** has been achieved through consensus for **prostate tumor classification**, allowing to group lowand high-grade tumors more precisely [72-74] (**Figure 5**).

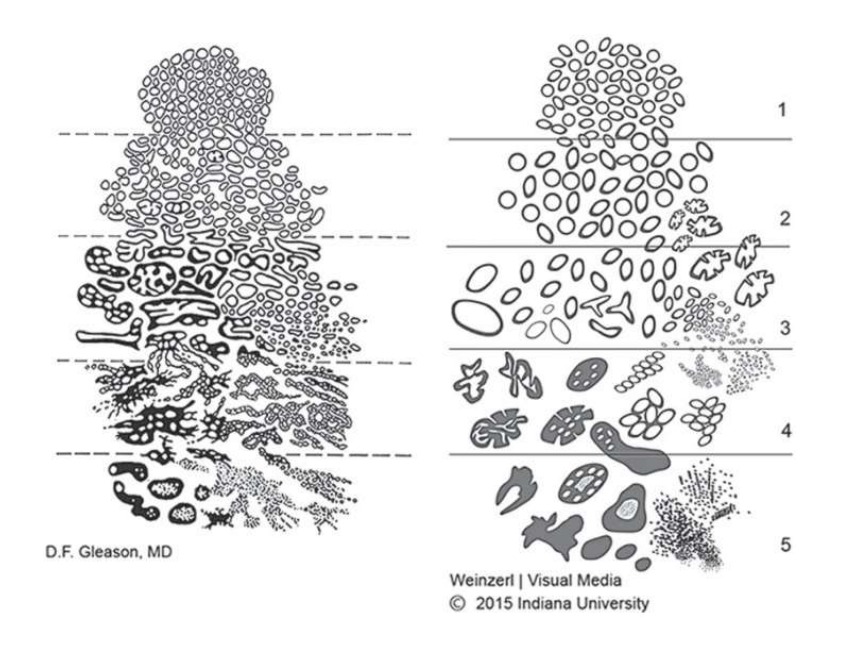


Figure 5. Grading of prostate cancer biopsies. Schematic comparison between the original Gleason grading and with the current model consisting of 5 groups. From Sehn, 2018 [72].

The necessity for **staging** is determined by PSA levels [75] and tumor grade, only being recommended to be performed **in high-risk cancer** [76]. Staging, which aims to assess the extent of cancer spread, continues to rely primarily on the **tumor-node-metastasis** (TNM) system. This system takes into account the size of the primary tumor (including its invasion of nearby tissues, T1-4), involvement of nearby lymph nodes (N0 or 1) and the presence of distant metastasis (M0 and 1a-c) [71, 77].

2.2.3. Indolent vs aggressive disease

The majority of early-stage prostate cancers that are diagnosed exhibit an indolent course, characterized by low-grade features. These patients often experience a long period without tumor progression or metastasis [78, 79]. However, the inability to precisely

distinguish between indolent and aggressive PCa tumors is a **major clinical challenge**. Particularly, low Gleason grade tumors represent the main controversial paradigm in clinical management. Consequently, there is a pressing need to comprehend the molecular mechanisms of tumor initiation and progression in order to identify **novel prognostic markers** capable of distinguishing between indolent and aggressive tumors.

2.3. MANAGEMENT OF PROSTATE CANCER

Although screening guidelines have advanced in preventing and reducing the overtreatment of non-lethal PCa, the management of aggressive variants remains a challenge. Existing therapies are insufficient to significantly reduce mortality rates associated with metastatic PCa.

2.3.1. Active surveillance and watchful waiting

While watchful waiting involves monitoring the clinical progression of cancer to determine the need for immediate treatment, active surveillance entails repetitive PSA test and biopsies [80, 81]. Active surveillance an accepted approach for managing men with low-risk PCa [82]. It aims to guarantee the quality of life (QOL) of patients with favorable tumor characteristics by delaying or avoiding adverse effects associated with aggressive therapies, thus allowing for a more measured intervention strategy.

2.3.2. Surgery

Radical perineal prostatectomy technique was firstly described in 1905 as a treatment for PCa [83]. In 1947, retropubic approach was introduced [84], which gradually became the standard approach to perform prostatectomy. Furthermore, advancements in understanding continence mechanisms and nervous physiology led to the development of modern retropubic radical prostatectomy [85] resulting in reduced morbidity. The introduction of this nerve-sparing technique further improved erectile function and continence, ultimately becoming the standard option for prostatectomy [86].

2.3.3. Radiotherapy

Initially, radiotherapy as a monotherapy was used to eradicate PCa cells until the discovery of Androgen Deprivation Therapy (ADT) [87]. The utilization of combination therapy demonstrated that **ADT enhances the radiosensitivity** of cancer cells, rendering them more susceptible to the damaging effects of radiation. This synergistic approach has led to notable improvements in various clinical outcomes, including overall survival, local progression, disease-free survival, biochemical failure, and control of metastatic sites, particularly in men diagnosed with localized but high-risk PCa [88-91].

2.3.4. Androgen Deprivation Therapy (ADT)

The androgen-dependence of PCa [92] constitute the basis for the use of ADT in the treatment of this disease, mainly in patients with disseminated PCa. **Pharmacological methods of castration** (inhibiting androgenic synthesis or action) have replaced surgical castration as the standard treatment of PCa patients.

Luteinizing hormone-releasing hormone (LHRH) agonists are among the compounds used in this approach, with Goserelin acetate being the first to be discovered [92]. The subsequent characterization of AR has enabled the development of antiandrogens with increased specificity, allowing them competitively bind to the AR and effectively block the actions of testosterone and DHT, such as cyproterone acetate [93] or flutamide [94]. However, despite de use of ADT, prostate cancers often recur and progress even in the presence of reduced circulating testosterone, leading to the development of primary Castration-Resistant Prostate Cancer (CRPC) or metastatic CRPC (mCRPC).

2.3.5. Chemotherapy

The therapeutic benefit for chemotherapy in PCa patients with locally advanced disease or as a primary treatment option is limited. However, in the context of mCRPC, chemotherapy has demonstrated improvements in QOL and progression-free survival [71].

In 2004, the combination of **docetaxel** (a cytotoxic agent) with prednisone (a glucocorticoid) was shown to improve QOL and overall survival in mCRPC patients [95]. As a result, taxanes, including docetaxel, became the standard chemotherapy regimen for treating hormone-refractory PCa. Furthermore, the TROPIC study revealed that treatment with **cabazitaxel** plus prednisone led to increased overall survival in mCRPC patients who had experienced disease progression during or after docetaxel-based therapy [96].

3. ANDROGEN RECEPTOR AND CASTRATION-RESISTANT PROSTATE CANCER (CRPC)

3.1. RETENTION OF AR SIGNALING IN CRPC

As previously explained, despite the initial success of antiandrogens in prolonging the survival of PCa patients, the majority of these cancers eventually develop resistance to combined ADT after a few years. Despite castration, levels of testosterone and DHT in the local PCa are reduced, but still sufficient to activate the AR [97]. Consequently, the expression of AR-target genes is sustained in castration-resistant tumors [98].

In CRPC, there is **intratumoral** *de novo* **synthesis of androgens**, allowing the cancer cells to bypass the low levels of circulating androgens [99]. This shift in the androgen pathway involves a transition from androgen-dependent cells using a paracrine mechanism involving stromal cells to an **autocrine mechanism** within the castration-resistant cells themselves [100, 101]. As a result, the potential **upregulation of steroidogenic enzymes** sustains the production of local testosterone and DHT in CRPC, which is sufficient to activate the AR and partially restore its transcriptional activity [102].

Therefore, androgen depletion ultimately leads to a rise in PSA levels (PCa recurrence) in most of the cases. This recurrent state of the disease is commonly referred to as "castration resistant". It is crucial to differentiate this stage from "advanced" PCa, which remains AR-dependent for growth and survival.

Various mechanisms have been reported to be involved in the **transition to CRPC**, which contribute to the increased transcriptional activity of the AR observed in most cases.

The improved understanding of these molecular mechanisms has facilitated the identification of novel therapeutic targets.

- AR expression can be upregulated through the amplification of AR gene copy number, which is observed in approximately one-third of castration-resistant carcinomas [103, 104]. Additionally, amplification of AR enhancers can also contribute to increased AR expression[105].
- 2. Certain AR mutations enhance the **receptor's response to agonists** [106], resulting in a gain-of-function effect that may lead to increased protein stability.
- Other AR mutations are associated with a receptor that becomes responsive to alternate non-androgen ligands, like glucocorticoids [107], or responsive to antagonistic drugs [108].
- 4. Ligand-independent activation of AR can occur through dysregulated cofactors, aberrant signal transduction pathways, or specific mutations [109, 110]. Constitutively active AR variants lack ligand binding domains (LBD) due to alternative splice (alternative splice isoforms) [111].
- 5. AR-independent mechanisms also contribute to the progression to mCRPC and treatment resistance [106]. Several signaling pathways, including glucocorticoid receptor activation, epigenetic regulation, immune-mediated resistance, and NE differentiation, play a role in this process [112].

In fact, **AR gene amplification** occurs in a significant proportion (63%) of CRPC patients, whereas it is extremely rare in hormone-sensitive primary patients [56].

AR variants (ARVs) gained focus over the 2000s decade as a mechanism to explain resistance. ARVs are truncated isoforms of AR protein that often lack the ligand-binding domain (AR-LBD), leading to AR activation in the absence of androgens [113]. ARVs are frequently observed in CRPC, but are rare in benign prostate tissues and primary cancers. Structural rearrangements and alternative splicing of the AR gene generate ARVs in CRPC [114]. Among these variants, AR splice variant-7 (AR-V7) has been extensively studied due

to its high frequency of detection in CRPC [115] and its potential utility as a marker for treatment selection in mCRPC patients [116], since AR-V7 has been **implicated in antiandrogen resistance** [117].

The improved understanding of AR biology and reactivation mechanisms has led to the development of therapeutic agents that provide a survival benefit in CRPC patients, thereby influencing drug treatment and patient management.

3.2. TREATMENTS OF CRPC

Second-generation antiandrogens were developed as more potent drugs to overcome castration-resistance. These drugs act through two main mechanisms: a) the inhibition of the testosterone biosynthesis (**abiraterone**), or b) the antagonism of the AR, preventing the binding of androgens to the AR and its nuclear translocation (**enzalutamide**, **apalutamide**, and **darolutamide**) (**Figure 6**).

Abiraterone was developed as an irreversible steroid inhibitor of CYP17, an enzyme involved in androgen biosynthesis. It has proven to become an effective therapy for mCRPC and chemotherapy-resistant PCa patients, showing a 3.9 months benefit in overall survival compared with placebo [118]. Additionally, data from the phase III LATITUDE trial demonstrated that combination of abiraterone, prednisone and ADT resulted in significant improvements in progression-free and overall-survival in newly diagnosed high-risk metastatic castration-sensitive PCa [119].

Enzalutamide, an AR antagonist that prevents the translocation of AR into the nucleus, has shown clinical benefits in CRPC patients. The phase III PREVAIL trial, which included chemotherapy-naïve CRPC patients, reported a reduction in radiographic progression and death with enzalutamide treatment [120]. Similarly, the phase II TERRAIN trial compared enzalutamide and bicalutamide (the previously agent antiandrogen) in asymptomatic or mildly symptomatic mCRPC patients, demonstrating superior progression-free survival with enzalutamide [121]. Furthermore, enzalutamide treatment has shown favorable outcomes in CRPC patients who experienced disease progression after chemotherapy, leading to increased survival rates (AFFIRM trial) [122].

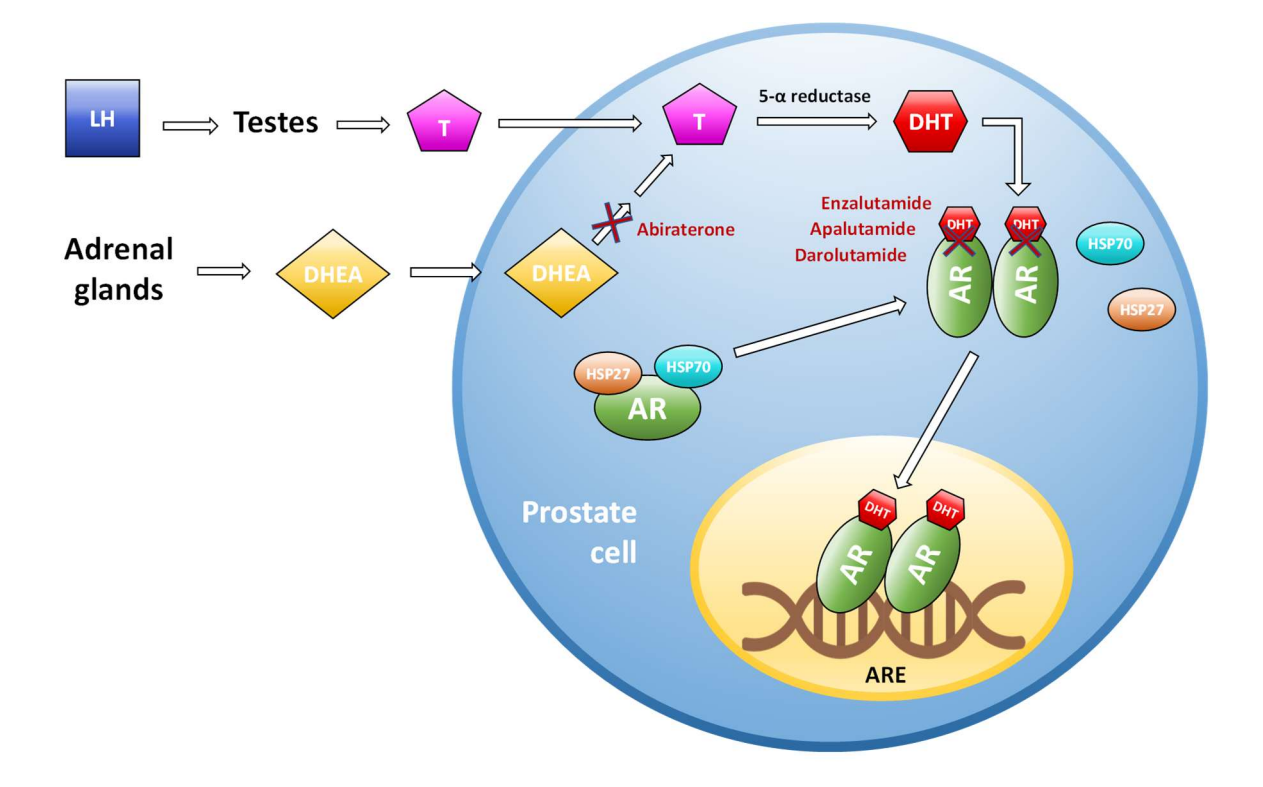


Figure 6. Biosynthesis of dihydrotestosterone (DHT) and the subsequent signaling via the Androgen Receptor. Luteinizing hormone (LH) stimulates the Leydig cells of the testes, which produce the majority of testosterone (T) in the body (ranging from 50% to 90%, depending on age) [123]. Nevertheless, testosterone precursor compounds like dihydroepiandrostenedione (DHEA) are produced in adrenal glands. These adrenal precursors are transported and absorbed by the prostate, where they undergo enzymatic conversion to testosterone by the action of sequential enzymes, including 17α -hydroxylase/C17,20-lyase (CYP17), which is the target of abiraterone. Subsequently, testosterone is converted into DHT, its most common and active metabolite, by the enzyme 5α -reductase. Androgens, particularly DHT, bind to the AR, leading to the dissociation of chaperone proteins (HSP27 and HSP70). Upon ligand binding, AR molecules form homodimers and translocate to the nucleus, where they interact with androgen responsive elements (ARE) to activate downstream target genes. Enzalutamide, apalutamide and darolutamide compete with androgens for the ligand-binding site of the AR, thereby preventing the translocation of this transcription factor into the nucleus.

However, about 20–40% of CRPC patients do not initially respond to abiraterone and enzalutamide [122, 124]. Even among those who initially respond, the rate of patients acquiring **treatment-resistance** is high [125]. Notably, patients who become resistant to abiraterone also develop cross-resistance to enzalutamide and vice versa, which is mediated by AR reactivation [126].

In addition, **glucocorticoid receptor** (GR) **activation** confers resistance to antiandrogens such as enzalutamide by circumventing AR blockade [127]. This resistance mechanism arises from the high homology between the DNA binding domains of the GR and AR. Consequently, both receptors can recognize similar DNA response elements to activate target genes that are crucial for the survival and growth of PCa.

The AR variant **AR-V7** has also been **associated with resistance** to abiraterone and enzalutamide [117]. Niclosamide, an inhibitor of AR-V7, has demonstrated efficacy in overcoming enzalutamide resistance in precranial models [128].

In conclusion, **CRPC** is characterized by **high metastatic potential** and remains challenging to treat. Current antiandrogenic standard therapies provide only modest survival benefit, with modest extensions of a few months. Unveiling the vulnerabilities that emerge due to the acquisition of resistance to antiandrogen therapies is crucial for developing novel treatments for prostate cancer and guiding future clinical trials.

3.3. METASTATIC PROSTATE CANCER

The **primary cause of mortality PCa** is attributed to **metastatic disease** that fails to respond to treatment and progresses into castration-resistance [129]. In most of PCa metastases, tumor cells reach the **bone**, leading to the formation of osteoblastic lesions [130, 131]. **Lymph nodes** adjacent to the primary tumors also serve as significant sites of metastasis [132]. The **lung**, **liver**, and **pleura** are common locations for PCa metastasis.

When PCa cells metastasize in the bone marrow, a complex interplay takes place between cancer cells, osteoblasts, and osteoclasts, resulting in **dynamic bone remodeling** processes that support the survival and growth of cancer cells [19].

The paramount interest of understanding the mechanisms involved in cancer metastasis aims to develop more effective treatments for this lethal disease, which is intrinsically related with CRPC.

4. PROSTATE CANCER MODELS

In order to comprehend the initiation, progression, and drug resistance mechanisms of PCa, various models have been employed in research over the past decades. However, each model possesses inherent limitations, necessitating the utilization of complementary models to address specific challenges.

4.1. PROSTATE CANCER CELL LINES

Despite the fundamental role that two-dimensional (2D) models have played in PCa research and their continued widespread use in *in vitro*, their primary limitation lies in their inability to replicate the complex tumor microenvironment. Unlike other tumor types, the pool of **available PCa cell lines is notably limited (Table 1)**, thereby restricting the exploration of the diverse phenotypes and genetic backgrounds observed in patients.

Cell line	Origin	AR
LNCaP	Lymph node from metastatic PCa	AR sensitive
LNCaP-AI	From LNCaP	AR insenstive
LNCaP C4-2	From LNCaP	AR insensitive
VCaP	Bone metastasis	AR splice variants
PC3	Bone metastasis	AR-negative
DU145	Brain metastasis	AR-insensitive
22Rv1	Xenograft	AR splice variants/sensitive

Table 1. Most commonly used PCa cell lines for research.

4.2. XENOGRAFT MODELS

Xenograft models of human PCa involve the implantation of patient-derived tumors (known as **patient-derived xenografts** or PDX) or cell lines into **immunodeficient mice**, either **orthotopically** within the prostate or transplanted onto the flank. These models have proven invaluable in elucidating the molecular mechanisms underlying PCa tumor progression and therapeutic resistance, as well as predicting clinical outcomes and guiding drug development efforts [133].

Unlike cancer cell lines, **PDXs maintain** the histopathology, tumor heterogeneity, genomic alterations, and molecular profiles of the original patient tumor. However, these models have several **limitations**:

- The heterologous microenvironment is a consequence of grafting human cells or tumors into a different species, a factor that may not completely reproduce the native tumor microenvironment.
- 2) If the engraftment is not performed orthotopically, the models may fail to account for the influence of **stromal components**.
- 3) The use of immunodeficient hosts precludes the study of interactions between PCa cells and immune cells, limiting our understanding of the immune response during tumor progression.

4.3. GENETICALLY ENGINEERED MICE MODELS (GEMM)

The utilization of engineered transgenic and knock-out represents a **pivotal** approach in PCa research, allowing to recapitulate specific and relevant genotypes. Initially, transgenic models were developed to overexpress potent viral oncogenes such as Myc and ERG, resulting in highly aggressive PCa with frequent metastatic progression [134].

The second-generation of Genetically Engineered Mice Models (GEMM) was focused on introducing **loss-of-function mutations** in candidate genes implicated in human PCa development, utilizing various transcriptional regulatory elements from PSA, Nkx3.1,

Hoxb13, and TMPRSS2 [44, 135-138]. The compliance of GEMM has proven to be valuable in replicating a **wide range of disease evolution of PCa**, from precursors (PIN) to metastases. However, a major limitation of these models is their inability to accurately reproduce the metastatic characteristics observed in human PCa, predominantly bone metastases. Nevertheless, different models show visceral metastasis to the lungs and liver, including Pten/p53 [139], Pten/Myc [140] and Pten/p53/Rb1 [141].

4.4. A GEMM MODEL TO RECAPITULATE CRPC

Multiples investigations have demonstrated the significant involvement of the tumor suppressor *Pten* in PCa given its impact on activating the AKT/mTOR signaling pathway through AR signaling [142]. Furthermore, mutations in *p53* are often correlated with tumor recurrence, castration resistance, and tumor grade [143]. The concurrent inactivation of both *Pten* and *p53* triggers the development invasive and lethal PCa [144].

More interesting, **loss-of-function mutations of** *p53* **and** *PTEN* are predicted to be among the most **common somatic alterations in human CRPC**. According to findings from The Stand Up To Cancer (SU2C) consortium, approximately 53% mCRPC patients display somatic alterations in *p53*, while approximately 41% present alterations in *PTEN* [145]. It is noteworthy that these alterations are less frequently observed in locally invasive primary tumors. However, in the context of mCRPC, approximately 30% of cases are characterized by **concurrent alterations** in both *p53* and *PTEN* [145-147].

In GEMM, the deletion of *Pten* produce PCa initiation through PIN formation, followed by progression to adenocarcinoma and eventual metastasis It is important to note that the reduction or loss of *Pten* in prostate cancer predisposes to CRPC [142, 148]. However, GEMM of single *p53* loss-of-function show modest PCa phenotypes [149, 150].

Given the high prevalence of co-mutation involving p53 and PTEN in human CRPC, it becomes pertinent to employ this genetic context in a GEMM that incorporates **an inducible Nkx3.1**^{CreERT2} **driver**. This methodology allows for the targeted deletion of these genes in the **adult prostate epithelium**, mirroring the occurrence of somatic mutations observed in

Introduction

human cancer. As a result, this approach recapitulates and models the key characteristics of the human disease.

The Nkx3.1^{CreERT2} driver is a knock-in allele in which a **tamoxifen-inducible CreERT2** cassette is placed under the transcriptional control of the endogenous **Nkx3.1 promoter**, a **prostate-specific gene**. This design enables the heterozygous inactivation of Nkx3.1, resulting in the **formation of PINs** [44]. by administering tamoxifen in a controlled manner, gene deletion can be specifically controlled in adult mice, particularly targeting the **luminal epithelial cells** of the prostate [44], which are known to be a cell of origin for PCa [151]. Within our laboratory, we have conducted further investigations to characterize the phenotypes arising from Nkx3.1^{CreERT2/+}; Pten^{flox/flox}; Trp53^{flox/flox} (**NPp53**) and Nkx3.1^{CreERT2/+}; Pten^{flox/flox} mice (**NP**) mice models (**Figure 7**), which were originally generated by the research group led by Cory Abate-Shen.

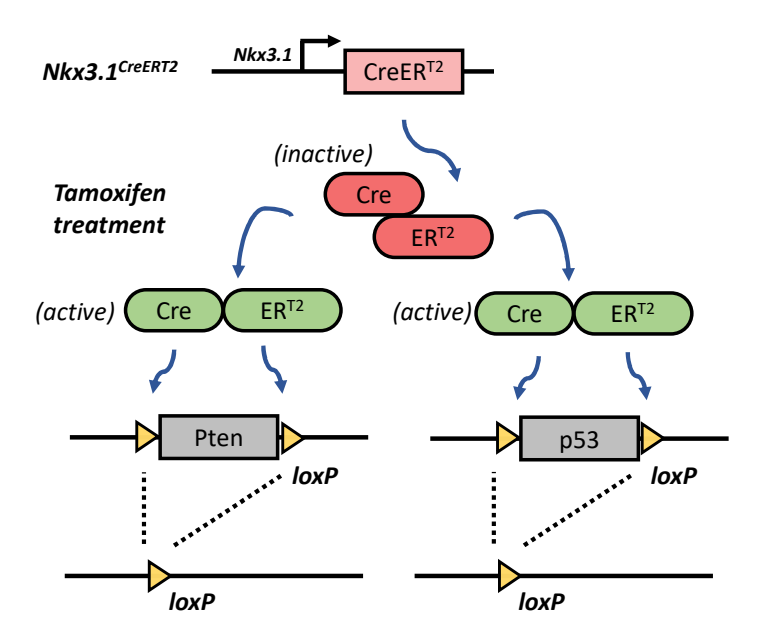


Figure 7. Schematic representation of NPp53 GEMM generation. Upon tamoxifen treatment, Cre-Lox recombination occurs specifically in the prostate by the Nkx3.1 promoter, provoking the deletion of Pten and p53 genes.

In both **NP and NPp53 models**, the androgen-ablation achieved by surgical castration resulted in a profound reduction of androgen levels and the **development of CRPC** with **adenocarcinoma features**, resembling the human counterpart. By employing computational

algorithms, it was demonstrated they demonstrated that molecular drivers underlying NPp53 CRPC closely resemble those observed in human tumors exhibiting low *PTEN* and low *p53* status [152].

The administration of abiraterone on NP CRPC mice with resulted in a modest but significant reduction of this cancer phenotype. However, NPp53 CRPC growth was not inhibited by abiraterone treatment. This suggests that the co-inactivation of *Pten* and *p53* may inherently exhibit reduced responsiveness to abiraterone. Furthermore, among the abiraterone-treated NPp53 CRPC mice, there was a higher prevalence of non-adenocarcinoma phenotypes, including small-cell neuroendocrine-like characteristics, accompanied by increased tumor volume. Consequently, NPp53 CRPC possesses an underlying potential for non-adenocarcinoma phenotypes, which is further augmented by abiraterone treatment [152].

In summary, the NPp53 GEMM represents a good model for studying **mechanisms** of resistance to antiandrogens in the context of CRPC.

5. CRISPR/Cas9 IN BIOMEDICAL RESEARCH

The utilization of CRISPR/Cas9 technology has notably advanced the field of genome editing, allowing to rapidly generate germline and somatic modifications in mice [153]. This technology facilitates the precise manipulation of genes by enabling the insertion, deletion, point mutation, and translocation of relevant genetic elements. Moreover, CRISPR libraries can be employed to conduct high-throughput functional screenings, which prove valuable for investigating cancer in animal and *in vitro* models [154].

Genome-wide genetic screens using CRISPR/Cas9 offer a powerful approach to identify essential genes for cell survival and elucidate **synthetic lethal interactions**. These screens enable the systematic exploration of gene function in both healthy and diseased states, thus shedding light on underlying mechanisms and **potential therapeutic strategies** for various human diseases, including cancer [155-157].

Consequently, such screenings hold great potential for uncovering the intricate mechanisms underlying PCa development and antiandrogen resistance acquisition. In the following sections, we will outline the fundamental principles and implementation of CRISPR/Cas9 technology to address our research objectives.

5.1. CRISPR/Cas9 FUNCTION

CRISPR, which stands for Clustered Regulatory Interspaced Short Palindromic Repeats, is an adaptive immune system found in many bacteria and most archaea, serving as a defense mechanism against viruses. This system incorporates short DNA sequences derived from previous viral or plasmid invaders into the bacterial genome at a specific locus known as the CRISPR locus. This integration process establishes a "cellular memory" that enables the organism to recognize and combat future infections by identifying the newly encountered invaders as foreign entities. Subsequently, this system triggers the degradation of these invading sequences [158].

The short regions of the invader genome are integrated into the CRISPR locus called spacers, separated by repeat sequences. Transcription of these spacers generates RNA molecules known as CRISPR RNAs (crRNAs), which are subsequently loaded onto a Cas protein. This interaction forms an active ribonucleoprotein (RNP) complex. The crRNA guides the Cas protein to specifically recognize the invading sequences, leading to cleavage of the exogenous DNA through the nucleolytic activity of the Cas protein The identification of complementary sequences in the invading DNA is facilitated by the binding of Cas9 to specific regions within the foreign genome called Proto-spacer Adjacent Motifs (PAMs) [159]. Cas9 cleaves the DNA three base pairs upstream of the PAM site. Different Cas proteins derived from various bacterial or archaeal species exhibit specificity for distinct PAM sites. The most commonly employed Cas variant for genome editing originates from Streptococcus pyogenes (SpCas9, usually abbreviated as Cas9) and recognizes a PAM sequence of 5'-NGG-3'.

5.2. CRISPR/Cas9 FOR GENOME EDITING IN EUKARYOTES

Cas9 cleavage induces a double strand break (DSB), a form of cellular damage that can be repaired by two different DNA damage repair pathways: non-homologous end joining (NHEJ) and homologous recombination (HR). The canonical NHEJ directly rejoins the broken ends of the damaged DNA molecule. However, NHEJ is an error-prone repair mechanism, resulting in imperfect repair of the lesions. Consequently, this mechanism can generate deletions, insertions, or frameshift mutations, which are advantageous for generation of gene/protein knock-out. In contrast, HR is capable of introducing specific mutations, requiring a template to be used for accurate error-free DNA repair.

Hence, taking into account the regulation and the effects of DNA repair pathways in eukaryotes, it is feasible to generate precise mutations and indels in the genome utilizing CRISPR/Cas9 techniques. In this regard, Cas9 can be directed to specific sequences given the presence of a nearby PAM site. In mammalian cell culture, one prevalent approach involves employing plasmids encoding both the sgRNA sequence and the Cas9 protein is the most. The choice between a one-vector or two-vector system depends on whether the sgRNA and Cas9 are encoded within the same plasmid or separate plasmids, respectively.

5.3. ACTIVATION OR REPRESSION OF TARGET GENES USING CRISPR

CRISPR technology offers great flexibility for genome manipulation, as Cas enzymes can bind to the targeted DNA independently of their ability to cleave this target. By introducing specific point **mutations** in the **catalytic domains of Cas9**, a **nuclease-dead** form called **dCas9** can be generated. Unlike active Cas9, dCas9 does not cleave the DNA but can be directed to specific genomic sites by the sgRNA.

Targeting transcription start sites with dCas9 is sufficient to repress transcription by blocking the initiation process. However, dCas9 can also be utilized for gain and loss of function studies by fusing it with transcriptional activator domains (e.g. VP64) or repressor domains (e.g. KRAB). This fusion generates an RNA-guided transcription activator or inhibitor, enable precise **control over gene expression**. These strategies, known as **CRISPR**

activation (CRISPRa) and **CRISPR interference** (CRISPRi), respectively, allow for gene regulation without modifying the underlying nucleotide sequence [160, 161].

5.4. CRISPR SCREENINGS

Various types of CRISPR screens are available, each serving different purposes such as assessing cell survival/proliferation, drug sensitivity, fluorescent reporters, and single-cell transcriptomes.

Prior to the development of CRISPR interference (CRISPRi), gene silencing in eukaryotes relied on **RNA interference** (RNAi) techniques like miRNA and siRNA. However, it is important to note that CRISPRi and RNAi approaches have distinct characteristics and properties [162].

- 1. The dCas9-sgRNA complex functions by **inhibiting** both the initiation and elongation of RNA polymerase (RNAP) **at the transcriptional level**, whereas RNAi operates by blocking the initiation of ribosomes at the post-transcriptional level.
- 2. RNAi gene silencing targets the 5' untranslated region (UTR) of mRNA. In contrast, **CRISPRi** is directed towards the **promoter or the ORF** of the gene, enabling more stable and efficient interference.
- 3. The interaction between the RNAi molecule and its target mRNA relies on chaperone proteins for stabilization, while in CRISPRi, the Cas9 protein acts as a roadblock.

As a result, CRISPRi offers a more **robust mechanism** for gene silencing, making it particularly suitable for implementation in screenings.

5.4.1. Screenings for synthetic lethal interactions

The concept of synthetic lethality describes a scenario in which the **combined** presence of mutations or **alterations** in **two separate genes** results in cell death, while individual mutations in either gene alone do not have the same effect.

In the field of cancer research, synthetic lethality has been extended to include the inactivation of one gene and the targeted **inhibition of the other through pharmacological** means. This leads to death of cancer cells, while normal cells lacking the specific genetic modification remain unaffected by the drug [163].

Synthetic lethal screenings are typically carried out in a pooled format to facilitate high throughput with various internal controls. Typically, target cell lines are infected with lentivirus containing a library of sgRNAs. This allows for the evaluation of the individual effects of gene knock-down on cell growth via next-generation sequencing. Following a defined period of drug treatment, typically 1-3 weeks, the abundance of each gRNA is assessed. Guide sequences associated with the loss of cell viability will exhibit reduced abundance in the drug-treated condition compared to their abundance in the untreated pool [163]. In this manner, genes implicated in drug response can be efficiently identified.

The recent success of **PARP inhibitors** in treating **BRCA-mutant ovarian cancers** represents the primary clinical example of applying synthetic lethality to target the loss of tumor suppressor genes [164]. This discovery relies on the fact that PARP, BRCA1, and BRCA2 all participate in DNA repair by HR. Consequently, tumor cells harboring BRCA1 or BRCA2 mutations become susceptible to PARP inhibition. In contrast, normal cells possess at least one functional copy of BRCA1 or BRCA2, thereby minimizing the impact and toxicity of such treatment on healthy cells.

Hence, synthetic lethal screenings provide crucial insights into the mechanisms involving drug resistance or sensitivity. Additionally, these **vulnerabilities** can be exploited to develop targeted drug treatments that mimic the identified **synthetic lethal interactions**, thereby improving the efficacy of current therapies. Consequently, the implementation of **combination therapies** presents a potential strategy to **overcome drug resistance** mechanisms.

6. ROS METABOLISM AND HYPOXIA

6.1. ROS AND CELLULAR DAMAGE

6.1.1. Free radicals and ROS

A free radical is defined as a molecule that contains one or more unpaired electrons, rendering it highly reactive to easily participate in chemical reactions with other molecules. Free radicals, which arise as byproducts of regular cellular metabolism, exhibit a transient and unstable nature. Their high reactivity permits to abstract electrons from other compounds to attain a state of stability. Consequently, the attacked molecule losses an electron, thereby becoming a free radical itself. This cascade of chain reactions culminates in cellular damage [165].

Both the reactive oxygen species (ROS) and reactive nitrogen species (RNS) collectively constitute the free radicals and other non-radical reactive species. Non-radical species, like hydrogen peroxide (H₂O₂), can readily convert to free radicals through various reactions during cellular metabolism [166]. Therefore, pro-oxidants/oxidants are commonly referred to as ROS and RNS. The most relevant free radicals generated as a result of metabolic reactions are oxygen-derived, ROS [165].

Among ROS, the **hydroxyl radical** (OH^{*}) is the **most unstable** and quicky reacts with other biomolecules. In contrast, **hydrogen peroxide** is **relatively stable** and capable of exerting extracellular effects by crossing cell membranes [167]. Hence, several types of ROS exhibit distinct characteristics regarding their reactivity, half-life, target specificity, and cellular localization [168]. The different ROS molecules (both radicals and non-radicals) produced during metabolism are listed in **Table 2**.

The availability of ROS is determined by both their production rate and their detoxification by antioxidant mechanisms, which can be categorized into two main groups [169]:

1. <u>Enzymatic antioxidants</u>. Among these enzymes, **superoxide dismutase** plays a significant role by catalyzing the partitioning of the superoxide radical into oxygen

and hydrogen peroxide. **Catalase**, on the other hand, catalyzes the decomposition of hydrogen peroxide to water and oxygen. Additionally, **glutathione peroxidase** serves a dual function, catalyzing the reduction of hydrogen peroxide to water and oxygen, as well as the reduction of peroxide radicals to alcohols and oxygen. Other enzymes included in this category are heme oxygenase-1 and redox proteins.

2. <u>Non-enzymatic antioxidants</u>, which include <u>low-molecular-weight molecules</u>, such as vitamins (vitamins C and E), β -carotene, and glutathione (GSH).

Name	Symbol	Half-life	
Radicals			
Superoxide	02-	10 ⁻⁶ s	
Hydroxyl	OH*	10 ⁻¹⁰ s	
Alkoxyl radical	RO*	10 ⁻⁶ s	
Peroxyl radical	ROO*	17 s	
Non-radicals			
Hydrogen peroxide	H_2O_2	Stable	
Singlet oxygen	¹O ₂	10 ⁻⁶ s	
Ozone	O_3	seconds	
Organic peroxide	ROOH	Stable	
Hypochlorous acid	HOCl	Stable (min)	
Hypobromous acid	HOBr	Stable (min)	

Table 2. List of ROS produced during cellular metabolism. Adapted from Phaniendra, A., Jestadi, D. B., & Periyasamy, L. (2015) [165].

Due to their elevated reactivity, free radicals have the ability to damage all three essential categories of biological molecules [165]:

 <u>DNA and RNA</u>. Excessive ROS production is causative of DNA damage and is associated with the promotion of oncogenes and/or the inhibition of tumorsuppressor genes. For instance, hydrogen peroxide can induce an activating mutation in a proto-oncogene [170], while inhibiting the function of the *p53* tumor-suppressor gene [171]. ROS-induced genetic alterations encompass modifications in DNA bases, single and double strand breaks, and DNA-protein crosslinks, among other changes. These modifications lead to an increased mutational rate in genes that are implicated in critical cellular pathways, such as DNA repair. Furthermore, the accumulation of DNA damage resulting from incomplete or erroneous repair mechanisms can **disrupt genome stability**, thereby potentially triggering **cellular transformation**, particularly when coupled with a defective apoptotic pathway [167].

- 2. <u>Lipids</u>. Membrane lipids can be compromised by **lipid peroxidation**, particularly affecting the polyunsaturated fatty acid residues found in phospholipids, which are more susceptible to oxidation.
- 3. <u>Proteins</u>. Several radical and non-radical species of ROS can oxidize different amino acids. This process results in <u>protein-protein crosslinks</u> and other oxidation products, depending on the amino acid attacked. As a consequence, the affected protein may undergo <u>denaturation</u>, leading to a loss of functionality and activity.

6.1.2. Oxidative stress and cancer

The presence of an **oxidation-reduction imbalance** is an important feature of tumor microenvironment that contributes to **cancer pathogenesis**, closely associated with inflammation [172]. Moreover, oxidative stress serves as a shared underlying mechanism for most chronic diseases, including cardiovascular diseases, neurodegenerative disorders, and diabetes [173].

Oxidative stress is defined as the imbalance between ROS and the cellular antioxidant defenses. Overproduction of ROS by several sources may influence the underlying molecular mechanisms implicated in the initiation, promotion, and progression of cancer. Notably, ROS exert **modulation on** various signaling molecules and proteins, including **MAPK and ERK1/2** (involved in cell proliferation [174, 175]), **NFKB** (associated with cell proliferation and the cell cycle [176]), **PDK-1** (participating in cell proliferation and apoptosis [175]), and **PI3K/AKT** (involved in cancer cell proliferation [177]).

6.1.2.1. Sources of ROS contributing to oxidative stress

Therefore, cancer cells exhibit elevated levels of ROS compared with their normal counterparts. The action of specific enzymes and processes in different subcellular compartments generates diverse types of ROS, which have the capacity to travel through channels or vesicles [168].

Endogenous ROS are produced by several mechanism, including: 1) the **mitochondrial electron transport chain** (ETC) [178], 2) the members of the **NADPH oxidase** (NOX) **family** of proteins [179], 3) **peroxisomes**, and 4) the **endoplasmic reticulum** (which produces hydrogen peroxide as a byproduct during protein folding). Additionally, exposure to exogenous agents such as **ionizing radiation or chemotherapeutic** drugs can contribute to ROS production [180].

Furthermore, several redox-active enzymes can produce ROS as byproducts, including xanthine oxidase, cytochrome P450, cyclooxygenases, and lipoxygenases [181]. In fact, activation of one of these enzymatic systems can trigger the activation of others, creating an interplay that forms a **feed-forward mechanism**, whereby ROS induces an increased ROS production [182].

6.1.2.2. Targeting ROS for cancer treatment

The use of **ROS modulators** has been proposed for therapeutic purposes or prevention [183]. However, most clinical trials investigating the effectiveness of antioxidants in cancer prevention have yielded negative results [184]. This underscores the importance of acquiring further fundamental knowledge regarding the underlying cellular processes involved.

Tumor cells exhibit a diminished capacity of the antioxidant system, rendering them more susceptible to fluctuations in ROS levels compared to normal cells. While certain levels of ROS can regulate determined signaling pathways, the cellular accumulation of an overwhelming amount ROS within tumor cells, surpassing a certain threshold, can trigger secondary oxidative damage, leading to various forms of cell death, including apoptosis,

autophagic cell death, necrosis, and ferroptosis [167]. Therefore, certain anticancer drugs necessitate a remarkable upregulation in ROS levels to induce tumor cell death.

Despite the initial consideration of ROS as a hazardous byproduct of cellular metabolism, discoveries in the last decades have emphasized the **role of ROS at low or moderate levels** in immune function, crucial molecular pathways, and redox regulation [165]. In fact, there is substantial evidence supporting the involvement of **ROS produced by NOX proteins** in tumor growth and survival [185, 186]. Therefore, the biological roles of ROS are complex and paradoxical, contributing to the maintenance of redox homeostasis.

6.2. NADPH OXIDASES AND CANCER

6.2.1. NOX family

The NOX family of proteins participate in a enzymatic process that is NADPH-dependent, wherein the **reduction of oxygen** results in the **generation of superoxide radical** (O2*-) or **hydrogen peroxide** (H₂O₂) across biological membranes, concomitant with NAPDH oxidation [187]. Among mammals, four NOX isoforms (NOX1–3 and NOX5) primarily generate superoxide, while NOX4 and the dual oxidases (DUOX1 and DUOX2, encoded by two homologous genes) produce hydrogen peroxide [179]. These proteins share a **common catalytic core** composed of a heme-coordinating transmembrane domain and a cytosolic dehydrogenase (DH) domain. The DH domain consists of two lobes: the NADPH Binding Lobe (NBL), responsible for binding the NADPH substrate, and the FAD Binding Lobe (FBL), which interacts with the flavin adenine dinucleotide (FAD) cofactor [188].

Each NOX protein is **anchored to the plasma membrane**, forming six membrane helices that bind two heme cofactors, constituting a heme-coordinating transmembrane (TM) domain (**Figure 8**). The FAD/NADPH binding regions (C-terminal) facilitate intramolecular electron transfer [182]. The NOX4 protein exhibits a slightly larger E-loop region compared to NOX1-3 proteins, which could promote hydrogen peroxide formation. NOX4 activity is regulated at the expression level and only requires interaction with the P22-phox subunit [181]. NOX5 is unique as it contains four N-terminal calcium-binding EF hand domains (EF, **Figure 8**) [189].

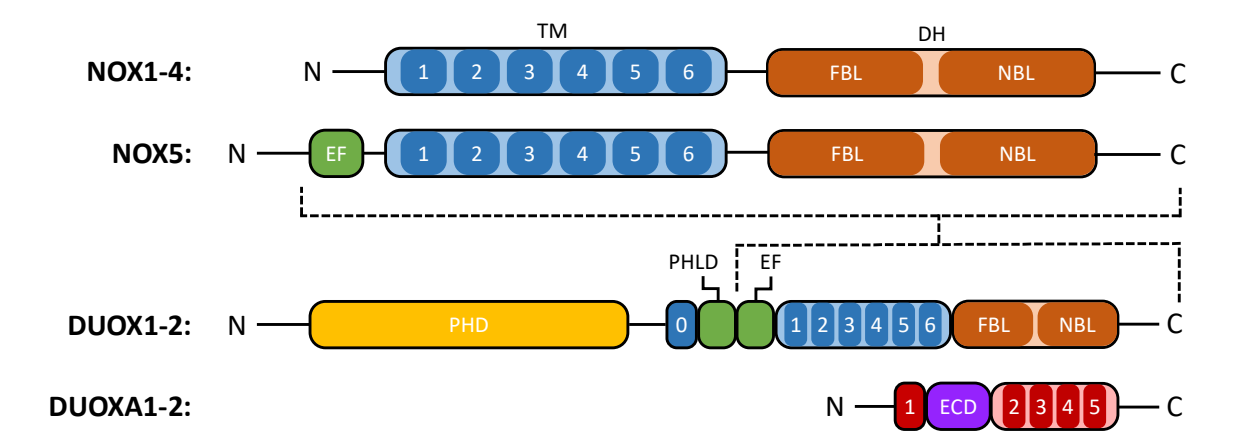


Figure 8. Primary sequence of the NOX family and DUOXA maturation factors. Adapted from Ogboo, B. C. et al., (2022) [189].

Dual oxidases (DUOXes) are responsible for generating hydrogen peroxide by transferring electrons from intracellular NADPH to extracellular oxygen. Particularly, each DUOX member comprises an **extracellular N-terminal peroxidase homology domain** (PHD, also known as peroxidase-like domain), followed by a unique transmembrane helix, one Pleckstrin homology-like domain (PHLD) and two calcium-binding EF hand domains (**Figure 8** and **Figure 9**).

The PHD domain is believed to be **responsible for hydrogen peroxide production** [190]. This region exhibits predicted structural homology to mammalian peroxidases based on sequence analysis. However, investigations into PHD domain indicates that it does not function as a superoxide dismutase or peroxidase for the generation of hydrogen peroxide, suggesting the presence of as-yet-**unidentified functions** [190, 191]. Furthermore, this domain exhibits a lower sequence identity conserved between DUOX1 and DUOX2 when compared to the full-length protein. This finding suggest that **isoform-specific** functions may rely on regulatory elements within this region [192]. Therefore, unraveling the precise mechanism by which these enzymes directly produce hydrogen peroxide remains a prominent area of research interest [179].

Introduction

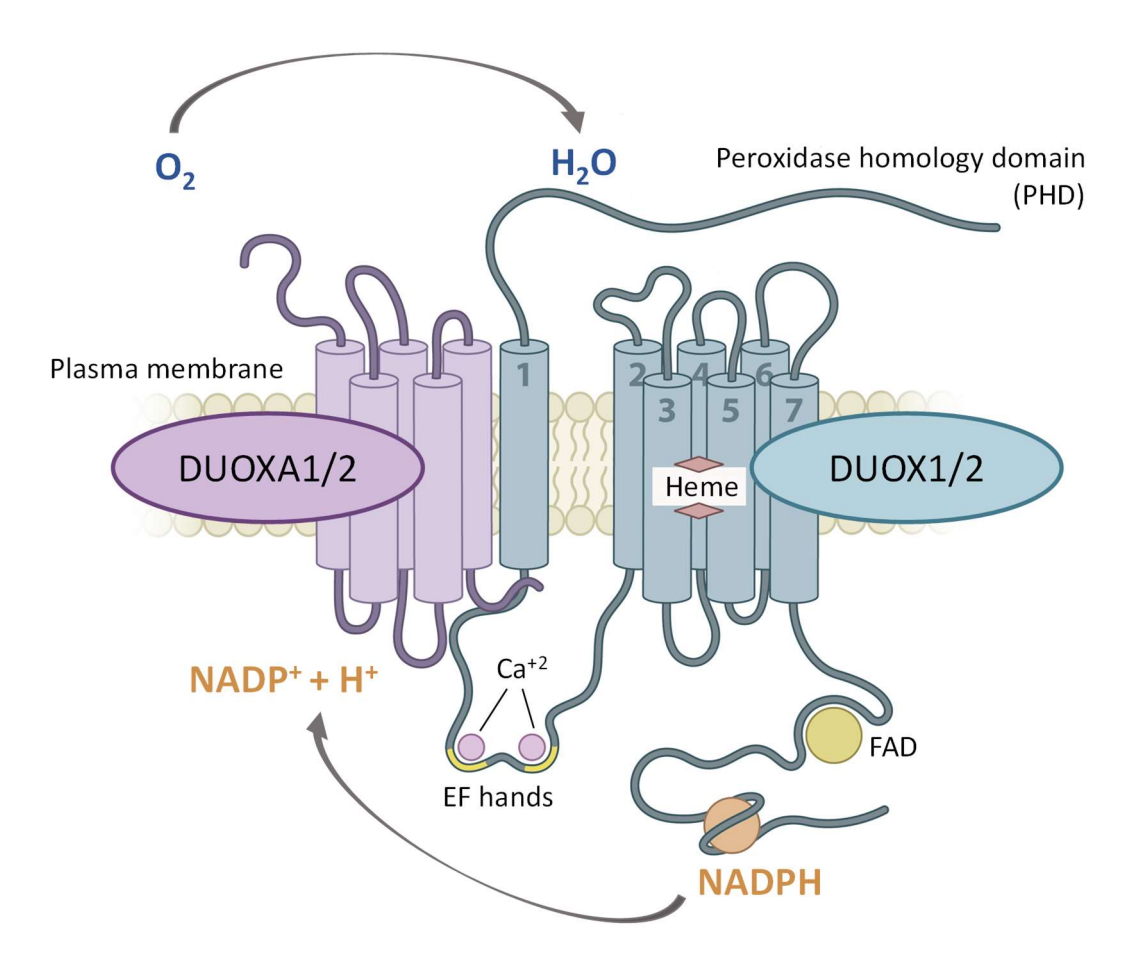


Figure 9. Structures of DUOX and DUOXA proteins as a schematic representation. The DUOX enzymes are composed by transmembrane domains, a large intracellular loop that contains two calcium-binding sites, and an extracellular peroxidase homology domain (N-terminal). The DUOXA1 and DUOXA2 proteins, known as DUOX activator proteins (DUOXAs), play a crucial role in facilitating the ER-to-Golgi transition and co-translocation of DUOXs to the plasma membrane. Adapted from Faria, C. C., & Fortunato, R. S. (2020) [193].

The functional activity of DUOX enzymes relies on their interaction with **maturation** factors, known as **DUOXA proteins**, forming a **stable heterodimer** that facilitates their cotranslocation to the plasma membrane surface [194]. DUOXA proteins consist of an extracellular domain (ECD) and five transmembrane helices (**Figure 8** and **Figure 9**).

Although a significant amount of information is available regarding the biological functions of NOX proteins, there remains a considerable gap in our understanding of the mechanisms controlling their activity at a structural level. Recently, **atomic-resolution structures** of NOX5 [195] and DUOX1 [188, 196] enzymes have provided initial insights into the regulation of these proteins at the molecular level. These structural studies have

suggested that the PHD domain of DUOX1 lacks heme-dependent peroxidase activity [196], corroborating previous biochemical analyses [191].

Hydrogen peroxide serves dual roles as both a pro-survival factor that regulates kinase-driven pathways and a mediator of oxidative damage [197]. Elevated levels of hydrogen peroxide are associated with its classical "destructive" role, leading to aberrant cellular functions, genomic instability, apoptosis, and carcinogenesis [181]. However, this molecule also plays a positive role in proliferation [198], response to growth factors [199, 200] and activating several signaling pathways, such as the ERK pathway [181, 201].

6.2.2. DUOX enzymes and cancer

DUOX enzymes are highly expressed in the thyroid gland, in which DUOX2 is essential for **thyroid hormone biosynthesis** [202]. Nonetheless, the expression of *DUOX* has been observed in various other normal tissues of the body. In fact, each DUOX isoform performs a unique role within the thyroid and different tissues. DUOX1 expression is also important for the **defense mechanisms** of normal epithelial cells in the airway and urothelial cells in the bladder [193, 203]. In contrast, DUOX2 shows prominent expression and involvement in the host defense of bronchial epithelium and throughout the gastrointestinal tract [204, 205]. Notably, DUOX proteins are highly expressed in thyroid and esophageal carcinomas [181]. However, **each DUOX isoform** is **independently expressed in** other types of **carcinomas**.

Duox2 is upregulated in liver [206], pancreatic [207], and prostate cancer [208]. High levels of DUOX2 have been reported in colorectal cancer [209, 210], although other evidence suggests a downregulation of DUOX2 in this cancer type, leading to conflicting conclusions regarding its association with prognosis [211, 212]. Additionally, analysis of microarray data from The Cancer Genome Atlas (TCGA) cohorts indicates elevated levels of DUOX2 in stomach, colorectal, and pancreatic adenocarcinomas [181].

Regarding **DUOX1** expression in human tumors, it has generally been found to be **low**, with a few exceptions [213]. For instance, DUOX1 was found downregulated in liver cancer tissues and cell lines. Furthermore, its expression was associated with genes that

inhibit tumor progression and correlated with a favorable prognosis for liver tumor patients [214].

Furthermore, there is an **interplay** between **cancer cells and the inflammatory microenvironment** to facilitate survival, invasion, metastasis, and immune evasion [215]. In fact, inflammatory cells present in the tumor microenvironment can stimulate **NOX-mediated ROS production** by tumor cells. This phenomenon, in turn, promotes angiogenesis and increases genomic instability. Specially, the production of ROS by specific NOX isoforms in vascular tissues can be induced by growth factors and sustainably activated by inflammatory cytokines [179].

6.3. ROS METABOLISM IN PROSTATE CANCER

The likelihood of developing PCa is considerably higher in males over the age of 65, and this is associated with a decline in the activity of the antioxidant defense system [216]. According to the **free radical theory of aging**, the balance between prooxidants and antioxidants is disrupted with age, resulting in an oxidative state within various tissues of the body [217]. Consequently, the outcome of this process is the accumulation of damage caused by ROS, thereby increasing the risk of oncogenesis.

Oxidative stress plays a crucial role in prostate carcinogenesis, particularly in the early stages of development, as well as in the progression and response to therapy [218, 219]. PCa cells exhibit a significant downregulation of antioxidant enzymes, which contributes to the occurrence of oxidative stress [216]. Among the most prevalent ROS in PCa are superoxide radicals, hydroxyl radicals, and nitric oxide (NO) [219]. Moreover, signaling pathways involving MAPK, Nrf2, NF-κB and AR are interconnected with ROS levels and can modulate signaling cascades in cancer cells [219, 220].

6.3.1. Redox-dependent signaling in prostate cancer cells

The acquisition of an **aggressive phenotype** by cancer cells is accompanied by adaptive changes in cell signaling, which are driven by the development of **chronic oxidative stress in PCa**, primarily attributed to elevated levels of ROS [220].

Oxidizing agents and stressors that induce oxidative stress stimulate the activation of a transcription factor known as NF-E2-related factor 2 (Nrf2). This transcription factor governs the cell's fate by upregulating the expression of stress-response genes. Consequently, Nrf2 enhance cellular antioxidant defense mechanisms and preserving redox homeostasis against oxidative stress [221]. Importantly, oxidative stress and inflammation processes are regulated by a complex interplay between Nrf2 and NF-kB [222].

Moreover, the **activation of NF-κB** is observed in different tumor types, including **PCa**, and is associated with cancer progression, chemoresistance, and metastasis [223]. Furthermore, increased NF-κB activity **suppresses JNK activation** [224]. JNK is a crucial component of the MAPK signaling pathway that is essential for PCa cell growth, presenting a novel therapeutic target in the treatment of PCa [225].

ROS have also been related with the suppression of PTEN activity, leading to the constitutive activation of AKT signaling and promoting the abnormal growth of PCa [226]. Remarkably, ROS were found to increase CXCR4-mediated metastasis by inactivating PTEN in DU145 cells [227].

6.3.2. Mitochondrial activity and ROS

Mitochondrial activity is widely recognized as the **principal endogenous source of ROS**, which are generated as byproducts during fatty acid (FA) metabolism and **oxidative phosphorylation** (OXPHOS) for ATP synthesis [168]. The mitochondrial electron transport chain (ETC), consisting of complex I, III, and IV, drives OXHPOS **to produce ATP**. This process involves the transfer of electrons from reduced nicotine adenine dinucleotide (NADH) or flavin adenine dinucleotide (FADH2) to oxygen through inner membrane of mitochondria, resulting in the simultaneous **production of ROS** as a **byproduct**. This inherent production of ROS stems from electron leakage at complex I and complex III, which leads to partial reduction of oxygen to form superoxide [167, 228].

Among the 37 genes present in mitochondrial DNA (mtDNA), 13 encode protein components that participate in OXPHOS. Interestingly, mitochondrial DNA is more susceptible to ROS-induced damage compared to nuclear DNA. Additionally, **mutations in**

mtDNA exacerbate ROS production, thereby contributing to cancer development [228]. Unlike other types of cancer, PCa does not universally exhibit depleted mtDNA content. Instead, alterations in mtDNA content show significant variability, reflecting the well-established heterogeneity of the PCa genome. Patients exhibiting high levels of mtDNA content demonstrate an unfavorable pathology and worse prognosis [229]. In fact, the burden of potentially deleterious mutations in mtDNA is elevated in malignant human prostate tissue samples compared with paired benign samples, and this burden is correlated with unfavorable risk factors [230].

6.3.3. NOX family in prostate cancer

NOX1 expression has been strongly associated with PCa oncogenesis and progression in various PCa cells and patient cohorts [231-233]. While some studies suggest upregulation of NOX2 expression in PCa cells, patient data indicate that neither NOX2 nor NOX3 play a role in PCa development [213, 220]. Furthermore, NOX4 shows high expression in different PCa cell lines and tumors but not in normal prostate cells or benign tissues [234, 235]. ROS generated by NOX5, which is widely expressed in PCa cell lines [236], have been reported to be essential for PCa growth [235]. However, no significant differences in the expression of NOX5 gene were found in malignant tumors [235].

Although **DUOX1 expression** has been detected **in PCa cells**, its **pathological significance** is not fully understood, and **conflicting evidence** exists. It has been reporter to be highly expressed in both normal and prostate tumor tissues [213]. However, DUOX1 protein expression was not detected in tumor cells or non-tumoral epithelium according to the Human Protein Atlas [236]. Furthermore, DUOX1 expression in PCa tissues was significantly lower than that in non-malignant tissues [213].

DUOX2 expression in PCa cell lines is generally low at RNA levels [213], with some exceptions like overexpression observed in DU145 cells. Furthermore, DUOX2 expression in PCa tissues did not differ from non-tumoral samples [213]. However, DUOX proteins have been related with pathological roles in PCa [208]. For instance, the **DUOX2 protein** was detected at **elevated levels** in **many human cancers** from a tissue microarray (TMA), with **prostate adenocarcinoma** with the **highest frequency** of expression [237].

6.4. ROS AND HYPOXIA

6.4.1. Hypoxia in tumors

Hypoxia is defined as a condition in which cells or tissues are exposed to oxygen percentage below 2%, while most healthy mammalian tissue homeostasis requires oxygen percentages ranging from 2% to 9% [238].

Initially, small tumor growth occurs with absent, insufficient, or abnormal angiogenesis within the tumor microenvironment. This favors the formation of hypoxic regions with poor blood perfusion, resulting in increased ROS levels and promoting the survival and progression of tumor cells [239]. Thus, hypoxia is a characteristic hallmark of solid tumors.

Furthermore, these **poorly oxygenated** areas in solid tumors contribute to the **failure of** effective **cancer therapies** [240] by protecting from the cytotoxic effect of radiotherapy and chemotherapy [241]. Interestingly, **radiation resistance** of hypoxic tumors arises from the increased production of **ROS induced by radiotherapy**, including the case of PCa. In fact, both prostate carcinoma and BPH exhibit areas of hypoxia, which correlate with more aggressive forms of PCa [242]. Notably, compared to other tissues, the **prostate** is an organ known to **have relatively low oxygenation** [243].

The sequencing of tumor genomes has provided evidence that **hypoxia** is strongly associated with genomic instability in several types of tumors, including PCa. In localized PCa, hypoxia has been linked with high rates of chromothripsis, allelic loss of PTEN, and shorter telomeres [244]. In addition, elevated levels of hypoxia also correlated with increased mutational burden across different cancer types, regardless of the underlying mutations [245]. These factors collectively contribute to tumor aggressiveness and ultimately lead to poor prognosis [246].

Hypoxia has been shown to indirectly **induce DNA damage** in the form of **replication stress**, which is a major contributor of genomic instability in cancer and triggers the activation of DNA damage response (DDR) pathways [247]. Moreover, hypoxia can

downregulate the DDR by inactivating DDR genes via alternative splicing induction [248], as well as through other genetic and epigenetic mechanisms [249]. Consequently, hypoxiamediated suppression of DDR pathways results in increased genomic instability.

Interestingly, hypoxia promotes **resistance to apoptosis** in cancer cells through mechanisms such as upregulation of anti-apoptotic proteins or downregulation of apoptosis proteins These alterations enable tumor cells to continue proliferating despite the presence of unrepaired DNA [249].

In light of this, hypoxic tumors could be targeted using alternative approaches, such as **synthetic lethality**, which involve the simultaneous targeting of DDR (by PARP inhibition) and hypoxia signaling [250].

6.4.2. Hypoxia-inducible factors (HIFs)

Cells have the ability to adapt to variations in oxygen levels by controlling the expression of metabolic enzymes and signaling molecules. This adaptive response is mediated by **hypoxia-inducible factors** (HIFs), which act as oxygen-labile transcription factors governing **cellular adaptation to hypoxic stress** [251].

HIFs are **heterodimeric proteins** that contain an **oxygen-sensitive** α **subunit** (HIF-1 α or HIF-2 α) and a constitutively expressed β subunit (HIF-1 β). Both subunits belong to the basic helix-loop-helix-PAS (bHLH/PAS) family of transcription factors [252]. The bHLH domain within is responsible for binding the transcription factor to the **hypoxia-response element** (HRE) located in the DNA, while the PAS domain facilitates HIF dimerization (**Figure 10**) [253]. The regulation of HIFs involves post-translational modifications and stabilization mechanisms, which are detailed in **Figure 10**.

While HIF-1 α is ubiquitously expressed, the expression of HIF-2 α is significantly more restricted to specific tissues. Specifically, HIF-2 α can be found at high levels in vascular endothelial cells and myeloid-derived cells [254-256]. The focus in the following sections will predominantly center on HIF-1 α role, which have been traditionally more relevant and targeted in cancer.

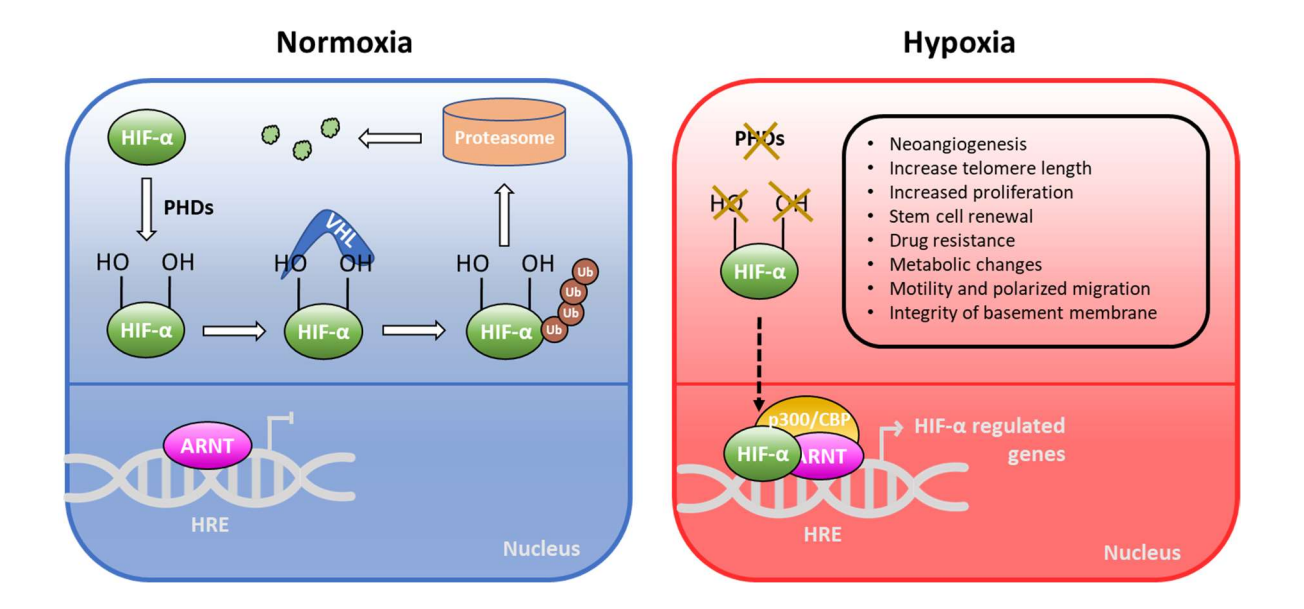


Figure 10. Regulation of hypoxia-inducible factors. In normal oxygen levels, prolyl hydroxylases (PHDs) hydroxylate two conserved proline residues present in the oxygen-dependent degradation (ODD) domain of the HIF subunit. This hydroxylation is detected by the von Hippel-Lindau (VHL) tumor suppressor E3 ligase complex, which polyubiquitinates HIFs and targets them for degradation by the 26S proteasome [255, 257]. However, under hypoxic conditions, PHDs no longer modify HIFs. Instead, the HLH and PAS domains of HIFs can interact with ARNT/HIF-16 for dimerization, allowing translocation to the nucleus and recruitment of cofactors. Ultimately, the HIF heterodimers bind to hypoxia-response elements (HREs) present in target genes, promoting the transcription of HIF-regulated genes [255]. Adapted from Mucaj, V., Shay, J.E.S. & Simon, (2012) [255].

6.4.3. HIF-dependent genes and mechanisms

Activation of HIF- 1α initiates the expression of **hundreds of regulated genes**, thereby triggering molecular mechanisms to sustain survival, growth, motility, metastasis, and metabolic changes of tumor cells:

Vascular Endothelial Growth Factors (VEGFs) and VEGF Receptors (VEGFRs),
which are involved in promoting tumor-specific neoangiogenesis. Tumor
vascularization increases the supply of oxygen and nutrients to facilitate
tumor growth [258]. Additionally, ROS can directly activate the MAPK
pathway, leading to increased VEGF expression [64]. While VEGF inhibitors

Introduction

have been successful and approved by the FDA in different settings, PCa has exhibited **resistance to antiangiogenic therapy** [259].

- TERT (telomerase), whose activation allows for the extension of telomeres,
 providing cells with increased replicative potential [260].
- Reprogramming factors (such as c-Myc, SOX2, OCT4, NANOG) and Notch signaling. These factors play a role in facilitating stem cell renewal, maintaining a stem-like state, and promoting the tumorigenic potential of cancer cells [261, 262].
- **ABC transporters**, which are overexpressed in drug-resistant tumor cells, actively **extrude** a variety of structurally and **functionally unrelated drugs from cancer cells** [263]. Specifically, HIF-1α has been shown upregulate the expression of MDR1/P-glycoprotein (MDR1/P-gp), with ROS levels playing a significant role [264]. In fact, elevated ROS levels resulting from NOX1 overexpression led to a decrease in HIF-1α and MDR1/P-gp expression, as well as improved survival in spheroids derived from AR-negative PCa cells [265].
- Metabolic proteins, including ALDA, PGK and GLUT-1. These proteins play a crucial role in the metabolic reprogramming of cancer cells, with ROS and HIF-1 α activation being implicated in this process [168]. The detailed explanation of this mechanism will be provided in the following section.
- Matrix metalloproteinases, which are involved in the degradation of the basement membrane and invadopodia formation, which are actin-based structures that drive the proteolytic invasion of cells [168].

Through these hypoxia-induced mechanisms, tumor cells demonstrate the ability to sustain high proliferation rates and acquire invasive properties, even under conditions of low oxygen and limited nutrients. Consequently, cellular metabolism undergoes adaptations to accommodate the dynamic conditions of the tumor microenvironment.

6.4.4. HIF activity on tumor cell metabolism

Glycolysis is a metabolic process that converts glucose into pyruvate, resulting in a net energetic yield of two ATP molecules. In healthy cells, pyruvate enters the mitochondrial tricarboxylic acid (TCA) cycle, producing 34 ATP molecules per pyruvate when there is abundant oxygen (normoxia). However, in hypoxia, pyruvate is converted to lactate, allowing re-generation of NAD+, which is instrumental in maintaining glycolysis (anaerobic glycolysis) [266]. The "Warburg effect" describe the phenomenon where cancer cells uptake high glucose levels to produce lactate even in the presence of abundant oxygen. Therefore, tumor glycolysis is often referred to as "aerobic glycolysis" to distinguish it from the anaerobic glycolysis observed in healthy cells (Figure 11). This effect represents a key feature of tumor cells, although the underlying rationale and molecular mechanisms are not yet fully understood [255, 267].

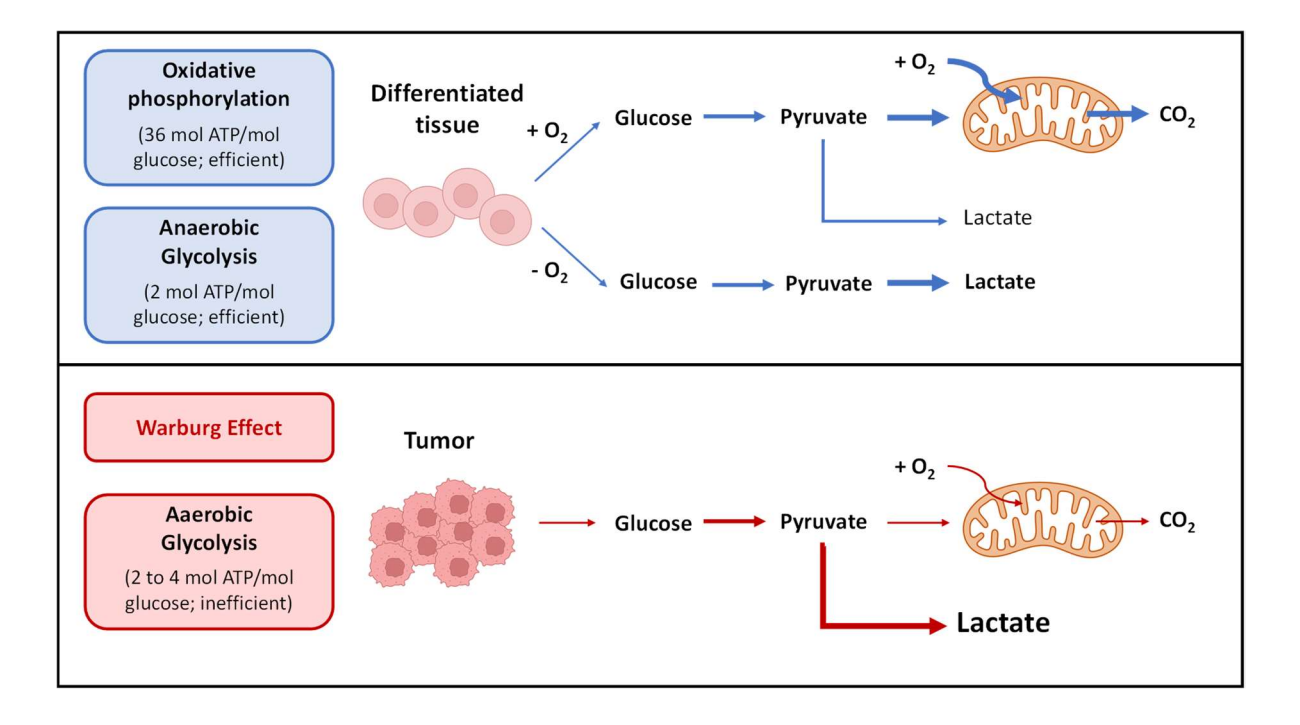


Figure 11. Schematic representation of oxidative phosphorylation, anerobic glycolysis and anaerobic glycolysis. Usage of each metabolic pathway depends on differentiated/tumor cells, and it is conditioned by oxygen availability. Adapted from Kim, Y., Kang, H., Lawler, S. (2014).

Hence, in a hypoxic environment, anaerobic glycolysis becomes a crucial pathway as it enables energy production independent of oxygen-dependent OXHPOS. To facilitate this metabolic shift, HIF-1α activates the transcription of genes encoding various metabolic enzymes and transporters. These include glucose transporter 1 (GLUT1) for glucose uptake, glutaminase for glutamine utilization, and hexokinase II (HK2), lactate dehydrogenase A (LDHA), and phosphoglycerate kinase 1 (PGK-1) for glycolysis, among others [168]. The expression of HIF-1α induces the upregulation of pyruvate dehydrogenase Kinase 1 (PDK1), which, in turn, deactivates the enzyme pyruvate dehydrogenase (PDH) responsible for converting pyruvate to acetyl coenzyme A (acetyl-CoA). Consequently, HIFs impede the progression of the TCA cycle, redirecting the flow of glucose from OXPHOS to glycolysis [255, 268].

Moreover, HIF-1 α also governs the transcription of genes associated with the mitochondrial ETC activity to ensure the efficient utilization of oxygen and prevent the harmful accumulation of ROS. For example, HIF-1 α regulates the transcriptional activation of cytochrome c oxidase subunits, such as COX4-2 (cytochrome oxidase 4-2), leading to more efficient aerobic respiration in hypoxic conditions and protecting cells from excessive ROS production [269]. Additionally, the HIF-1 α -mediated promotion of aerobic glycolysis increases HIF-1 α transcriptional activity, establishing a feed-forward loop that sustains tumor growth [270]. Yet, there are additional mechanisms involved in the attenuation of OXPHOS and mitochondrial functions that remain unknown or not fully elucidated.

6.4.5. Hypoxia-induced ROS

The precise mechanism implicated in the generation of ROS under hypoxic conditions is still a topic of ongoing debate. It has been proposed that the **mitochondrial ETC** may play a role in this process, in which **hypoxia** would **drive ROS increase** by acting on complexes I, II and III [271]. Furthermore, once these hypoxia-driven ROS exit the mitochondria, they trigger the **destabilization of Prolyl Hydroxylases** (PHDs) and the **stabilization of HIF-1** α [168, 271].

This increase of ROS upon hypoxia has been extensively demonstrated using different techniques [272], inducing replication stress in different types of cancers [273].

However, obtaining precise quantification of ROS generation levels in tumors is challenging due to the presence of multiple antioxidant pathways and molecular mechanisms activated by tumors to survive to such an increase. In addition, hypoxia-induced ROS can also **activate** other transcription factors, such as **NRF2**, to mediate the antioxidant defense [274].

In a hypoxic environment, both **NOX and HIF-1α** have been observed to **mutually induce each other's expression** [275, 276]. One proposed mechanism of NOX activation by hypoxia is via the increase of the intracellular calcium concentration, which is induced in this low oxygen environment [275]. This elevated calcium level can serve as an upstream signal to activate **calcium-regulated NOX isoforms**. For instance, the upregulation of NOX1 upon hypoxia has been shown to result in increased **ROS generation**, which may, in turn, **activate HIF-1α-dependent pathways** [277]. Furthermore, it has been demonstrated that Graviola pulp extract exhibits inhibitory effects on hypoxia-induced NOX activity in PCa cells (LNCaP, 22Rv1 and PC3), accompanied by a reduction in NOX1 and NOX2 expression. Notably, these effects were not observed in non-neoplastic prostate epithelial cells [231]. Moreover, **mitochondrial ROS production** have been found to participate in the **hypoxic activation of NOX enzymes**, leading to further ROS increase and cellular damage [278].

In summary, there exists a intricate interaction between HIF- 1α and NOX enzymes [279], indicating the potential advantages of **co-targeting** them. Furthermore, several clinical studies provide substantial evidence supporting the role of hypoxia and **HIF-1\alpha** in the **progression of PCa**, the development of **CRPC**, and **treatment resistance** [280-282]. However, other genes and mechanisms that could be targeted are involved in this regulatory network. Unraveling the molecular pathways involved will enhance therapeutic outcomes in CRPC by implementing efficient combination therapies.

HYPOTHESIS AND OBJECTIVES

PREMISES AND HYPOTHESIS

The global aim of this thesis is to identify new druggable mechanisms responsible for prostate cancer (PCa) resistance to androgen receptor signaling inhibitors.

The molecular mechanisms underlying how androgen-sensitive PCa cells acquire resistance to hormone deprivation remains elusive, which complicates development of effective therapies. Therefore, we hypothesize that unveiling the vulnerabilities that arise as a consequence of the acquisition of antiandrogenic therapy resistance will contribute to novel PCa treatments.

For that purpose, we proposed to perform a CRISPR-based screening to obtain candidate genes involved the antiandrogen treatment response.

OBJECTIVES

Therefore, the objectives of this thesis are:

- To perform a CRISPRi/dCas9 synthetic lethal screen to obtain candidate genes (hits)
 responsible for the acquisition of resistance or sensibility to abiraterone.
- To investigate the underlying mechanisms of resistance to abiraterone within that biological context, using in vitro models to perform functional validation.
- To evaluate actionable targets to overcome antiandrogen resistance based on the elucidated mechanism and validate the effectiveness of combination therapies to improve antiandrogen treatment, using *in vitro* and *in vivo* models.

MATERIALS AND METHODS

1. CELL CULTURE

1.1. CELL LINES MAINTEINANCE

Cells were cultured in either DMEM (Dulbecco's Modified Eagle Medium; with high glucose and pyruvate, Gibco) or RPMI (RPMI 1640; with L-Glutamine and 25mM HEPES, Lonza), both supplemented with 10% fetal bovine serum (FBS, Gibco) (**Table 3**). Cells were maintained at 37°C and 5% CO₂ in the incubator under humidified conditions.

The different cell lines employed were maintained according to standard protocols of cell culture. The morphology and growth of these lines were monitored regularly by microscopy. When the cells reached 90% confluence in flask or plate, they were passaged. For that purpose, the cell media was aspirated, and the cells were washed with Dulbecco's phosphate-buffered saline (DPBS, without calcium and magnesium, Gibco). Next, trypsin (trypsin-EDTA 0.05%, Gibco) was used to detach the cells during a 3-minute incubation at 37°C. Trypsinization was neutralized with the appropriate media (with FBS) in a 1:5 (v/v) ratio. This process was repeated approximately 2-3 times a week, depending on cells' growth.

Medium	Reference	Manufacturer
RPMI Medium 1640	H3BE12-115F	Lonza
Dulbecco's Modified Eagle Medium (DMEM)	41966-052	Gibco

Table 3. Media used for cell culture.

1.1.1. Cell lines

The prostate cancer (PCa) cell utilized in this thesis were isolated from malignant primary or metastatic tumors and were cultured in RPMI medium (**Table 4**). The authenticity of the cell lines was verified at QGenomics through their QCellIdentity service.

- <u>NPp53</u> cells were derived from PCa tumors of tamoxifen-induced NPp53 genetically engineered mice that have combined loss of Pten and Trp53.
- <u>LNCaP</u> cells are human prostate adenocarcinoma cells derived from a lymph node metastasis. These cells are androgen receptor (AR) positive (mutated) and androgen dependent. They also express prostate-specific antigen (PSA).
- 22Rv1 cells are human prostate carcinoma epithelial cell line that were derived from a xenograft that underwent castration-induced regression and relapse after serial propagation in mice. Therefore, 22Rv1 cells are derived from the parental androgen-dependent CWR22 xenograft and express AR (H874Y mutant AR) [283]. Additionally, these cells express constitutively active AR variants that lack the ligand-binding domain, including the variant AR-V7, which is associated with androgen resistance [284].

Cell line	Species	Origin	Anti-androgen response	AR status	Medium
NPp53	Mouse	Prostate adenocarcinoma	Sensitive	+	RPMI
LNCaP	Human	Prostate carcinoma lymph node metastasis	Sensitive	+	RPMI
22Rv1	Human	Prostate carcinoma	Resistant	+ and AR-V7	RPMI

Table 4. Cell lines

Nonetheless, the 293FT cells were employed as lentiviral packaging cell lines after transfection with the corresponding plasmids to generate lentiviral particles. These cells were grown in DMEM medium.

1.1.2. Mycoplasma test

Regular mycoplasma bacterial contamination testing was performed on all cell lines via PCR analysis, utilizing the following oligonucleotides indicated in the following **Table 5**.

Oligonucleotide	Sequence
MICO-1	5'- GGCGAATGGGTGAGTAACACG-3'
MICO-2	5'-CGGATAACGCTTGCGACTATG-3'

Table 5. Oligonucleotides used for the detection of mycoplasma contamination.

We utilized cell media as a PCR template, which had not been changed for at least 48 hours and was collected from confluent cells.

1.1.3. Cell counting

To seed a specific number of cells in a plate or flask, cells were counted using disposable Neubauer improved chambers (C-Chip) after diluting and staining them with trypan blue (Sigma) dye exclusion to distinguish viable and non-viable cells.

To calculate the number of cells per mL, the following formula was used:

Concentration (cells/mL) = Mean viable cells per quadrant \times Dilution factor \times 10⁴

1.1.4. Cell freezing and cryopreservation

After the cells were trypsinized and centrifuged (250g, 5 min), they were resuspended in freezing medium consisting of 90% FBS and 10% DMSO (Sigma). Then cells were distributed in cryotubes (1 mL each) and placed in a MrFrosty[™] container (ThermoFisher) filled with 2-propanol, at -80°C for at minimum of 24h. Subsequently, the cryotubes were transferred to a liquid nitrogen tank for storage.

To thaw the cells, they were carefully placed in a water bath at 37°C and then diluted in Dulbecco's phosphate-buffered saline (DPBS) (Gibco). After centrifugation, the obtained cell pellet obtained was then resuspended in the appropriated medium and placed into a culture plate or flask.

1.2. LENTIVIRAL PRODUCTION AND INFECTION

1.2.1. 293FT transfection for lentiviral production

For lentivirus production the HEK293-FT cell line, known for its ability to generate high-titer lentivirus, was utilized. The cells were maintained in DMEM media supplemented with 10% FBS and Geneticin antibiotic (500 μ g/ml).

The HEK cells were seeded in 150 mm dishes and allowed to reach ~70% confluence the following day for transfection. The psPAX2 plasmid (Addgene #12260) contains the HIV gag, pol, rev, and tat genes in a single vector, while pCMV-VSV-G (Addgene #8454) encodes the envelope protein Env. Therefore, transfection was performed by preparing two mixes in Opti-MEM (Gibco):

- Mix A: 15 μg pSPAX, 10 μg pVSV-G, 20 μg of desired plasmid, Opti-MEM up to 1 mL
- Mix B: 120 μL PEI (1 mg/mL initial concentration), Opti-MEM up to 1 mL

Subsequently, the Mix A was gently combined with Mix B and incubated at room temperature for 30 minutes. The resulting mixture was added to the HEK-containing plate with fresh medium without FBS. The cells were incubated with the complexes at 37°C for 6-8 hours. At this time, the supernatant was aspirated and replaced with fresh medium containing 10% FBS (20 mL). To maximize the virus concentration in the supernatant, it has been optimized to collect the media 72h after transfection.

Finally, the media containing the virus was collected in a tube and centrifuged for 15 minutes at 1250 g to pellet the cells. Afterwards, the supernatant was collected and filtered using a 0.45 μ M nitrocellulose filter. The obtained viral supernatant can be used for immediate infection or stored for a few days at 4°C before use. For longer periods of storage, viral supernatants were maintained at -80°C.

It is possible to concentrate the obtained virus to enhance the infection efficiency. To achieve this, on the day of supernatant collection, we utilized the Lenti-X™ Concentrator (Takara) according to the manufacturer's protocol. The resulting viral pellet was gently resuspended in 1/10 to 1/100th of the original volume using complete RPMI. The resuspended concentrated virus can be used immediately or stored at -80°C in single-use aliquots.

1.2.2. Cell line transduction with lentivirus

This spin-infection protocol allows for a significant increase the yield of lentiviral infection, especially in cell lines that are difficult to transduce, such as mouse-derived PCa cell lines. First, we seeded the desired cells in 6-well plates, with a number of cells to reach a 50-60% confluence next day (100,000 cells/well in case of NPp53).

- A. For non-concentrated virus, cells were seeded in 1 mL and then mixed with 1 mL of the virus. Then 2 μ L of polybrene (at 8 mg/mL) were added to reach a final concentration of 8 μ g/mL.
- B. For concentrated virus, the desired amount of virus was added, followed by the addition of media to reach a final volume of 2 mL. For example, 0.5 mL of a 10x concentrated virus is added, followed by 1.5 mL of media and polybrene (8 μ g/mL final concentration).

The 6-well plate was then covered with parafilm and centrifuged at $1000\,\mathrm{g}$ for 1 hour and 30 minutes at 32°C. After centrifugation, the plate was left in the incubator overnight. The following day, fresh medium was added to remove virus from the supernatant. Finally, 48h post-transfection, a selection antibiotic was added according to each vector resistance. The cells were washed, and fresh antibiotic was added for 3-4 days until the non-transduced control cells were fully dead, with additional passages performed if necessary. For example, puromycin (Merck) was added at a final concentration of 5 $\mu \mathrm{g/mL}$.

2. MOLECULAR ANALYSES

2.1. PROTEIN DETECTION

2.1.1. Protein lysates preparation from cell culture

Cells from culture were trypsinized, submitted to centrifugation after inactivation with media. Cell pellet was washed with PBS and then centrifuged again. After removing supernatant, pellet can be stored at -80°C or proceed directly for protein extraction.

For protein extraction, a mixture of several components in RIPA lysis and extraction buffer was added to the pellet. The mixture includes 0.1% SDS, 1% NP-40, 0.5% sodium deoxycholate, NaCl 125 mM, TRIS-HCl 50 mM, cOmplete[™] Protease Inhibitor Cocktail (Roche) 1x, PMSF (phenylmethylsulphonyl fluoride, a serine protease inhibitor) at 1,74 μg/mL and Phosphatase Inhibitor Cocktail 3 (Merck) at 10 μL/mL. The samples were incubated with this mixture on ice for 30 minutes and subsequently centrifuged at 16.000 g for 30 minutes. The supernatant was transferred to a new tube, taking care to avoid any cellular debris. The resulting protein samples were stored at -80 °C to prevent degradation.

2.1.2. Protein lysates quantification

The total protein content of each collected sample was determined using the PierceTM BCA Protein Assay Kit (Thermo Scientific), which is a spectroscopic analytical procedure. The purple-colored reaction product of this assay is formed by the chelation of two molecules of BCA (bicinchoninic acid) with one cuprous ion. This water-soluble complex shows a strong absorbance at 562 nm that is nearly linear with increasing protein concentrations over a wide working range (20–2000 μg/mL). Diluted bovine serum albumin (BSA) solutions were prepared as a set of protein standards. Samples were diluted (1:10) and prepared following manufacturer's instructions in a 96-well plate. The absorbance was measured using spectrophotometry in a in Victor Multilabel Plate reader (PerkinElmer). Finally, the protein concentration of each sample (μg/mL) was extrapolated from the standard curve with known concentration of BSA.

After determining the protein concentration of the samples, a 4x Laemmli buffer (Bio-Rad) containing 10% of β -Mercaptoethanol was added to each protein sample at a final concentration of 1:4. Following a 5-minute of incubation at 95°C, samples were immediately utilized for SDS-PAGE electrophoresis or preserved at -20°C until further use.

2.1.3. Protein analysis by western blotting

2.1.3.1. SDS-PAGE electrophoresis

Gel electrophoresis in poli-acrylamide gels in presence of SDS (Sodium dodecyl sulfat) detergent (SDS-PAGE) is a technique used to separate protein by size. These gels consist of two different parts, which are prepared using 1.5 mm glass plates (Bio-Rad):

- The staking gel, which enables the proteins to enter the gel and to become
 electrophoretically concentrated in one band, so that they will start migrating in
 the running gel simultaneously.
- The resolving gel, which allows the separation of proteins in each sample based on their molecular weight.

To ensure that the separation of proteins is solely based on their size, without any interference of other features (e.g. charge or tertiary and quaternary structure), it is crucial to perform electrophoresis under denaturing conditions (SDS) and include a reducing agent like β -Mercaptoethanol in the samples. Moreover, heat shock ensures that samples are truly denatured.

To prepare the SDS-PAGE gel, we mixed 40% Acrylamide-Bis Solution 29:1 (Bio-Rad), Resolving or Stacking Gel Buffer (Bio-Rad) and SDS solution 10% (Bio-Rad) in water. Polymerization of acrylamide was initiated by adding APS (Ammonium Persulfate) and TEMED (Bio-Rad). Firstly, the Resolving gel (bottom of the gel) was prepared with a variable acrylamide percentage (normally between 6-12%), depending on the molecular weight of the proteins of interest. After polymerization of this part, the Stacking mixture (top of the gel) was prepared and added, introducing the comb to create the wells in the gel in which samples were loaded (1.5 mm glasses).

After the SDS-PAGE has been fully polymerized, it was placed into a gel cassette, which is then mounted in an electrophoresis tank containing Running Buffer (25 mM Tris-HCl, 192 mM glycine and 0.1% SDS in H_2O). To each well of the SDS-PAGE gel, we added 20 to 30 μ g of protein, as well as a molecular weight marker (Page RulerTM prestained protein ladder, Thermo Scientific). Finally, the tank was closed, and both the anode and cathode were connected, with the voltage on the electrophoresis power supply set to a constant 120 V. The proteins can enter the gel and run, with separation occurring based on their molecular weight.

2.1.3.2. Protein transfer

After the proteins have been separated in the gel, they were transferred to a nitrocellulose membrane using the TransBlot Turbo Transfer System (Bio-Rad). A specific transfer program from the Bio-Rad List was selected according to the molecular weight of the proteins of interest. Once the transfer is completed, the membrane with the proteins was blocked with 5% skimmed milk (Nestle®) in TBS-T (Tris 50 mM, NaCl 150 mM, 0.1% TWEEN-80, pH 7.5) for 1 hour at room temperature with agitation. This is done to prevent non-specific binding of the antibodies used subsequently used to the membrane.

2.1.3.3. Immunoblotting

The blocked membrane containing the proteins was incubated overnight in the cold room (4 °C) with the primary antibody, which is diluted in 1% milk in TBS-T + Tween 0.1%. The dilution used in each case is specific for each antibody, and we followed the instructions provided in the datasheet, optimizing if necessary (**Table 6**). After this incubation step, the membrane was washed three times with TBS 1X + Tween 0.1% for 10 minutes. The secondary antibody was diluted (1:10.000, **Table 7**) in 1% milk in TBS 1X + Tween 0.1%, and the membrane was incubated with this antibody for 1 hour at room temperature on a shaker.

Finally, the membrane was washed 3 times with TBS 1X + Tween 0.1% for 10 minutes, after which protein detection was carried out. Chemiluminescent signal detection is based in luminol oxidation by the peroxidase that is conjugated to the secondary antibody.

Housekeeping proteins were detected using a standard enhanced chemiluminescent (ECL) substrate kit (ECL Western Blotting Detection Reagents, Amersham Biosciences). On the other hand, ultra-sensitive ECL substrate was used to detect other proteins of interest at low levels (SuperSignal West Femto Maximum Sensitivity Substrate, Thermo Scientific). Chemiluminescence was measured using a ChemiDoc Imaging System (BioRad) and quantified using Image Lab software (Bio-Rad).

Antibody	Antigen	Species	Dilution	Manufacturer
13E5, 4970	β-actin	Rabbit	1:1000	Cell signaling
2087	HIF-1α	Rabbit	1:500	Gift from Dr. Edurne Berra [285]

Table 6. Primary antibodies used for the Western blot detections.

Antibody	Antigen	Dilution	Manufacturer
7076	Anti-mouse	1:10,000	Cell signaling
7074	Anti-rabbit	1:10,000	Cell signaling

Table 7. Secondary antibodies used for the Western blot detections.

2.2. RNA DETECTION

2.2.1. RNA extraction of cells

Cells from culture were trypsinized and subsequently centrifuged following trypsin inactivation with fresh medium. The resulting cell pellet was then washed with PBS and subjected to another round of centrifugation (250 G for 5 minuntes). After removing the supernatant, the pellet was either stored at -80°C or directly processed for RNA extraction. The Maxwell® RSC simplyRNA Tissue Kit and the Maxwell® Platform were utilized for RNA extraction according to manufacturer's instructions. This kit also facilitates DNA digestion of

the samples to prevent contamination from DNA molecules. The obtained RNA was quantified in the spectrophotometer NanoDrop TM1000 (Thermo Scientific).

2.2.2. RNA retro-transcription into cDNA

The reverse transcription of RNA to cDNA was performed using a High-Capacity cDNA Reverse Transcription kit (Applied Byosystems), following the manufacturer's instructions. We prepared a mix containing 2 μ l of RT Buffer, 2 μ l of Random primers, 0.8 of dNTPs, 1 μ l of Reverse Transcriptase and 4.2 μ l of sterile water (up to 10 μ l per reaction). Finally, 10 μ l of each sample containing 1 μ g of RNA was added to attain a final reaction volume of 10 μ l. The retro-transcription process is carried out using the thermal cycling conditions provided by the provided protocol: 10 min at 65 °C, 120 min at 37 °C, 5 min at 85 °C and ∞ at 4 °C. The resulting cDNA (complementary DNA) was diluted 1:5 and stored at -20 °C until use.

2.2.3. Real-Time quantitative PCR

For conducting quantitative PCR, the PowerUp SYBR Green Master Mix (Applied Biosystems) was utilized, which consist of a Dual-Lock Taq DNA Polymerase enzyme. The combination of two hot-start mechanisms prevents undesirable early activity of the polymerase at low temperatures, which could result in non-specific amplification.

Such reactions were performed using specific primers for each gene, which are designed using the PrimerBlast tool or obtained from the available sequences provided by the Origene website. The resulting oligonucleotides were synthetized using the Thermofisher service (Table 8).

A volume of 5 μ L of the Master Mix was mixed with 0.5 μ L of each 10 μ M Forward and Reverse Primer and 3 μ L of water. This resulting volume was pipetted into each well of a LightCycler® 480 Multiwell Plate 384 (Roche). Following this, 1 μ L of cDNA was added to each corresponding well of the plate. The plate was then sealed using the provided plastic transparent film and subjected to a brief centrifugation (1 minute at 1000 g). The plate was then read in a LightCycler® 480 (Roche), which performs the thermal cycles required for cDNA amplification. Samples were measured in 3 replicates. Results were visualized and analyzed using LightCycler 480 SW 1.5 software.

In order to identify and discard potential DNA contamination, we used a no reverse transcriptase control and confirmed the absence of amplification in this sample. Additionally, we verified that each primer pair employed exhibits a single peak in the melting curve. To compare the expression level of a specific gene, we used absolute quantification. For each sample we calculated the C_T value (cycle threshold), which is the number of cycles required for the fluorescent signal to surpass the threshold (exceeding background level). The quantification of an endogenous reference gene (housekeeping gene) was performed for every measured sample, serving as an internal standard for normalization (GAPDH). After normalization, we compared each condition to a designated. The Relative Quantity (RQ) of RNA is calculated using the following equations:

$$\Delta C_T = C_T$$
 Gene of interest $-C_T$ housekeeping gene
$$\Delta \Delta C_T = \Delta C_T \, sample - C_T \, control \qquad RQ = \, 2^{-\Delta \Delta C_T}$$

Gene	Species	Forward primer 5'-3'	Reverse primer 5'-3'
Gapdh	Mouse	GGTCGGTGTGAACGGATTTG	GTAGACCATGTAGTTGAGGTC
Bnip3	Mouse	TCCTGGGTAGAACTGCACTTC	GCTGGGCATCCAACAGTATTT
Ca9	Mouse	TGCTCCAAGTGTCTGCTCAG	CAGGTGCATCCTCTTCACTGG
Hif1a	Mouse	CCTGCACTGAATCAAGAGGTTGC	CCATCAGAAGGACTTGCTGGCT
Nfe2l2 (Nrf2)	Mouse	CAGCATAGAGCAGGACATGGAG	GAACAGCGGTAGTATCAGCCAG
Pdk1	Mouse	GGACTTCGGGTCAGTGAATGC	TCCTGAGAAGATTGTCGGGGA
Vegfa	Mouse	TGTACCTCCACCATGCCAAGT	TGGTAGACATCCATGAATTG

Table 8. Primers used for RT-qPCR.

3. BACTERIA AND CLONING

3.1. HANDLING OF BACTERIA

Bacterial amplification was employed to generate substantial quantities of plasmids. To achieve this, each plasmid must possess a replication origin that enables their replication on the desired strain and an antibiotic resistance gene to facilitate selection of the desired bacteria and avoid contaminations. Some of the plasmids obtained from Addgene or GenScrip were supplied in the form of a bacteria stab, which were subsequently amplified in accordance with the manufacturer's guidelines. In contrast, plasmids that are delivered as low quantities of DNA plasmid necessitate required bacterial transformation for amplification.

3.1.1. Glycerol stock

Glycerol stocks facilitate the preservation of bacteria containing plasmids. For that purpose, bacteria growth in Luria-Bertani (LB) medium (10mg/ml NaCl, 10mg/ml Tryptone, 5mg/ml yeast extract and 1mM NaOH in H₂O) were mixed in a 1:2 ratio with filtered 70% glycerol and, immediately placed in dry ice. Glycerol stocks were stored at -80 °C.

3.1.2. Bacterial chemical transformation of competent cells

For bacterial transformation, we employed MAX Efficiency™ Stbl2™ Competent Cells, a E. coli strain which is suitable for chemical transformation. The Stbl2 were prepared and manipulated according to the manufacturer's instructions.

First, we prepared a mix containing 100-1000 ng of plasmid DNA, 20 μ L of 5x KCM 5X (0.5M KCl, 0.15M CaCl₂, 0.25M MgCl₂ in H₂O) and water up to 100 μ L, chilling this mix on ice. If DNA is a production of ligation, the entire volume from this reaction is added to the mixture. Next, 100 μ L of STBL2 competent cells are added to the DNA mix, and the sample was incubated on ice for 20 min. Following this, the sample was incubated for 10 minutes at room temperature. Finally, 750 μ L of S.O.C medium (Invitrogen) was added to the sample, and the mixture was incubated at 37°C with agitation at 200 rpm (60 minutes for regular plasmids and 90 minutes for ligation products).

After incubation, for regular plasmids, a volume of 10-20 μ L was directly plated onto a culture dish containing LB agar (10mg/ml NaCl, 10mg/ml Tryptone, 5mg/ml yeast extract, 7.5mg/ml Bacto-Agar and 1mM NaOH in H₂O) with the corresponding antibiotic. However, for ligation products, the growth bacteria were centrifuged at 3,000 g for 3 minutes. The resulting pellet was then resuspended in 20 μ L of SOC, and this volume was plated in LB agar containing antibiotic. The dish was subsequently incubated overnight at 37°C.

3.1.3. Obtaining plasmidic DNA from bacteria cultures

The plasmid DNA was obtained from Stbl2 cultures which grew in LB containing the appropriate antibiotic. Initially, a colony grown on an LB agar plate was inoculated into 2-5 mL of LB medium with antibiotic. This preculture was incubated with agitation (200 rpm) at a temperature of 37°C for 6 to 8 hours. Once bacteria had reached sufficient growth, we can perform plasmid DNA extraction at low scale, using a NucleoSpin Plasmid, Mini kit for plasmid DNA (Macherey-Nagel), according to manufacturer's instructions. For large scale preparations, this cultured volume is added to an Erlenmeyer flask containing 250 mL of LB medium with antibiotic, and incubated overnight at 37°C with agitation (200-250 rpm).

3.1.4. Large scale DNA preparations

The total volume of LB medium saturated with bacteria were centrifuged at 700g for 15 minutes at 4°C. The resulting pellet was resuspended and processed using the NucleobondTM Xtra Midi kit (Macherey-Nagel), following the manufacturer's instructions to purify the plasmid DNA. The concentration of this DNA was subsequently measured with the NanoDrop TM1000 (Thermo Scientific).

3.1.5. Characterization of the plasmid DNA by restriction digest

To confirm the identity of the plasmid DNA obtained through bacterial transformation, we performed a restriction digestion with one or more enzymes to generate at least two linear DNA fragments. To this end, we mixed 1 μ g of plasmid DNA, 1 unit of enzyme (or enzymes if necessary), the appropriate buffer volume (provided by the at 10x) and ddH₂O up to the desired final volume (**Table 9**). This reaction mixture was then incubated in a block heater at the optimal temperature for the specified enzymatic reaction.

Finally, a Loading Dye (NEB) was added to the reaction product to facilitate loading onto a 1% agarose electrophoresis gel prepared in Tris-Acetate-EDTA (TAE) buffer. In order to compare the size of restriction bands with the expected fragments, we employed a 1 Kb Plus DNA ladder (Invitrogen) as a molecular weight marker.

Enzyme	Reference	Manufacturer	Buffer	Incubation temperature
Agel-HF	R3552	NEB	CutSmart™	37°C
Bsmbl	R0580	NEB	NEBuffer™ 3.1	55 °C
BstXI	R0113	NEB	NEBuffer™ 3.1	37 °C
EcoRI-HF	R3101	NEB	CutSmart™	37 °C
SbfI-HF	R3642	NEB	CutSmart™	37 °C
XhoI	R0146	NEB	CutSmart™	37°C

Table 9. Restriction enzymes used to confirm correct plasmid genomes.

4. CRISPRI SCREENING

4.1. CRISPRI OPTIMIZATION

4.1.1. Cloning of sgRNA sequences into pCRISPRia-v2 vector

For CRISPR interference (CRISPRi) we used a 2-vector system, wherein one vector expresses dCas9 fused to a transcription-repressor domain (pHR-SFFV-KRAB-dCas9-P2A-mCherry, Addgene #60954), and the other vector is employed to clone the specific sgRNA responsible for inhibiting the expression of the targeted gene (pCRISPRia-v2, Addgene #84832). To demonstrate the CRISPRi activity of cloned sgRNA sequences in this vector, we developed a strategy based on PCR amplification and restriction sites.

The pCRISPRia-v2 plasmid contains a cloning sequence in this sgRNA site. Thus, the strategy consists of generating a new plasmid that carries the desired sgRNA sequence. For that purpose, we performed a PCR using a Forward Primer containing the sgRNA sequence (and including BstXI site) and a Reverse Primer downstream this region (**Table 10**). Therefore, the Forward primer is complementary to the site in the plasmid where the sgRNA will be inserted, except for the sgRNA-specific sequence that will be present in the PCR product (**Figure 12**).

Gene	Guide	Forward Primer	Reverse Primer
Duox2	g5	5'-CCCTTGGAGAACCACCTTGTTGGTCGGAGCTGC TCCCAGGAGGTTTAAGAGCTAAGCTGGAAACAG-3'	
	g1	5'-CCCTTGGAGAACCACCTTGTTGGATCTTGGCAA GAGGCGAAGGTTTAAGAGCTAAGCTGGAAACAG-3'	
Arcn1	g2	5'-CCCTTGGAGAACCACCTTGTTGGTTGGCAAGAG GCGAAGCGGGTTTAAGAGCTAAGCTGGAAACAG-3'	
	g3	5'-CCCTTGGAGAACCACCTTGTTGGGCCAGAGCTC CGCGTCTCTGTTTAAGAGCTAAGCTGGAAACAG-3'	5'-CGTTCACGGC
	g1	5'-CCCTTGGAGAACCACCTTGTTGGACTCACCGGC GAGGGAAGAGTTTAAGAGCTAAGCTGGAAACAG-3'	GACTACTGCAC-3'
Rps15a	g2	5'-CCCTTGGAGAACCACCTTGTTGGGATACCACAC GGATGAACAGTTTAAGAGCTAAGCTGGAAACAG-3'	
	g3	5'-CCCTTGGAGAACCACCTTGTTGGGAGCTCCCGC AGACACCGGGTTTAAGAGCTAAGCTGGAAACAG-3'	
Non- target	Control	5'-CCCTTGGAGAACCACCTTGTTGGGGAACCACAT GGAATTCGAGTTTAAGAGCTAAGCTGGAAACAG-3'	

Table 10. Forward and reverse sequences for the oligonucleotides used in the PCR step of sgRNA cloning for CRISPRi. The specific 20-nt sgRNA sequence is highlighted in red.

The PCR was performed using the Phusion® High-Fidelity DNA Polymerase kit (New England Biolabs), preparing a mix containing the desired amount of template, 2.5 μ L of Forward Primer (10 μ M), 2.5 μ L of Reverse Primer (10 μ M), 1 μ L of 10 mM dNTPs, 1.5 μ L of DMSO, 10 μ L of 5x Buffer HF, 0.5 μ L of Phusion Polymerase, and water up to 50 μ L. The melting temperature was adjusted to 68°C and an extension time of 30 seconds was used for 35 cycles, following the provided protocol to set up the PCR program. The template for the reaction was 5 ng of pCRISPRia-v2 plasmid. The resulting linear PCR product contained both BstXI and XhoI restriction sites, as well as the desired sgRNA sequence (**Figure 12**).

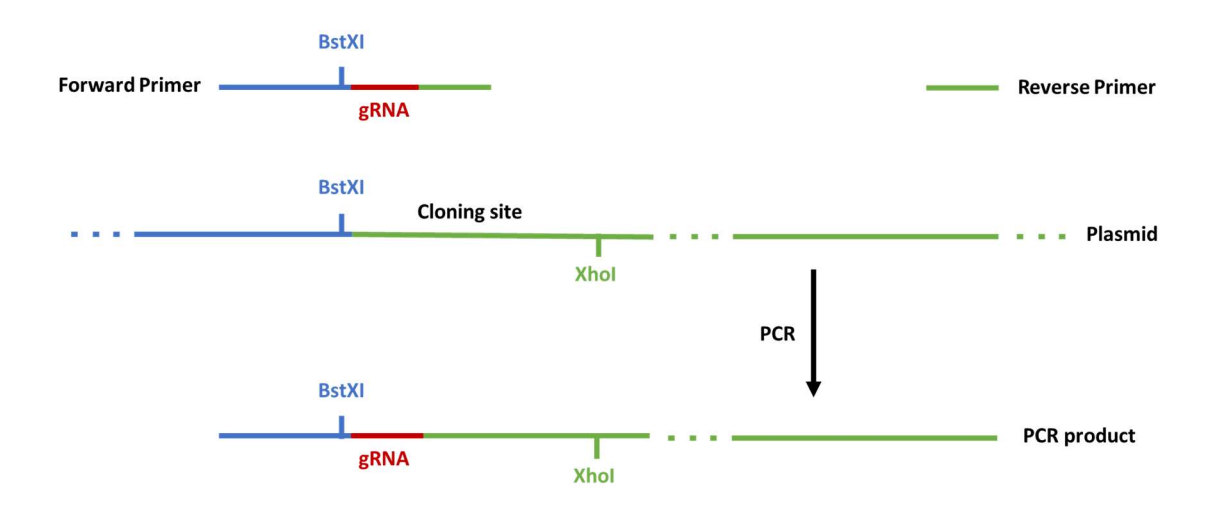


Figure 12. Schematic representation of the PCR design used for sgRNA cloning.

The PCR product obtained and the pCRISPRia-v2 vector underwent digestion with BstXI and XhoI restriction enzymes. For plasmid digestion, 5 μ g of pCRISPRia-v2 were added to a final volume of 100 μ L, containing both restriction enzymes and the restriction buffer (NEBbuffer 3.1). For the PCR product, the entire volume from the reaction was digested.

- The restricted plasmid was separated by agarose gel electrophoresis (TAE 1%), and compared with a non-digested control. Using a UV lamp, the high-size band, corresponding to a linearized plasmid lacking the region contained between the two restriction sizes, was sliced.
- 2. The restricted PCR product was subjected to separation by agarose gel electrophoresis (TBE 3%), utilizing agarose with low melting point. As a result, several

bands were observed, corresponding to I) the non-digested product, II) the product digested with only one of the restriction enzymes, III) the product digested with both restriction enzymes. The last band was identified through a comparison with the 1 kb DNA ladder (NEB), and subsequently excised from the gel.

The bands that were sliced from the digested and separated plasmid and PCR product were processed to extract the corresponding DNA using the NucleoSpin Gel and PCR Clean-up kit (Macherey Nagel), according to manufacturer's instructions. The obtained DNA was quantified using NanoDrop TM1000 (Thermo Scientific), considering concentrations for further ligation. Therefore, once restricted with the same restriction enzymes and purified, both products are ligated to obtain a vector containing the sgRNA sequence between XhoI and XhoI restriction sites, as desired (Figure 13).

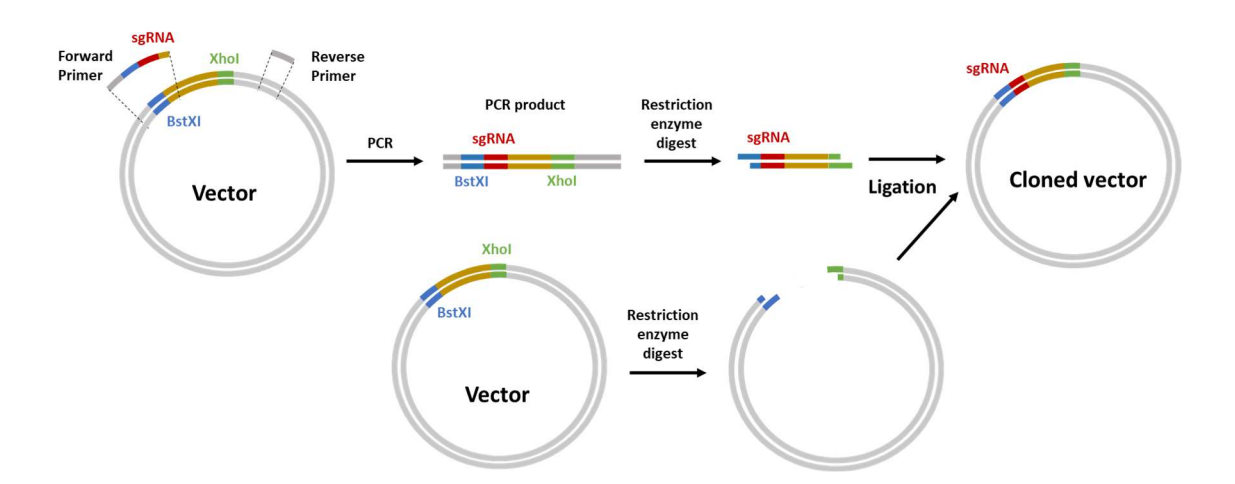


Figure 13. Cloning strategy for a particular sgRNA into the pCRISPRia2 vector, involved the use of PCR, restriction enzymes and ligation.

For the subsequent ligation step, was DNA Ligation Kit (Takara) utilized, containing a one-solution premix ligation reagent with a high efficiency, particularly for blunt-ended ligation. The reaction was initiated by mixing 150 ng of plasmid and 5.6 ng of PCR product (vector: insert = 25:75 fmol), and then left to incubate overnight at 16°C. Controls with no ligation mix or PCR product were included prevent the possibility of contamination and self-recircularization of the plasmid. The ligation product was used for bacterial transformation, following the previously explained protocol, and resulting bacterial clones were selected and cultured for further DNA extraction the

aforementioned Miniprep kit. For each bacterial clones, a glycerol stock was prepared for preservation.

The accuracy of the cloning of each sgRNA was confirmed by sequencing. For this purpose, each putative plasmid DNA was submitted for sequencing with the Reverse primer that had been previously used for cloning, using the sequencing service of Stab Vida. Each DNA sequence was then thoroughly examined and validated by using SnapGene Viewer software. To undergo large-scale preparations, one correctly confirmed bacterial clone was selected from the corresponding bacterial stock of each desired sequence.

4.1.2. Library amplification

The CRISPRi library (Addgene, #83987) was provided as DNA powder, which needed to be amplified to obtain a sufficient DNA quantity for the screening process. To achieve this, Endura™ ElectroCompetent Cells (Lucigen) were transformed with the pool library by using 4 reactions in total. Briefly, 100 ng of DNA library (25 ng/reaction) were mixed with 100 μL of electrocompetent cells (25 μL/reaction). Next, 26 μL of this mixture were distributed into each cuvette and electroporation was performed in a BTX ECM™ 630 electroporator using the following settings: 25 μF, 200 Ohms and 1600 Volts. Upon completion of each run, 975 μL of Recovery Medium (LGC Biosearch Technologies) were added into the electroporated cuvette, collecting all the volume into 4 separate tubes, each of which already contained 1 mL of Recovery Medium. Following a short period of bacterial growth (1 hour, 250 rpm, 37° C), the entire volume was collected in one single tube, from which 10 μ L were taken for serial dilutions that were subsequently plated onto LB agar dishes containing ampicillin. The remaining volume was then distributed into 4 Erlenmeyer flasks, each containing LB medium with ampicillin, for large-scale plasmid DNA production. The plates and large-scale cultures were incubated overnight at 37°C, with the Erlenmeyers being agitated at 250 rpm (250 rpm).

On the following day, we confirmed the desired DNA library's representation by colony counting, ensuring a minimum of 200x coverage based on the number of colonies counted in each performed dilution. Afterwards, the large-scale culture was processed for

plasmid DNA purification. The purified library was subsequently sequenced to validate the proper representation of the sgRNAs (quality control). The sequencing was carried out using an Illumina HiSeq 2500 with 50 million reads. To enable multiplexing, we amplified the sample through PCR and introduced a specific barcode (explained below in the 'PCR for sequencing' section).

4.2. SCREENING PERFORMANCE

Initially, we conducted a large-scale lentivirus production from the pool library. It is recommended to produce virus sufficient to infect a minimum of 200x the library's size. . In our case, we aimed to prepare for 400x. Our CRISPRi library has approximately 100,000 different sgRNAs due to the inclusion of 5 sgNRAs per gene. Multiplying this number by 400x yields 40 million cells that need to be infected. However, since we infected at 0.3 multiplicity of infection (MOI), the actual total number of cells required was 134 million. An MOI below 0.5 ensured that each cell was infected by a maximum of one vector containing a unique sgRNA.

To achieve the desired MOI, we optimized the transfection conditions in HEK cells and infection conditions for NPp53, as detailed in the lentivirus production section above. For this purpose, we employed 1 mL of fresh virus supernatant to infect 500,000 cells per well in a 6-well plate. Consequently, for the required number of wells, a minimum of 268 mL of virus supernatant was required, utilizing the spin-infection protocol described earlier.

On the day following infection, the cells from all the 6-well plates were transferred to 150 mm plates. After 48h post-infection, puromycin (5 μ g/mL) was added to eliminate non-transduced cells. Puromycin selection was maintained for 72h, passaging and amplifying the population of cells once confluent. Finally, cell pellets were obtained from samples of time zero (T_0) condition, collecting 10 million of cells per tube. The MOI was determined based on the percent of BFP-positive cells after 5 passages following puromycin selection, which was measured by FACS.

In order to initiate treatment with abiraterone, we established 3 replicates for both untreated and treated conditions. It is recommended to have at least 100x the number of guides in the library in each replicate, and we used 200x coverage for our experiment. Therefore, we required at least 20 million of cells each replicate To achieve confluence 48 hours after the last passage, we optimized conditions for culturing 3.4 million NPp53 cells in 150 mm plates. Consequently, we needed at least 6 plates of 150 mm for each replicate. Each replicate was treated, passaged, and managed independently. Cell passage was carried out each other day, counting cells and seeding again 3.4 million cells per plate. Abiraterone treatment was replenished daily with fresh drug $(7.5 \mu M)$.

At the end of the experimental period, which was 14 days after the initiation of treatment (T₁₄), cells from each replicate were individually harvested and subsequently centrifuged to form cell pellets (10 million cells per tube).

4.3. SAMPLE PREPARATION FOR SEQUENCING

4.3.1. gDNA isolation

Genomic DNA (gDNA) was isolated from the different samples obtained in the screening experiment, including 3 replicates of T_0 , 3 replicates of untreated cells at T_{14} and 3 replicates of abiraterone-treated cells at T_{14} .

Cell pellets stored at -80°C were resuspended in 1 mL of PBS for each and processed using NucleoSpin® Blood XL kit (Machery Nagel), following the manufacturer's instructions. For each replicate, the gDNA was extracted from 40 million of cells, which is 400x the size of the library, to ensure a good sgRNA representation. The concentration of gDNA obtained was determined using NanoDrop TM1000 (Thermo Scientific).

4.3.2. Size fractionation of genomic DNA

The purpose of this step is to enrich for the sgRNA-containing fragments of genomic DNA, so that the total amount of DNA required for the following step is considerably reduced, and thus requiring far fewer PCR reactions. To achieve this, gDNA from each replicate was digested with Sbf1-HF restriction enzyme (400 U/mg, overnight, 37 °C).

After overnight digestion, loading dye (NEB) was added to run each sample in a large 0.8% agarose TAE gel. Size selection was performed using a 100 bp ladder (NEB). The restriction band, expected to appear at approximately 500 bp, was excised with a generous window to collect all the DNA. The sliced bands for each sample were weighted and processed using a Gel Purification Kit (Machery Nagel), following the provided protocol. The extracted and purified DNA was quantified with NanoDrop TM1000 (Thermo Scientific) to prepare PCR reactions.

4.3.3. PCR for sequencing

We utilized the Phusion DNA polymerase kit to conduct the PCR reactions for sequencing the samples (**Table 11**).

PCR preparation			
Reagent	V of reagent	PCR program	
Water	Up to 100 µL	1) 98°C, 30 s	
Buffer	20 µL		98°C, 15 s
DMSO (100%)	3 µL	2) 23 cycles	56°, 15 s
Forward Primer (100 μM)	0.4 μL		72°C, 15 s
Reverse Primer (100 μM)	0.4 μL	72°C, 15 s	
dNTPs (10 mM)	2 µL	7°C, hold	
Phusion Polymerase	1 µL		
DNA	Up to 500		

Table 11. Components of PCR reaction mix and program conditions for generating the product that will be sequenced for screening analysis.

Each reaction was carried out using a maximum of 500 ng of DNA. Depending on the amount of DNA extracted from sample, we needed to perform 4-5 PCR reactions per replicate. We used a different Forward Primer per replicate, thus allowing to introduce a unique Index for Illumina sequencing to distinguish sgRNAs from each condition (**Table 12**). Forward primer position was designed to aligns upstream the sgRNA sequence region. The reverse primer was common for all the samples, generating a PCR product of 274 bp.

Sample ID	TruSeq ID	Index (5' Primer)	
Quality control	20	GTGGCC	
T ₀ A	14	AGTTCC	
T ₀ B	10	TAGCTT	
T ₀ C	3	TTAGGC	
T ₁₄ Vehicle A	1	ATCACG	
T ₁₄ Vehicle B	23	GAGTGG	
T ₁₄ Vehicle C	13	AGTCAA	
T ₁₄ Abiraterone A	5	ACAGTG	
T ₁₄ Abiraterone B	4	TGACCA	
T ₁₄ Abiraterone C	7	CAGATC	
5' Primer	aatgatacggcgaccaccgagatctacacgatcggaagagcacac		
	gtctgaactccagtcacXXXXXXgcacaaaaggaaactcaccct		
Common 3' Primer	CAAGCAGAAGACGGCATACGAGATCGACTCGGTGCCA CTTTTTC		
Sequencing Primer	GTGTGTTTTGAGACTATAAGTATCCCTTGGAGAACCAC CTTGTTG		

Table 12. Illumina Hiseq2500 compatible Primers (for PCR and sequencing)

After completion of the PCR, the reaction products from each replicate were combined into a single tube. To concentrate and purify the samples, they were ran in a 1.5% agarose TBE gel with 100 bp ladder. This process separates the actual PCR product (274 bp) from the Primer dimer (~150 bp). The 274 bp band was then excised from the gel and purified using the Gel Purification Kit (Machery Nagel). A small amount of this purified DNA from each sample is run on a final 1.5% agarose TBE gel to confirm the presence of a single band corresponding to the desired size. Once confirmed, samples were sent for sequencing with the Sequencing primer.

4.4. CRISPRI SCREENING BIOINFORMATIC ANALYSIS

4.4.1. Quality control

Initially, raw reads obtained from the pool library were subjected to quality control analysis with FastQC (https://www.bioinformatics.babraham.ac.uk/projects/fastqc/) to ensure data integrity. Next, the read counts were aligned to the sgRNA library comprising 107,415 target sgRNAs that corresponded to 20,004 target genes (5 sgRNAs per gene). The total number of reads, distribution of single guides by gene, and the mismatches were subsequently analyzed.

4.4.2. CRISPRi screening

The subsequent step involved the analysis of the CRISPRi experiment. Raw reads were used to generate the sgRNA counts matrix using the sgRSEA package. Quality control of the raw data was performed with FasQCf (https://www.bioinformatics.babraham.ac.uk/projects/fastqc/) and CaRpools R package [286]. The sgRNA counts were normalized by library size and collapsed to genes. As negative control, a total of 2170 non-target sgRNAs were used to determine the expression in the different phenotypes. Principal components analysis (PCA) was performed to cluster the samples based on sgRNAs read counts, and one sample was filtered out for quality concerns.

4.4.2.1. Hits calling

The identification of essential genes for abiraterone treatment was performed by DESeq2 [287] comparison of Vehicle at t=14 vs abiraterone at t=14 at sgRNA level. The final list of sgRNAs selected were those meeting the following criteria: 1) average intensity of reads in Control at t=0 samples \geq 100 reads; 2) log2 fold change enrichment (of treated over vehicle samples) \leq -1.5, and 3) adjusted p-value \leq 0.05. A total of 419 genes were identified as essential genes to survive abiraterone treatment. For the selection of the final list of hits, genes with at least two independent sgRNAs with significant differences between treated and untreated samples were selected. A total of 8 genes were selected as "top hits".

4.4.2.2. Functional analysis

For enrichment identification of specific cellular functions and pathways of the selected essential genes for abiraterone treatment, the genes with at least one sgRNA depleted with log2 fold change ≤ -1.5 were selected. Gene set enrichment analysis (GSEA) was performed with Enrichr tool [288]. Hallmarks, Canonical pathways and Gene Ontolohy (GO) terms from MSigDB were interrogated. Besides, a GSEA pre-ranked analysis was performed with the ranked list of genes from the differential expression results at gene level [289].

4.5. BIOINFORMATIC ANALYSIS FROM SU2C PROSTATE CANCER DATASET

The SU2C/PCF RNA-seq and clinical data were obtained from cBioPortal (https://www.cbioportal.org/study/summary?id=prad_su2c_2019) [290].

The gene expression signature levels or scores were computed from the combined analysis of the corresponding gene constituents using the single-sample Gene Set Expression Analysis (ssGSEA) algorithm [291], calculated in Gene Set Variation Analysis (GSVA) (https://github.com/rcastelo/GSVA) [292]

The gene signatures were compiled from the corresponding publications [293, 294] and uncertain gene names curated using ENSEMBL BioMart annotations [295]. Spearman's

correlation and statistical significance level were computed in R software using the functions cor and cor.test from stats (version 4.3.0) package.

Univariate survival analyses were performed using the Kaplan–Meier method and log-rank test, computed with the survival (version 3.5–5) R package. Categorization of high/low AR and NEPC scores was based on 0.3 and 0.1 cut-off values respectively. Categorization of high/low gene expression was based on the median value.

5. FUNCTIONAL ASSAYS

5.1. CELL VIABILITY ASSAY

To evaluate the effects of different drug treatments on cell survival and proliferation, we conducted MTT (Thiazolyl Blue Tetrazolium Bromide) assay. For this purpose, cells were seeded in 96-well plates (500 cells/well for NPp53; 5000 cells/well for 22Rv1 and LNCaP),, and the treatments were administered on the following day to allow for cell attachment and the acquisition of their corresponding morphology after trypsinization. Each treatment, either alone or in combination with others was prepared to achieve the desired final concentration once added in each well. Subsequently, 72 hours post-treatment, the MTT reagent (Merck) was added (10 μ L of MTT at 5 mg/mL). After 3 hours in the incubator, 100 μ L of the MTT dissolving buffer (SDS 10%, HCl 10mM, H₂O) were added to solubilize the formazan crystals formed. Plates were incubated overnight at 37°C and readed the next day using the Victor Multilabel Plate reader (PerkinElmer). This assay is based on the metabolic reduction of MTT in a blue-colored compound, which is catalyzed by the mitochondrial succinate dehydrogenase enzyme. This method, based on cell metabolism, is widely used to measure survival and cell proliferation, as the number of viable cells is proportional to the amount of formazan produced.

5.2. COLONY FORMATION ASSAY

The clonogenic assay or Colony formation assay (CFA) is a quantitative *in vitro* technique that measures the ability of a single cell to survive and grow into a colony. To

perform this assay, cells were seeded at low densities in a 6-well plate (500 cells/well for NPp53), and the media containing the treatment was replaced every 48 hours. After 8 days of treatment, the media was aspirated from the wells, and a crystal violet solution (0.5% w/v in 10% EtOH and 90% formaldehyde) was added to visualize colonies formed. Finally, the plates were scanned, and quantification of colonies was performed using image J software (https://imagej.nih.gov/ij/).

5.3. SYNERGY OF DRUGS

In order to investigate the impact of specific drug combinations, we developed an MTT-based assay to assess the potential synergy between two tested compounds. To this end, cells were seeded in three 96-well plate and treatments were added to obtain 6 serial single-drug concentrations, as well as the combination of these concentrations between both drugs. After 72 hours of treatment, the plates were submitted to the MTT protocol and read as previously explained. To analyze the results, the Combenefit software was utilized, allowing for the generation of a matrix with synergy values for the different drug combinations, using synergy analysis LOEWE option.

In addition, we selected the drug concentrations with the highest synergy scores to perform a regular MTT viability assay. Here, we compared the cell viability curve obtained for one of the drugs with that resulting from the addition of a fixed concentration of the other drug.

5.4. AR TRANSCRIPTIONAL ACTIVITY REPORTER

We generated a stable NPp53 cell line that expresses a Pb-PSE-EGFP construct (Probasin and Prostate Specific Enhancer-GFP) by lentiviral transduction with this plasmid [296]. Probesin is an androgen-regulated protein and is specifically expressed in the differentiated mouse prostate. The aforementioned reporter cell line was cultivated in 6-well plates and treated with abiraterone (7.5 μ M) for 24 and 96 hours, with daily replacement of the drug. In order to evaluate the AR transcriptional activity, flow cytometry was used to quantify GFP, considering both the percentage of GFP-positive cells and the mean fluorescence value of the GFP-positive cells.

5.5. TOTAL ROS QUANTIFICATION

To quantify intracellular reactive oxygen species (ROS), a fluorescent-based assay was performed, using CM-H₂DCFA, that reacts with this type of molecules.

Cells were seeded in 6-well plates and treated on the following day (50-70% confluence) with the chosen drug of choice. Next, 2- or 8-hours post-treatment, cells were trypsinized and collected in flow cytometry tubes. To eliminate any interference caused by molecules present in the media, the tubes were centrifugated 5 minutes at 250 G and washed twice with 2 mL of PBS between the centrifugation steps. Following the third centrifugation, the cells were resuspended in 200 μ L of PBS containing the respective probe for each case, as described below:

CM-H₂DCFA probe detects total ROS and is prepared as a stock solution in DMSO at 400 μ M. The working solution for staining is prepared in PBS at 10 μ M. The product of the reaction has an excitation and emission spectra (Ex/Em) of ~492–495/517–527 nm. CM-H2DCFDA is a chloromethyl derivative of H2DCFDA, which enhances its retention in living cells. This particular probe exhibits passive diffusion into cells, where intracellular esterases effectively cleave its acetate groups. Furthermore, its thiol-reactive chloromethyl group undergoes a reaction with intracellular glutathione (GSH) and other thiols. Following subsequent oxidation, a fluorescent adduct is formed and trapped within the cell, thus facilitating long-term studies.

The cells were briefly vortexed for homogenization, and then incubated with the corresponding probe for 45 minutes in a cell culture incubator (37 °C, 5% CO₂). Upon completion of the incubation period, the probe was diluted in 2 mL of PBS and the cells were centrifuged and washed again with PBS. Finally, after the second centrifugation step, cells were resuspended in an appropriate volume of PBS for flow cytometry analysis.

5.6. RNA-seq

For the purpose of RNA-seq performance, NPp53 cells (Control and Duox2 KD) were seeded in 150 mm plates. Once the cells reached a confluence of 50-70%, they were treated

with Abiraterone at a final concentration of 20 μ M. After 8 hours of treatment, the cells were trypsinized and subjected to the RNA extraction protocol previously described.

RNA quality control was performed, followed by library preparation. The library was sequenced using an Illumina HiSeq2500 platform at the CNAG-CRG platform. The sequencing was carried out with paired-end reads (2x100 bp), generating over 25 million reads per sample. The mRNA-sequencing was performed in a stranded manner, allowing for the identification and analysis of the mRNA transcripts.

5.6.1. RNA-seq bioinformatic analyis

Raw files obtained from the sequencing were merged, and their quality was assessed using the FastQC software (https://www.bioinformatics.babraham.ac.uk/projects/fastqc/). Trimmomatic was used to trim Illumina adaptors and bad quality reads [297]. Subsequently, the reads were mapped over the human reference transcriptome (hg19/GRCh38) with the STAR tool [298]. The aligned sequences were quantified with the RSEM software [299], and a gene expression matrix was generated in terms of transcripts per million. The expression values were then transformed to a log2 scale. Genes that were not expressed were excluded from the analysis. Finally, to mitigate the influence of batch effects, an adjustment was performed using the ComBat function from the R package sva.

A differential expression analysis was performed to identify differentially-expressed genes (DEGs) between the different experimental conditions with R package edgeR. A list of DEGs with p-value ≤ 0.05 and logFC \geq abs(1.5) was extracted. To identify enrichment in specific cellular functions and pathways, a GSEA analysis was performed comparing the different conditions. Hallmarks collection from MsigDB was interrogated, including a total of 50 gene sets that summarized the most representative biological states and processes.

5.7. METABOLIC ASSAYS

We utilized the Seahorse XFe 96 (Agilent) equipment, along with commercially purchased kits, to conduct in vitro metabolic and bioenergetic measurements. The experimental procedures were performed following the manufacturer's instructions.

The day prior to initiating the treatment, cells were seeded in the provided Seahorse 96-well plate (1100 cells/well for NPp53; 7500 cells/well for 22Rv1 and LNCaP), with in a total volume of 100 μ L per well. On the following day, cells are treated with abiraterone at two different concentrations (7.5 and 20 μ M). In parallel, the cartridge included in the kit is rehydrated with sterile H₂O and incubated overnight at 37 °C and 0% CO₂. Additionally, within the same incubator, an aliquot of the calibration solution provided, RPMI Seahorse medium and the stocks of glucose (1 M), pyruvate (100 mM), and L-Glutamine (200 mM) were placed.

Compound	ATP Rate Assay			Mitostress Assay		
	[Stock]	[Port]	[Well]	[Stock]	[Port]	[Well]
Oligomycin	150 μΜ	15 μΜ	1.5 μΜ	100 μΜ	15 μΜ	1.5 μΜ
FCCP	-	-	-	100 μΜ	10 μΜ	1 μΜ
Rotenone + Antimycin A	50 μΜ	5 μΜ	0.5 μΜ	50 μΜ	5 μΜ	0.5 μΜ

Table 13. Preparation of the ETC inhibitors used in the ATP Rate Assay and Mitostress Assay kits, indicating stock and final concentrations.

After 24 hours of treatment, we remove the water of the cartridge and add 200 μ L of pre-warmed calibration solution to each well, returning the cartridge to the incubator at least 1 h. Meanwhile, we prepared the complete Seahorse RPMI medium, containing glucose (10 mM), pyruvate (1 mM) and L-Glutamine (2 mM). This medium was used to wash the cells once, and after removing the media, fresh medium (180 μ L) was added to each well. The cells were incubated for 1 hour in the 0% CO₂ incubator.

Furthermore, dilutions of different inhibitors that would be used with the various kits to interact with the electron transport chain (ETC) were prepared, as indicated in **Table 13**.

Each cartridge consists of 96 sensors (one per well). Each sensor is surrounded by 4 ports (A, B, C and D) that were loaded with the inhibitor concentrations from **Table 13**. The positioning for each inhibitor within the ports is dependent on the type of assay being conducted, as specified in **Table 14**. In both assay types, the position D is filled with Hoechst staining from a stock prepared at 20 μ M. Hoechst is a blue, fluorescent dye used to stain cellular DNA. This staining procedure facilitates the normalization of data based on the number of cells.

	ATP I	Rate Assay	MitoStress Assay		
Port position	Compound	Volume added to the port (stock)	Compound	Volume added to the port (stock)	
А	-	-	Oligomycin	20 μL	
В	Oligomycin	20 μL	FCCP	22 μL	
С	Rotenone + Antimycin A	22 μL	Rotenone + Antimycin A	25 μL	
D	Hoesch	25 μL	Hoesch	25 μL	

Table 14. Port positions used for each Seahorse kit, along with the respective compound and volume loaded in each position.

After the loading of the different compounds into the wells of the cartridge, the cartridge is inserted into the Seahorse equipment. Following the calibration of the wells, the utility plate is removed, and the cell culture plate is positioned on the tray to commence the reading process.

Once the reading is completed, the 96-well cell culture plate was examined using a fluorescence microscope (Zeiss Axio Observer Z1+Apotome inverted fluorecent microscope) to identify viable cells based on Hoechst staining. Images were captured from each well, and the number of nuclei was quantified using an algorithm implemented in ImageJ by the IDIBELL Microscopy Platform Service. Subsequently, the data was normalized by the cell

count in each well to facilitate calculations of key parameters using the Wade analysis software.

5.7.1. ATP Rate Assay calculations

Both glycolysis and oxidative phosphorylation (OXPHOS) contribute to the acidification of the medium, although only OXHPOS consumes O_2 . The Seahorse XF technology enables the simultaneous measurement of the flux of both H^+ production (ECAR) and O_2 consumption (OCR), providing the possibility to calculate different ATP production rates using the following equations.

5.7.1.1. Glycolytic ATP production rate calculation

$$Glucose + 2 ADP + 2 Pi \rightarrow 2 Lactate + 2 ATP + 2 H_2O + 2 H^+$$
 (Equation 1)

glycoATP Production Rate
$$\left(\frac{pmol\ ATP}{min}\right) = GlycoPER\left(\frac{pmol\ H^+}{min}\right)$$
 (Equation 2)

Therefore, the rate of glycolytic ATP production (glyco ATP) is equivalent to the Glycolytic Proton Efflux Rate (glycoPER, **Equation 2**).

5.7.1.2. Mitochondrial ATP production rate calculation

The ATP production rate linked to OXHPOS metabolism can be determined as the OCR that is inhibited by the addition of oligomycin, an inhibitor of ATP synthase (**Equation 3**):

$$OCR_{ATP}\left(\frac{pmol\ O_2}{min}\right) = OCR\left(\frac{pmol\ O_2}{min}\right) - OCR_{Oligomycin}\left(\frac{pmol\ O_2}{min}\right)$$
 (Equation 3)

The conversion of OCR to the rate of mitochondrial ATP production can be computed using the **Equation 4**:

$$glycoATP\ Production\ Rate\ \left(\frac{pmol\ ATP}{min}\right) = OCR_{ATP}\left(\frac{pmol\ O_2}{min}\right) *\ 2\ \left(\frac{pmol\ O}{pmol\ O_2}\right) *\ P/O\left(\frac{pmol\ ATP}{pmol\ O}\right)$$
 Equation 4

5.7.1.3. Total ATP Production Rate calculation

Finally, the total amount of ATP production rate can be calculated as the sum of the glycolytic and mitochondrial ATP production rates (**Equation 5**):

$$ATP\ Production\ Rate\ \left(\frac{pmol\ ATP}{min}\right) =\ glycoATP\ Production\ Rate\ \left(\frac{pmol\ ATP}{min}\right) +\ mitoATP\ Production\ Rate\ \left(\frac{pmol\ ATP}{min}\right)\ \ \textbf{Equation}\ \textbf{5}$$

5.7.2. Mito Stress Assay calculations

In this assay, three distinct mitochondrial modulators are sequentially injected into each well to facilitate the calculation of key parameters (**Table 15**) related to mitochondrial function.

Parameter value	Equation		
Non-mitochondrial Oxygen Consumption	Minimum rate measurement after Rotenone/antimycin A injection		
Basal Respiration	(Last rate measurement before first injection) – (Non- Mitochondrial Respiration)		
Maximal Respiration	(Minimum rate measurement after FCCP injection) – (Non- Mitochondrial Respiration)		
H+ (Proton) Lead	(Minimum rate measurement after Oligomycin injection) – (Non-Mitochondrial Respiration)		
ATP production	(Last rate measurement before Oligomycin injection) – (Minimum rate measurement after Oligomycin injection)		
Spare Respiratory Capacity	(Maximal Respiration) – (Basal respiration)		

Table 15. Calculations of the various parameters associated with the OXPHOS metabolism that can be derived from the ATP Mito Stress Assay.

Firstly, oligomycin is utilized to inhibit the ATP synthase. Secondly, Carbonyl cyanide 4-(trifluoromethoxy)phenylhydrazone (FCCP) collapses the proton gradient and disrupts the mitochondrial membrane potential, enabling the achievement of the maximum oxygen consumption through complex IV. Lastly, the combination of rotenone (complex I inhibitor) and antimycin A (complex III inhibitor) allows to shut down mitochondrial respiration.OCR measurements obtained during the experiment can be utilized to calculate various parameters related to OXPHOS metabolism, as indicated in Table 15. The use and interpretation of these parameters will be further elucidated in the corresponding Results section.IN VIVO

5.8. ETICHS AND HOUSING

The animal study performed in this thesis project was conducted at the IDIBELL Animal Core Facility (AAALAC unit 1155) and was approved by the Ethics Committee for Animal Experimentation of the Biomedical Research Institute of Bellvitge (IDIBELL) and the Generalitat de Catalunya. This study was performed in compliance with the European directives on ethical usage of rodents for animal research.

The mice utilized in this study were male athymic nude mice (Envigo). They were housed in ventilated cages under controlled temperature conditions (20-25°C) in a SPF (Specific Pathogen Free) environment to ensure sterility. The animals were subjected to a regulated artificial circadian 12h light/dark cycle and provided with *ad libitum* access to standard diet and water. All experimental procedures were performed within a vertical laminar flow cabinet.

5.9. ORTOTHOPIC ENGRAFTMENT

The 22Rv1 cell line was transduced with a lentiviral plasmid containing both GFP and Luciferase reporter genes for the purpose of *in vivo* tracking. Transduced cells were subsequently selected by FACS, which allowed for the isolation of GFP-positive cells (from now, 22Rv1-reporter cells).

22Rv1-reporter cells were injected orthotopically into the prostate. For this purpose, the cells in culture were trypsinized and prepared in a mixture consisting of Matrigel (Cultek) and PBS in a 1:1 ratio. The resulted mix contained 3 million of cells in a volume of 10 μ L, which was injected in the anterior prostate (AP) region of each mouse using a 10 μ L Hamilton syringe.

Following injection, mice were randomly assigned to different treatment groups and tumors were monitored using an IVIS® Spectrum In Vivo Imaging System. To detect tumor growth, mice were intraperitoneally injected with D-luciferin (150 mg Luciferin/kg body weight). Each photographic measure was taken after a 10-minute incubation period, adjusting exposure in each case based on the size of the tumor (2, 5 and 20 seconds of exposure using "medium" binding). Photon radiance was measured in each animal and monitored twice a week, using Average Radiance (p/s/cm²/sr) as an indicator of tumor growth. A threshold of 50·10⁶ p/s/cm²/sr of average radiance was established as the criterion for including each mouse in the assigned treatment group.

5.10. DRUG TREATMENT

Enzalutamide (Sigma-Aldrich; #PHB00235) was dissolved in DMSO at 40 mg/mL. Working solution was prepared at 4 mg/ml in PBS containing 5% DMSO, 0.1% carboxymethyl cellulose and 0.1% Tween-80. The administration dose was 20 mg/kg body weight (5 times a week by oral gavage).

PX-478 (MedChemExpress) was dissolved in DMSO at a concentration of 78.82 mg/mL (200 mM). A working solution was prepared at 4 mg/mL in PBS, and the administration dose was 20 mg/kg body weight, (3 days a week by intraperitoneal injection).

Each mouse, which has been previously assigned to one of the treatment groups (vehicle, Enzalutamide, PX-478, combination), began the scheduled treatment once it reached the stablished threshold of tumor-associated luminescence. The treatment was continued for the duration of the animal's life in order to study potential differences in survival. Each mouse was euthanized when animal health tis was compromised, taking in consideration several indicators of health (closed or squinted eyes, reluctance to move even

when handled, hunched position, etc.). Factors such as weight loss, high tumor volume, and signs of tumor necrosis were also taken into account when determining the appropriate time for euthanasia.

6. GRAPHIC REPRESENTATION AND STATISTICAL ANALYSIS

Besides for the in-Silico analysis (described in the previous section), graphs and statistic tests were performed using GraphPad Prism v8 software (GraphPad Software, Inc. USA). Error bars were usually represented using the SD (standard deviation).

Statistical test used in grouped analysis was the Two-way ANOVA's Tukey's Test or Bonferroni Test. For individual comparison between 2 conditions, analysis was performed with parametric t-test, with a p value <0.05 (*P < 0.05, **P < 0.01, ***P < 0.001, and ****P < 0.0001).

RESULTS

1. Genome-wide CRISPRi screening

1.1. PREMISES

As previously indicated, the objective of this CRISPRi genetic screening is to identify actionable mechanisms implicated in antiandrogen resistance. To achieve this objective, a genome-wide CRISPRi library was utilized in a classical drop-out strategy, in which sgRNAs negatively enriched in the treated cells compared to an untreated control suggest a synthetic lethal effect of the combination of abiraterone and the loss of function of the targeted gene.

resulting in a specific knock-down for each gene. This may affect cell survival upon abiraterone treatment, which is reflected in the sgRNA representation.

To conduct this experiment, we employed an established prostate cancer (PCa) cell line that was derived from a Nkx3.1^{CreERT2/+}; Pten^{flox/flox}; Trp53^{flox/flox} GEMM mouse (NPp53) (**Figure 7**). This model exhibits castration-resistant prostate cancer (CRPC) with adenocarcinoma features and it has been demonstrated to be resistant to abiraterone [152].

1.2. SCREENING OPTIMIZATION

1.2.1. Library preparation and quality control

We used a CRISPRi library (Addgene; Cat #83987), targeting 20,003 mouse genes and comprising 5 sgRNA per gene. This is a dual-plasmid system wherein dCas9 and sgRNA are cloned in two independent lentiviral vectors. This strategy ensured that CRISPR interference occurs when stable dCas9-expressing cells are transduced with the pooled sgRNA library.

First, the library CRISPRi library, cloned in the pCRISPRia-v2 backbone, was subjected to bacterial amplification to obtain an adequate DNA quantity for screening purposes. The amplified and purified pooled DNA was sent for sequenced to confirm that the complexity and representation of sgRNA was preserved (quality control, **Figure 14**).

We confirmed that most of the genes (95%) contained at least three of the five sgRNAs, with over 350 mapped reads. For optimal screening performance, it is recommended to have between 250-500 reads per sgRNAs per sample. Total reads in sgRNA sequences were equal to 97,256,405.

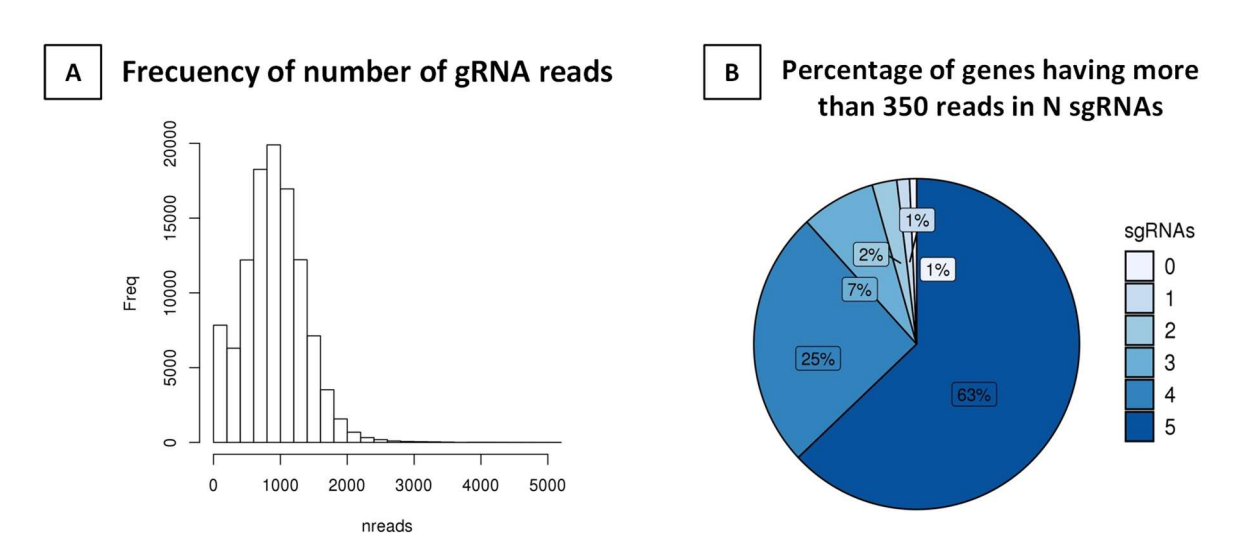


Figure 14. Analysis of sequencing results to assess quality control of the CRISPRi library preparation. A) Histogram distribution of the total number of reads per sgRNA. Y axis represents the frequency of sgRNAs; X axis represents the number of reads per sgRNA. Most sgRNAs have a representation between 607 reads (1st quantile) and 1188 reads (3rd quantile), with a mean of 901.5 reads, indicating that most guides in the library are equally represented. **B)** Percentage of genes that possess least N number of sgRNAs (from 0 to 5) with more than 350 reads mapped. It is recommended to maintain a range of 250-500 reads per sgRNAs per sample.

1.2.2. Engineering of CRISPRi functional cells

As previously stated, CRISPRi requires the constitutive expression of dCas9-KRAB in the targeted cells (**Figure 15A**). For that purpose, NPp53 mouse-derived PCa cell line was transduced with lentivirus carrying a dCas9-expressing vector (pHR-SFFV-KRABdCas9-P2A-mCherry, Addgene #60954), obtaining a NPp53-dCas9 isogenic cell line.

To confirm the CRISPRi activity, we evaluated the reduced expression of control targeted genes. Thus, we quantified the knock-down efficiency of two genes, Rps15a and Arcn1, which were found essential for survival in different cancer cell lines. For that, we

cloned three different sgRNAs targeting these essential genes in the pCRISPRia-v2 backbone, which was transduced into NPp53-dCas9 expressing cells to obtain stable knocked-down cell lines. We observed that the proliferation rate of these cell lines was severely affected by the knock-down of both genes As expected, qPCR analysis showed a significant reduction in the expression levels of the targeted genes in the knocked-down cell lines compared to the non-targeting control sgRNA (**Figure 15B**). Collectively, the efficacy of knock-down across various sgRNAs, as assessed by transcriptional inhibition, ranged from 59% to 75% (p-value <0.01).

As a result, the implementation of CRISPRi in our NPp53 cell line enabled us to create a model of reduced expression for the desired gene, even in cases where the gene is essential, which cannot be accomplished through conventional CRISPR knock-out. This functional system is therefore well-suited for conducting synthetic lethal screening using drugs, which will inhibit the molecular target in a manner more closely resembling gene inhibition rather than complete protein knock-out.

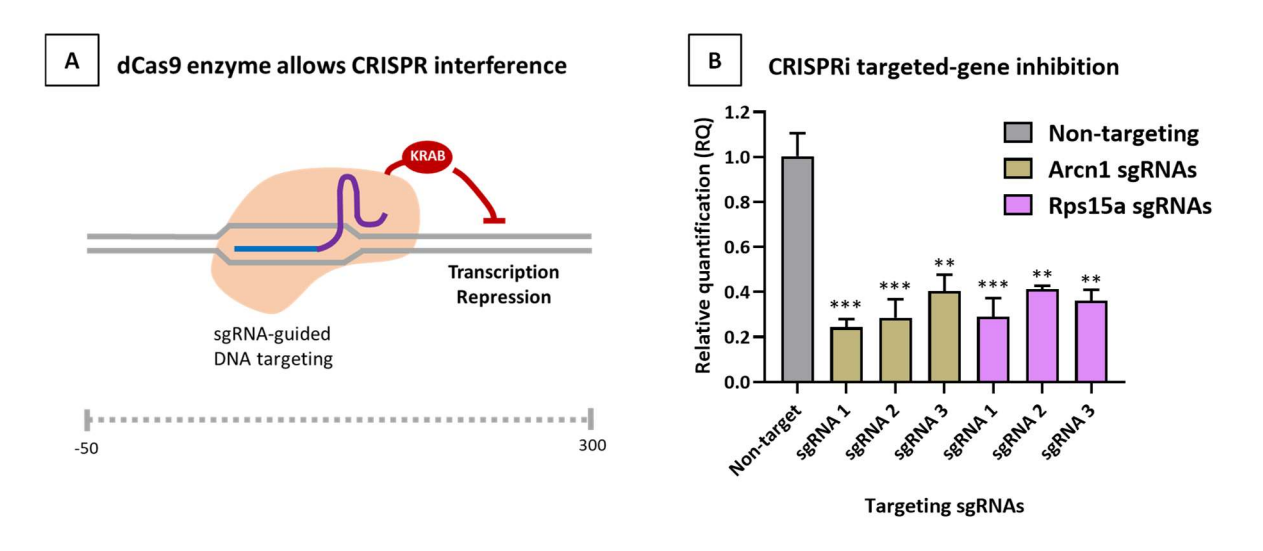


Figure 15. CRISPRi system functionality. A) Cas9 can be converted into an RNAguided transcription inhibitor via inactivation of its two catalytic domains (dCas9) and fused to transcription repressive domains as KRAB (CRISPR interference, CRISPRi). **B)** Transduction of NPp53-dCas9 cells with sgRNA vector results in a specific expression decrease of targeted essential genes (**P < 0.01, ***P < 0.001, n = 3).

1.2.3. Drug concentration optimization

A crucial optimization step in any drug sensitivity-based screening process involves the selection of an appropriate drug concentration that allows for cell growth on the one hand, while preventing non-specific toxic effects on the other. Cells must sustain continuous proliferation to passage cells every 2-3 days, as recommended for screenings.

Based on optimization cell viability assays, an optimal concentration range was identified, with an inhibitory concentration (IC) being determined to reduce cell viability at 10%. Subsequently, the concentration of Abiraterone was selected at 7.5 μ M based on optimization results (**Figure 16A**). To confirm the effect of this sub-lethal concentration range on AR, various experiments were conducted, focusing on AR transcriptional activity and the expression of AR-targeted genes.

First, treatment of NPp53-dCas9 cells with sub-lethal abiraterone concentration (7.5 μ M) was associated with a significant decrase in the expression of *Tmprss2*, a classical androgen-responsive gene, in a time-dependent dependent manner, measured by qRT-PCR (**Figure 16B**), thus confirming that abiraterone influences the transcriptional cascade initiated by AR. However, this effect is more significant at early times (2, 6 and 12h), thus demonstrating the rapid mechanism of action of abiraterone. Consequently, given that screening trials necessitate the cultivation of targeted cells under drug selection for numerous days, it was expedient replace abiraterone treatment on a daily basis (24h) to ensure selective pressure.

Next, we created a NPp53 cell line by lentivirus transduction with an endogenous stable Pb-PSE-EGFP construct (Probasin and Prostate Specific Enhancer-GFP). Probasin is an androgen-regulated protein specifically expressed in the differentiated mouse prostate. As expected, treatment of NPp53 cells expressing the AR-regulated EGFP reporter (Pb.PSE.EGFP) with a sub-lethal abiraterone concentration (7.5 μ M) results in AR transcriptional activity decrease (**Figure 16C**). This decrease was significant by measuring 1) percentage of GFP positive cells and 2) the mean fluorescence intensity values. In fact, this decrease is modest but significant at 24h post-treatment (p-value <0.01). However, AR

transcriptional activity drop was higher after 96h of abiraterone treatment, for both percentage of positive cells (p-value <0.01) and fluorescent intensity (p-value <0.001). For this long-term exposure, abiraterone was replaced daily, thus establishing the conditions for the screening.

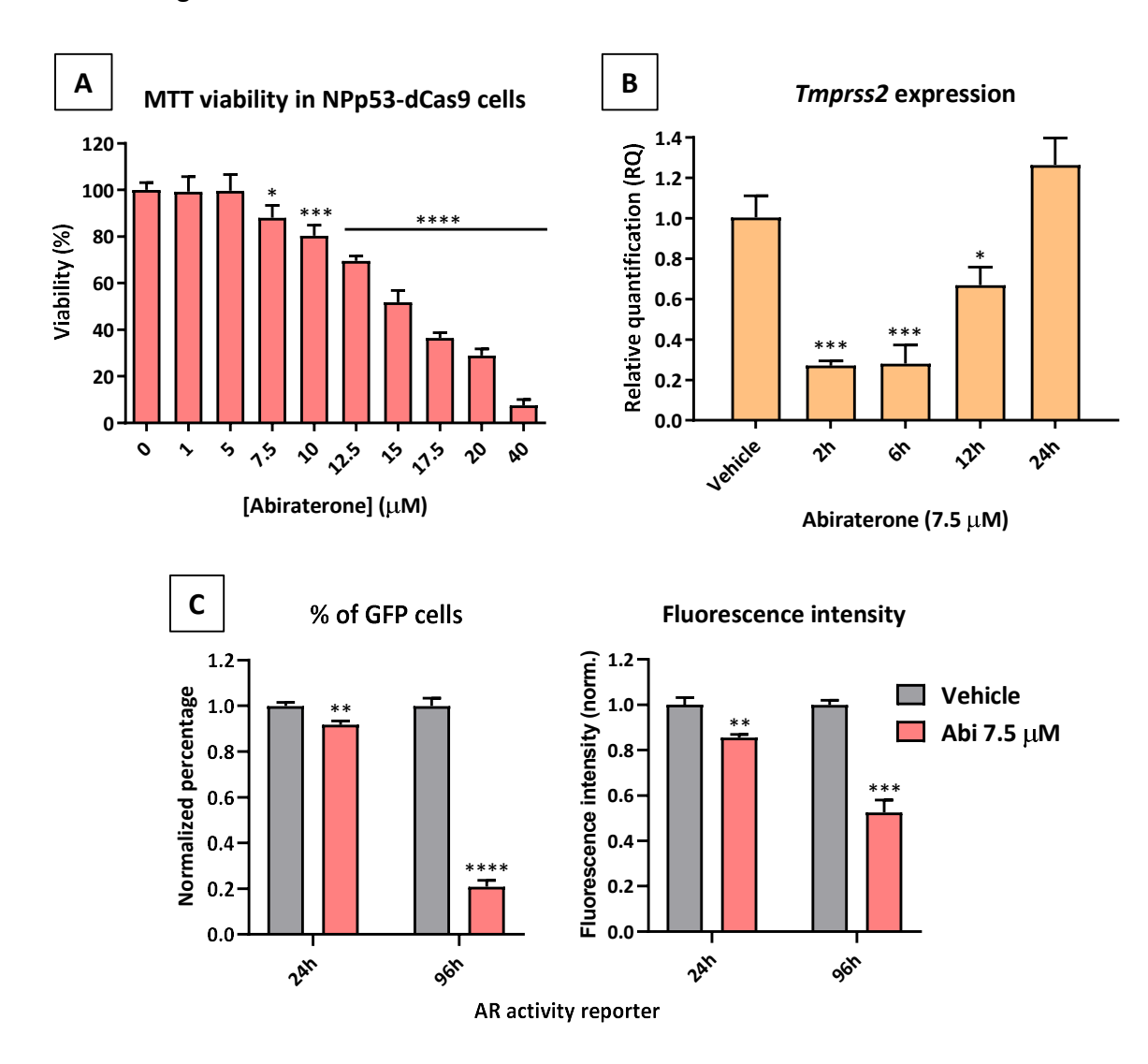


Figure 16. Abiraterone dose selection. (A Toxicity range of abiraterone to select an IC(<10) to ensure that drug concentration during the screening allows convenient cellular growth, measured as MTT viability after 72h of abiraterone treatment. **(B** Changes of AR-targeted genes induced by abiraterone treatment (qRT-PCR) in a dose-dependent manner (N = 3). **(C** AR reporter assay using NPp53 with a stably integrated Pb-PSE-EGFP construct. Cells were treated with Abiraterone for 24h in a single dose or 96h replacing fresh drug daily. FACS analysis were performed to obtain and compare the percentage of positive GFP cell population and the mean fluorescence intensity (N = 3) *P < 0.05, **P < 0.01, ***P < 0.001, and ****P < 0.0001.

Hence, the utilization of a sub-lethal concentration abiraterone allows the growth of NPp53 cells during the screening, necessitating the daily replacement of the drug to maintain its impact on AR transcriptional activity.

1.2.4. Genome-wide screen

The screening pipeline was optimized at various critical steps (**Figure 17**). First, the lentiviral production using HEK239-FT cells was refined by optimizing packaging vectors ratio, time of virus recovery, media conditions to achieve a high virus titer. Second, NPp53-dCas9 were transduced with the aim of achieving an infection rate of 20-50% (multiplicity of infection, MOI< 0.5), as determined by percentage of BFP-positive cells. This rate is crucial to guarantee that each cell is infected with a single sgRNAs. To this end, we previously optimized the number of transduced cells, the amount of virus used and the spin-infection conditions to raise this yield.

After antibiotic selection of transduced cells (t=0), we collected cells from this condition as a control. Then cells were treated daily with Abiraterone for 14 days, passaging cells every other day to maintain the sgRNA representation. At the end of the screening, we collected cells of this endpoint (t=14) to compare the sgRNA representation between treated and vehicle conditions, using massive parallel sequencing of sgRNAs from isolated genomic DNA (gDNA) (Figure 17).

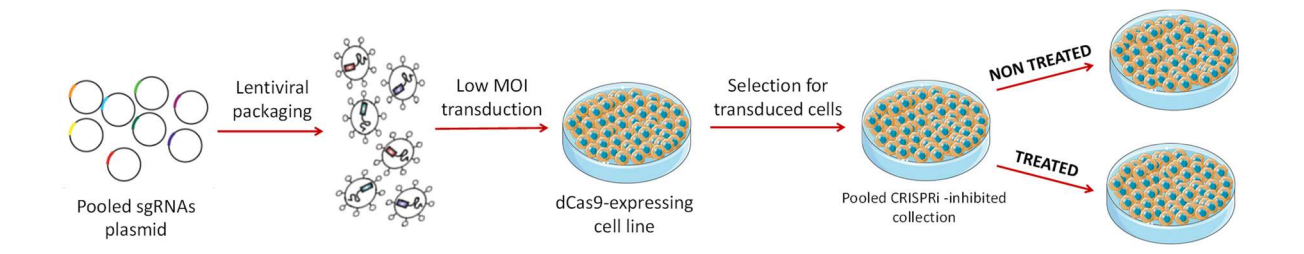


Figure 17. Schematic representation of the CRISPRi screening performance.

For more information about the screening performance and optimization steps, see the corresponding Materials and Methods section.

1.3. SCREENING RESULTS ANALYSIS

After quality control analysis on the raw data, the sgRNA counts were normalized and collapsed to genes. Principal components analysis (PCA) was then performed for clustering the samples based on their respective sgRNAs read counts (**Figure 18A**). As a control, samples from t=0 time were utilized to filter out essential genes that dropped in both t=14 time points (vehicle and treated).

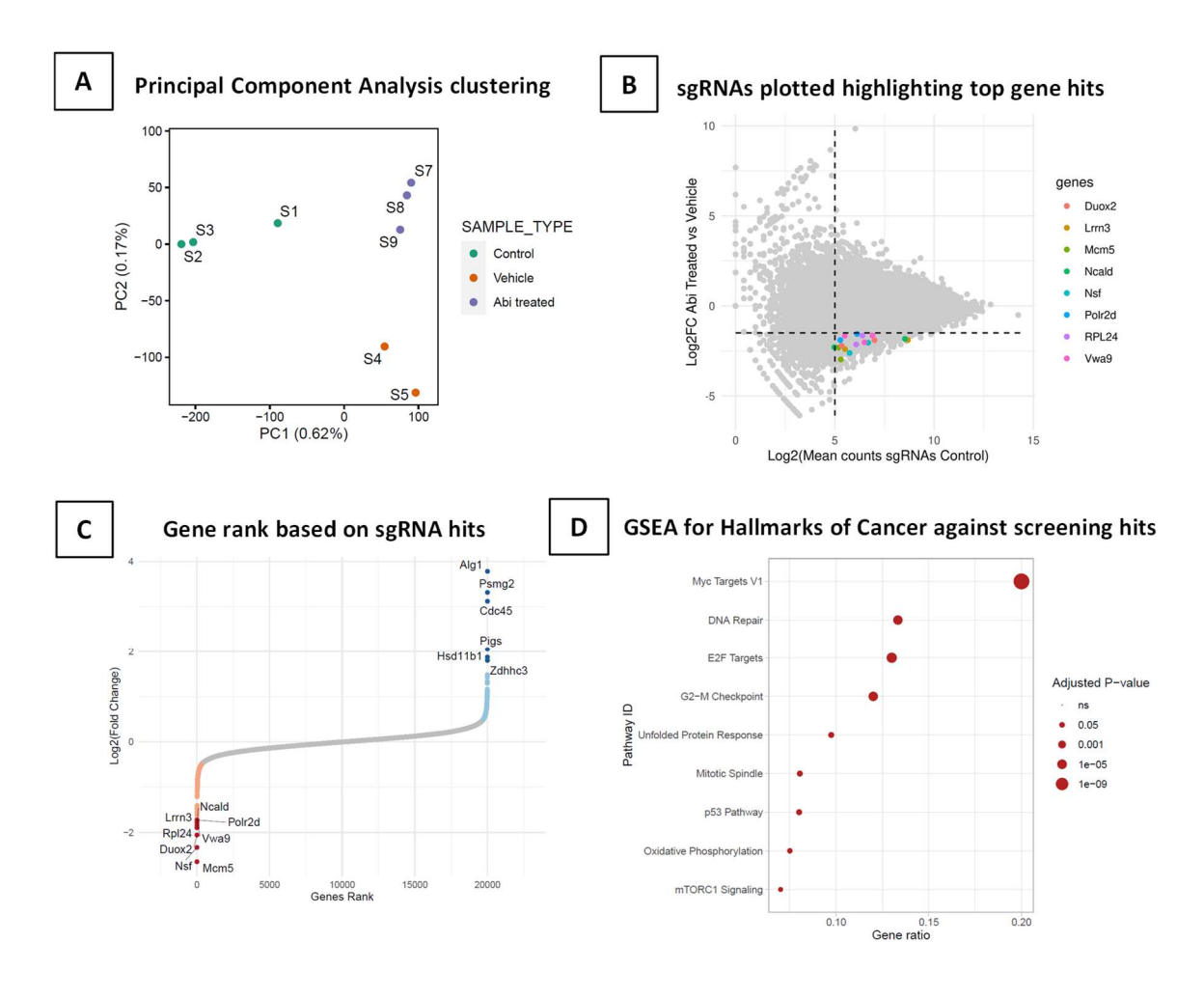


Figure 18. CRISPRi screening results. A) Principal components analysis (PCA) clustering the samples based on sgRNAs read counts. **B)** Representation of the relative abundance of the sgRNA sequences from the sgRNA screen. The y-axis shows log2 of the fold change of sgRNA abundance of the treated versus untreated samples. The x-axis indicates the log2 of the average read count of each sgRNA in the control (t=0) samples. **C)** Gene rank based on sgRNA hits (ranked fold change). In light red, those sgRNAs with fold change \leq -1.5. In darker red, the most significant sgRNAs from gene having at least two hit sgRNAs. **D)** GSEA using Hallmarks of Cancer with the genes having at least one hit sgRNAs in the screening.

The resulting PCA plot demonstrated that samples from the same condition were closely clustered together and were distinguishable from replicates of other conditions (Figure 18A).

The identification of essential genes was carried out using DESeq2 to compare vehicle versus treated condition at the final time point of the experiment (t=14). Individual sgRNAs had to meet the following criteria to be considered positive hits: 1) a minimum number of reads in control (t=0) samples, \geq 100 reads, 2) a fold change (log2) \leq -1.5, and 3) an adjusted p-value (FDR) \leq 0.05. Finally, genes were considered "top hits" when at least 40% (2 or mor out of 5) sgRNAs met the above-mentioned criteria. A total of 419 gene hits involved in abiraterone response were found, with 8 genes were identified as top hits, namely Duox2, Lrrn3, Mcm5, Ncald, Nsf, Pol2rd, RPL24, and vwa9 (**Figure 18B and C**). For more information about the bioinformatic analysis of the CRISPRi screening, please refer to the Materials and Methods section.

We next performed a functional analysis on the sgRNAs hits to identify common signatures or pathway shared among the identified gene resulting from the CRISPRi screening. We used the Hallmarks of cancer gene set from the Human Molecular Signatures Database (MSigDB) (Figure 18D). Not surprisingly, and similar to other screenings, we identified that sgRNAs were enriched for genes of the "Myc targets", "E2F targets", "G2-M checkpoint" or "p53" pathways, among others. Together, these analyses identified gene and pathways that play a crucial role in abiraterone treatment sensitivity.

Since sgRNA depletion in abiraterone versus vehicle treated cells resulted from increased cell death, genes and pathways enriched in the negative (dropped out) tail represented candidate actionable mechanisms to overcome abiraterone resistance. Interestingly, three of the "top hit" candidates *Lrrn3*, *Ncald* and *Nsf* (FC = -3.96, p. adjust = 0.002; FC = -2.29, p. adjust = 0.043 and FC = -2.62, p. adjust = 0.013, respectively) has been described as neural markers and associated to neural differentiation and neurological disorders [300-302], compatible with a role in antiandrogen resistance trough neuroendocrine differentiation [303, 304]. There It is possible that these candidate genes

play a role in the development of resistance to abiraterone through the neuroendocrine differentiation process, as will be further discussed later.

Remarkably, significant dropped out sgRNAs were found targeting 2 out of the 7 members of the NADPH oxidases (NOX) family; Duox2 (FC = -3.96, p. adjust = 0.002); and the maturation factor of Duox1, Duoxa1 (FC = -1.49, p.adjust = 1.56e-6). Together, these data strongly suggest that reactive oxygen species (ROS) signaling plays a critical role in mediating the response to abiraterone treatment.

More specifically, *Duox2* emerged as a "top hit", targeted by two distinct sgRNAs hits (**Figure 19A**), while the *Duoxa1* gene exhibited only one sgRNAs hit (**Figure 19B**). Moreover, although one of the gRNAs targeting Duox1 exhibited a significant p-adjusted value (equal to 0.047) when comparing the vehicle and treated conditions, the fold change enrichment was insufficient to meet the established threshold.

sgRNAs hits targeting Duox family members

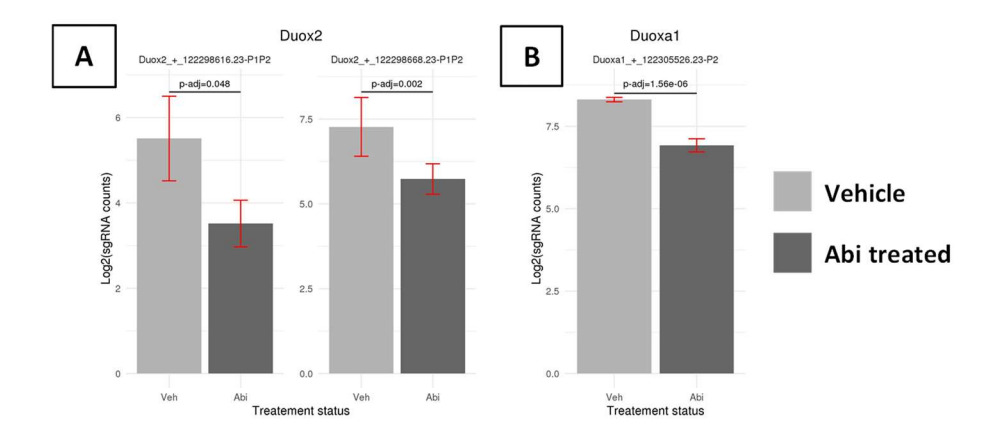


Figure 19. DUOX genes in the CRISPRi screening. sgRNAs hits targeting Duox2 **(A)** and Duoxa1 **(B)**, comparing untreated and treated conditions. Changes in sgRNA counts represented in log2 scale.

Of note, *Duox2* and other members of the NADPH oxidase family can be targeted by existing drugs, which could be valuable in proposing potential combinatory therapies and facilitating a better understanding of the underlying mechanism.

2. CLINICAL CORRELATES

2.1. CORRELATIONS BETWEEN DUOX MEMBERS AND AR

Given the potential role of NADPH oxidases, and DUOX1/2 in particular, in modulating the response to anti-androgenic treatment, we next evaluated association of the *Duox* genes disease progression. Specifically, we included for this analysis *Duox1*, *Duox2* and its maturation factors, *Duoxa1* and *Duoxa2*. To do this, we interrogated the SU2C/PCF Dream Team database (from now, SU2C) [290], which contains genomic, clinicopathological and outcome data from 444 samples from metastatic CRPC patients (mCRPC).

Considering the pivotal role of AR signaling in CRPC, we used a previously published "AR score" [290] as an indicator of AR activity, based on the activation of the AR-associated transcriptional program. AR score is negatively correlated with the expression of Duox members (Figure 20A-D, p-value <0.05), with a remarked significance for Duox2 (p-value <0.001) (Figure 20A). This is consistent with a model of high Duox2 expression and low AR activity in metastatic PCa patients that are poorer responders to antiandrogenic treatment. This observation highlights the interplay between Duox2 and AR activity that was suggested from the synthetic lethal CRISPR screening, since CRPC patients become more independent from AR as a mechanism of resistance to antiandrogens. Hence, our attention was directed towards investigating the impact of ROS metabolism mediated by DUOXes on the modulation of AR signaling.

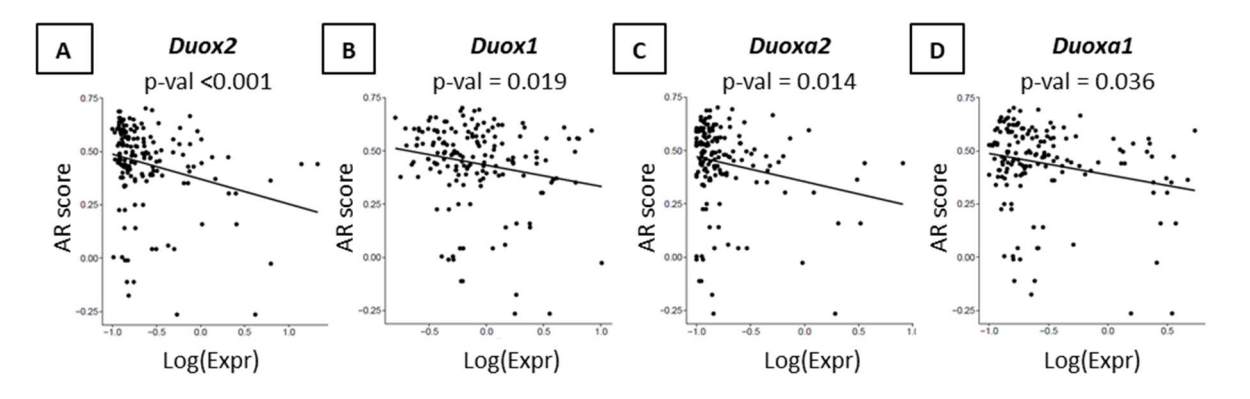


Figure 20. Correlation of Duox gene expression with AR score from SU2C dataset. This score is used as a reporter of AR transcriptional activity.

We conducted further correlation analysis using different signatures against the *Duox* genes. Consistent with the established function of the DUOX enzymes as producers of hydrogen peroxide, we found that all *Duox* genes were positively correlated with published ROS signature (p-value ≤0.04) [293], hereafter named "ChuangROS" signature (**Figure 21A-D**). The "ChuangROS" signature encompasses a highly comprehensive gene expression signature that was derived from the cellular response to three distinct oxidants, including hydrogen peroxide. Notably, *Duox2* (**Figure 21A**) and its corresponding maturation factor, *Duoxa2* (**Figure 21C**), showed the strongest correlations with this signature (p-value <0.001).

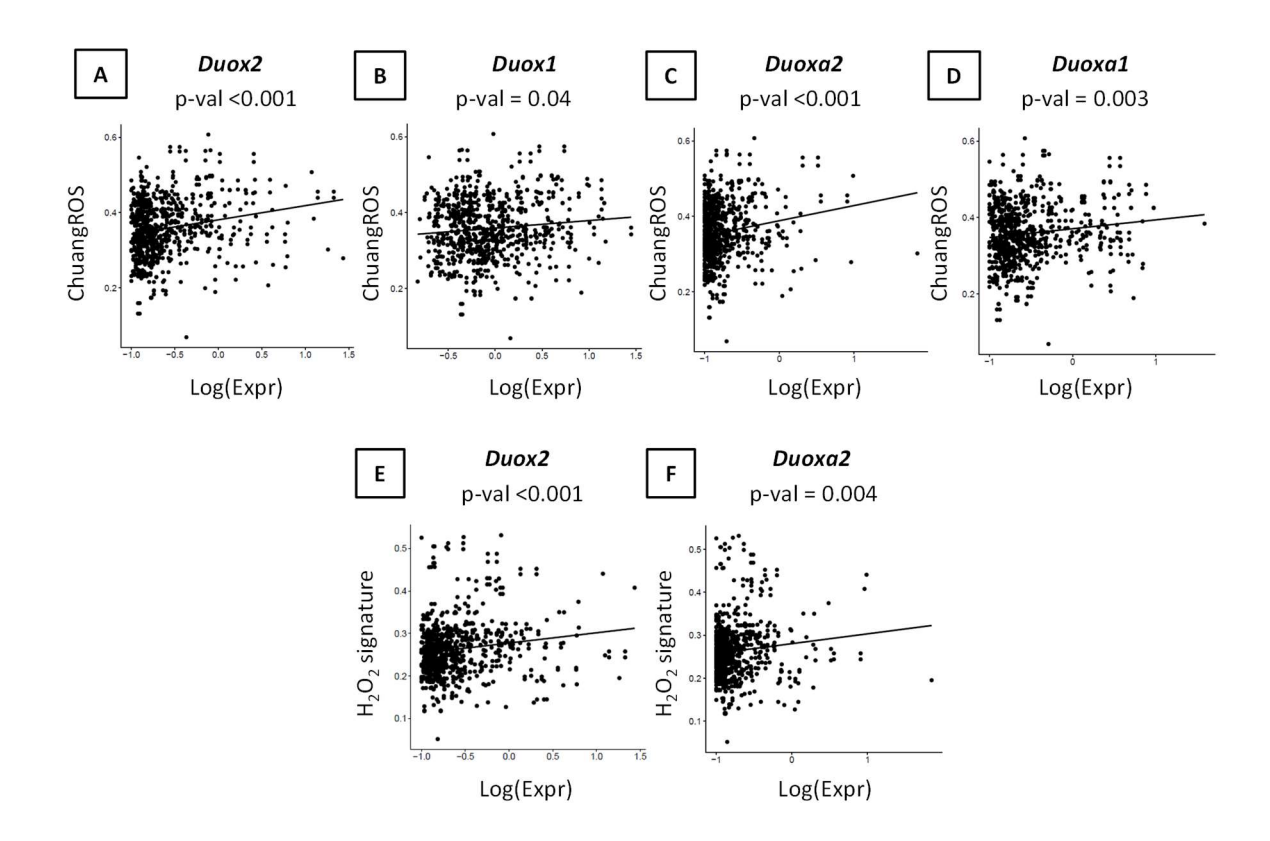


Figure 21. Correlation of Duox gene expression with relevant ROS signatures extracted from SU2C dataset. Correlations of the different Duox genes with A-D) "ChuangROS" signature signature, and E-F) H_2O_2 protein associated signature, extracted from HMDB. In this case, it is showed those correlations which are statistically significant (p-value <0.05), which are the case for *Duox2* (E) and Duoxa2 (F).

Moreover, when employing a gene signature based on enzymes and other proteins associated with hydrogen peroxide (extracted from the "metabocard" of the Human Metabolomic Database, HMDB), only Duox2 (Figure 21E, p-value <0.001) and Duoxa2 (Figure 21F, p-value = 0.004), but not Duox1 and Duoxa1, exhibited a significant positive correlation. Thus, in this patient dataset, Duox2 appears to play a more prominent role in H_2O_2 production than Duox1. This underscores the notion that the contribution and function of Duox1 and Duox2 is contingent on the specific context.

2.2. DUOX2 AND ROS SIGNALING PREDICT PATIENT SURVIVAL

The results arising from the synthetic lethal screening and the analysis of different signatures in PCa patients encouraged us to focus our attention in *Duox2* and ROS signaling on PCa outcome. Consequently, we conducted survival analysis using data obtained from the SU2C dataset. To distinguish between patient groups, we combined the information of Duox2 expression data with NEPC and AR scores.

Neuroendocrine PCa (NEPC) is an aggressive and AR-independent form of PCa progression that has been in the recent years shown to evolve from CRPC upon antiandrogen blockade [152, 305]. As such, a transcriptional signature associated to this differentiates stage, hereafter a "NEPC score" is often an anti-correlated with the AR score [306]. In agreement with our observed role of Duox2/ROS signaling in AR-independent aggressive PCa progression, patients with high NEPC scores and elevated NEPC scores and elevated Duox2 expression exhibited the poorest outcome (p-value = 0.0022, Figure 22A). In contrast, no association was found between AR score patients with high Duox2 expression (Figure 22B), supporting the idea that high ROS signaling promotes AR indifference and resistance to antiandrogens [307-310].

In summary, patients with more advanced and resistant tumors that display high Duox2 levels are associated with a reduction on survival probability. The fact that very few patients were categorized in the *Duox2* low/NEPC high suggest that almost all NEPC patients express high levels of *Duox2* and increased ROS signaling.

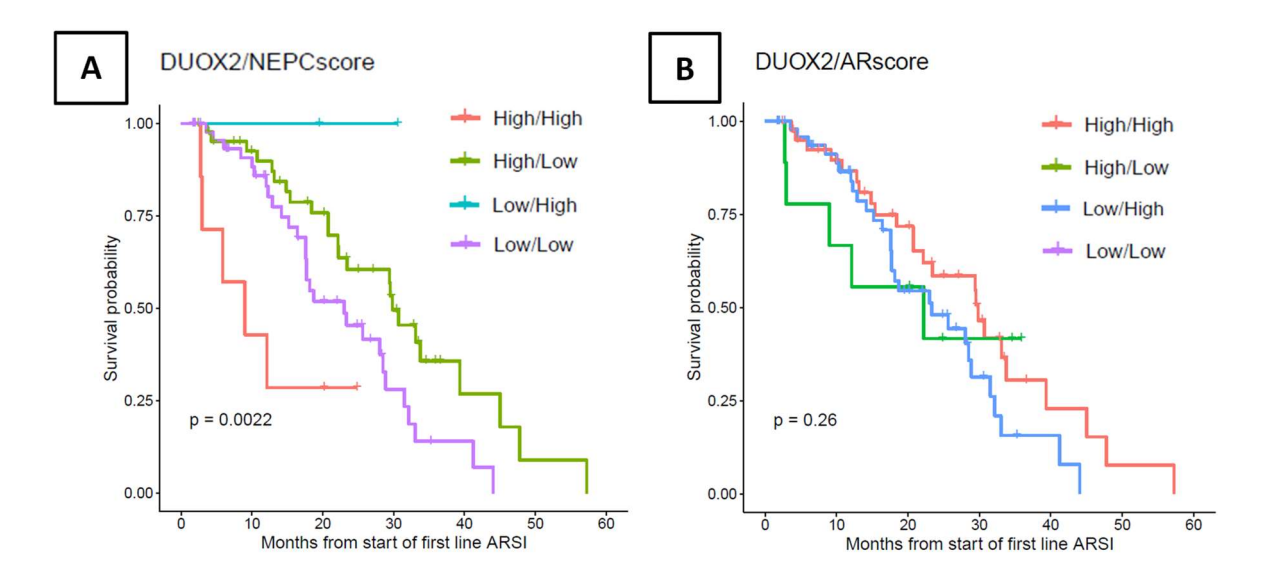


Figure 22. Survival analysis from SU2C database based on Duox2 signature. Survival data form patients from the SU2C were clustered based on Duox2 high/low expression combined with A) NEPC score (> 0.1 high, < 0.1 low), and B) ARscore (> 0.3 high, < 0.3 low). Each high/low value was stablished based on the signature distribution values.

3. DUOX2 REGULATES ANTIANDROGEN RESPONSE

3.1. EFFECT OF DUOX2 KD IN ABIRATERONE RESISTANCE

To confirm the potential and the role of Duox2 as a candidate identified from the synthetic lethal CRISPRi screening, we selected the best sgRNA targeting this gene to establish an optimal knock-down model.

To do so, we cloned the sgRNA sequence (**Figure 13**) into the same backbone used in the library, and then introduced in our NPp53-dCas9 cells by lentiviral transduction, as we did previously for the *Arcn1* and *Rps15a* essential genes.

After selection, knocked-down (KD) cells were utilized for viability and colony formation assays (CFAs) to verify that KD cells exhibited and increased sensitivity to antiandrogens. Additionally, as a control, cells were transduced with a non-targeting sgRNAs sequence that was cloned in the same backbone.

Through implementation of the MTT viability assay, we observe that the killing curve and IC50 value are significantly different when we compare the Duox2 KD cells with the

Results

control (p-value = 0.003, **Figure 23A**). Moreover, we observe a significant reduction in the number and growth of colonies when Duox2 was knocked-down and treated with abiraterone, compared with the non-targeting control (**Figure 23B**).

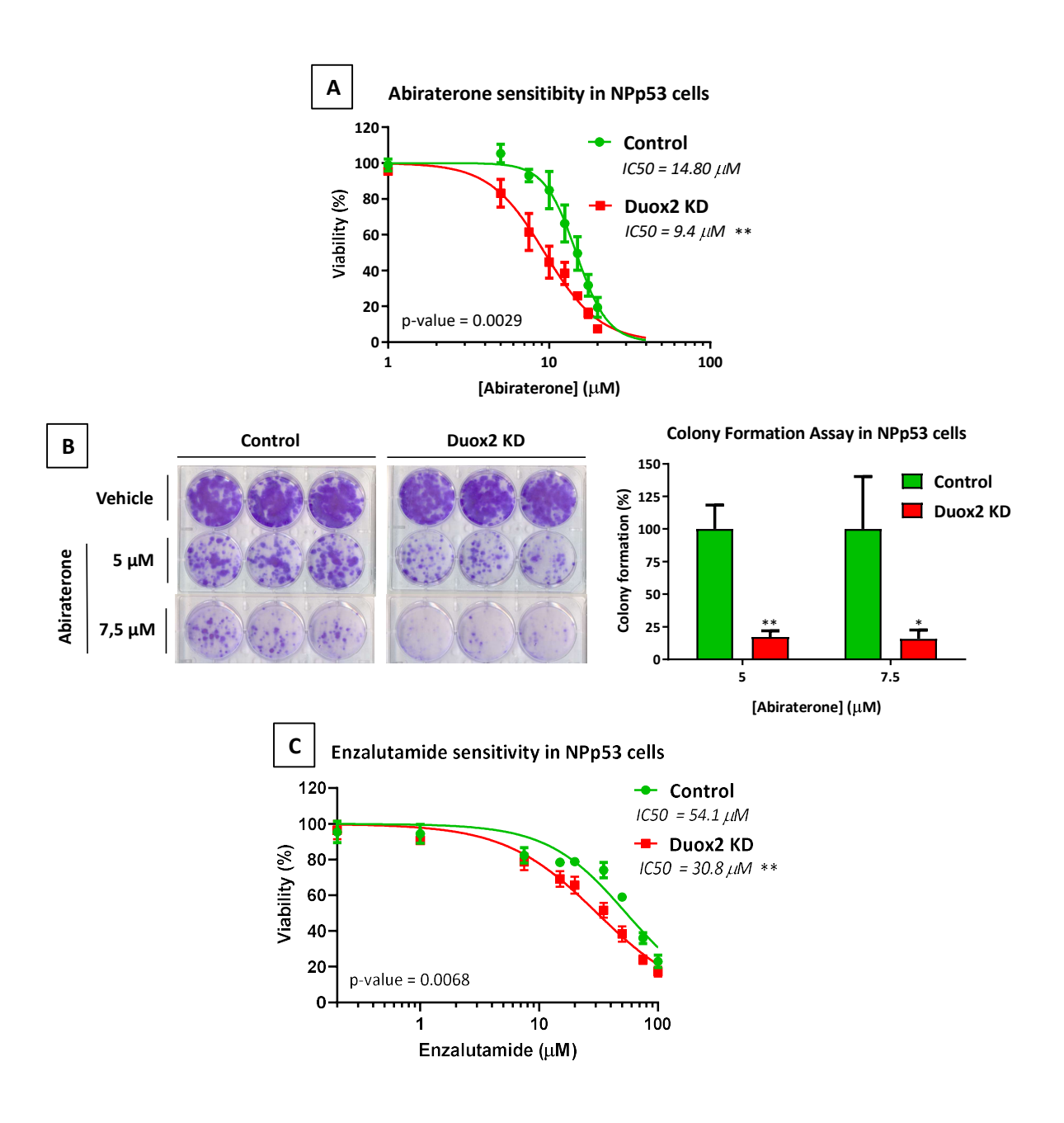


Figure 23. Validation of Duox2 as a candidate to be targeted to improve antiandrogen therapy. A) Abiraterone MTT viability assay in NPp53 Duox2 KD B) Colony formation assay in NPp53 Duox2 KD. C) Enzalutamide MTT viability assay in NPp53 Duox2 KD. **P < 0.01.

We assessed the effect of this KD upon abiraterone treatment at concentrations of 5 μ M (p-value = 0.0017) and 7.5 μ M (p-value = 0.023). Importantly, Duox2 silencing also sensitized NPp53 cells to Enzalutamide (an AR-antagonist, p-value = 0.0068), thereby confirming the role of Duox2 in antiandrogen response (**Figure 23C**).

In summary, these data emphasize the central role of ROS modulating NADPH oxidases as mediators of anti-androgen therapy response.

3.2. NOX/DUOX INHIBITION SENSITIZES PCa CELLS TO ABIRATERONE

To further validate the importance of NADPH oxidases and ROS levels in abiraterone sensitivity, NPp53 cells were treated with Diphenylene iodonium (DPI), a potent inhibitor of the NOX family, including DUOX proteins.

Frist, a one-vs-one dose scalation synergy assay was conducted by combining various concentrations of abiraterone and DPI, using Combenefit software to calculate Loewe synergy score (Figure 24A).

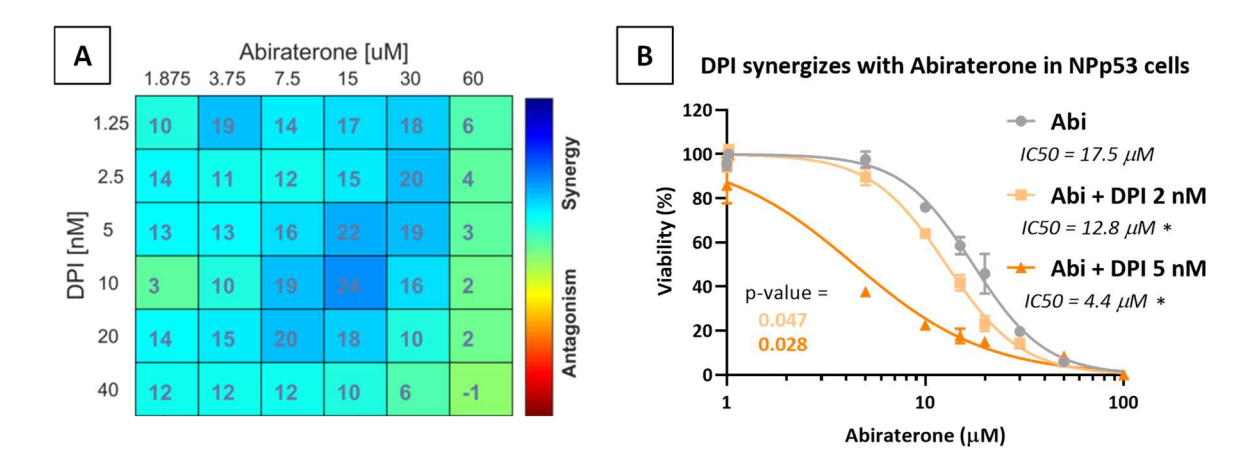


Figure 24. DPI synergizes with Abiraterone in NPp53 cells. (A) Synergy quantification between DPI and abiraterone in NPp53 cells using Combenefit software. (B) MTT viability assay comparing Abiraterone dose-response curve alone or combined with a fixed concentration of DPI based on IC50 values. *P < 0.05

The results indicate the achievement of synergistic effects (indicated in blue) for several combinations of abiraterone and DPI concentrations. This observation replicates the effect of Duox2 KD as a pharmacological inhibition.

Second, based on the results from the synergy matrix, a comparison of the abiraterone concentration-response curves with and without a fixed concentration (2 nM and 5 nM, **Figure 24B**) of this inhibitor revealed that DPI enhances the sensitivity of NPp53 cells towards abiraterone treatment (p-value = 0.047 and 0.028, correspondingly).

Moreover, we treated LNCaP and 22Rv1 human PCa cell lines with abiraterone and DPI, alone and in combination, to perform synergy studies. Both cell lines are AR-positive; however, while LNCaP is AR-responsive, 22Rv1 exhibits features of CRPC.

As the IC50 values of DPI for these cell lines were found to be higher (2 orders of magnitude) than those of the NPp53 mouse cell line (**Figure 25A**), the DPI concentration was adjusted accordingly. Additional determinations of the IC50 values for other cell lines revealed species-related differences as the cause of the observed variations (data not shown).

The synergy matrices calculated by Combenefit analysis illustrated several synergistic combinations between abiraterone and DPI for both cell lines at high concentrations, notably at LNCaP cells (**Figure 25B** and **D**). Accordingly, comparing concentration-response curves, it was observed that both 22Rv1 (p-values ≤ 0.0048) and LNCaP (p-value = 0.015) cell lines displayed significatively heightened sensitivity to abiraterone following DPI treatment (**Figure 25C** and **E**).

Therefore, the inhibition of the NADPH oxidase family can render PCa cells more responsive to abiraterone therapy, implying a potential benefit in co-targeting ROS metabolism and AR signaling to enhance the efficacy of the therapy.

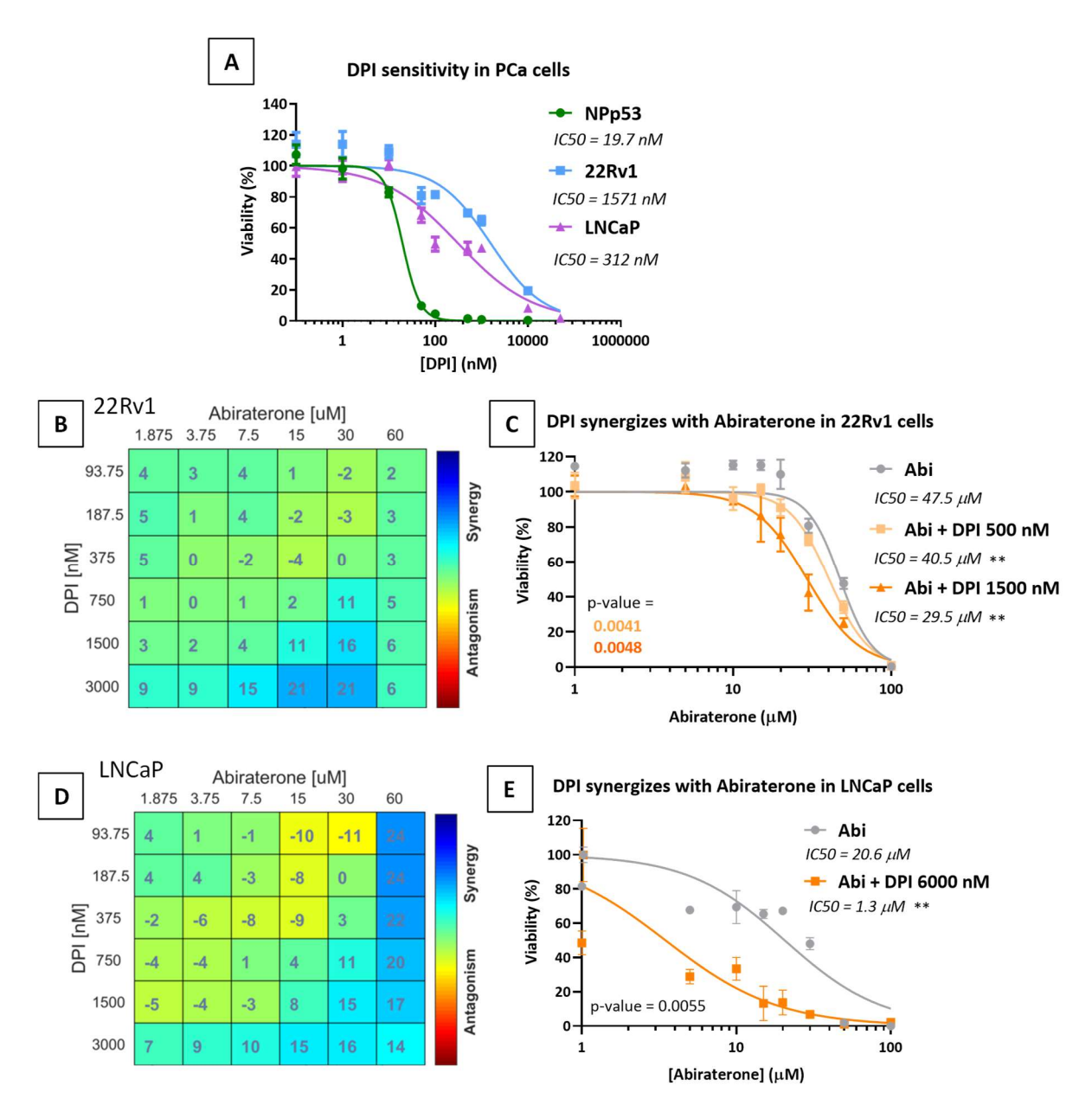


Figure 25. DPI synergizes with Abiraterone in 22Rv1 and LNCaP cells. (A) Concentration-response curves based on MTT viability of human PCa cells, treated with DPI. (B, D) Synergy quantification between DPI and abiraterone in 22Rv1 and LNCaP cells, correspondingly. (C, E) MTT viability assay comparing Abiraterone dose-response curve alone or combined with a fixed concentration of DPI based on IC50 values. **P < 0.01 and ***P < 0.001.

4. Cross-talk between AR targeting and ROS metabolism

Considering the role of Duox2 in ROS production, we decided to study the role of the redox balance and how *Duox2* knock-down and abiraterone treatment influences ROS levels.

4.1. ABIRATERONE INFLUENCING TOTAL ROS LEVELS

First, we tuned to flow cytometry assays to measure total ROS production, using the non-fluorescent probe CM-H2DCFDA, which is converted to a green-fluorescent upon oxidation due to removal of acetate groups by intracellular esterases. Cells are incubated with this probe to measure total ROS levels in each condition, using flow cytometry.

Interestingly, while no differences were observed between control cells and *Duox2* KD cells at basal levels (**Figure 26A**), abiraterone treatment did result in a rapid dose-dependent increase in total ROS levels, notably at 20 μ M concentration (p-value = 0.002, FC = 1.73 at 2h; p-value = 0.01, FC = 1.67).

This lack of differences at basal levels can be attributed to the fact that Duox2 is responsible for the production of hydrogen peroxide (H₂O₂), whereas other abundant ROS species within the cell can contribute significantly to overall ROS levels.

It is important to note that this increase in ROS levels was not associated with any long-term harmful effects or toxicity from abiraterone, as these effects were only observed at higher concentrations after 24-48 hours.

In order to confirm the induction of ROS as a response to abiraterone treatment, we quantified total ROS levels in both 22Rv1 and LNCaP cells (**Figure 26B** and **C**). In the androgen-insensitive 22Rv1 cell line (**Figure 26B**), we observe a modest increase in total ROS levels production due to abiraterone treatment at 8h (p-value = 0.006, FC = 1.13 at 15 μ M; p-value <0.0001, FC = 1.32 at 30 μ M)

. Conversely, in the androgen-sensitive LNCaP cell line, the increase in total ROS levels was more consistent at both time points, (**Figure 26C**) particularly at 8h, where concentrations of 7.5 μ M (p-value = 0.04, FC = 1.93) and 20 μ M (p-value <0.0001, FC = 3.04) resulted in a remarked fold increase in total ROS levels.

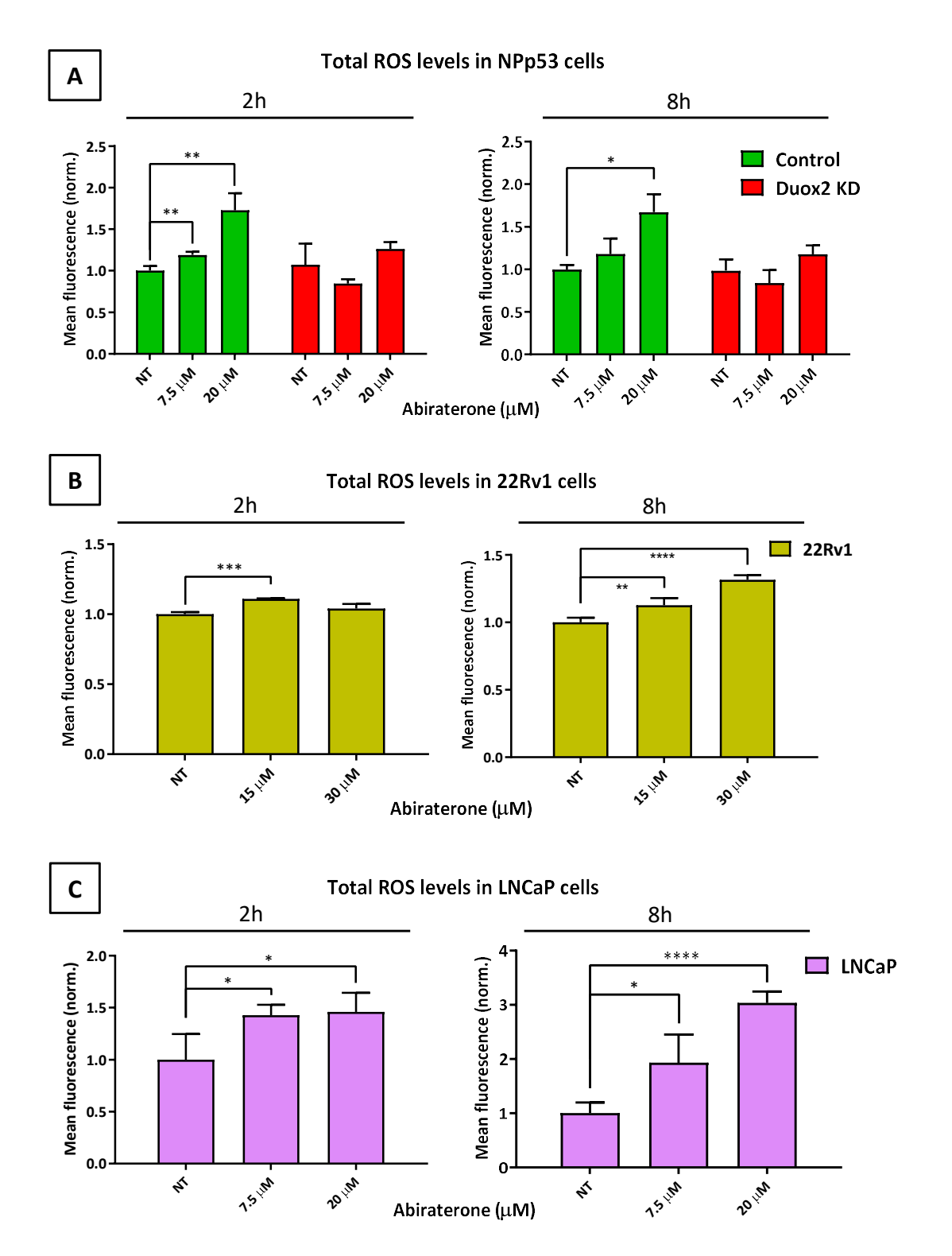


Figure 26. Total ROS quantification by CM-H2DCFA probe. Quantification was performed in NPp53, 22Rv2 and LNCaP cells after abiraterone treatment at two different concentrations. Cells were seeded in six-well plates (100.000 cells per well) and treated the next day with abiraterone for 2 and 8 hours. Cells are stained with H2DCFA probe (10 μ M) and measured by FACS (N = 3). *P < 0.05, **P < 0.01, ***P < 0.001, and ****P < 0.0001.

5. MECHANISMS OF ABIRATERONE RESISTANCE VIA DUOX2

To gain insights into the mechanism and molecular pathways underlying the interplay between ROS signaling and abiraterone resistance, we performed an RNA-seq on isogenic control and Duox2 KD NPp53 cells exposed to abiraterone (**Figure 27**). RNA quality control, library preparation and 2x100 bp, >25 M pair-end reads, stranded mRNA-sequencing was performed by Centro de Análisis Genómico (CNAG-CRG, Spain), using an Illumina HiSeq2500.

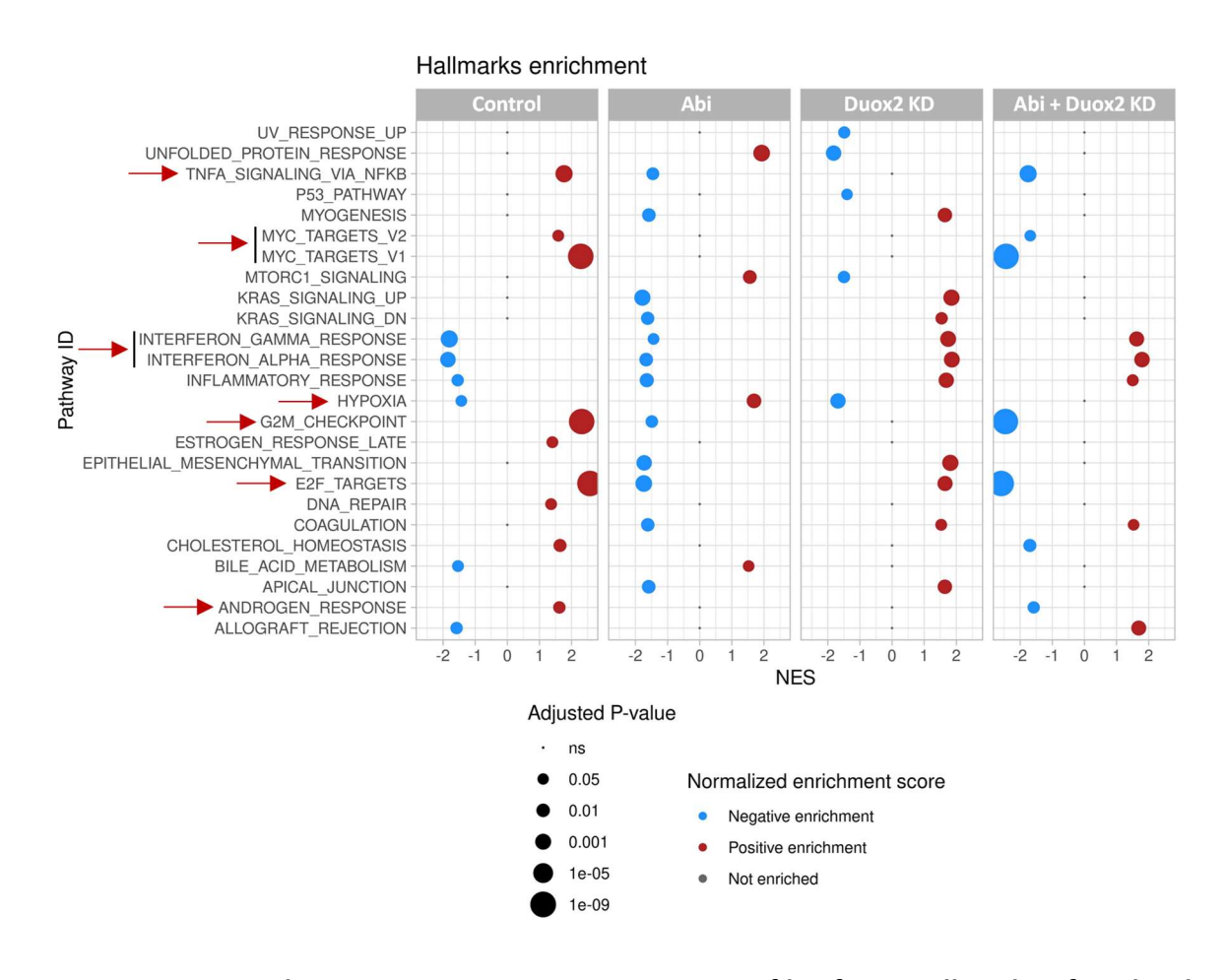


Figure 27. GSEA data comparing gene expression profiles from Hallmarks of Molecular Signatures Database (MSigDB). Each condition against the others. In blue, negatively enriched pathways (negative NES score) of each condition. In red, positively enriched pathways (positive NES score). Size of each dot is related with the significance of the enrichment measured by the adjusted p-value.

The obtained RNA-seq raw data was then analyzed for differentially expressed genes (DEG), which allowed us to evaluate the transcriptional changes in genes across different conditions.

Gene set enrichment analysis (GSEA) on the Molecular Signatures Database (MSigDB) identified cancer hallmarks enriched upon abiraterone, Duox2 silencing and the combination (**Figure 27**). As expected, AR signaling was significantly positively enriched in the NPp53 cells (NES = 1.619, p.adjust = 0.02; **Figure 28**), and only partially repressed in either abiraterone treated or Duox2 KD cells. However, AR signaling became strongly antagonized by abiraterone in Duox2 KD cells (NES = -1.578, p.adjust = 0.03; **Figure 28**).

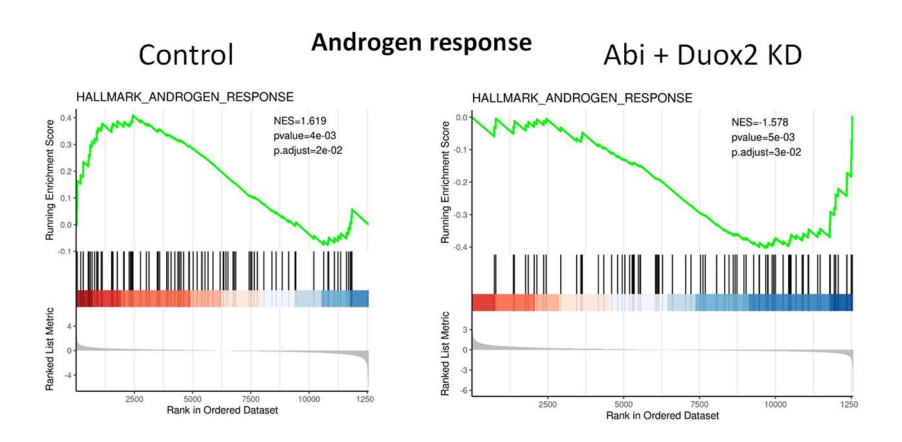


Figure 28. GSEA enrichment plots for androgen response pathway.

Importantly, key oncogenic pathways known to drive CRPC were strongly repressed by the combined use of abiraterone and Duox2 silencing, including the "TNF signaling via NFκB" (NES = -1.752, p.adjust = 0.0003; **Figure 29A**), "MYC targets" (NES = -2.436, p.adjust = 2e-09; **Figure 29B**), "G2M checkpoint" (NES = -2.459, p.adjust = 2e-09; **Figure 29C**) and the "E2F targets" (NES = -2.59, p.adjust = 2e-09; **Figure 29D**) pathways. It is noteworthy that the synthetic lethal CRISPRi screening yielded hit genes that were also found to be enriched in the last three pathways mentioned. This observation emphasizes the involvement of these oncogenic pathways in antiandrogen resistance and suggests that Duox2 plays a role in modulating the activation of these pathways.

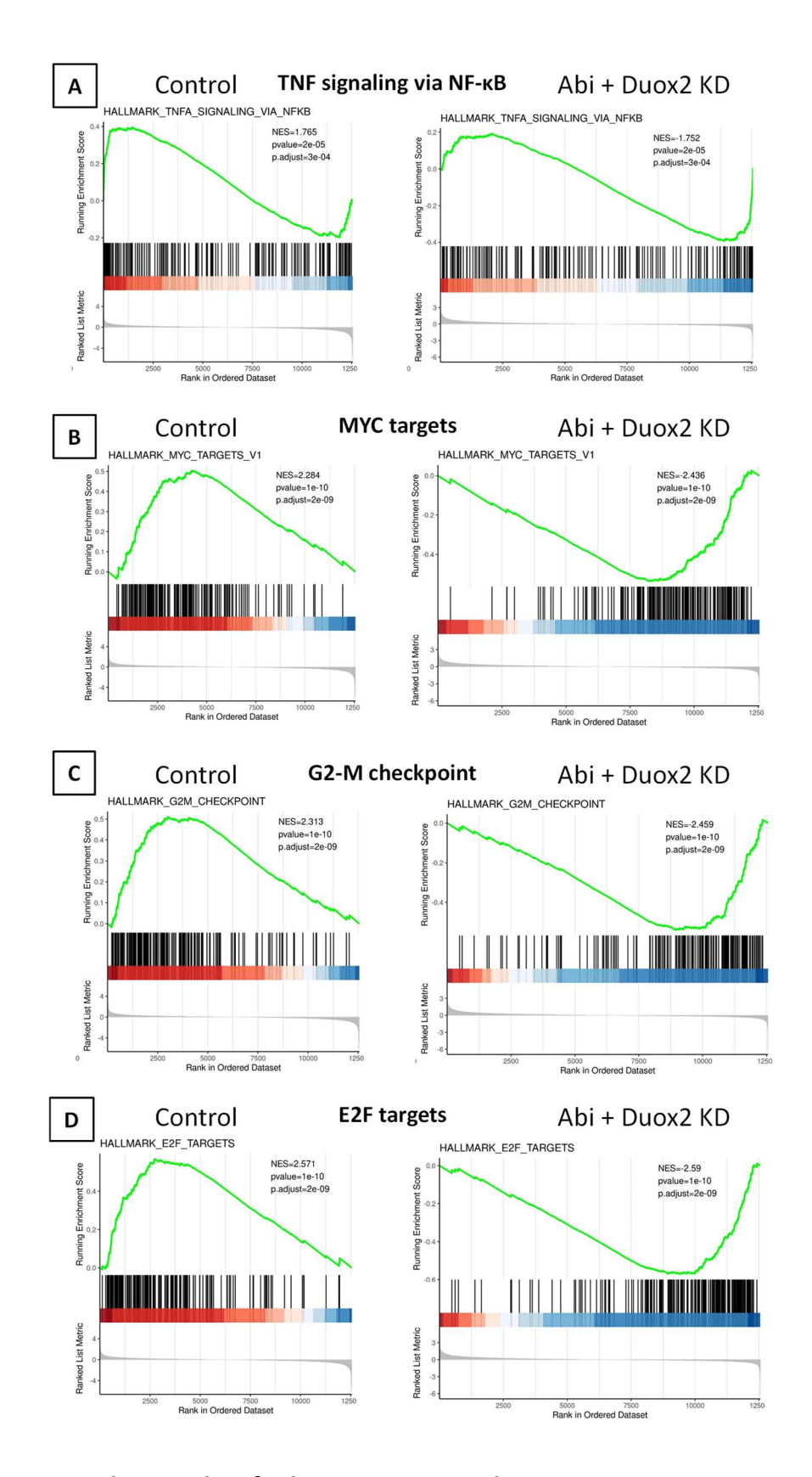


Figure 29. GSEA enrichment plots for key oncogenic pathways.

Production of intracellular ROS has been shown to trigger the repression or activation of a plethora of signaling pathways to balance ROS levels, including hypoxia-inducible factors (HIFs) [311-313], NF κ B [314] or interferon response pathways, among others. Indeed, the interferon α and γ pathways, together with the inflammatory response were found strongly upregulated by Duox2 KD (NES = 1.86, p.adjust = 0.001, **Figure 30A**; NES = 1.745, p.adjust = 0.003, **Figure 30B**; NES = 1.686, p.adjust = 0.002, **Figure 30C** respectively), while abiraterone-treated cells exhibited downregulation of such pathways (NES = -1.665, p.adjust = 0.009, **Figure 30A**; NES = -1.437, p.adjust = 0.04, **Figure 30B**; NES = -1.647, p.adjust = 0.006, **Figure 30B** respectively). Considering the reported inhibitory effect of ROS on interferon production [315], the activation of this signaling upon Duox2 abrogation suggest that this enzyme and the ROS it generates may play a role in modulating the interferon and inflammatory responses [316].

Given the above-mentioned implication of ROS activating HIF transcriptional activity [311-313], and consistent with our *in vitro* and functional data about the Duox2-dependent increase in ROS signaling in response to abiraterone, a significant positive enrichment was shown for the hypoxia signaling pathway upon abiraterone treatment (NES = 1.69, p.adjust = 0.0005, **Figure 30D**), which was strongly repressed by the Duox2 KD (NES = -1.683, p.adjust = 0.002, **Figure 30D**). Interestingly, the combination balanced hypoxia-response, with no significant upregulation or downregulation of the pathway, balancing hypoxia response.

We were interested in identifying signaling pathways that exhibit upregulation in cells treated with abiraterone, but are no longer upregulated in cells treated with a combination of abiraterone and Duox2 KD, as the case of the hypoxia signaling. This way, drugs targeting such upregulated molecular pathways can be used to improve the response to abiraterone.

In summary, the functional and transcriptomic analyses suggest a strong mechanistic association between the inhibition ROS signaling and the repression of oncogenic pathways likely through the hypoxia-regulated transcriptional network, hence providing a rationale for the use of hypoxia signaling inhibitors as a therapeutic strategy to sensitize otherwise resistant PCa cells to antiandrogenic treatment.

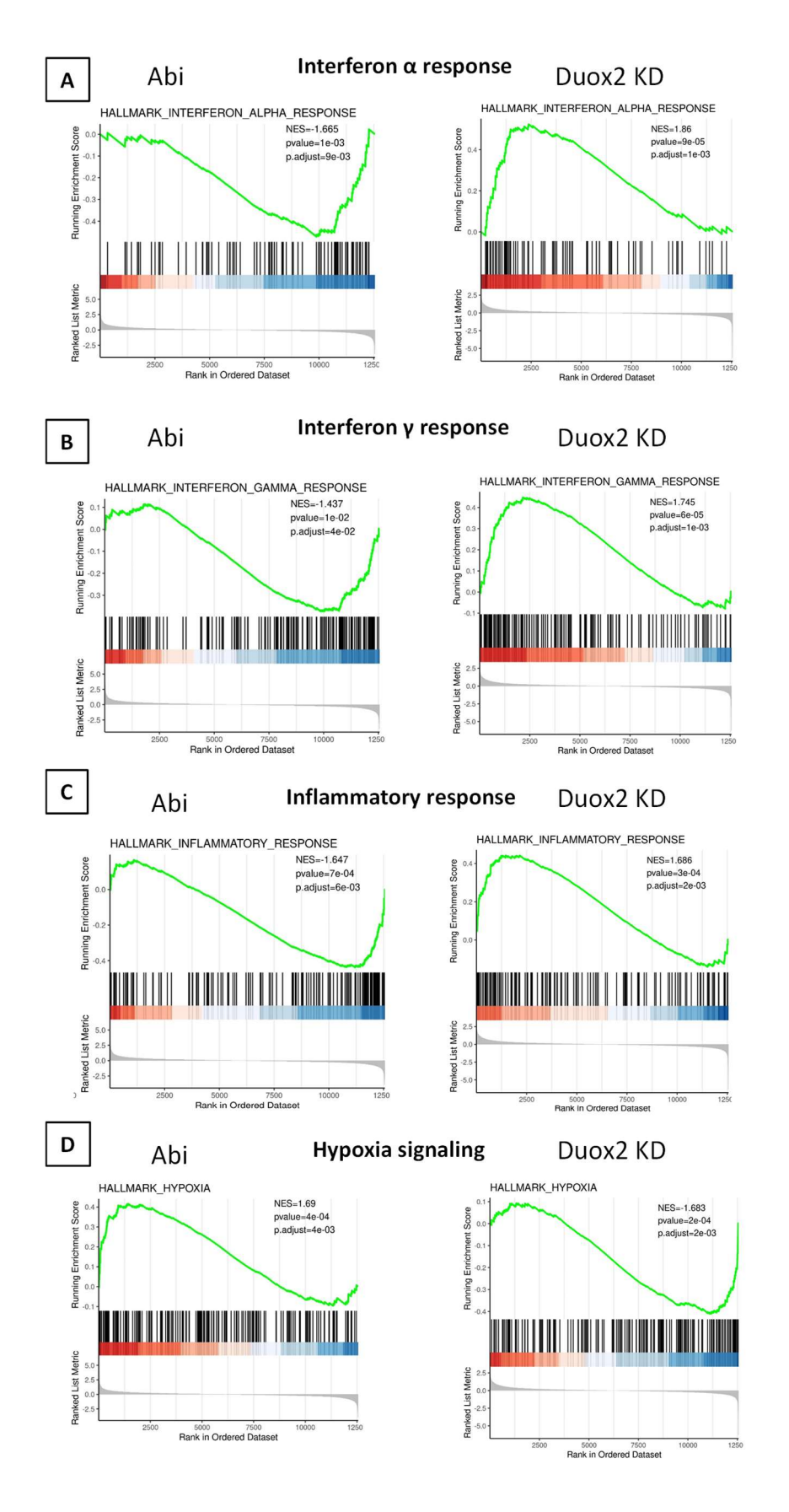


Figure 30. GSEA enrichment plots for interferon and hypoxia response pathways.

6. ANTIANDROGENS REGULATION ON HIF-1 α and HYPOXIA SIGNALING

6.1. ABIRATERONE AND HIF-1α STABILIZATION

Tumor hypoxia refers to the condition where tumor experience a deficiency of oxygen. "Pseudohypoxia" is a process in which cells express hypoxia-associated proteins irrespective of the oxygen status. Consequently, it is not appropriate to assume that abiraterone induces hypoxia. Instead, it activates the transcriptional program that is linked to hypoxia, thus the term pseudohypoxia may be utilized to describe this process.

Building upon our prior findings which indicate that abiraterone treatment upregulates pseudohypoxia, which can be repressed by targeting ROS-producing NADPH oxidases, and given the central role of HIF- 1α in the hypoxia-response transcriptional programs, we hypothesize that abiraterone treatment may induce HIF- 1α stabilization as a means of mediating this resistance.

Exposure to cobalt chloride ($CoCl_2$), a hypoxia mimetic drug, is widely use to investigate the impact of hypoxia signaling under normoxic conditions. In line with this practice, we utilized $CoCl_2$ as a chemical inducer of HIF-1 α stabilization to trigger hypoxia signaling as a control. Additionally, we incorporated N-Acetyl-L-cysteine (NAC), an antioxidant compound that allows quenching ROS and mitigate oxidative stress. This allowed us to assess whether abiraterone's impact on pseudohypoxia is mediated by antiandrogen-induced ROS.

Consequently, we subjected our NPp53 cells to two different concentrations of abiraterone, either alone or in conjunction with NAC, for a duration of 8 hours. As a positive control, we observed the accumulation of HIF-1 α induced by CoCl₂-induced stabilization (**Figure 31A**). Interestingly, we observed a notable, dose-dependent increase in HIF-1 α accumulation upon abiraterone treatment at 7.5 μ M and 20 μ M. This abiraterone-induced HIF-1 α stabilization was abrogated by the addition of NAC, indicating that the process is reliant on ROS production by abiraterone.

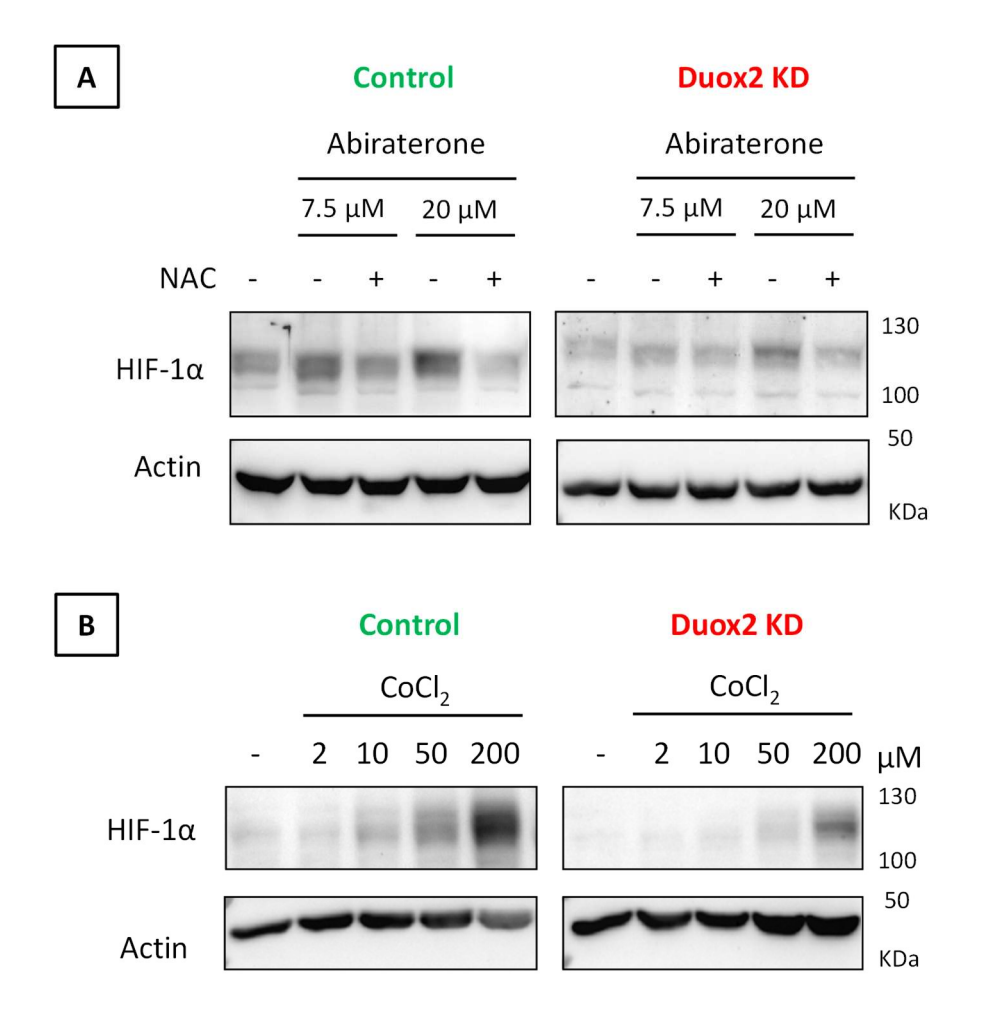


Figure 31. HIF-1 α accumulation and abiraterone sensitivity in response to hypoxia in NPp53 cells, control and Duox2 KD. A) HIF-1 α accumulation in response to abiraterone (7.5 and 20 μ M), with or without NAC. B) Dose-dependent HIF-1 α accumulation induced by CoCl₂, in control and Duox2 KD cells. HIF-1 α is measured at protein levels by Western-Blot.

Further, exposure to 7.5 μ M abiraterone in Duox2 depleted cells did not elicit an increase in the levels of HIF-1 α accumulation and only, a modest induction at 20 μ M. These findings suggest that the knock-down of Duox2 can partially abrogate the stabilization of HIF-1 α induced by abiraterone-generated ROS, highlighting the role of ROS signaling as inducer of the pseudohypoxia transcriptional program.

As anticipated, we have observed a dose-dependent increase in HIF-1 α accumulation following CoCl₂ treatment (**Figure 31B**). Conversely, the expression of HIF-1 α decreased in

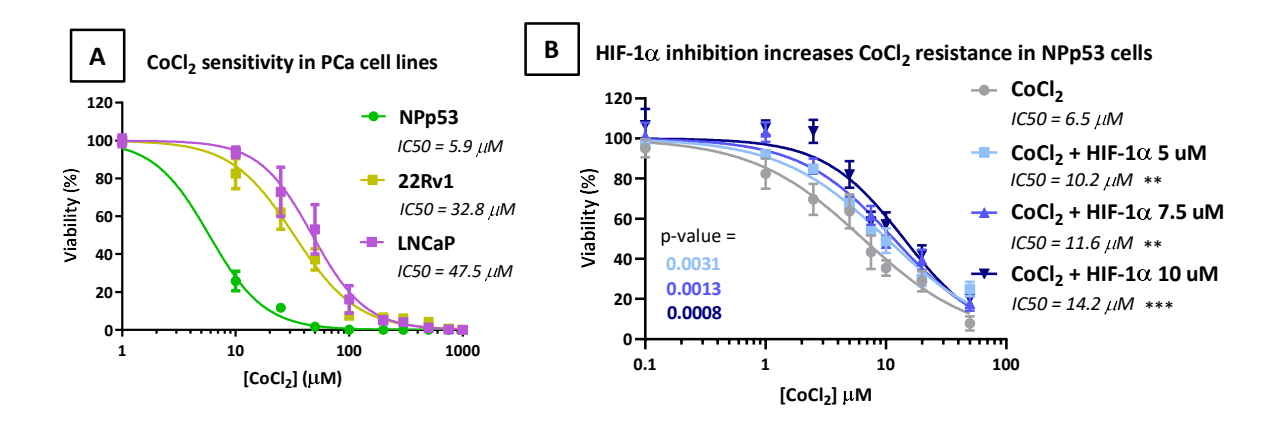
Duox2 KD cells, thereby mitigating the hypoxic effect induced by this compound (**Figure 31B**).

As a result, we have demonstrated that NPp53 can lead to HIF- 1α accumulation in response to chemically-induced hypoxia, and furthermore, we have established that this response can be reduced via Duox2 KD, as was observed with the abiraterone-induced pseudohypoxia from the RNA-seq data.

Moreover, we also provide evidence that an exacerbated pseudohypoxia response induced by $CoCl_2$ produced a reduction on cell viability that could be partially alleviated by PX-478, a HIF-1 α inhibitor. This finding is supported by the significant increase in IC50 values (**Figure 32**) upon comparing the concentration-response curves of $CoCl_2$ alone and in combination with fixed doses of PX-478 (p-value = 0.003, 0.0013 and 0.0008 corresponding with PX-478 at 5, 7.5 and 10 μ M) in NPp53 cells.

Finally, to evaluate the impact of hypoxia on abiraterone sensitivity, we induced a highly hypoxic environment by treating PCa cells with $CoCl_2$ and assessed the alteration in abiraterone sensitivity, based in IC50 values (**Figure 32A**). We observe that NPp53 (**Figure 32C**, p-value = 0.016) and 22Rv1 (**Figure 32D**, p-value = 0.006) cells exhibited a significant increase in resistance to abiraterone treatment (as indicated by higher IC50 values) in a pseudohypoxia context, following treatment with $CoCl_2$ at 5 and 10 μ M concentrations, respectively. However, AR-responsive LNCaP cells did not display significant changes in the abiraterone curve upon $CoCl_2$ treatment (**Figure 32E**).

Consequently, we concluded that hypoxia-related signaling mediated by HIF-1 α serves as a resistance mechanism of CRPC cells to survive to abiraterone treatment, but not in AR-sensitive cells.



CoCl₂ treatment effect in abiraterone response

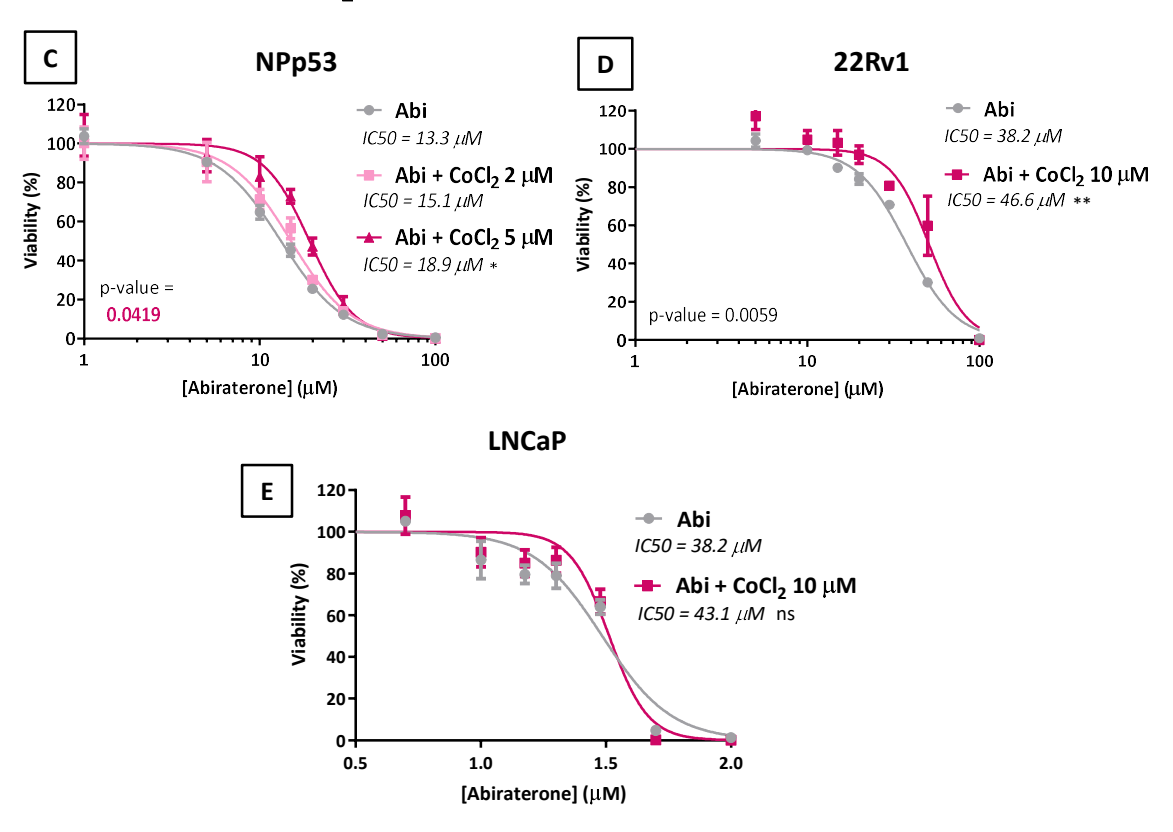


Figure 32. Pseudohypoxia induced by CoCl₂ increases abiraterone resistance in CRPC cells. **(A)** MTT viability curve with increasing doses of CoCl₂ to extrapolate IC50 value from our PCa cells. **(B)** MTT viability curve of CoCl₂ alone or in combination with fixed concentrations (7, 7.5 and 10 μM) of the HIF-1α inhibitor in NPp53 cells. **(C-E)** MTT viability curve of abiraterone alone or in combination with fixed concentrations of the CoCl₂ in NPp53 (2 an 5 μM), 22Rv1 and LNCaP (10 μM) cells. *P < 0.05, **P < 0.01, ***P < 0.001.

6.2. HIF-1 α ACTIVITY ON TRANSCRIPTIONAL TARGETS

In order to assess the effect of antiandrogens on the HIF- 1α activity, we measured by qPCR the expression of HIF- 1α and its transcriptional targets. To this end, we treated NPp53 cells with abiraterone and enzalutamide.

Our observations indicate there is no significant alteration in the expression of $HIF-1\alpha$ in response to any of the treatments administered (**Figure 33Figure 33A**). However, the expression transcriptional targets of $HIF-1\alpha$ expression were found to be increased due to antiandrogens, including Bnip3 (p-values < 0.0015, RQ > 1.7, **Figure 33B**), Ca9 (p-values < 0.0015, RQ > 1.4 **Figure 33C**) and Vegfa (p-values < 0.0001, RQ > 2.2, **Figure 33D**,). Additionally, enzalutamide treatment resulted in a high elevation in Pdk1 expression (p-value < 0.0001, FC = 1.68, **Figure 33E**).

Therefore, antiandrogens do not exert any influence on $HIF-1\alpha$ transcriptional levels. However, we previously demonstrated abiraterone can produce changes at the protein level by inducing the accumulation of HIF-1 α through stabilization. This provides a possible explanation for how abiraterone can potentially modulate the hypoxia-response genes that are regulated by the transcriptional activity of HIF-1 α .

Furthermore, we found that NRF2 levels, a transcription factor which upregulates stress-response genes to activate the cellular antioxidant defense to counteract oxidative stress [221], was also increased upon abiraterone treatment (p-value < 0.0013, FC = 1.61, Figure 33F). Hence, it is plausible to propose that the ROS induced by abiraterone may serve as a mediator for the observed elevation in NRF2 expression levels. This ROS-mediated response could potentially act as a resistance mechanism by activating pathways involved in the restoration of oxidative homeostasis. Interestingly, NRF2 has been described to promote cell survival in hypoxia [317], resulting in a complex interplay between HIF and NRF2 signaling in which one influences the other [318].

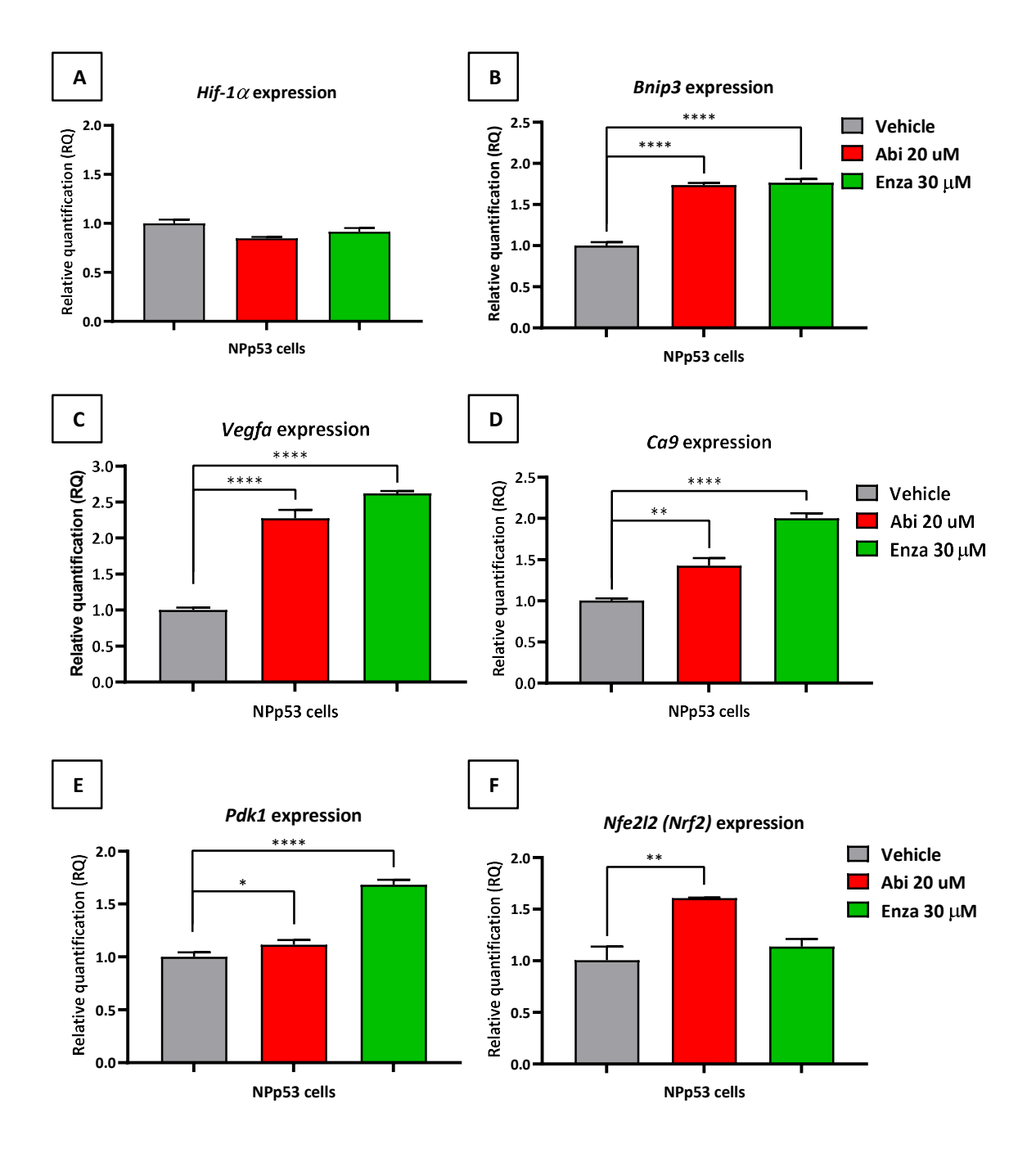


Figure 33. qPCR of HIF-1 α and its transcriptional targets. (A-C) The gene expression levels were quantified in NPp53 cells that were treated with different compounds either alone or in combination for a duration of 8 hours. The obtained data were initially normalized using Gapdh expression as a loading control and then normalized further by considering the vehicle condition as a control (RQ = 1). The specific amplification was achieved by using oligonucleotides that targeted HIF-1 α (A), Bnip (B) Vegfa (C), Ca9 (D), Pdk1 (E), and Nrf2 (F). *P < 0.05, **P < 0.01, ***P < 0.001, and *****P < 0.0001.

6.3. METABOLIC CHANGES INDUCED BY ABIRATERONE-INDUCED PSEUDOHYPOXIA

Taking into account the results obtained thus far, it appropriate to investigate how abiraterone induces changes in downstream processes that are activated by hypoxia signaling. Among the key processes that are regulated by HIF-1 α are angiogenesis, cell death, and glucose metabolism. In response to hypoxia, most eukaryotic cells can shift their metabolic strategy from mitochondrial respiration to increased glycolysis. Accordingly, we employed metabolic methodologies to assess this type of changes in NPp53, 22Rv1, and LNCaP cells. Considering IC50 values of abiraterone, NPp53 cells were treated with 7.5 (low) and 20 μ M (high) concentrations, while 22Rv1 we exposed to 15 (low) and 30 μ M (high) concentrations.

To this end, real-time cell metabolic assays were performed using Seahorse XFe96 Analyzer, which allows for the measurement of the oxygen consumption rate (OCR) and extracellular acidification rate (ECAR) of live cells. In other words, this approach enables the measurement of both O₂ levels and H⁺ production, respectively.

6.3.1. ATP Rate Assay

The rate of adenosine triphosphate (ATP) production is a pivotal informative measurement to describe cellular metabolism, since ATP is the main energy source for cells. In addition, those cells can regulate metabolism to adjust for changes in ATP demand to maintain total intracellular ATP levels.

The Real-Time ATP Rate Assay Kit serves the purpose of quantifying the rate of ATP production originating from glycolysis and mitochondrial oxidative phosphorylation (OXPHOS) in living cells. These two metabolic pathways are the primary means by which ATP is produced in mammalian cells. To achieve this, the kit employs metabolic modulators including oligomycin, and a combination of rotenone and antimycin A, which are sequentially introduced to the cell culture. The resulting data from OCR and ECAR measurements taken over time allows for the calculation of the rates of ATP production from both mitochondrial and glycolytic processes (Figure 34).

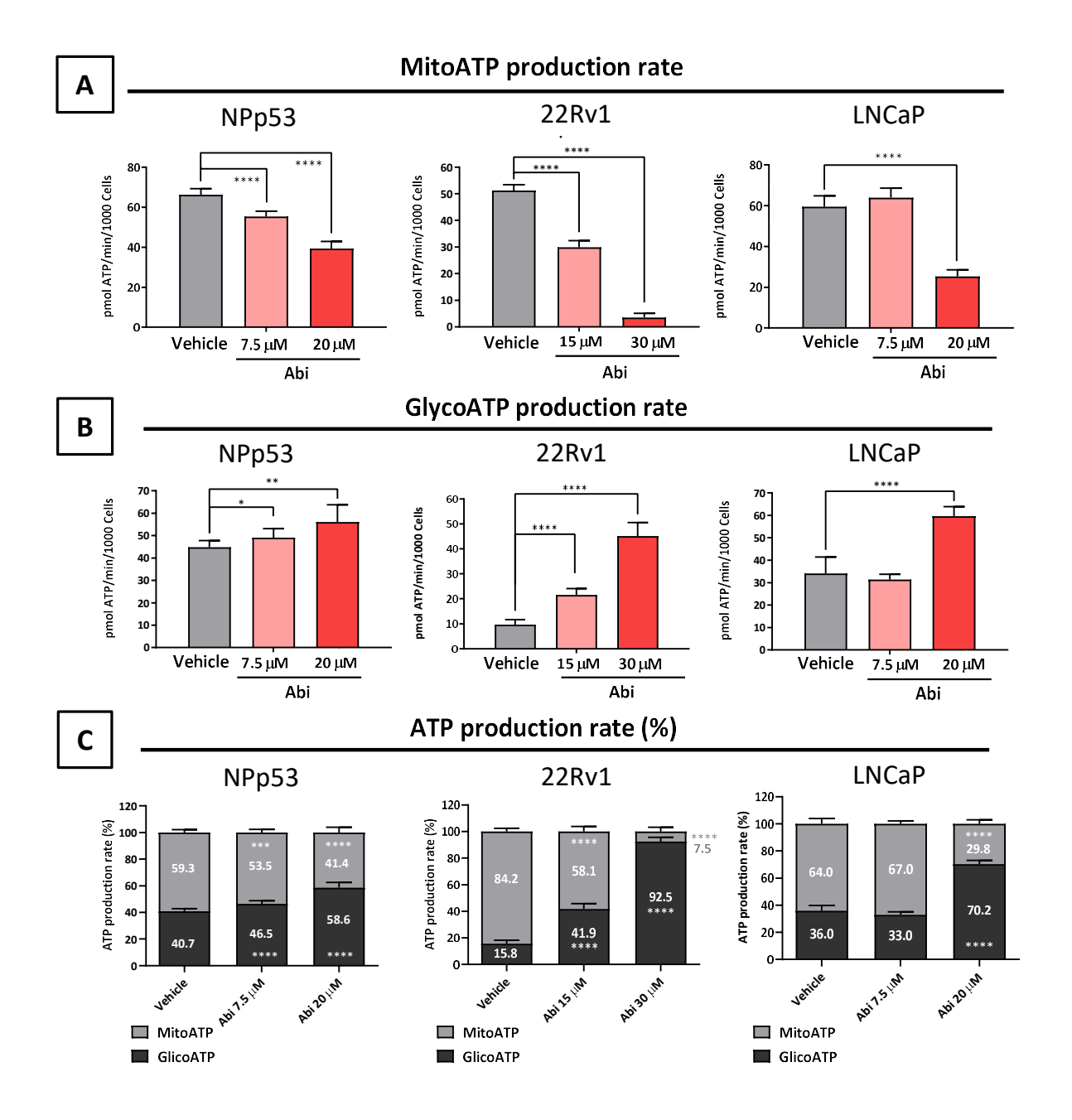


Figure 34. Real-Time ATP Rate Assay allows to distinguish between ATP production from OXPHOS and glycolysis. Cells were treated with abiraterone at 7.5 and 20 μ M (NPp53 and LNCaP) or 15 and 30 μ M for 24 hours. Subsequently, the XF Cell Mito Stress Test Kit to was employed to quantify ATP production rates. A) Mitochondrial ATP production rate, calculated from OCR that is inhibited by oligomycin after stoichiometry corrections. B) Glycolytic ATP production rate, which is equivalent to Glycolytic Proton Efflux Rate (glycoPER). C) Percentage ATP production rate, to easily compare the contribution of each source of ATP for each condition. With exception of percentages, all units are measured as pmol ATP/min/1000 cells. *P < 0.05, **P < 0.01, ***P < 0.001, and ****P < 0.0001.

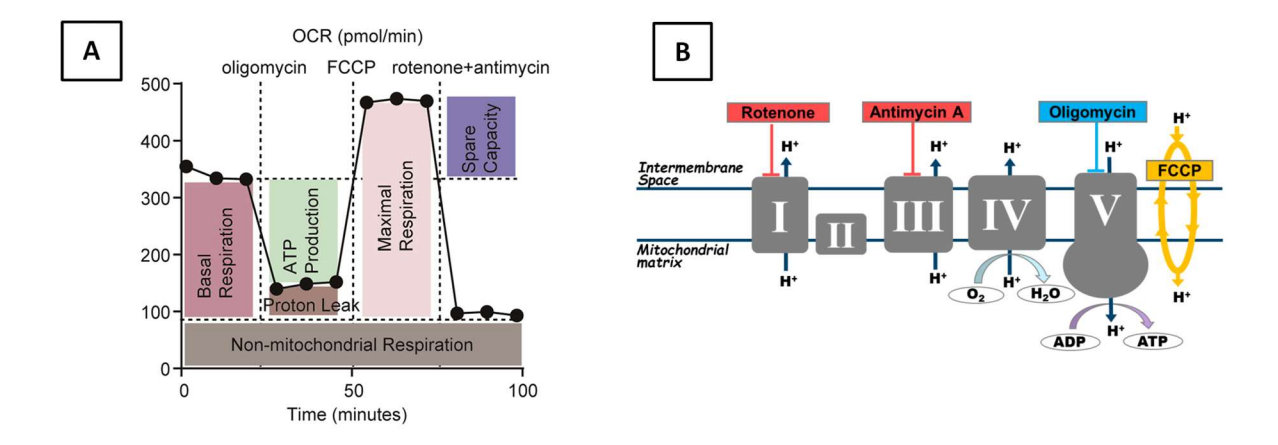
Based on the results of this assay, it is observed that the production of ATP from OXPHOS metabolism decreases in a dose-dependent manner due to abiraterone treatment (Figure 34A, p-value <0.0001), with exception of LNCaP cells at low concentration. Conversely, there is a significant increase in ATP molecules generated from glycolysis upon abiraterone treatment (Figure 34B), with the highest differences observed in 22Rv1 (p-value <0.0001), even at low concentration. While NPp53 and LNCaP cell lines showed modest (p-value <0.042) or absent increase in glycolytic ATP levels at low concentration of abiraterone, respectively, these cells showed a higher increase in this parameter using high concentrations of antiandrogen (p-values ≤ 0.0032).

This suggests a treatment-induced metabolic switch in favor of glycolysis as cellular mechanism to try to compensate for the reduction in energetic production from mitochondrial activity (**Figure 34C**), meaning that OXPHOS is the key energetic process for NPp53 cells to maintain ATP levels at basal. Hence, the observed metabolic switch could be induced by the accumulation of HIF- 1α due to the treatment with abiraterone. Interestingly AR-responsive LNCaP cells require a higher abiraterone treatment (considering the corresponding IC50) to induce this change, meaning that CRPC cells could more easily induce a metabolic reprogramming upon abiraterone treatment.

We also included the Duox2 KD model in this experiment. However, no significant differences were observed in any of the parameters measured when compared to the control cells. As a result, it can be concluded that Duox2 is not influencing the ATP rates at basal conditions, which is consistent with the observation that Duox2 KD failed to prevent the abiraterone-induced accumulation of HIF- 1α .

6.3.2. Mito Stress Test

In addition, the Cell Mito Stress Test was utilized to measure key parameters of mitochondrial function (**Figure 35A**), with the aim of comprehending the mechanisms through which abiraterone affects OXPHOS metabolism. This kit also includes Carbonyl cyanide 4-(trifluoromethoxy)phenylhydrazone (FCCP) as a metabolism modulator, in addition to the agents used in the previous assay.



Mitochondrial respiration

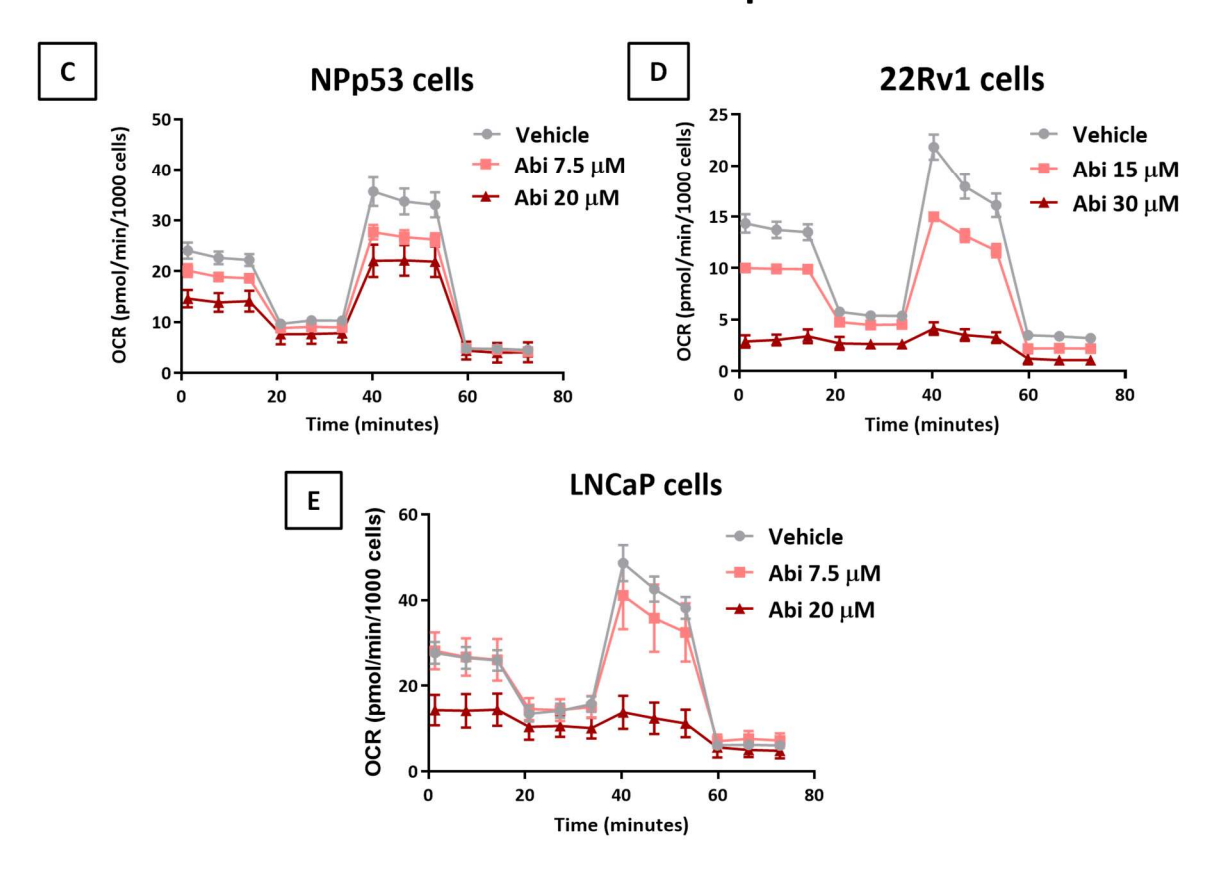


Figure 35. XF Cell Mito Stress deciphers the OXPHOS metabolism by mitochondria. Following treatment, the XF Cell Mito Stress Test Kit was utilized to quantify OCR levels over time. (A) Schematic representation of a typical respiration profile over time following the sequental addition of agents used in the Mito Stress Assay, targeting different complexes of the Electro Transport Chain (ETC). (B) A depiction of the ETC members acting in the mitochondrial membrane, illustrating the flux of protons and the modulators targeting each complex (C-E). Respiration profile of NPp53 (C), 22Rv1 (D) and LNCaP (E) cells based on OCR levels.

These molecules target different components form the Electron Transport Chain (ETC) and are added in a sequential manner following the basal measurements (**Figure 35A and B**). Therefore, by quantifying the different parameters involved in the OXPHOS upon abiraterone treatment, we have generated a respiration profile (**Figure 35C-D**) for each cell line that will be depicted and analyzed.

First, oligomycin inhibits ATP synthase (complex V) (**Figure 35B**), leading to a reduction in electron flow through the ETC and consequently, a decline in OCR. This decrease in mitochondrial respiration is correlated with cellular ATP production (**Figure 35A**). As anticipated from our previous findings, both the basal respiration (**Figure 36A**, p-value < 0.0001) and ATP generated through OXHPOS metabolism (**Figure 36B**, p-value < 0.0001) are significantly decreased upon abiraterone treatment, except for LNCaP cells treated at low abiraterone concentration, as anticipated from the previous ATP Rate Assay.

Interestingly, CRPC 22Rv2 cells displayed the lowest basal respiration levels (10.3 pmol O_2 /min/1000 Cells), compared with NPp53 (17.6 pmol O_2 /min/1000 Cells) and AR-sensitive LNCaP cells (19.3 pmol O_2 /min/1000 Cells).

Secondly, FCCP disrupts the mitochondrial membrane potential. Consequently, the electron flux through the ETC is no longer inhibited and oxygen consumption reaches its maximum (**Figure 36A** and **Figure 37B**). In fact, abiraterone treatment reduces the maximal respiratory capacity (**Figure 36C**, p-value < 0.0001), except for the modest decrease observed in LNCaP cells with low abiraterone concentration (p-value = 0.0173). This decrease is an important indicator of mitochondrial dysfunction.

Furthermore, spare respiratory capacity (SRC) can be calculated as by subtracting basal respiration from maximal respiration. This parameter measures the amount of extra ATP that the cell can produce as a response to counteract sudden increases in energy demand, stress, or heavy workload, and thus prevent an ATP crisis. As a result, cells treated with abiraterone showed a decreased SRC compared with untreated conditions (**Figure 36D**, p-value ≤ 0.0003).

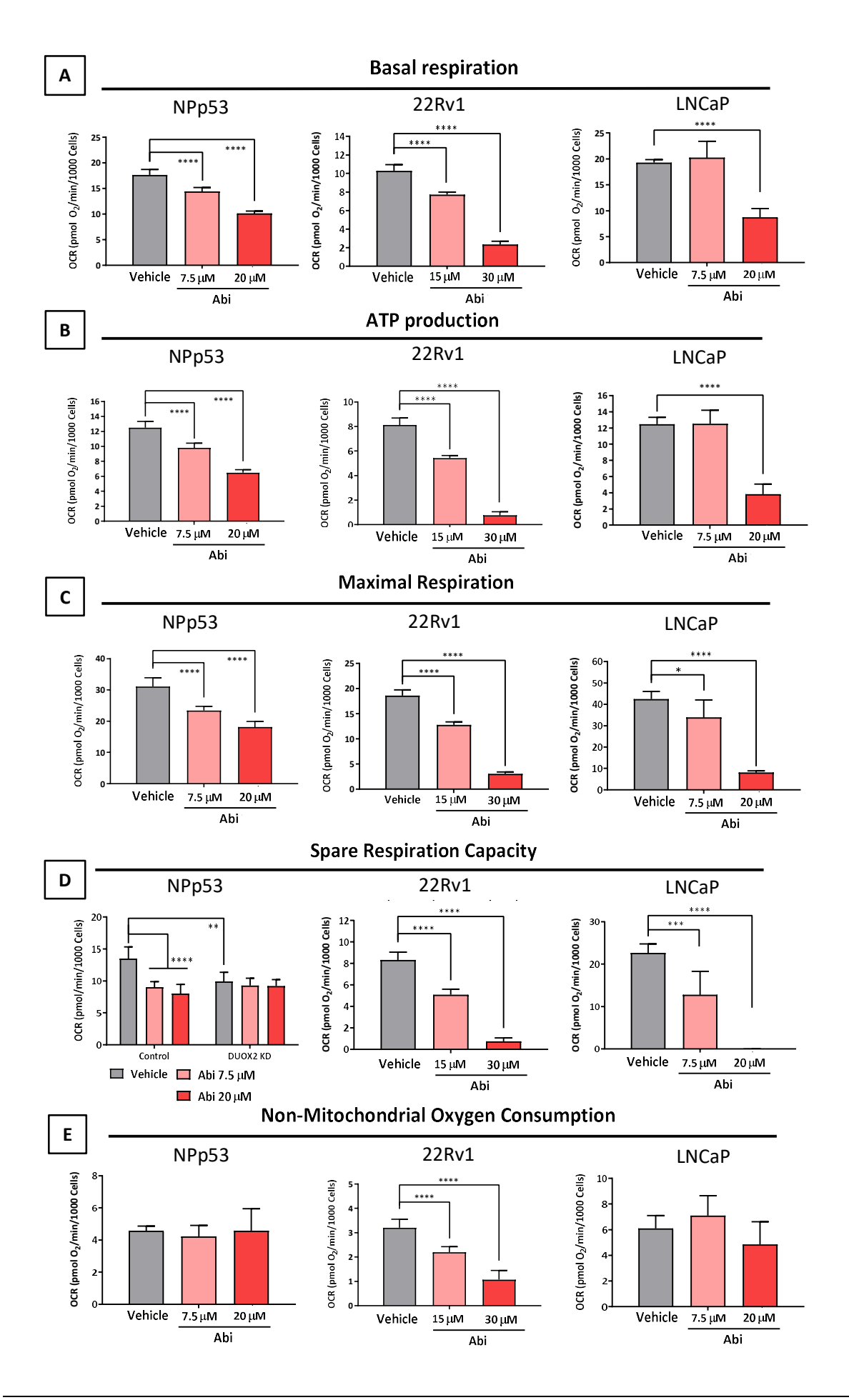


Figure 36. Key parameters of mitochondrial OXPHOS metabolism obtained from XF Cell Mito Stress, including A) Basal respiration levels for each condition. B) Mitochondrial ATP production levels. F) Maximal Respiration, and G) Spare Respiratory Capacity for treated and Duox2 KD conditions. H) Non-mitochondrial Oxygen Consumption. All units are expressed as pmol $O_2/\min/1000$ cells. *P < 0.05, **P < 0.01, ***P < 0.001, and ****P < 0.0001.

Notably, Duox2 KD in NPp53 cells was also associated with a significative reduction of this parameter, similar to the effect of Abiraterone (**Figure 36D**, p-value = 0.0036).

Therefore, Duox2 seems to be related with capacity to meet extra energy requirements. Consequently, cells threatened with abiraterone treatment necessitate a prompt source of extra ATP, which is compromised due to Duox2 KD. However, a mechanism of these cells to bypass this reduced SRC by abiraterone is the activation of glycolysis, as previously showed.

Finally, the injection of rotenone (complex I inhibitor), and antimycin A (complex III inhibitor) culminates in the complete cessation of mitochondrial respiration (**Figure 36A** and **B**). This enables the calculation of non-mitochondrial respiration, which is generated by all processes external to the mitochondria, including cyclo-oxygenases, lipoxygenases and NADPH oxidases. These enzymes are known to be linked with inflammation and are negative indicators of bioenergetic health [319]. In fact, we did not observe significant differences due to abiraterone in non-mitochondrial respiration, except for 22Rv1 cells (p-values < 0.0001, **Figure 36G**), which already have basal levels of this parameter (3.20 pmol O2/min/1000 Cells), compared with NPp53 (4.58 pmol O2/min/1000 Cells) and LNCaP cells (4.58 pmol O2/min/1000 Cells).

Hence, abiraterone induces a metabolic switch by activating glycolysis as a resistance mechanism, since OXHPOS metabolism is decreased It is worth noting that abiraterone-induced reactive oxygen species (ROS) could impair mitochondrial function, and this will be elaborated upon in the further discussion. Our proposal is that this mechanism could be controlled by the accumulation of HIF- 1α , which is stimulated by abiraterone treatment, leading to a pseudohypoxia state that triggers the activation of hypoxia-regulated genes.

7. CO-TARGETING HIF AND AR SIGNALING

7.1. In vitro SYNERGY BETWEEN HIF-1 α INHIBITION AND ANTIANDROGENS

Hypoxia-inducible factors (HIFs), as master regulators of the hypoxia-associated the transcriptional program [251], are object of intensive research aimed at developing potent and specific inhibitors [320, 321]. Building upon our prior findings, which have demonstrated the potential of abiraterone-induced pseudohypoxia to activate signaling pathways associated with cell survival and proliferation, we propose a pharmacological strategy that involves targeting hypoxia-inducible factors (HIFs) in combination with antiandrogens to overcome resistance.

For this purpose, NPp53 cells were treated with PX-478, a potent HIF-1 α inhibitor. Dose scalation synergy assay indicated a marked synergy between both drugs at several concentration combinations (**Figure 37A**). Through the use of MTT viability assay (**Figure 37B**), we observed a significant synergistic effect upon comparing the concentration-response curves of abiraterone alone or in combination with PX-478 at 15 μ M (p-value = 0.033) and 30 μ M (p-value = 0.047). Finally, this synergy was also evident in the colony formation capacity of NPp53 cells (p-value = **Figure 37C**).

We aimed to determine if the potential benefit of co-targeting both AR signaling and pseudohypoxia signaling could potentially be advantageous with other antiandrogens, such as enzalutamide. As for abiraterone, dose scalation drug response matrices confirmed a synergistic effect on the use of enzalutamide and the HIF-1 α inhibitor PX-478 (**Figure 37D**), which was again validated in our dose-response viability assays (**Figure 37E**), showing a significant dose-dependent reduction in enzalutamide IC50 when used in combination with PX-478 at 15 μ M (p-value = 0.037) and 30 μ M (p-value = 0.004).

Finally, we also validated this synergistic effect between antiandrogens and HIF-1 α inhibition in human PCa cell lines. Based on the IC50 values (**Figure 38A**), LNCaP cells showed

higher resistance to the PX-478 (IC50 = $68.1 \,\mu\text{M}$) compared with 22Rv1 (IC50 = $26.2 \,\mu\text{M}$) and NPp53 cells (IC50 = $21.5 \,\mu\text{M}$).

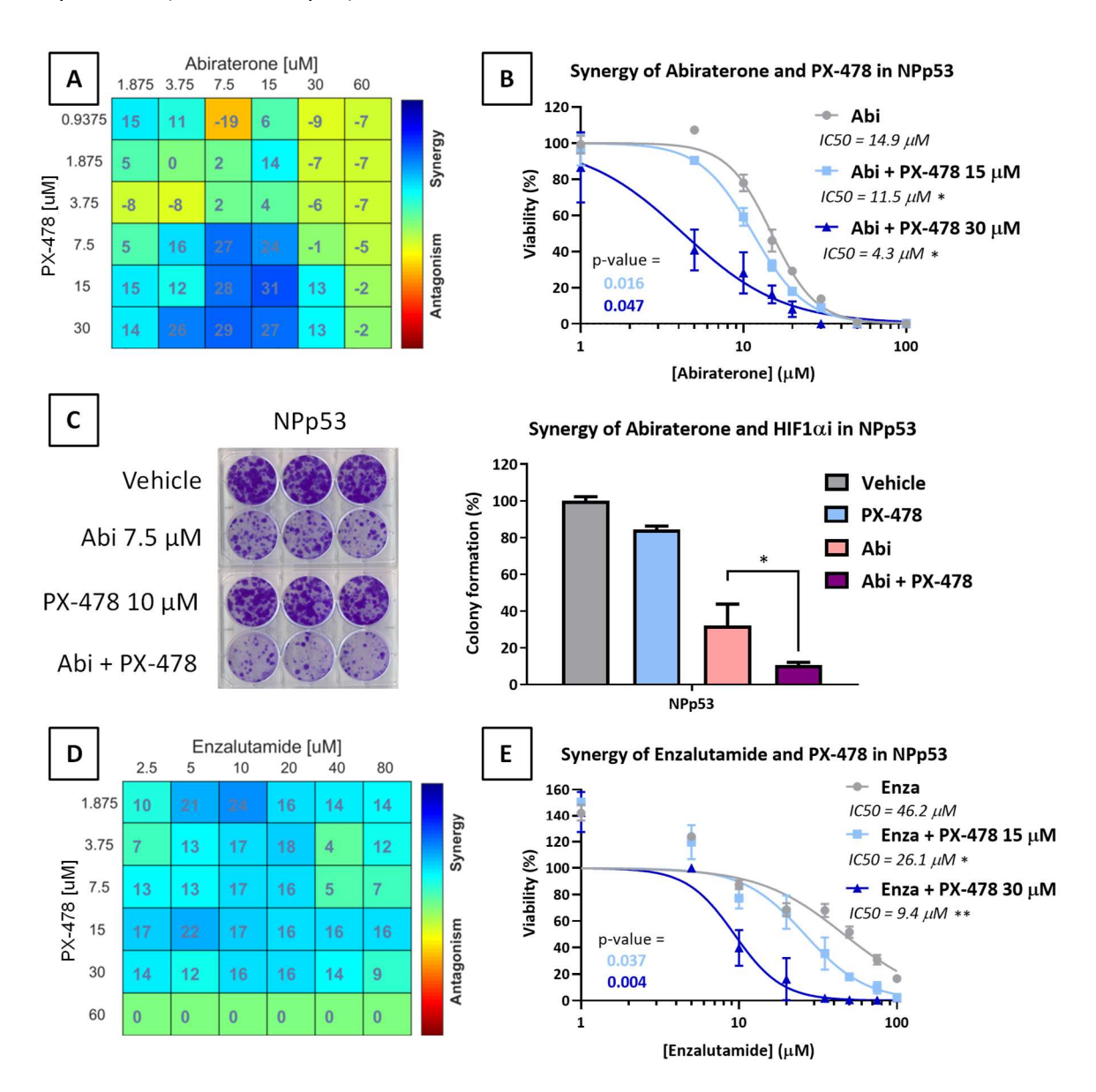


Figure 37. PX-478 synergizes with antiandrogens in NPp53 cells. A, D) Synergy quantification between PX-478 and abiraterone or enzalutamide, correspondingly. **B, E)** MTT viability assay comparing abiraterone or enzalutamide dose-response curves alone or combined with a fixed concentration of PX-478, based on IC50 values. **C)** Colony formation assay in NPp53 to assess the synergistic effect between abiraterone and PX-478.

22Rv1 cells exhibited a synergistic effect at high concentrations of both drugs (**Figure 38B**). We observed a significant decrease in the IC50 value extrapolated from the dose-

response curve of abiraterone upon addition of the PX-478 (**Figure 38C**) at a fixed concentration of 30 μ M (p-value = 0.0475).

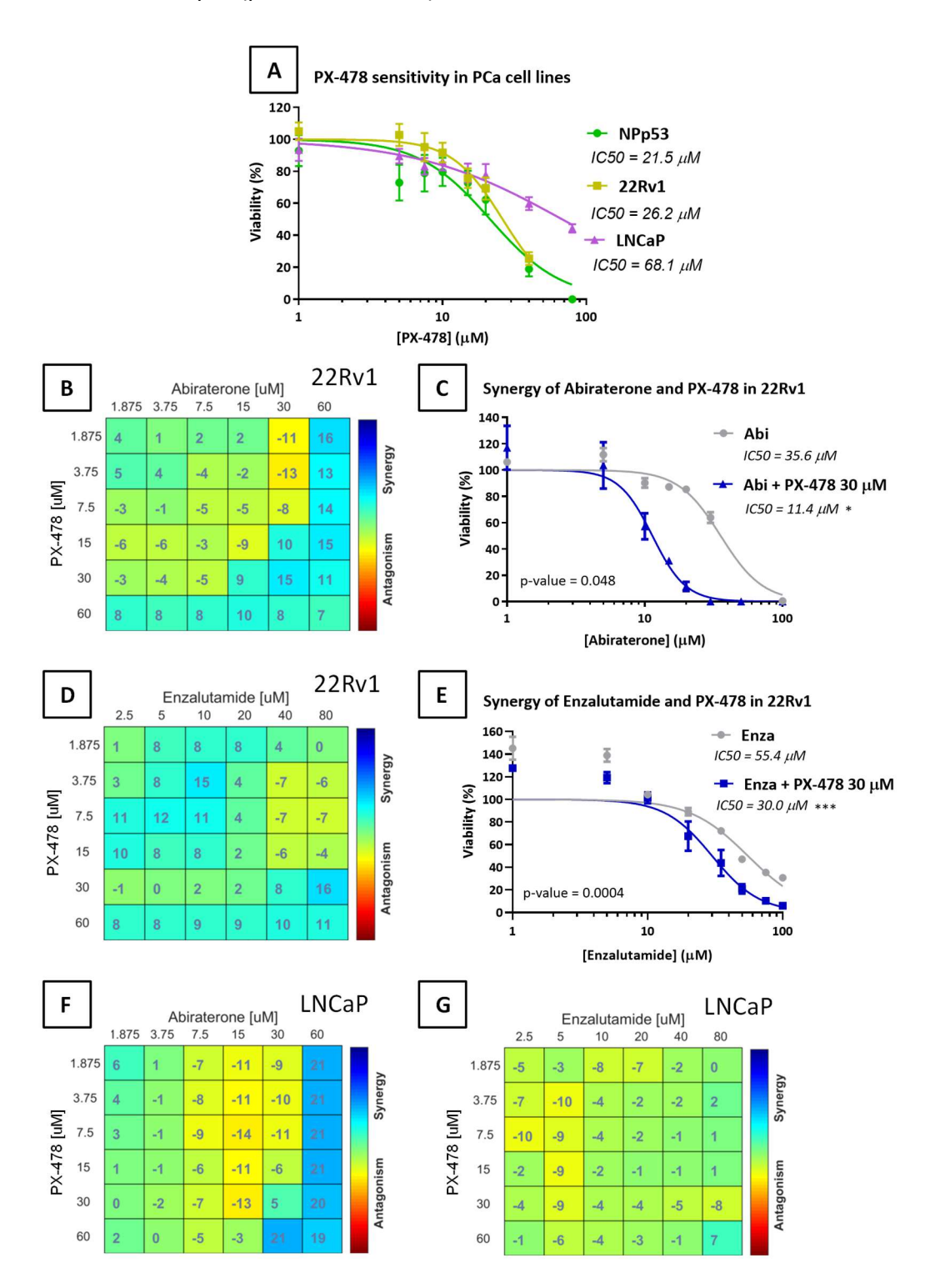


Figure 38. PX-478 synergizes with antiandrogens in castration-resistant 22Rv1 cells, but not in hormone sensitive LNCaP cells. A) MTT viability curve with increasing doses of PX-478 to extrapolate IC50 value from our PCa cells. **B, F)** Synergy quantification between PX-478

and Abiraterone in 22Rv1 and LNCaP. **D, G)** Synergy quantification between PX-478 and Enzalutamide in 22Rv1 and LNCaP, correspondingly. **C, E)** MTT viability assay for 22Rv1 cells comparing Abiraterone or Enzalutamide dose-response curves alone or combined with a fixed concentration of PX-478, based on IC50 value.

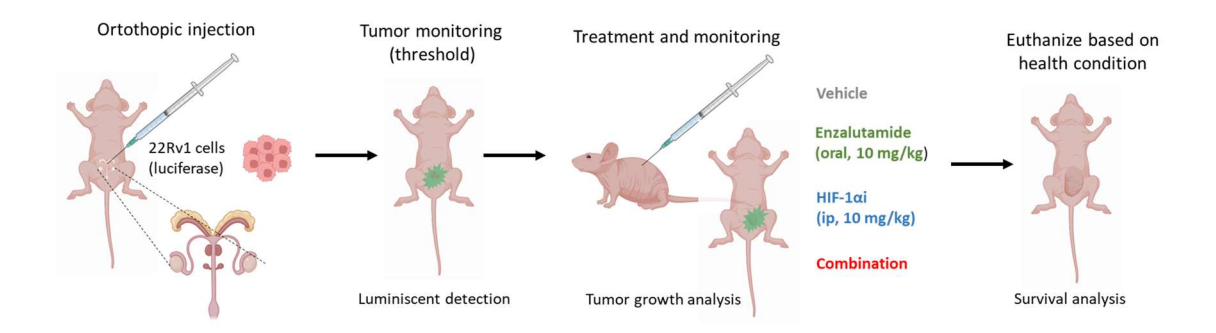
However, the synergy of this inhibitor with However, the combination of this inhibitor with Enzalutamide demonstrated more consistent synergy in this cell line, even at lower concentrations of the compounds **Figure 38D**). Based on the concentration-response curve of enzalutamide, 22Rv1 were sensitized upon treatment with the PX-478 at 30 μ M (**Figure 38E**, p-value = 0.0004). As expected, the combination of the HIF-1 α inhibitor with either abiraterone (**Figure 38F**) or enzalutamide (**Figure 38G**) did not exhibit in any observed synergy in the AR-sensitive LNCaP cells. The lack of synergy may be attributed mostly to the already potent antiproliferative effect of AR targeting in these cells, and to the inherent resistance of LNCaP to the PX-478 alone.

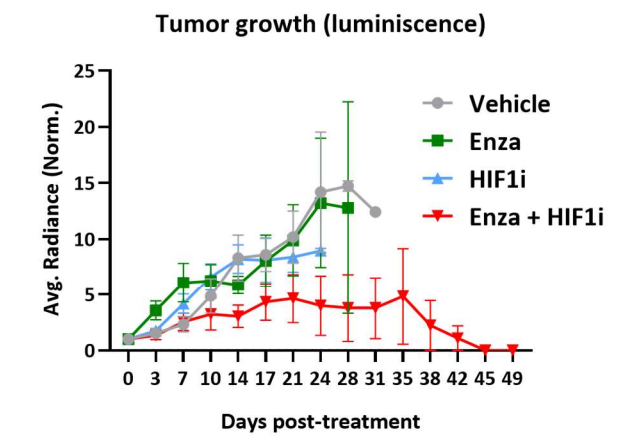
Together, the combined use of antiandrogens and hypoxia signaling inhibitors robustly restores AR sensitivity in mouse and human CPRC cell models. has been demonstrated in NPp53 and 22Rv1, which are cells that display CRPC.

7.2. In vivo VALIDATION OF THE SYNERGY

Based on the observed synergistic effect between androgen receptor (AR) inhibition and hypoxia signaling pathway targeting, we resolved to evaluate this benefit in an *in vivo* model as a preclinical validation. We chose to use immunodeficient mice to orthotopically engraft human PCa cells into the anterior prostate (**Figure 39A**). This approach allowed us to reproduce the paracrine signaling context and other characteristics of the tumor microenvironment of the prostate, compared with the subcutaneous or systemic injection.

We specifically selected the 22Rv1 cells for this preclinical validation due their ability to best replicate CRPC characteristics when orthotopically injected in the mice prostate, compared with NPp53 and LNCaP. Moreover, the synergy achieved by combining either abiraterone or enzalutamide and the PX-478 exhibited the potential to confer significant benefits in inhibiting prostate tumor growth.





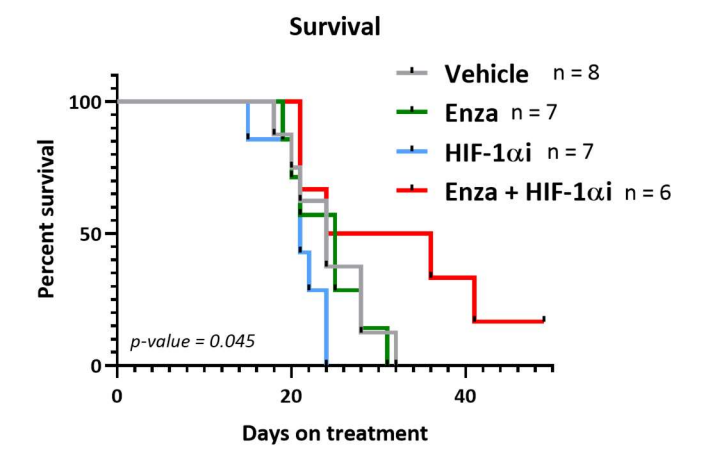


Figure 39. In vivo combination of enzalutamide and PX-478 results in tumor growth inhibition and survival improvement. (A) Schematic representation of the in vivo experimental procedure. (B) Tumor growth monitoring. Day 0 signifies the moment when each tumor attained the luminescence threshold value (average radiance, p/s/cm²/sr) to commence the corresponding treatment. Consequently, each tumor was normalized (equal 1) with the exact average radiance value of its assigned day 0. This normalization facilitates the monitoring of tumor growth as fold increase. (C) Survival analysis based of the number of mice remaining each group throughout the experiment. Mice that died due to non-tumor-related reasons were excluded from the analysis.

To monitor tumor growth *in vivo*, the 22Rv1 cells were transduced with a lentiviral plasmid containing a luciferase reporter gene under the control of a constitutively expressed promoter. Therefore, once implanted, upon D-luciferin injection, the luminescent reporter enabled easy tracing of the implanted tumor cells.

We conducted the experiment in non-castrated mice, as we selected enzalutamide as the antiandrogen therapy to target the AR signaling.

After reaching a predetermined threshold of tumor growth (50·10⁶ p/s/cm²/sr), quantified by the average radiance of luminescent signal, each mouse was randomized to one of the treatment groups (vehicle, enzalutamide, PX-478, or combination) (**Figure 39A**).

Each mouse remained in the same treatment group throughout its lifespan to enable the investigation of potential variations in survival rates. In case of a severe decline in a mouse's health, euthanasia was carried out, taking into account its health indicators.

Consistent with the CRPC phenotype of 22Rv1 cells, treatment with enzalutamide did not result in a significant reduction in tumor growth, exhibiting a similar trend to that of the vehicle mice (Figure 39B). Consequently, this was translated in no improve of survival (Figure 39C). Furthermore, the treatment with PX-478 alone did not confer any significant advantage in terms of tumor growth inhibition (Figure 39B) or survival increase (Figure 39C) compared with the vehicle treated group. Nicely, and confirming the *in vitro* data, the administration of both enzalutamide and PX-478 resulted in a significant reduction and delay in tumor growth (Figure 39B).

Initially, the tumors treated with the drug combination exhibited growth patterns similar to those observed in the other groups. However, after one week of treatment, this particular group diverged from the rest, exhibiting a slower growth rate of proliferation, including one mouse from this group exhibited complete regression of the tumor after two weeks of drug combination treatment (**Figure 40**).

The significant decrease in tumor growth achieved through the administration of the drug combination resulted in a notable increase in survival rates (p-value = 0.045) when compared with the other three groups (**Figure 39C**), with no signs of adverse side effects

associated with the combinatory treatment. Therefore, the fact that this mouse survived over such an extended period of time demonstrates the safety of this drug combination and the absence of toxic effects.

Therefore, this preclinic study provides evidence that the results obtained from in vitro synergy experiments can be extrapolated and validated with in vivo models. These findings suggest that targeting the hypoxia-signaling pathway with HIF-1 α may overcome antiandrogen-resistance in CRPC cells, thus supporting the use of combined treatment as a viable strategy to reduce tumor growth and improve survival rates in CRPC.

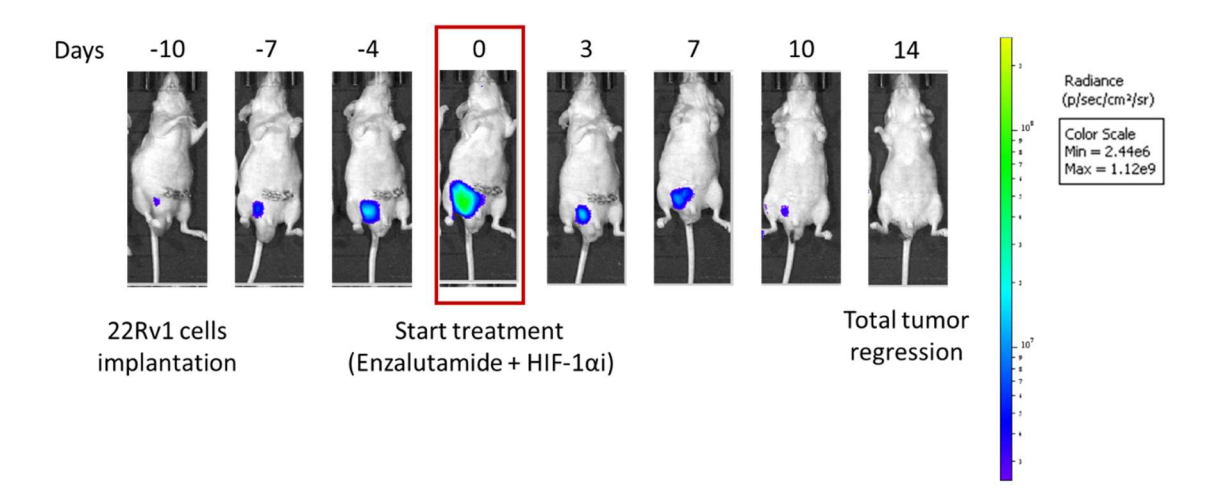


Figure 40. Total tumor regression from a mouse treated with the proposed drug combination. The tumor in this mouse was allowed to grow for 10 days to reach the established threshold for treatment randomization and was then assigned to the drug combination group. Following two weeks of treatment, complete regression of the tumor was observed, as evidenced by the luminescent reporter.

DISCUSSION

1. CRIPRI SCREENING AND NOX FAMILY

As mentioned earlier, the main objective of this thesis is to implement a CRISPR-based genetic screening methodology to uncover of druggable mechanisms associated with the development of antiandrogen resistance in PCa cells.

Several CRISPR-based screenings have been conducted in PCa context to identify essential genes, with some being specific to certain cell types. These screenings have enabled the identification of key contributors to PCa growth and potential targets for therapeutic interventions, such as JMJD1C demethylase [322], ribonucleoprotein L (HNRNPL) [323], and cyclin-dependent kinase 12 (CDK12) [324].

Additionally, similar to our study, CRISPR screenings can be employed to identify genes implicated in drug resistance and sensitivity. Previous research has predominantly focused on using enzalutamide as the antiandrogenic drug of choice to explore resistance mechanisms in PCa. Consequently, This approach has revealed novel genes and proteins that contribute to enzalutamide resistance, such as TLE3 [325], activated BRAF signaling [326] or paired-related homeobox 2 (PRRX2) [327]. Furthermore, to leverage the potential clinical advantages of synthetic lethality with drugs that target DNA damage response (DDR) pathways, several screenings using PARPi [328] or ATRi [329] in PCa have been conducted to find new vulnerabilities.

Nevertheless, to date, no reports have emerged on CRISPR or other types of genetic screenings conducted using abiraterone, a second-generation antiandrogen widely prescribed in CRPC patients but with the problem of acquired resistance [330]. This underscores the significance of the findings from our CRISPRi screening, conducted in a CRPC cell line, which allows for the identification of synthetic lethal interactions between abiraterone and genes on a whole-genome scale.

As the screening process and analysis yielded over 300 hit sgRNAs, we needed to undertake functional analysis and establish additional criteria to determine which category of gene to prioritize for further investigation. Upon analyzing the ranked genes associated

with each hit sgRNAs, we identified 8 genes with a minimum of 2 hit sgRNA, designating them as the "top hits".

Notably, three of the "top hit" genes have been reported to be related with neuronal functions and synapsis. Firstly, Leucine Rich Repeat Neuronal 3 (*Lrrn3*) has been identified as a direct target of MYCN [331], Secondly, the expression of Neurocalcin Delta (*Ncald*) demonstrated potential as a prognostic predictor for ovarian and non-small cell lung cancer (NSCLC) and acute myeloid leukemia [332-334]. Finally, a brief search of N-Ethylmaleimide-Sensitive Factor (*Nsf*) in The Human Protein Atlas survival analysis revealed that high expression levels are associated with a significant decrease of survival probability (p-score = 0.032) of PCa patients.

These identified candidates may be involved in the development of abiraterone acquired resistance related to the neuroendocrine differentiation process. Neuroendocrine prostate cancer (NEPC) cells and tumors are recognized by their immunohistochemical staining for common neuroendocrine markers, including CgA (chromogranin), SYP (synaptophysin), and neuron specific enolase (NSE) [335]. NEPC can be classified into *de novo* NEPC or treatment-related NEPC (t-NEPC) based on the presence or absence of pretreatment, [336]. t-NEPC arises due to treatment-induced lineage plasticity, where tumor cells transdifferentiate from AR-dependent adenocarcinoma to t-NEPC, thus circumventing AR pathway inhibition [304, 337].

As previously explained, NPp53 mice have been shown to progress to CRPC. However, NPp53 treated with abiraterone exhibited no response and instead developed highly aggressive phenotypes that exhibit molecular and phenotypic features similar to those observed in human t-NEPC, thereby suggesting an acquisition mechanism of drug resistance [152]. Furthermore, regions with neuroendocrine differentiation in these abiraterone-treated NPp53 tumors have a greater proliferative potential and arise by transdifferentiation of luminal adenocarcinoma cells [152]. However, this r, this phenomenon was not observed in NP mice, indicating the crucial role of TP53 and PTEN inactivation in the development of abiraterone resistance and t-NEPC progression.

Thus, Lrrn3, Ncald and Nsf genes could be involved in the process of abiraterone resistance acquisition through t-NEPC transdifferentiation. This would explain the fact that these genes are essential to survive abiraterone treatment, since sgRNAs targeting these genes were depleted in the treated conditions.

However, to have a more a broader understanding of the various molecular mechanism and pathways that could relate the high number of hit sgRNAs targeting different genes, we conducted an enrichment analysis. Using the Hallmark gene set from MSigDB, we performed a functional analysis which revealed several pathways enriched in our hit sgRNAs These pathways are of interest as they are known to be involved in therapeutic resistance in PCa, including DNA damage [338], G2-M checkpoint [339] and MYC targets [340]. Therefore, the implementation of CRISPRi screening in our cellular model has successfully identified genes and molecular pathways associated with abiraterone response, and can be applied to other therapies. Moreover, our interest relies in identifying mechanisms that are not so well characterized.

Interestingly, two hits from Duox2 occupied a high ranked position ("top hit"). In addition, Duoxa1 also contained a hit sgRNA in the list, while one of the guides targeting Duox1 showed a great significant p-adjusted, the fold change was close but did not reach the threshold stablished.

Duox2 expression at RNA levels in PCa cell lines is generally low, as detected by qRT-PCR [213], with some exceptions like overexpression in DU145 cells. Furthermore, Duox2 RNA levels in PCa tissues did not differ from non-tumoral samples [213]. However, even at low levels of expression, DUOX proteins have been related with pathological roles in PCa. Furthermore, the development of a novel Duox2 monoclonal antibody allowed to detect Duox2 at elevated levels in many human cancers from a tissue microarray (TMA), with prostate adenocarcinoma with the highest frequency of expression [237].

DUOX proteins have shown to contribute to maintaining ROS levels in PC3 cells, thus activating AKT signaling by phosphatases inactivation and leading to increased resistance to apoptosis [208]. Furthermore, DUOX2 have been shown to also regulate the AKT pathway in colorectal cancer cells [209].

For some tumor types, DUOX enzymes were found involved in drug resistance mechanisms. For example, ROS production by DUOX activity mediates 5-fluorouracil resistance by inducing epithelial-to-mesenchymal transition (EMT) in human colon cancer cells [210]. Furthermore, overexpression of DUOX2 has shown to mediate doxorubicin resistance of pancreatic cancer. Conversely, expression is decreased in breast cancer and its silencing has been related with high proliferation after doxorubicin treatment, thus modulating the response to genotoxic stress induced by this drug [341].

Therefore, since DUOX2 has been found overexpressed in many cancers and its presence has been related with different drug resistance, it was interesting for us to elucidate if this protein would be also involved in the acquisition of abiraterone resistance of CRPC cells. Thus, we moved to explore the role that Duox2 play in PCa patients, using the Standard Up To Cancer (SU2C) dataset, containing valuable information regarding mCRPC patients.

The negative correlation between Duox family expression and AR score in this dataset highlights the interplay between Duox genes and AR activity. Over progression, CRPC patients become more irresponsive to AR inhibitors, since tumors cells are less AR-dependent. Remarkably, the fact that Duox genes expression is positively correlated with "Chuang oxidative stress response" (ROS signature) reinforces the contribution of this family of proteins to the oxidative state. Interestingly, the fact that only Duox2 and its maturation factor, Duoxa2, were positively correlation with a H₂O₂ signature highlights the importance of this member in the generation of H₂O₂ in PCa patients. This is relevant considering the fact that Duox2 and Duox1 are regulated and expressed in a different way depending on the tissue or on the type of cancer, showing also opposite roles, prognostic value and in some cases [181, 211, 212]. However, expression of DUOX1 in tumors is in general low, with some exceptions [213].

Furthermore, we observed that Duox2 expression was more informative in survival analysis once patients are separated based on their respective NEPC score. In general, more advanced patients show a higher NEPC, which is related with a neuroendocrine phenotype. As commented above, t-NEPC arises in advanced CPRC, which means that Duox2 expression

is informative in the disease stage associated with higher resistance, where patients with higher Duox2 levels were associated with a decrease in survival.

Therefore, we concluded form this part that CRISPRi screening tool can be implemented successfully to identify synthetic lethal interactions between genes and antiandrogens in our CRPC cellular model. The correlation and the role of Duox2, obtained a one of the "top hits" form the screening, with relevant signatures and survival from an advanced CRPC patient database led us to focus our attention on the NADPH oxidase family as a key modulator of antiandrogen response.

2. DUOX AND ROS METABOLISM MODULATING ANTIANDROGEN RESPONSE

2.1. DUOX2 AND ANTIANDROGEN RESISTANCE

Based on the aforementioned results and considering the established role of Duox2 in cancer, we proposed that the reduction of Duox2 levels may contribute to increase antiandrogen sensitivity, as a synthetic lethal interaction mechanism to overcome drug resistance.

Results from MTT and colony formation assays confirmed the synergistic interaction between abiraterone and Duox2 abrogation. In addition, this synergy also was observed when NPp53 cells were treated with Enzalutamide, confirming that decreased Duox2 expression can enhance the response of NPp53 cells to other antiandrogens.

Hence, in order to validate this link between ROS metabolism and abiraterone resistance, it seemed appealing the pharmacological inhibition of Duox2. This way, cotargeting ROS generated by NADPH oxidase family emerged as an noteworthy therapeutic strategy.

Given the important role of oxidative stress and ROS in carcinogenesis and cancer progression, the use of antioxidants for cancer treatment has emerged as an appealing approach [342]. Accordingly, various antioxidants have been developed in recent decades,

which include 1) non-enzymatic antioxidants, like vitamins (vitamin C and E, mostly) [343, 344] or N-acetyl-L-cysteine (NAC) [345], and 2) enzymatic antioxidants, including NOX inhibitors [346] and SOD mimics [347]. NAC is regarded as one of the most extensively studied antioxidant agents. It is quickly absorbed through the anion exchange membrane and subsequently deacetylated to generate cysteine, thereby restoring the levels of glutathione (GSH).

Nevertheless, the lack of specificity of non-enzymatic antioxidants towards a particular ROS and to a specific compartment may significantly contribute to their clinical inefficacy in most cases. Overall, the controversial impact of these type of antioxidants on cancer raise to substantial concerns regarding antioxidant supplementation. Consequently, endeavors to mitigate oxidative stress have shifted towards targeting the sources of pathophysiological ROS rather than attempting to eliminate ROS in a general manner after their generation [348]. As a result, several small-molecule global inhibitors that can inhibit NOXs or flavoproteins in general have been developed [342].

One such compound, DPI, was the first identified and is commonly used as a potential inhibitor of NOXs. This small molecule is activated to a radical intermediate following interaction with flavin-containing components, thus forming relatively stable covalent adducts with FAD relatively stable covalent adducts which block electron flow from NADPH to molecular oxygen [349, 350]. This mechanism contributes to the reduction of ROS levels and has demonstrated anticancer properties [350, 351]. Notwithstanding that DPI is a non-selective, promiscuous inhibitor, it can target other flavin-dependent enzymes, such as xanthine oxidase and nitric oxide synthase [342]. Moreover, other NOX inhibitors, like ebselen, apocynin and diapocynin have been observed to exhibit unrelated effects [352].

In fact, researchers in a particular publication [353] undertook the design and synthesis of 36 analogs of DPI to enhance solubility and functionalization. They discovered a more potent and specific inhibitor of Duox2. However, this molecule is currently unavailable, and no other studies have been conducted on it. Therefore, due to the challenges in targeting Duox2 specifically, we proceeded to use DPI to assess the effect of inhibition the ROS production by targeting the NADPH oxidase family in a general manner.

Consequently, synergy experiments in our NPp53 cells were conducted using DPI as pan NOX/DUOX inhibitor Our findings indicate a significant combinatorial effect between Abiraterone and DPI, which was also observed in the treatment of other human PCa cell lines, namely 22Rv1 and LNCaP. These results provide further support for the notion that targeting NADPH oxidase activity is a viable strategy to overcome Abiraterone resistance in PCa, and that this mechanism is conserved among other PCa cell lines.

Furthermore, the generation of ROS leading to oxidative stress has been associated with the modulation of responses to chemotherapeutic drugs or radiotherapy through its impact on downstream signaling cascades that regulate cell survival or death [183, 354]. Chemotherapeutic agents, such as doxorubicin and cisplatin, have been found to elevate levels of ROS, thereby contributing to their genotoxic effects [355, 356]. Therefore, treatment with antioxidants in cancer patients may result in an antagonistic effect on chemotherapeutic drug-induced cell death.

2.2. ANDROGENS, ANTIANDROGENS AND ROS

Hence, we postulated that abiraterone may induce ROS levels as a resistance mechanism analogous to chemotherapy or radiotherapy. This would account for the synergistic effect with DPI, which would aid in the reduction of ROS levels by inhibiting the NADPH oxidase family. Therefore, we proceeded to quantify ROS levels through the use of different fluorescent-based assays.

As previously stated, Duox2 participates in the formation of an enzymatic complex that releases hydrogen peroxide [190, 191]. Our observations revealed that the reduction of Duox2 had no statistically significant effect on the total ROS levels (measured by the H2DCFDA probe) under basal conditions. It is important to note that other significant ROS molecules, such as the superoxide anion or hydroxyl radical, also contribute to these levels [357], and are not primarily affected by Duox2 activity. However, abiraterone treatment induces an increase in the intracellular total ROS levels, which is impeded by the knock-down of Duox2.

Various aspects of H_2O_2 and other ROS had limited past and current studies. These include: 1) the constant fluctuating intracellular concentrations caused by multiple events, 2) the cellular antioxidants mechanisms, which limit the biochemical effect ROS molecules [358], and 3) the complex interpretation of experimental results using redox-sensitive fluorescent probes, due to their subcellular diffusion dynamics and low specificity [181, 359]. Thus, reliable analytical probes for ROS quantification are scarce, and the findings of these experiments require careful interpretation.

Additionally, an increment in total ROS levels was observed following abiraterone treatment in 22Rv1 and LNCaP cells. However, the increase was modest in 22Rv1, while LNCaP cells showed a more substantial rise in this ratio. Notably, LNCaP cells are one of the most commonly used few AR-responsive PCa cell line, while 22Rv1 expresses AR and the splicing variant AR-V7, and is linked with CRPC, as evidenced by abiraterone and enzalutamide IC50 values in comparison with AR-responsive cells. Moreover, to demonstrate that this abiraterone-induced ROS is a specific mechanism involving AR, we treated DU145 cells with this antiandrogen. DU145 AR-null cells displayed a notable decrease in ROS levels due to abiraterone. Therefore, it is relevant to elucidate the role of androgen and antiandrogen therapy in ROS generation, and the subsequent effect of this regulation.

The stimulation of the androgen receptor (AR) pathway can result in the generation of ROS in specific circumstances. Nevertheless, it is important to acknowledge that the association between AR signaling and ROS production is complex and context-dependent. Therefore, multiple pieces of evidence support the interplay between androgens and oxidative stress.

Surgical castration has demonstrated to induce oxidative stress in the rat prostate by enhancing the expression of NOX enzymes (NOX1, NOX2 and NOX4) and downregulating key ROS-detoxifying enzymes [360, 361]. In this context, androgen replacement partially reduced ROS to pre-castration levels [360]. Complementary, depriving the culture media of androgens has been found to increase basal ROS levels in AR-positive CRPC LNAI [362] and 22Rv1 cells [307], and also in AR-responsive LNCaP cells [307]. Moreover, supplementing

LNCaP cells with a synthetic androgen resulted in an elevation of ROS levels, but not in ARnegative PC3 cells [363].

Therefore, it is possible that abiraterone treatment performs a similar function to androgen depletion by selectively targeting androgen biosynthesis, thereby leading to a common outcome, the increase of ROS levels. Interestingly, the increase in ROS resulting from androgen depletion in LNCaP cells was considerably higher than that observed in 22Rv1 cells [307], as we observed in response to abiraterone treatment. Furthermore, ROS induction triggered by androgen depletion in both 22Rv1 and LNCaP cells has been shown to induce AR overexpression, thereby promoting cell growth in a castration-resistant manner [307]. However, this induced growth was mitigated by NAC, which concurrently decreased LNCaP and 22Rv1 tumor growth in both castrated and non-castrated mice [307].

Despite this, conflicting evidence exists which suggests that androgens may have the opposite effect, with several reports indicating that they may actually increase oxidative stress. It has been observed that physiological levels of androgens can elevate ROS levels in androgen-responsive cells (LNCaP), but not in AR-negative CRPC cells (DU145) [364]. Furthermore, such an increase led to the activation of AKT signaling, which was subsequently reversed by ADT (using bicalutamide, which is an AR antagonist) or incubation with NAC.

Additionally, DHT has been found to elevate levels of oxidative DNA adducts, and effect that can be prevented upon flutamide treatment, a competitive AR antagonist [365]. Moreover, androgens have been observed to induce oxidative stress and radiation resistance in AR-positive CRPC cells (22Rv1) though NADPH oxidase activation [366].

Consequently, in AR-positive cells, androgens have been demonstrated to augment the basal levels of ROS, which are already higher in CRPC cells that express AR [308, 364, 366, 367]. For instance, CRPC cells derived from respective AR-responsive cells displayed elevated ROS levels and enhanced signaling of proliferation and survival pathways [308]. Hence, oxidative stress appears to play a role in the transformation of androgen-dependent PCa into CRPC by regulating AR expression [309, 310].

Indeed, androgens can modulate the response of PCa to radiation therapy by regulating the cellular oxidative homeostasis [366, 367]. The benefits of combining ADT with radiation in high-risk localized PCa are partially attributed to the anti-angiogenic and proapoptotic effects of ADT [368, 369]. However, it has been suggested that the radiosensitizing effect of ADT induced by bicalutamide is achieved by increasing the susceptibility of ARpositive CRPC cells to toxic oxidative stress induced by radiation [366, 367]. This benefit is based on the observation that androgens can increase basal ROS levels, which in turn enhance the expression of antioxidant enzymes and AKT signaling, thereby facilitating adaptation to oxidative stress [367]. Furthermore, androgens stimulate ROS production by increasing the expression of NOX2 and NOX4 in 22Rv1 cells [366]. In fact, it has been observed that the sensitivity of pre-radiated cells to radiation is enhanced to a degree that is similar to ADT when treated with NADPH oxidase inhibitors [366].

Therefore, it is important to make a distinction between basal and induced levels of ROS. The observation that 22Rv1 CRPC cells exhibit higher basal levels of ROS may provide an explanation for the comparatively milder induction of ROS by abiraterone in these cells as compared to LNCaP, as 22Rv1 cells are already more adapted to oxidative stress. Consequently, LNCaP cells could be more susceptible to induced ROS levels.

Taken together, the available evidence suggests that AR-negative CPRC cells exhibit increased basal levels of ROS [308, 370], making them more adapted to oxidative stress, as evidenced by the lack of increase in ROS levels observed in DU145 cells following abiraterone treatment. This implies that the activated AR pathway may promote ROS production most strongly in an androgen-deficient environment. However, the relationship or crosstalk between AR signaling and ROS production is complex and dependent on many factors, such as culturing conditions and the presence of other signaling pathways. Additionally, it is important to distinguish between basal and induced ROS levels and to consider how ADT is performed in each model. Consequently, the use of the term "ADT" to refer to both androgen depletion in the media and AR antagonists or hormones can lead to misinterpretations. However, we are using an androgen synthesis inhibitor as a second-generation antiandrogen, abiraterone.

Additionally, some evidence suggest that extremely high levels of ROS may have a negative regulatory effect on AR translational levels. This is as an example of how the complex interplay between ROS and AR signaling can lead to contradictory conclusions without considering different factors involved. Isoselenocyanate-4 (ISC-4) was found to inhibit LNCaP cell growth and survival via ROS-mediated suppression of AR axis signaling and induction of apoptosis [371]. Moreover, targeting Enzalutamide-induced BCL2 with inhibitor ABT263 increased Enzalutamide sensitivity in PCa cells through by inducing cellular ROS levels and suppressing ubiquitin specific protease 26 (USP26) activity. This led to an increase in the ubiquitin/proteasome-dependent degradation of AR and AR-V7 proteins [372]. Finally, the acute exposure of Bardoxolone-methyl (CDOO-Me), a triterpenoid antioxidant drug, was found to increase ROS levels, which was critical in decreasing the levels of AR and AR-V7 at both the transcriptional and translational levels [373].

In conclusion, the relationship between androgen and oxidative stress appears to be unequivocal. However, it is feasible that both androgen deprivation and androgen exposure can induce oxidative stress via distinct mechanisms. For instance, androgen deprivation in an androgen-positive environment or by androgen exposure in an androgen-negative environment may trigger different forms of stress in PCa cells [307]. Therefore, results based on the introduction of androgens to an androgen-negative environment may not precisely reflect the clinical reality of ADT. Nonetheless, in our case, abiraterone is not acting directly by antagonizing AR, but rather inhibiting the biosynthesis of androgens.

Moreover, the intricate interplay between androgen supplementation versus androgen ablation in regulating the production of reactive oxygen species is a topic of controversy concerning other associated effects as well. In a parallel study to this thesis project, we have demonstrated that supraphysiological levels of dihydrotestosterone (DHT) significantly reduced the proliferation and colony-forming capacity of AR-responsive LNCaP cells. However, AR-negative cells lines (DU145 and PC3), 22Rv1 CRPC cells, and RWPE-1 normal prostate epithelial cells were displayed a high degree of resistance to this effect. Interestingly, upon reintroduction of AR in AR-null cells (both DU145 and PC3), they became responsive to the inhibitory effect of DHT on cell growth.

Furthermore, this growth-inhibiting role of ligand-bound AR has been previously demonstrated in other studies [374, 375] and serves as the basis for the proposed use of supraphysiologic testosterone treatment in patients with under investigation in clinical settings as part of bipolar androgen therapy (BAT) [376]. Mechanistically, AR signaling exhibits a dichotomous behavior, promoting growth at lower activity levels while inhibiting it at higher levels [377]. Recently, a specific set of AR transcriptional outputs (AR cistrome) has been identified for patients responding to supraphysiologic testosterone, which inhibits PCa progression in a specific subset of patients [378].

Hence, this tightly regulated interplay between androgens levels and proliferative effects could potentially be modulated by ROS as well. We have previously showed that abiraterone, which exhibits a distinct impact on AR-expressing cells relative to AR-negative cells (as indicated by IC50 values), induces ROS production that is also specific to AR-expressing cells. Therefore, it would be interesting to assess this complex regulation between ROS, androgen levels, and AR activity. Nonetheless, our focus in this study is directed towards exploring the resistance mechanisms underlying the targeting of abiraterone-induced ROS.

2.3. ABIRATERONE-INDUCED ROS: MECHANISMS OF RESISTANCE

In order to complete the information concerning the influence of Duox2 on ROS levels, we confirmed that the levels of released H_2O_2 in NPp53 cells did not decline after Duox2 abrogation. We hypothesize that NOX4, another NOX enzyme that produces H_2O_2 , may play a role in sustaining H_2O_2 levels in situations when Duox function is hindered. Consequently, it is plausible that the effect of Duox2 on regulating abiraterone response is not dependent on the H_2O_2 production sustained by this enzymatic complex.

There are evidence pointing that Duox2 has the ability to regulate other signaling pathways by interacting with other proteins. For example, DUOX2 modulates the stability of ribosomal protein L3 (RPL3) by affecting its ubiquitination status. Moreover, overexpression of RPL3 can reverse the invasion and migration ability induced by DUOX2 [209]. The study showed that in colorectal tumor samples, DUOX2 is significantly more expressed and

interacts with RPL3 to enhance the invasion and metastasis capability of colorectal cancer cells [209].

As previously noted, although targeting Duox2 or other NOX members may appear to be an attractive therapeutic approach based on our observations, there are several concerns associated with directly targeting ROS metabolism. Furthermore, notwithstanding the considerable efforts made by researchers, few NOXs inhibitors have yet progressed to clinical trials. The identification of molecules that selectively target specific NOX enzymes with a significant impact in cancer is still challenging. Furthermore, most NOX functional domains lack of high-resolution crystal structures, which complicates the development of potent and selective inhibitors [379]. Consequently, the use of this type of compounds for preclinical validation could be difficulted by these limitations.

Consequently, we proceeded to investigate the effects of abiraterone-induced ROS on relevant signaling pathways, with the aim of identifying downstream mechanisms that could be targeted effectively. To this end, we conducted an RNA-seq analysis on NPp53 cells to obtain a comprehensive understanding of how abiraterone and Duox2 knock-down impact the regulation of key gene regulatory programs associated with cancer (hallmarks).

We have identified several of these that were upregulated or downregulated after abiraterone treatment or Duox2 inhibition. As expected, the "androgen response" pathway was found to be upregulated only in untreated NPp53 cells. However, this upregulation was no longer observed upon antiandrogen therapy or Duox2 knock-down. Notably, the combination of abiraterone and Duox2 knock-down led to a substantial downregulation of the "androgen response" pathway. These findings suggest that Duox2 plays a role in regulating AR activity, which is in agreement with our earlier experiments concerning abiraterone sensitivity in this context.

Furthermore, we have observed that several oncogenic pathways associated with CRPC were found strongly downregulated in the combination of abiraterone with Duox2 silencing, most of them were already suggested to play a role in abiraterone response from the CRISPR screening, which included MYC, cell-cycle regulation and E2F targets.

However, our preferred scenario involves identifying a molecular signaling pathway that is induced in response to abiraterone, but not in combination with Duox2 KD. By targeting and inhibiting this molecular pathway, we aim to improve the response to abiraterone. The hypoxia pathway appears to be less active in untreated NPp53 cells. However, when treated with abiraterone, this pathway becomes upregulated, leading to a condition known as pseudohypoxia. Hypoxia-associated phenotypes are often observed in cancer in even in normoxia conditions with normal oxygen levels [380]. Interestingly, when Duox2 KD cells are treated with abiraterone, there is no activation of the hypoxia signaling pathway. This suggests that the induction of this pathway is regulated by the ROS metabolism. Therefore, we propose that pseudohypoxia may be a mechanism triggered by abiraterone, and its inhibition may increase the effectiveness of therapy.

3. PSEUDOHYPOXIA IN PROSTATE CANCER

3.1. HIF- 1α AND PSEUDOHYPOXIA RESPONSE TO ABIRATERONE

In the context of PCa, tumor hypoxia has been suggested as a predictive factor for local recurrence and early biochemical relapse following radiotherapy [282]. As previously explained, tumor hypoxia is a key player involved in treatment resistance, including PCa [381]. Early studies suggested that hypoxia was responsible for increased VEGF production and epithelial cell apoptosis following surgical castration in animal models [382, 383]. These findings suggest that recurrent PCa cells must survive an acute transient hypoxia in order to expand clonally. Therefore, in light of our observations on the effect of abiraterone in activating the hypoxia-signaling, it is important to assess the role of hypoxia in AR regulation.

As a brief summary, the adaptation of cells to survive and proliferate in low oxygen levels (hypoxia) is mediated by hypoxia-inducible factors HIF-1 α and HIF-2 α [251]. These oxygen-labile factors are heterodimeric proteins whose activity is regulated through post-translational modification and stabilization. Specifically, the stability of HIF-1 α is controlled by its oxygen-dependent degradation domain via hydroxylation of proline residues 402 and 564 by prolyl hydroxylase domain proteins (PHDs). When subjected to hypoxic conditions,

HIFs proteins are no longer ubiquitinated for proteasome degradations, thus they can regulate the expression of the HIF-regulated genes upon nucleus translocation [255].

Nevertheless, in pseudohypoxia, the stabilization of HIF-1α and the subsequent activation of hypoxia-related signaling occurs under normoxia conditions [380]. Several chemical or biological molecules have been reported to induce pseudohypoxia, as we observed for abiraterone based on the results from RNA-seq. These compounds are known as hypoxia mimetic agents (HMAs) [384], and they predominantly function by targeting PHD. Iron chelates (like desferrioxamine (DFO) [385]) and analogues of 2-oxoglutarate (2-OG) [386], which is another PHDs substrate besides oxygen [384], are among the most commonly employed HMAs for this purpose. However, cobalt chloride (CoCl₂) remains the most extensively utilized HMA for research purpose [387, 388].

We showed that in our NPp53 model, HIF- 1α accumulation is induced chemically in a dose-dependent manner by CoCl₂. Additionally, Duox2 knocked-down cells showed a decreased accumulation of HIF- 1α compared to control cells, thus demonstrating that Duox2 could regulate hypoxia signaling activation. Therefore, reduced levels of Duox2 are associated with a decrease in the cellular capacity to induce pseudohypoxia.

More interestingly, we have demonstrated that abiraterone induced hypoxia-signaling activation via HIF- 1α stabilization. Our NPp53 cells treated with abiraterone exhibited a dose-dependent accumulation of HIF- 1α . Furthermore, this accumulation notably reduced when abiraterone was combined with NAC as an antioxidant agent. Consequently, we have confirmed that the pseudohypoxia state induced by abiraterone is mediated by abiraterone-induced ROS.

Moreover, partial alleviation of abiraterone-induced pseudohypoxia was observed with Duox2 KD, as evidenced by decreased accumulation of HIF-1 α under this condition. This may account for the increased sensitivity of Duox2 KD cells to abiraterone treatment, as these cells are unable to activate pseudohypoxia signaling, a process that is linked to molecular mechanisms supporting survival, growth, and metastasis, among others.

Previous reports have indicated that hypoxic treatment results in increased AR-transcriptional activity (as determined using a transcriptional reporter) in LNCaP AR-responsive cells, which could contribute to treatment resistance and the development of CRPC [389]. In fact, the introduction of AR into DU145 AR-negative cells led to hypoxia-enhanced AR function [389]. Therefore, it is possible that the activation of AR-transcriptional activity induced by hypoxia signaling is mediating the resistance associated with abiraterone treatment in NPp53, as we have demonstrated that this treatment also stabilizes HIF- 1α .

In addition, the cultivation of AR-responsive LNCaP cells under conditions of chronic hypoxia has been shown to promote the selection of androgen-independent PCa cells that possess a survival advantage and are more likely to produce invasion and metastasis [390]. This observation further underscores the notion that hypoxia is closely associated with the development of CRPC and suggests that it may be a promising target for therapeutic strategies in advanced stages of PCa.

Furthermore, androgen stimulation has been shown to upregulate HIF-1α expression, thus driving VEGF expression in LNCaP AR-responsive cells, but not in PC3 AR-negative cells [391]. This induction was blocked by flutamide treatment (AR-antagonist) [391]. However, the observation that both androgens and abiraterone could activate pseudohypoxia reinforces the idea previously discussed regarding the effect of both factors in ROS generation. It is possible that both treatments produce a similar effect via distinct mechanisms, and the context and experimental conditions in which they are performed are crucial for assessing this interplay. Notably, the aforementioned study used LNCaP cells instead of AR-positive CRPC cells, which may have different mechanisms for modulating hypoxia.

To date, the molecular mechanisms that underlie the development of insensitivity and resistance to antiandrogen therapy in response to hypoxia are not fully understood. Previous studies have been demonstrated that chronically treating AR-responsive cells (LNCaP and LAPC4) with multiple rounds of ADT (by androgen depleted media) in hypoxic conditions can induce enzalutamide resistance [392]. Therefore, there is a selection of cells capable to display AR independence and therapy resistance under hypoxia. This finding

reinforces the idea that hypoxia signaling can be activated as a resistance mechanism against antiandrogens. Mechanistically, we hypothesized that Duox2 mediates this mechanism via pseudohypoxia, given as its inhibition has been shown to reduce the accumulation of HIF- 1α induced by abiraterone under normoxic conditions.

3.2. HYPOXIA-ASSOCIATED GENES AND RESPONSE

To corroborate prior findings, we quantified the expression levels of HIF-1 α and certain transcriptional targets using qPCR. Our observations indicated that treatment with abiraterone and enzalutamide did not alter the levels of HIF-1 α expression. However, antiandrogen treatment resulted in an increase in the expression of HIF-1 α transcriptional targets. Hence, we substantiated that the abiraterone-induced pseudohypoxia activation observed in the RNA-seq data is not a result of direct modulation of HIF-1 α expression, but rather a consequence of protein stabilization.

Furthermore, abiraterone treatment also increased the expression of NRF2, which plays a role activating the cellular antioxidant defense to overcome oxidative stress [221]. The development of PCa is frequently accompanied by a decline in Nrf2 activity, leading to a disruption in cell defense mechanisms, which is associated with inflammation [393]. This reduction in Nrf2 activity could potentially stimulate the activation of the inflammation-promoting transcription factor NF-κB. Nonetheless, it is important to note that Nrf2 activation can also contribute to the survival of cancer cells and the development of acquired chemoresistance [394], which aligns with our findings concerning the elevated expression of NRF2 due to abiraterone treatment. Therefore, the interplay between Nrf2 and NF-κB plays a critical role in integrating oxidative stress and inflammation processes [222]. NF-κB exerts control over the expression of genes involved in several key processes, including cytokines, proinflammatory enzymes, cyclins, antiapoptotic proteins, as well as antioxidant and prooxidant genes [395].

Therefore, while NRF2 has been described to activate the HIF signaling [396], the detailed picture of this crosstalk remains elusive and is context dependent. Furthermore,

NF-κB pathway, which were found to be downregulated by also is involved in this regulatory network [397].

At his point, we have demonstrated that the induction of ROS by abiraterone can activate hypoxia signaling. However, there is evidence to suggest that hypoxia can also induce ROS, which are involved in a specific redox regulation of processes such as cell migration due to EMT activation [398]. The mechanism by which hypoxia increases ROS is still a matter of debate [168], and it may depend on the tissue type or represent a normal physiological response to oxygen supply imbalance or environmental stress [399]. It appears that hypoxia can induce an increase in ROS by acting on complexes I, II and III of on the mitochondria electron transport chain (ETC) [168, 271, 400], and inhibiting these complexes results in decreased ROS accumulation. Interestingly, mtDNA mutations have been shown to upregulate intracellular ROS levels, and lead to the development of malignancies [401], which is consistent with observations in which increased oxidative cellular damage accompanied by declining testosterone levels was associated with prostate malignancy [310, 402].

Moreover, it has been observed in isolated pulmonary artery myocytes that the expression of catalase or glutathione peroxidase-1 completely reversed the increase ROS induced [271], thus indicating that such ROS are mainly H_2O_2 . Consequently, these ROS would leave the mitochondria causing HIF- 1α stabilization. Hypoxia has also been demonstrated to cause chromosomal abnormalities in endothelial cells by inducing ROS and increasing the signaling of VEGF in the tumor microenvironment [400]. Finally, it has been reported that mitochondrial ROS are necessary for the induction of hypoxia signaling via HIF- 1α in primary human lung fibroblasts [311].

Therefore, the regulation between ROS and hypoxia is very complex and it is difficult to determine precisely in which direction one regulates the other. It seems that this bidirectional regulation is context and cell type dependent. Moreover, it has been suggested that the aerobic glycolysis promoted by HIF-1 α increases its transcriptional activity, resulting in the formation of a glycolysis-HIF-1 α feed-forward mechanism in hypoxic cancer cells that facilitates tumor growth [270].

In fact, the genes regulated by HIF- 1α activity are involved in various signaling pathways that promote tumor progression and metastasis, including neoangiongenesis, stem cell renewal, and drug resistance. It is firmly stablished that HIF- 1α activation is linked to a metabolic swift from mitochondrial respiration to increased glycolysis to maintain ATP levels [403]. This change is facilitated by the activation of glycolytic genes regulated by the HIF- 1α transcriptional activity, such as GLUT1, LDHA and PDK1. Hypoxic conditions elicit stress responses, and cancer cells overcome these unfavorable conditions by consuming glucose using a less efficient anaerobic glycolysis that does not require oxygen [404].

As a result, the activation of the HIF- 1α transcriptional program hinders the tricarboxylic acid (TCA) cycle (OXPHOS metabolism) by activating glycolysis [255, 268], while also regulating the transcription of genes involved in mitochondrial electron transport chain (ETC) activity. This leads to the utilization of aerobic respiration, which enables more efficient energy production in hypoxic conditions and protects cells from increased ROS production [269].

It is noteworthy that the functional analysis conducted during the initial synthetic lethal CRISPRi screening revealed that "oxidative phosphorylation" was one of the hallmark pathways enriched among the hit sgRNAs. Therefore, this process could be implicated in the response to abiraterone, given that sgRNAs targeting the genes involved in this pathway were significantly depleted as a result of abiraterone treatment. Furthermore, the functional analysis also showed that the hallmark category with the highest enrichment was associated with Myc targets. Interestingly, hypoxia and HIFs can also modify tumor metabolism by cooperating with proto-oncogenes, such as MYC, which are involved in cell proliferation and tumor progression [255].

HIF- 1α and HIF- 2α exhibit differential roles on Myc activity. While HIF- 1α inhibits MYC activity under hypoxia, HIF- 2α has the opposite effect [405]. However, MYC overexpression stabilizes HIF- 1α , resulting in increased accumulation of HIF- 1α and suggesting a complex interplay between the two transcription factors [406]. In fact Myc can cooperate with HIF- 1α to enhance PDK1 expression, leading to the promotion of glycolysis over oxidative phosphorylation [267]. Consequently, in cancer cells with elevated MYC

levels, the collaboration between MYC and HIFs induces a metabolic shift, tumor angiogenesis, and CSC renewal, ultimately promoting tumor cell growth and progression [407].

Given the considerations regarding 1) the involvement of hypoxia signaling in the regulation of glycolysis and oxidative phosphorylation pathways, 2) the intricate interplay between hypoxia and ROS, and 3) the findings from the CRISPRi screening highlighting the involvement of oxidative phosphorylation and Myc targets, we aimed to investigate the impact of the activation of hypoxia signaling induced by abiraterone on metabolic regulation, to shed light on our previous results.

3.3. ABIRATERONE-INDUCED METABOLIC CHANGES

As above mentioned, our focus shifted towards characterizing the metabolic alterations in our NPp53 model upon abiraterone treatment. This was done to determine the roles of oxidative phosphorylation and glycolysis in these changes. Moreover, real-time metabolic assays provided specific parameters to evaluate mitochondrial function.

Our observations indicated that cells treated with abiraterone exhibit a robust metabolic switch from oxidative phosphorylation to glycolysis. The ATP produced by mitochondrial respiration was dose-dependently reduced by abiraterone, while the glycolytic ATP demonstrated an increase following treatment. This activation of glycolysis partially compensated total ATP levels that were compromised due to abiraterone. Based on the various respiration parameters, we concluded that abiraterone treatment significantly impaired mitochondrial function, including basal and maximal respiration. However, non-mitochondrial oxygen consumption remained unaffected by abiraterone treatment, thus demonstrating that this effect is specific for mitochondrial respiration. Interestingly, peroxisomal respiration has been reported to contribute to approximately 20% of total oxygen consumption, and peroxisomal oxidases can produce up to 35% of total H_2O_2 in certain mammalian cells [408].

In addition, it was observed that the spare respiration capacity (SRC) diminishes upon abiraterone treatment. This parameter measures the cells' capacity have to generate an additional amount of ATP in response to a sudden energy demand. Notably, Duox2 KD was also associated with a significant reduction of this parameter, comparable with the effect of abiraterone. Therefore, Duox2 appears to be linked to the cells' ability to meet extra energy requirements.

Over progression, cancer cells then to increase their SRC levels, which has been proposed as a mechanism for drug resistance in cancer cells, promoting cell survival through a metabolic switch in favor of oxidative phosphorylation (OXPHOS) metabolism. [409]. Variations in SRC levels in cancer cells are often observed following treatment with anticancer drugs, partly mediated by induced oxidative stress Thus, a reduction in SRC levels may be correlated with the efficacy of these anticancer drugs [410], primarily due to the decreased maximal respiration rate [411]. Elevated SRC levels have also been linked to chemotherapy [412] or DNA-damaging agent resistance [409]. Additionally, high SRC levels are a characteristic feature of cancer cells that are resistant to targeted agents as tyrosine kinase [413] or BRAF/MEK inhibitors [414] compared with their sensitive counterparts.

The observation that Duox2 KD cells exhibit lower SRC than control cells may be related with to their heightened sensitivity to Abiraterone treatment. Thus, one possible mechanism through which Duox2 modulates resistance to Abiraterone may involve regulation of the OXPHOS metabolism, specifically through SRC. This way, cells threatened with abiraterone treatment require an immediate source of additional ATP that it is compromised due to Duox2 KD. However, a mechanism employed by these cells to overcome the reduction in SRC is the activation of glycolysis, as previously demonstrated.

Taking into account these considerations, we propose that the observed metabolic changes in our NPp53 cells are attributable to the activation of hypoxia signaling induced by abiraterone and mediated by ROS. Consequently, co-targeting the glycolytic pathway together with abiraterone emerges as a promising combinational therapy to increase cancer treatment efficacy.

Notwithstanding efforts to target the glycolytic pathway for therapy, its translation to clinical practice has yet to materialize and consolidate. This is primarily attributed to the ubiquitous presence of enzymes involved in glucose metabolism, which results in a systemic toxicity upon administering glycolysis inhibitors [415]. Although there have been solid advances in imaging technology for targeted tumor delivery [416, 417], such approaches have only been effective by treating in treating localized disease, and not metastatic cancers.

Hence, there is a need to develop more potent and specific inhibitors of glycolysis to target tumor glycolysis, which is a characteristic feature of most cancer cell types. It has been observed that tumor glycolysis is associated with chemoresistance in cancer cells, and therefore, glycolytic inhibitors have been suggested as a combinatory therapy to overcome drug resistance by re-sensitizing cancer cells [415]. This approach has led to improved efficacy when used in conjunction with chemotherapeutic agents or radiation therapy along with 2-deoxyglucose (2DG), a Hexokinase 2 (HK2) inhibitor [418, 419], which also was reported to boost the antitumor immune response, thus opening new opportunities for immunotherapy [420]. Similarly, combining chemotherapy with 3-bromopyruvate (3-BrPA), has also resulted in improved efficacy [421].

An aberrant increment in glycolysis due to upregulation of related enzymes has been described as an early metabolic alteration in PCa [392, 422]. Moreover, the inhibition of glycolysis by GLUT1 knock-down results in growth inhibition of tumors derived from the 22Rv1 cells [423]. Interestingly, GLUT1 was also identified as an AR target that contributes to tumor growth and glycolysis in CRPC and enzalutamide-resistant PCa. It has been previously mentioned that chronic ADT of AR-responsive cells in hypoxia can induce enzalutamide resistance [392]. Specifically, after AR inhibition, glucose flux is redirected from the androgen/AR-dependent pentose phosphate pathway to the hypoxia-induced glycolysis pathway, thus reducing the growth inhibitory effect of enzalutamide [392]. Therefore, this reinforces the potential benefit of targeting glycolysis to overcome antiandrogen resistance.

However, a few inhibitors that directly target the glycolytic pathway have been efficiently tested in PCa, since improvement through more selective effects of this type of

drugs is still challenging [424]. other drugs have been shown to indirectly impact glycolysis by targeting upstream signaling pathways, as we suggest with the case of abiraterone.

For example, SU086 is a small molecule that binds and decrease heat shock protein 90 (HSP90) levels, ultimately affecting glycolysis [425]. This intervention resulted in the inhibition of PCa cell and tumor growth *in vitro* an *in vivo*, displaying an enhanced effect when combined with abiraterone or enzalutamide [425].

Morevoer, combination of PX-478 as a HIF-1 α inhibitor with dichloroacetate (a pyruvate dehydrogenase kinase inhibitor, PDKi) demonstrated robust synergistic effects in all 8 cancer cell line tested, including colorectal, lung, breast, cervical, liver and brain cancer [426], but not including PCa among the tested cell lines.

Thus, we suggest that co-targeting HIF- 1α with antiandrogens represents a viable strategy to counteract the induced hypoxia-signaling activation mediated by ROS, and which is linked to metabolic changes that may facilitate tumor progression. This approach could circumvent the potential side effects associated by directly targeting ROS metabolism or the glycolytic pathway, both of which operate ubiquitously, necessitating efforts to enhance the efficacy and specificity of drugs targeting such processes.

3.4. CO-TARGETING PSEUDOHYPOXIA WITH ANTIANDROGENS

Remarkably, studies have shown that hypoxia induces neuroendocrine plasticity, resulting in higher hypoxia levels in NEPC compared to prostate adenocarcinomas [427]. Furthermore, as we have suggested based in our findings that advanced CRPC patients exhibit higher levels of Duox genes, whose expression correlates with distinct ROS signatures, we postulate that this increase in ROS could mediate the pseudohypoxia activation. This finding may seem to contradict the earlier observation that hypoxic treatment can increase AR-transcriptional activity [389]. However, it is important to note that CRPC initially relies on mechanisms that reactivate AR transcriptional activity to sustain growth and resistance to ADT. Nonetheless, over time, CRPC patients may develop new mechanisms of drug resistance to antiandrogens, which could lead to complete AR independence, and in some cases, the progression to NEPC.

More interestingly, pharmacologically targeting hypoxia using a hypoxia-activated prodrug, TH-302, resulted in a potent reduction in NEPC tumor growth, highlighting the potential of hypoxia-directed therapy for NEPC patients [427]. Moreover, TH-302 was shown to restore T cell infiltration and sensitize PCa to immunotherapy based on checkpoint inhibitors in transgenic mice by reducing tumor hypoxia [428]. Hence, combining hypoxia-directed therapy with abiraterone may prove to be a promising approach to enhance therapeutic response, as several drugs targeting this pathway have been successfully employed to treat cancer cells [429-431].

We employed the compound PX-478 to target hypoxia signaling trough the inhibition of HIF-1α. Inhibitor. It has been demonstrated to be effective in both normoxia and hypoxia conditions, with demonstrated antitumoral properties [430]. In addition, the antitumor efficacy of this drug was studied in a phase I clinical trial (NCT00522652) involving patients with advanced solid tumors or lymphoma. In that study, PX-478 was well tolerated and associated with prolonged stable disease in patients.

PX-478 elicited cytotoxic effects on PC3 and DU145 AR-negative cell lines, with enhanced toxicity observed under hypoxic conditions in the latter [432]. Additionally, PX-478 augmented the radiosensitivity of normoxic and hypoxic PC3 cells, but displayed diminished efficacy in inhibiting HIF-1 α and enhancing radiosensitivity in DU145 cells relative to PC3 cells. Nevertheless, given our prior observations, it would be valuable to investigate the impact of this compound on AR-positive cells.

Our findings revealed a synergistic interaction between abiraterone and PX-478 in NPp53 cells, consistent with the results obtained from RNA-seq analysis. The activation of hypoxia signaling induced abiraterone treatment can be averted through the addition of a HIF-1 α inhibitor, thereby reinstating sensitivity in PCa cells and enhancing treatment efficacy.

Moreover, a comparable synergistic effect between antiandrogen therapy and HIF- 1α inhibition was observed in the 22Rv1 cell line. In fact, we found a robust synergistic effect between enzalutamide and PX-478 in both NPp53 and 22Rv1 cells. Conversely, LNCaP cells

displayed substantial resistance to HIF- 1α inhibition, as evidenced by their high IC50 values relative to the other tested cell lines. Neither abiraterone nor enzalutamide demonstrated any synergistic interaction with PX-478 in LNCaP cells. It is worth noting that the cell line that exhibited the greater response to abiraterone in terms of abiraterone-induced ROS and AR dependency is also with a higher resistance to pesudohypoxia inhibition.

Furthermore, HIF-1 α overexpression in LNCaP cells were reported to result in enhanced proliferation and increased resistance to ADT (by androgen depletion of the media), and also accelerated tumor growth in non-castrated and castrated mice [433]. In this study cited, it was observed that hypoxia decreased AR binding sites, while HIF binding sites increased upon androgen treatment in hypoxic conditions [433].

As a result, we propose this drug combination that targets both AR and hypoxia signaling pathways as a means of enhancing therapeutic approaches in CRPC. While various combinations of PX-478 with other molecules have been suggested for this objective, none have been tested within a PCa model [365].

Thus, we proceeded to demonstrate *in vivo* the effectiveness of the combination of antiandrogens and pseudohypoxia inhibition by employing immunodeficient mice for this purpose. Specifically, these mice were orthotopically injected in the prostate with 22Rv1 cells, given the noteworthy CRPC characteristic of these cells and the consistent previously validated *in vitro* synergy. Tumor growth was assessed utilizing a luminescent reporter, while monitoring the survival rates associated with each treatment, both individually and in combination. Our observations indicate that the combination of enzalutamide with PX-478 resulted in a notable and significant improved response, in terms of tumor growth and survival, whit no discernible difference between the efficacy of individual treatments and the control group.

Hence, the strategy of co-targeting both AR signaling by antiandrogens and hypoxia signaling by HIF- 1α inhibition represents a promising approach to improve preclinical outcomes in the context of CRPC. This approach has the potential to be exploited and refined in order to apply a translational approach to patients.

Moreover, a hypoxia signature exhibits a strong and independent prognostic value for PCa patients, given that hypoxia is associated with a poor prognosis in PCa [434]. Consequently, there has been a proposal to employ combinatory methods of characterizing genomic instability and hypoxia in patients with localized PCa, which yields more prognostic information than classical methods of PCa stratification such as Gleason score or PSA alone [146, 435, 436].

In addition, increased expression VEGF, HIF-1 α and GLUT1 have been shown to identify patients at high risk of biochemical failure [437], while a more recent meta-analysis has also suggested a negative prognostic role of HIF-2 α for metastasis-free survival[438]. Therefore, hypoxia have an remarked impact on the progression of prostate cancer, promoting invasion and migration properties, and facilitating androgen independence, leading to NEPC [435] (**Figure 41**).

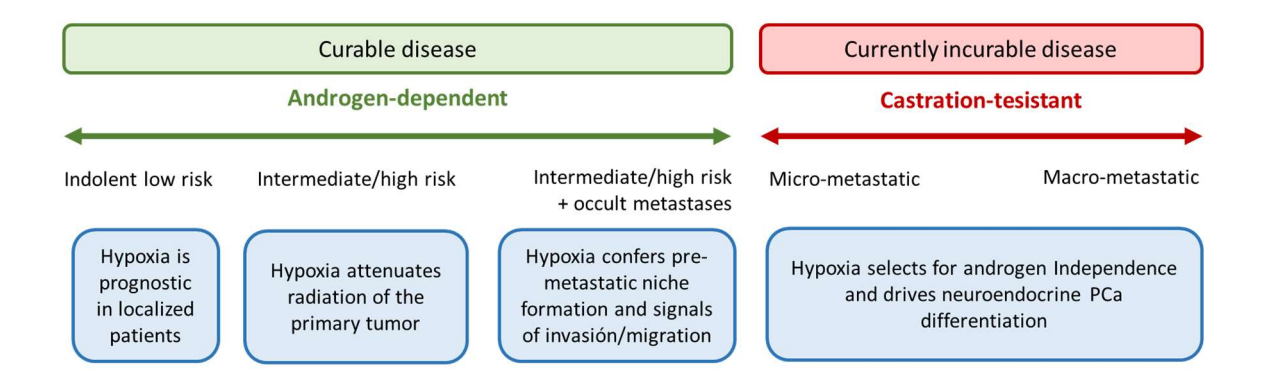


Figure 41. **Role of hypoxia in the clinical course of PCa**. Adapted from Ashton, J., & Bristow, R. (2020).

CONCLUSIONS

- 1. The CRISPRi system is a highly effective and adaptable method for inhibiting gene expression, which can be utilized for synthetic lethal screening in conjunction with antiandrogens or other antineoplastic drugs. By conducting such screening in PCa cells that have been treated with abiraterone, we were able to identify genes that are involved in the acquisition of resistance to antiandrogens.
- 2. The functional analysis of sgRNA hits from the screening revealed a focus on genes that participate in key cancer-related processes, like cell cycle, oxidative phosphorylation, and Myc activity. Notably, members of the NAPDH oxidase family, involved in ROS metabolism, were among the hits identified in this screening, remarkably *Duox2*.
- 3. In a dataset of advanced CRPC patients, the expression levels of *Duox* genes were negatively correlated with AR activity, but positively correlated with a signature of genes involved in ROS response. Furthermore, patients with high *Duox2* levels and high neuroendocrine score, which recapitulates AR indifference and resistance to antiandrogens, exhibited the lowest probability of survival.
- 4. As a mechanism, we demonstrated that abiraterone treatment leads to ROS generation, which can be prevented by Duox2 knock-down. The abrogation of *Duox2* sensitizes PCa cells to antiandrogens, which also was observed by the pharmacological inhibition of the NAPDH oxidase family, thus demonstrating a synergistic effect between both drugs and the role of this family and the ROS metabolism modulating antiandrogen response.
- 5. From the RNA-seq data obtained from our NPp53 model, we shown that abiraterone treatment induces hypoxia signaling as a resistance mechanism in normoxia conditions (pseudohypoxia), which can be mitigated by Duox2 KD silencing. Our findings reveal that this pseudohypoxia state is mediated by HIF-1 α stabilization, which is induced by abiraterone-induced ROS. Consequently, the HIF-1 α

accumulation is alleviated by an antioxidant treatment to or by *Duox2* abrogation to decrease ROS levels.

- 6. The impairment of mitochondrial function is a marked consequence of abiraterone treatment. As a result, PCa cells undergo a metabolic shift from oxidative phosphorylation to glycolysis to maintain ATP production in response to abiraterone. This change is the result of the ROS-induced activation of HIF-1 α transcriptional program to promote cell survival and proliferation.
- 7. The synergistic effect observed between antiandrogens and PX-476, a HIF-1 α inhibitor, in our CRPC cell lines could be exploited as a drug combination to enhance treatment efficacy. We have confirmed this synergy *in vivo* by conducting experiments in orthotopically-grafted mice. While single treatments resulted ineffective, the combination leads to a significant decrease in tumor growth and improved overall survival rates compared to single treatments and vehicle condition.

REFERENCES

- 1. Lee, C.H., O. Akin-Olugbade, and A. Kirschenbaum, *Overview of prostate anatomy, histology, and pathology.* Endocrinol Metab Clin North Am, 2011. **40**(3): p. 565-75, viii-ix.
- 2. McNeal, J.E., *Normal histology of the prostate*. Am J Surg Pathol, 1988. **12**(8): p. 619-33.
- 3. Haffner, J., et al., *Peripheral zone prostate cancers: location and intraprostatic patterns of spread at histopathology.* Prostate, 2009. **69**(3): p. 276-82.
- 4. Toivanen, R. and M.M. Shen, *Prostate organogenesis: tissue induction, hormonal regulation and cell type specification.* Development (Cambridge, England), 2017. **144**(8): p. 1382-1398.
- 5. McNeal, J.E., *The zonal anatomy of the prostate.* Prostate, 1981. **2**(1): p. 35-49.
- 6. Marker, P.C., et al., *Hormonal, cellular, and molecular control of prostatic development.* Dev Biol, 2003. **253**(2): p. 165-74.
- 7. Aaron, L., O.E. Franco, and S.W. Hayward, *Review of Prostate Anatomy and Embryology and the Etiology of Benign Prostatic Hyperplasia*. Urol Clin North Am, 2016. **43**(3): p. 279-88.
- 8. Kourambas, J., et al., A histological study of Denonvilliers' fascia and its relationship to the neurovascular bundle. Br J Urol, 1998. **82**(3): p. 408-10.
- 9. Walsh, P.C. and P.J. Donker, *Impotence Following Radical Prostatectomy: Insight into Etiology and Prevention.* J Urol, 2017. **197**(2s): p. S165-s170.
- 10. Cunha, G.R., et al., *The endocrinology and developmental biology of the prostate.* Endocr Rev, 1987. **8**(3): p. 338-62.
- 11. Oliveira, D.S., et al., *The mouse prostate: a basic anatomical and histological guideline*. Bosn J Basic Med Sci, 2016. **16**(1): p. 8-13.
- 12. Shen, M.M. and C. Abate-Shen, *Molecular genetics of prostate cancer: new prospects for old challenges.* Genes & development, 2010. **24**(18): p. 1967-2000.
- 13. Sasaki, T., O.E. Franco, and S.W. Hayward, *Prostate—Overview*, in *Encyclopedia of Reproduction (Second Edition)*, M.K. Skinner, Editor. 2018, Academic Press: Oxford. p. 309-314.
- 14. Shappell, S.B., et al., Prostate pathology of genetically engineered mice: definitions and classification. The consensus report from the Bar Harbor meeting of the Mouse Models of Human Cancer Consortium Prostate Pathology Committee. Cancer Res, 2004. **64**(6): p. 2270-305.
- 15. Berquin, I.M., et al., *Expression signature of the mouse prostate*. J Biol Chem, 2005. **280**(43): p. 36442-51.
- 16. Crowley, L., et al., A single-cell atlas of the mouse and human prostate reveals heterogeneity and conservation of epithelial progenitors. 2020: p. 2020.05.29.123836.
- 17. Suwa, T., et al., Spontaneous lesions in control B6C3F1 mice and recommended sectioning of male accessory sex organs. Toxicol Pathol, 2002. **30**(2): p. 228-34.
- 18. Barron, D.A. and D.R. Rowley, *The reactive stroma microenvironment and prostate cancer progression*. Endocrine-related cancer, 2012. **19**(6): p. R187-R204.
- 19. Wang, G., et al., *Genetics and biology of prostate cancer*. Genes & development, 2018. **32**(17-18): p. 1105-1140.

- 20. Verhagen, A.P., et al., Differential expression of keratins in the basal and luminal compartments of rat prostatic epithelium during degeneration and regeneration. Prostate, 1988. **13**(1): p. 25-38.
- 21. Verhagen, A.P., et al., *Colocalization of basal and luminal cell-type cytokeratins in human prostate cancer*. Cancer Res, 1992. **52**(22): p. 6182-7.
- 22. Hayward, S.W., et al., *Malignant transformation in a nontumorigenic human prostatic epithelial cell line.* Cancer Res, 2001. **61**(22): p. 8135-42.
- 23. Mirosevich, J., et al., *Androgen receptor expression of proliferating basal and luminal cells in adult murine ventral prostate.* J Endocrinol, 1999. **162**(3): p. 341-50.
- 24. Abrahamsson, P.A., *Neuroendocrine cells in tumour growth of the prostate.* Endocr Relat Cancer, 1999. **6**(4): p. 503-19.
- 25. Hayward, S.W., et al., Stromal development in the ventral prostate, anterior prostate and seminal vesicle of the rat. Acta Anat (Basel), 1996. **155**(2): p. 94-103.
- 26. Shafi, A.A., A.E. Yen, and N.L. Weigel, *Androgen receptors in hormone-dependent and castration-resistant prostate cancer.* Pharmacology & Therapeutics, 2013. **140**(3): p. 223-238.
- 27. Azeem, W., et al., An androgen response element driven reporter assay for the detection of androgen receptor activity in prostate cells. PLoS One, 2017. **12**(6): p. e0177861.
- 28. Ehsani, M., F.O. David, and A. Baniahmad, *Androgen Receptor-Dependent Mechanisms Mediating Drug Resistance in Prostate Cancer*. Cancers (Basel), 2021. **13**(7).
- 29. Nadal, M., et al., *Structure of the homodimeric androgen receptor ligand-binding domain.* Nature Communications, 2017. **8**(1): p. 14388.
- 30. Alegre-Martí, A., et al., A hotspot for posttranslational modifications on the androgen receptor dimer interface drives pathology and anti-androgen resistance. 2023. **9**(11): p. eade2175.
- 31. Gottlieb, B., et al., *The androgen receptor gene mutations database: 2012 update.* Hum Mutat, 2012. **33**(5): p. 887-94.
- 32. Heemers, H.V. and D.J. Tindall, Androgen receptor (AR) coregulators: a diversity of functions converging on and regulating the AR transcriptional complex. Endocr Rev, 2007. **28**(7): p. 778-808.
- 33. Koochekpour, S., *Androgen receptor signaling and mutations in prostate cancer.* Asian J Androl, 2010. **12**(5): p. 639-57.
- 34. Heinlein, C.A. and C. Chang, *Androgen receptor (AR) coregulators: an overview.* Endocr Rev, 2002. **23**(2): p. 175-200.
- 35. Schatten, H., Brief Overview of Prostate Cancer Statistics, Grading, Diagnosis and Treatment Strategies, in Cell & Molecular Biology of Prostate Cancer: Updates, Insights and New Frontiers, H. Schatten, Editor. 2018, Springer International Publishing: Cham. p. 1-14.
- 36. Jemal, A., et al., *Global patterns of cancer incidence and mortality rates and trends.* Cancer Epidemiol Biomarkers Prev, 2010. **19**(8): p. 1893-907.
- 37. Ferlay, J., et al., *Estimates of worldwide burden of cancer in 2008: GLOBOCAN 2008.* Int J Cancer, 2010. **127**(12): p. 2893-917.
- 38. Torre, L.A., et al., *Global cancer statistics*, *2012*. CA Cancer J Clin, 2015. **65**(2): p. 87-108.

- 39. Bostwick, D.G., et al., Independent origin of multiple foci of prostatic intraepithelial neoplasia: comparison with matched foci of prostate carcinoma. Cancer, 1998. **83**(9): p. 1995-2002.
- 40. Aihara, M., et al., *Heterogeneity of prostate cancer in radical prostatectomy specimens*. Urology, 1994. **43**(1): p. 60-6; discussion 66-7.
- 41. Macintosh, C.A., et al., *Precise microdissection of human prostate cancers reveals genotypic heterogeneity.* Cancer Res, 1998. **58**(1): p. 23-8.
- 42. Sakr, W.A., et al., High grade prostatic intraepithelial neoplasia (HGPIN) and prostatic adenocarcinoma between the ages of 20-69: an autopsy study of 249 cases. In Vivo, 1994. **8**(3): p. 439-43.
- 43. Shiraishi, T., et al., *The frequency of latent prostatic carcinoma in young males: the Japanese experience.* In Vivo, 1994. **8**(3): p. 445-7.
- 44. Wang, X., et al., *A luminal epithelial stem cell that is a cell of origin for prostate cancer.* Nature, 2009. **461**(7263): p. 495-500.
- 45. Choi, N., et al., Adult murine prostate basal and luminal cells are self-sustained lineages that can both serve as targets for prostate cancer initiation. Cancer Cell, 2012. **21**(2): p. 253-65.
- 46. Wang, Z.A., et al., Lineage analysis of basal epithelial cells reveals their unexpected plasticity and supports a cell-of-origin model for prostate cancer heterogeneity. Nat Cell Biol, 2013. **15**(3): p. 274-83.
- 47. Yoo, Y.A., et al., *Bmi1 marks distinct castration-resistant luminal progenitor cells competent for prostate regeneration and tumour initiation.* Nat Commun, 2016. **7**: p. 12943.
- 48. Lawson, D.A., et al., *Isolation and functional characterization of murine prostate stem cells*. Proc Natl Acad Sci U S A, 2007. **104**(1): p. 181-6.
- 49. Goldstein, A.S., et al., *Identification of a cell of origin for human prostate cancer.* Science, 2010. **329**(5991): p. 568-71.
- 50. Lawson, D.A., et al., *Basal epithelial stem cells are efficient targets for prostate cancer initiation*. Proc Natl Acad Sci U S A, 2010. **107**(6): p. 2610-5.
- 51. Emmert-Buck, M.R., et al., *Allelic loss on chromosome 8p12-21 in microdissected prostatic intraepithelial neoplasia.* Cancer Res, 1995. **55**(14): p. 2959-62.
- 52. Haggman, M.J., et al., *Allelic loss of 8p sequences in prostatic intraepithelial neoplasia and carcinoma*. Urology, 1997. **50**(4): p. 643-7.
- 53. Bethel, C.R., et al., Decreased NKX3.1 protein expression in focal prostatic atrophy, prostatic intraepithelial neoplasia, and adenocarcinoma: association with gleason score and chromosome 8p deletion. Cancer Res, 2006. **66**(22): p. 10683-90.
- 54. Tomlins, S.A., et al., *ETS gene fusions in prostate cancer: from discovery to daily clinical practice.* Eur Urol, 2009. **56**(2): p. 275-86.
- 55. Jenkins, R.B., et al., *Detection of c-myc oncogene amplification and chromosomal anomalies in metastatic prostatic carcinoma by fluorescence in situ hybridization.* Cancer Res, 1997. **57**(3): p. 524-31.
- 56. Kumar, A., et al., Substantial interindividual and limited intraindividual genomic diversity among tumors from men with metastatic prostate cancer. Nat Med, 2016. **22**(4): p. 369-78.
- 57. Gurel, B., et al., *Nuclear MYC protein overexpression is an early alteration in human prostate carcinogenesis*. Mod Pathol, 2008. **21**(9): p. 1156-67.

- 58. Ruggero, K., et al., *Epigenetic Regulation in Prostate Cancer Progression*. Curr Mol Biol Rep, 2018. **4**(2): p. 101-115.
- 59. Pourmand, G., et al., *Role of PTEN gene in progression of prostate cancer.* Urol J, 2007. **4**(2): p. 95-100.
- 60. Verhagen, P.C., et al., *The PTEN gene in locally progressive prostate cancer is preferentially inactivated by bi-allelic gene deletion.* J Pathol, 2006. **208**(5): p. 699-707.
- 61. Sircar, K., et al., PTEN genomic deletion is associated with p-Akt and AR signalling in poorer outcome, hormone refractory prostate cancer. J Pathol, 2009. **218**(4): p. 505-13.
- 62. Taylor, B.S., et al., *Integrative genomic profiling of human prostate cancer.* Cancer Cell, 2010. **18**(1): p. 11-22.
- 63. Siegel, R., D. Naishadham, and A. Jemal, *Cancer statistics*, 2012. 2012. **62**(1): p. 10-29.
- 64. Lilja, H., D. Ulmert, and A.J. Vickers, *Prostate-specific antigen and prostate cancer:* prediction, detection and monitoring. Nat Rev Cancer, 2008. **8**(4): p. 268-78.
- 65. Catalona, W.J., et al., Measurement of prostate-specific antigen in serum as a screening test for prostate cancer. N Engl J Med, 1991. **324**(17): p. 1156-61.
- 66. Etzioni, R., et al., *The prostate cancer conundrum revisited: treatment changes and prostate cancer mortality declines.* Cancer, 2012. **118**(23): p. 5955-5963.
- 67. Draisma, G., et al., Lead time and overdiagnosis in prostate-specific antigen screening: importance of methods and context. J Natl Cancer Inst, 2009. **101**(6): p. 374-83.
- 68. Grossman, D.C., et al., Screening for Prostate Cancer: US Preventive Services Task Force Recommendation Statement. Jama, 2018. **319**(18): p. 1901-1913.
- 69. Humphrey, P.A., Gleason grading and prognostic factors in carcinoma of the prostate. Mod Pathol, 2004. **17**(3): p. 292-306.
- 70. Gleason, D.F., *Classification of prostatic carcinomas*. Cancer Chemother Rep, 1966. **50**(3): p. 125-8.
- 71. Sathianathen, N.J., et al., *Landmarks in prostate cancer*. Nature Reviews Urology, 2018. **15**(10): p. 627-642.
- 72. Sehn, J.K., *Prostate Cancer Pathology: Recent Updates and Controversies.* Missouri medicine, 2018. **115**(2): p. 151-155.
- 73. Moch, H., et al., *The 2016 WHO Classification of Tumours of the Urinary System and Male Genital Organs-Part A: Renal, Penile, and Testicular Tumours.* Eur Urol, 2016. **70**(1): p. 93-105.
- 74. Epstein, J.I., et al., The 2014 International Society of Urological Pathology (ISUP) Consensus Conference on Gleason Grading of Prostatic Carcinoma: Definition of Grading Patterns and Proposal for a New Grading System. Am J Surg Pathol, 2016. 40(2): p. 244-52.
- 75. Wymenga, L.F., et al., Routine bone scans in patients with prostate cancer related to serum prostate-specific antigen and alkaline phosphatase. BJU Int, 2001. **88**(3): p. 226-30.
- 76. Sanda, M.G., et al., Clinically Localized Prostate Cancer: AUA/ASTRO/SUO Guideline. Part I: Risk Stratification, Shared Decision Making, and Care Options. J Urol, 2018. 199(3): p. 683-690.

- 77. Ohori, M., T.M. Wheeler, and P.T. Scardino, *The New American Joint Committee on Cancer and International Union Against Cancer TNM classification of prostate cancer. Clinicopathologic correlations.* Cancer, 1994. **74**(1): p. 104-14.
- 78. Johansson, J.E., et al., *Natural history of early, localized prostate cancer.* Jama, 2004. **291**(22): p. 2713-9.
- 79. Albertsen, P.C., J.A. Hanley, and J. Fine, *20-year outcomes following conservative management of clinically localized prostate cancer.* Jama, 2005. **293**(17): p. 2095-101.
- 80. Parker, C., Active surveillance: towards a new paradigm in the management of early prostate cancer. Lancet Oncol, 2004. **5**(2): p. 101-6.
- 81. Adolfsson, J., *Watchful waiting and active surveillance: the current position.* BJU Int, 2008. **102**(1): p. 10-4.
- 82. Klotz, L., *Active surveillance for low-risk prostate cancer*. Curr Opin Urol, 2017. **27**(3): p. 225-230.
- 83. Young, H.H., The early diagnosis and radical cure of carcinoma of the prostate. Being a study of 40 cases and presentation of a radical operation which was carried out in four cases. 1905. J Urol, 2002. **168**(3): p. 914-21.
- 84. Millin, T., *Retropubic urinary surgery*. London: Livingstone 1947.
- 85. Walsh, P.C. and H. Lepor, *The role of radical prostatectomy in the management of prostatic cancer.* Cancer, 1987. **60**(3 Suppl): p. 526-37.
- 86. Saranchuk, J.W., et al., *Achieving optimal outcomes after radical prostatectomy.* J Clin Oncol, 2005. **23**(18): p. 4146-51.
- 87. Bagshaw, M.A., H.S. Kaplan, and R.H. Sagerman, *Linear Accelerator Supervoltage Radiotherapy*. 1965. **85**(1): p. 121-129.
- 88. Denham, J.W., et al., Short-term androgen deprivation and radiotherapy for locally advanced prostate cancer: results from the Trans-Tasman Radiation Oncology Group 96.01 randomised controlled trial. Lancet Oncol, 2005. **6**(11): p. 841-50.
- 89. Pilepich, M.V., et al., Androgen suppression adjuvant to definitive radiotherapy in prostate carcinoma--long-term results of phase III RTOG 85-31. Int J Radiat Oncol Biol Phys, 2005. **61**(5): p. 1285-90.
- 90. D'Amico, A.V., et al., Androgen suppression and radiation vs radiation alone for prostate cancer: a randomized trial. Jama, 2008. **299**(3): p. 289-95.
- 91. Horwitz, E.M., et al., *Ten-year follow-up of radiation therapy oncology group protocol* 92-02: a phase III trial of the duration of elective androgen deprivation in locally advanced prostate cancer. J Clin Oncol, 2008. **26**(15): p. 2497-504.
- 92. Huggins, C. and C.V. Hodges, Studies on Prostatic Cancer. I. The Effect of Castration, of Estrogen and of Androgen Injection on Serum Phosphatases in Metastatic Carcinoma of the Prostate. 1941. 1(4): p. 293-297.
- 93. Goldenberg, S.L. and N. Bruchovsky, *Use of cyproterone acetate in prostate cancer.* Urol Clin North Am, 1991. **18**(1): p. 111-22.
- 94. Labrie, F., et al., *New hormonal therapy in prostatic carcinoma: combined treatment with an LHRH agonist and an antiandrogen.* Clin Invest Med, 1982. **5**(4): p. 267-75.
- 95. Tannock, I.F., et al., *Docetaxel plus prednisone or mitoxantrone plus prednisone for advanced prostate cancer.* N Engl J Med, 2004. **351**(15): p. 1502-12.
- 96. de Bono, J.S., et al., *Prednisone plus cabazitaxel or mitoxantrone for metastatic castration-resistant prostate cancer progressing after docetaxel treatment: a randomised open-label trial.* Lancet, 2010. **376**(9747): p. 1147-54.

- 97. Titus, M.A., et al., *Testosterone and dihydrotestosterone tissue levels in recurrent prostate cancer.* Clin Cancer Res, 2005. **11**(13): p. 4653-7.
- 98. Gregory, C.W., et al., Androgen receptor expression in androgen-independent prostate cancer is associated with increased expression of androgen-regulated genes. Cancer Res, 1998. **58**(24): p. 5718-24.
- 99. Montgomery, R.B., et al., Maintenance of intratumoral androgens in metastatic prostate cancer: a mechanism for castration-resistant tumor growth. Cancer Res, 2008. **68**(11): p. 4447-54.
- 100. Gao, J., J.T. Arnold, and J.T. Isaacs, Conversion from a paracrine to an autocrine mechanism of androgen-stimulated growth during malignant transformation of prostatic epithelial cells. Cancer Res, 2001. **61**(13): p. 5038-44.
- 101. Feng, Q. and B. He, Androgen Receptor Signaling in the Development of Castration-Resistant Prostate Cancer. Frontiers in oncology, 2019. **9**: p. 858-858.
- 102. Locke, J.A., et al., Androgen levels increase by intratumoral de novo steroidogenesis during progression of castration-resistant prostate cancer. Cancer Res, 2008. **68**(15): p. 6407-15.
- 103. Visakorpi, T., et al., *In vivo amplification of the androgen receptor gene and progression of human prostate cancer.* Nat Genet, 1995. **9**(4): p. 401-6.
- 104. Linja, M.J., et al., *Amplification and overexpression of androgen receptor gene in hormone-refractory prostate cancer*. Cancer Res, 2001. **61**(9): p. 3550-5.
- 105. Quigley, D.A., et al., *Genomic Hallmarks and Structural Variation in Metastatic Prostate Cancer*. Cell, 2018. **174**(3): p. 758-769.e9.
- 106. Watson, P.A., V.K. Arora, and C.L. Sawyers, *Emerging mechanisms of resistance to androgen receptor inhibitors in prostate cancer*. Nat Rev Cancer, 2015. **15**(12): p. 701-11.
- 107. Zhao, X.Y., et al., Glucocorticoids can promote androgen-independent growth of prostate cancer cells through a mutated androgen receptor. Nat Med, 2000. **6**(6): p. 703-6.
- 108. Balbas, M.D., et al., Overcoming mutation-based resistance to antiandrogens with rational drug design. Elife, 2013. **9**(2): p. 00499.
- 109. Pienta, K.J. and D. Bradley, *Mechanisms underlying the development of androgen-independent prostate cancer*. Clin Cancer Res, 2006. **12**(6): p. 1665-71.
- 110. Dehm, S.M., et al., Splicing of a novel androgen receptor exon generates a constitutively active androgen receptor that mediates prostate cancer therapy resistance. Cancer Res, 2008. **68**(13): p. 5469-77.
- 111. Hu, R., et al., Ligand-independent androgen receptor variants derived from splicing of cryptic exons signify hormone-refractory prostate cancer. Cancer Res, 2009. **69**(1): p. 16-22.
- 112. Crona, D.J. and Y.E. Whang, Androgen Receptor-Dependent and -Independent Mechanisms Involved in Prostate Cancer Therapy Resistance. Cancers (Basel), 2017. **9**(6).
- 113. Antonarakis, E.S., et al., *Androgen receptor variant-driven prostate cancer: clinical implications and therapeutic targeting.* Prostate Cancer Prostatic Dis, 2016. **19**(3): p. 231-41.

- 114. Luo, J., et al., Role of Androgen Receptor Variants in Prostate Cancer: Report from the 2017 Mission Androgen Receptor Variants Meeting. European urology, 2018. **73**(5): p. 715-723.
- 115. Lu, C. and J. Luo, *Decoding the androgen receptor splice variants*. Translational andrology and urology, 2013. **2**(3): p. 178-186.
- 116. Luo, J., Development of AR-V7 as a putative treatment selection marker for metastatic castration-resistant prostate cancer. Asian journal of andrology, 2016. **18**(4): p. 580-585.
- 117. Antonarakis, E.S., et al., AR-V7 and Resistance to Enzalutamide and Abiraterone in Prostate Cancer. 2014. **371**(11): p. 1028-1038.
- 118. de Bono, J.S., et al., *Abiraterone and increased survival in metastatic prostate cancer.* N Engl J Med, 2011. **364**(21): p. 1995-2005.
- 119. Fizazi, K., et al., Abiraterone acetate plus prednisone in patients with newly diagnosed high-risk metastatic castration-sensitive prostate cancer (LATITUDE): final overall survival analysis of a randomised, double-blind, phase 3 trial. Lancet Oncol, 2019. **20**(5): p. 686-700.
- 120. Beer, T.M., et al., *Enzalutamide in metastatic prostate cancer before chemotherapy.* N Engl J Med, 2014. **371**(5): p. 424-33.
- 121. Shore, N.D., et al., Efficacy and safety of enzalutamide versus bicalutamide for patients with metastatic prostate cancer (TERRAIN): a randomised, double-blind, phase 2 study. Lancet Oncol, 2016. 17(2): p. 153-163.
- 122. Scher, H.I., et al., *Increased survival with enzalutamide in prostate cancer after chemotherapy*. N Engl J Med, 2012. **367**(13): p. 1187-97.
- 123. Hurwitz, M. and D.P. Petrylak, *Sequencing of agents for castration-resistant prostate cancer*. Oncology (Williston Park), 2013. **27**(11): p. 1144-9, 1154-8.
- 124. Scher, H.I., et al., *Antitumour activity of MDV3100 in castration-resistant prostate cancer: a phase 1-2 study.* Lancet, 2010. **375**(9724): p. 1437-46.
- 125. Nelson, W.G. and S. Yegnasubramanian, *Resistance emerges to second-generation antiandrogens in prostate cancer.* Cancer Discov, 2013. **3**(9): p. 971-4.
- 126. Simon, I., et al., Cross-Resistance to Abiraterone and Enzalutamide in Castration Resistance Prostate Cancer Cellular Models Is Mediated by AR Transcriptional Reactivation. Cancers (Basel), 2021. **13**(6).
- 127. Arora, V.K., et al., *Glucocorticoid receptor confers resistance to antiandrogens by bypassing androgen receptor blockade*. Cell, 2013. **155**(6): p. 1309-22.
- 128. Liu, C., et al., Niclosamide inhibits androgen receptor variants expression and overcomes enzalutamide resistance in castration-resistant prostate cancer. Clin Cancer Res, 2014. **20**(12): p. 3198-3210.
- 129. Sethi, S., et al., Molecular signature of epithelial-mesenchymal transition (EMT) in human prostate cancer bone metastasis. Am J Transl Res, 2010. **3**(1): p. 90-9.
- 130. Bubendorf, L., et al., *Metastatic patterns of prostate cancer: an autopsy study of 1,589 patients.* Hum Pathol, 2000. **31**(5): p. 578-83.
- 131. Logothetis, C.J. and S.H. Lin, *Osteoblasts in prostate cancer metastasis to bone.* Nat Rev Cancer, 2005. **5**(1): p. 21-8.
- 132. Datta, K., et al., *Mechanism of lymph node metastasis in prostate cancer*. Future Oncol, 2010. **6**(5): p. 823-36.

- 133. Lin, D., et al., *High fidelity patient-derived xenografts for accelerating prostate cancer discovery and drug development.* Cancer Res, 2014. **74**(4): p. 1272-83.
- 134. Kasper, S., Survey of genetically engineered mouse models for prostate cancer: analyzing the molecular basis of prostate cancer development, progression, and metastasis. J Cell Biochem, 2005. **94**(2): p. 279-97.
- 135. Ratnacaram, C.K., et al., Temporally controlled ablation of PTEN in adult mouse prostate epithelium generates a model of invasive prostatic adenocarcinoma. Proc Natl Acad Sci U S A, 2008. **105**(7): p. 2521-6.
- 136. Luchman, H.A., et al., *Temporally controlled prostate epithelium-specific gene alterations*. Genesis, 2008. **46**(4): p. 229-34.
- 137. Birbach, A., E. Casanova, and J.A. Schmid, *A Probasin-MerCreMer BAC allows inducible recombination in the mouse prostate.* Genesis, 2009. **47**(11): p. 757-64.
- 138. Gao, D., et al., A Tmprss2-CreERT2 Knock-In Mouse Model for Cancer Genetic Studies on Prostate and Colon. PLoS One, 2016. **11**(8): p. e0161084.
- 139. Ittmann, M., et al., Animal models of human prostate cancer: the consensus report of the New York meeting of the Mouse Models of Human Cancers Consortium Prostate Pathology Committee. Cancer Res, 2013. **73**(9): p. 2718-36.
- 140. Hubbard, G.K., et al., *Combined MYC Activation and Pten Loss Are Sufficient to Create Genomic Instability and Lethal Metastatic Prostate Cancer*. Cancer Res, 2016. **76**(2): p. 283-92.
- 141. Ku, S.Y., et al., *Rb1* and *Trp53* cooperate to suppress prostate cancer lineage plasticity, metastasis, and antiandrogen resistance. Science, 2017. **355**(6320): p. 78-83.
- 142. Shen, M.M. and C. Abate-Shen, *Pten inactivation and the emergence of androgen-independent prostate cancer.* Cancer Res, 2007. **67**(14): p. 6535-8.
- 143. Aparicio, A.M., et al., *Combined Tumor Suppressor Defects Characterize Clinically Defined Aggressive Variant Prostate Cancers*. Clin Cancer Res, 2016. **22**(6): p. 1520-30.
- 144. Chen, Z., et al., Crucial role of p53-dependent cellular senescence in suppression of Pten-deficient tumorigenesis. Nature, 2005. **436**(7051): p. 725-30.
- 145. Robinson, D., et al., *Integrative clinical genomics of advanced prostate cancer*. Cell, 2015. **161**(5): p. 1215-1228.
- 146. Fraser, M., et al., *Genomic hallmarks of localized, non-indolent prostate cancer.* Nature, 2017. **541**(7637): p. 359-364.
- 147. The Molecular Taxonomy of Primary Prostate Cancer. Cell, 2015. 163(4): p. 1011-25.
- 148. Mulholland, D.J., et al., *PTEN and GSK3beta: key regulators of progression to androgen-independent prostate cancer.* Oncogene, 2006. **25**(3): p. 329-37.
- 149. Zhou, Z., et al., Synergy of p53 and Rb deficiency in a conditional mouse model for metastatic prostate cancer. Cancer Res, 2006. **66**(16): p. 7889-98.
- 150. Trotman, L.C., et al., *Pten dose dictates cancer progression in the prostate.* PLoS Biol, 2003. **1**(3): p. E59.
- 151. Wang, Z.A., et al., Luminal cells are favored as the cell of origin for prostate cancer. Cell Rep, 2014. **8**(5): p. 1339-46.
- 152. Zou, M., et al., Transdifferentiation as a Mechanism of Treatment Resistance in a Mouse Model of Castration-Resistant Prostate Cancer. Cancer Discov, 2017. **7**(7): p. 736-749.

- 153. Kersten, K., et al., *Genetically engineered mouse models in oncology research and cancer medicine*. EMBO Mol Med, 2017. **9**(2): p. 137-153.
- 154. Chow, R.D. and S. Chen, *Cancer CRISPR Screens In Vivo*. Trends Cancer, 2018. **4**(5): p. 349-358.
- 155. Chen, S., et al., *Genome-wide CRISPR screen in a mouse model of tumor growth and metastasis.* Cell, 2015. **160**(6): p. 1246-60.
- 156. Katigbak, A., et al., *A CRISPR/Cas9 Functional Screen Identifies Rare Tumor Suppressors*. Scientific Reports, 2016. **6**(1): p. 38968.
- 157. Kampmann, M., CRISPRi and CRISPRa Screens in Mammalian Cells for Precision Biology and Medicine. ACS Chem Biol, 2018. **13**(2): p. 406-416.
- 158. Bhaya, D., M. Davison, and R. Barrangou, *CRISPR-Cas systems in bacteria and archaea:* versatile small RNAs for adaptive defense and regulation. Annu Rev Genet, 2011. **45**: p. 273-97.
- 159. Sternberg, S.H., et al., *DNA interrogation by the CRISPR RNA-guided endonuclease Cas9.* Nature, 2014. **507**(7490): p. 62-7.
- 160. Larson, M.H., et al., CRISPR interference (CRISPRi) for sequence-specific control of gene expression. Nat Protoc, 2013. **8**(11): p. 2180-96.
- 161. Konermann, S., et al., *Genome-scale transcriptional activation by an engineered CRISPR-Cas9 complex*. Nature, 2015. **517**(7536): p. 583-8.
- 162. Zhang, R., et al., *Gene Silencing Through CRISPR Interference in Bacteria: Current Advances and Future Prospects.* Front Microbiol, 2021. **12**: p. 635227.
- 163. Huang, A., et al., *Synthetic lethality as an engine for cancer drug target discovery.*Nature Reviews Drug Discovery, 2020. **19**(1): p. 23-38.
- 164. Lord, C.J. and A. Ashworth, *PARP inhibitors: Synthetic lethality in the clinic.* Science, 2017. **355**(6330): p. 1152-1158.
- 165. Phaniendra, A., D.B. Jestadi, and L. Periyasamy, *Free radicals: properties, sources, targets, and their implication in various diseases.* Indian J Clin Biochem, 2015. **30**(1): p. 11-26.
- 166. Genestra, M., *Oxyl radicals, redox-sensitive signalling cascades and antioxidants.* Cell Signal, 2007. **19**(9): p. 1807-19.
- 167. Han, C., et al., Roles of Reactive Oxygen Species in Biological Behaviors of Prostate Cancer. Biomed Res Int, 2020. **2020**: p. 1269624.
- 168. Tafani, M., et al., *The Interplay of Reactive Oxygen Species, Hypoxia, Inflammation, and Sirtuins in Cancer Initiation and Progression*. Oxidative Medicine and Cellular Longevity, 2016. **2016**: p. 3907147.
- 169. Birben, E., et al., *Oxidative stress and antioxidant defense*. World Allergy Organ J, 2012. **5**(1): p. 9-19.
- 170. Du, M.Q., P.L. Carmichael, and D.H. Phillips, *Induction of activating mutations in the human c-Ha-ras-1 proto-oncogene by oxygen free radicals*. Mol Carcinog, 1994. **11**(3): p. 170-5.
- 171. Xie, S., et al., Reactive oxygen species-induced phosphorylation of p53 on serine 20 is mediated in part by polo-like kinase-3. J Biol Chem, 2001. **276**(39): p. 36194-9.
- 172. Wu, Y., et al., Molecular mechanisms underlying chronic inflammation-associated cancers. Cancer Lett, 2014. **345**(2): p. 164-73.
- 173. Reuter, S., et al., Oxidative stress, inflammation, and cancer: how are they linked? Free Radic Biol Med, 2010. **49**(11): p. 1603-16.

- 174. Lee, K.H., S.W. Kim, and J.R. Kim, Reactive oxygen species regulate urokinase plasminogen activator expression and cell invasion via mitogen-activated protein kinase pathways after treatment with hepatocyte growth factor in stomach cancer cells. J Exp Clin Cancer Res, 2009. **28**(1): p. 73.
- 175. Liou, G.Y. and P. Storz, *Reactive oxygen species in cancer.* Free Radic Res, 2010. **44**(5): p. 479-96.
- 176. Li, Q. and J.F. Engelhardt, *Interleukin-1beta induction of NFkappaB is partially regulated by H2O2-mediated activation of NFkappaB-inducing kinase.* J Biol Chem, 2006. **281**(3): p. 1495-505.
- 177. Fresno Vara, J.A., et al., *PI3K/Akt signalling pathway and cancer*. Cancer Treat Rev, 2004. **30**(2): p. 193-204.
- 178. Liu, Y., G. Fiskum, and D. Schubert, *Generation of reactive oxygen species by the mitochondrial electron transport chain.* J Neurochem, 2002. **80**(5): p. 780-7.
- 179. Roy, K., et al., NADPH oxidases and cancer. Clin Sci (Lond), 2015. **128**(12): p. 863-75.
- 180. Srinivas, U.S., et al., *ROS and the DNA damage response in cancer.* Redox Biol, 2019. **25**: p. 101084.
- 181. Meitzler, J.L., M.M. Konaté, and J.H. Doroshow, *Hydrogen peroxide-producing NADPH oxidases and the promotion of migratory phenotypes in cancer.* Arch Biochem Biophys, 2019. **675**: p. 108076.
- 182. Li, W.G., et al., H(2)O(2)-induced O(2) production by a non-phagocytic NAD(P)H oxidase causes oxidant injury. J Biol Chem, 2001. **276**(31): p. 29251-6.
- 183. Ma, Y., et al., High-dose parenteral ascorbate enhanced chemosensitivity of ovarian cancer and reduced toxicity of chemotherapy. Sci Transl Med, 2014. **6**(222): p. 222ra18.
- 184. Wright, M.E., et al., Effects of alpha-tocopherol and beta-carotene supplementation on upper aerodigestive tract cancers in a large, randomized controlled trial. Cancer, 2007. **109**(5): p. 891-8.
- 185. Wu, Y., et al., Activation of TLR4 is required for the synergistic induction of dual oxidase 2 and dual oxidase A2 by IFN-y and lipopolysaccharide in human pancreatic cancer cell lines. J Immunol, 2013. **190**(4): p. 1859-72.
- 186. Meitzler, J.L., et al., *NADPH oxidases: a perspective on reactive oxygen species production in tumor biology.* Antioxid Redox Signal, 2014. **20**(17): p. 2873-89.
- 187. Bedard, K. and K.H. Krause, *The NOX family of ROS-generating NADPH oxidases:* physiology and pathophysiology. Physiol Rev, 2007. **87**(1): p. 245-313.
- 188. Wu, J.-X., et al., Structures of human dual oxidase 1 complex in low-calcium and high-calcium states. Nature Communications, 2021. **12**(1): p. 155.
- 189. Ogboo, B.C., et al., *Architecture of the NADPH oxidase family of enzymes*. Redox Biology, 2022. **52**: p. 102298.
- 190. Meitzler, J.L. and P.R. Ortiz de Montellano, Structural stability and heme binding potential of the truncated human dual oxidase 2 (DUOX2) peroxidase domain. Arch Biochem Biophys, 2011. **512**(2): p. 197-203.
- 191. Meitzler, J.L. and P.R. Ortiz de Montellano, *Caenorhabditis elegans and Human Dual Oxidase 1 (DUOX1) "Peroxidase" Domains: INSIGHTS INTO HEME BINDING AND CATALYTIC ACTIVITY**. Journal of Biological Chemistry, 2009. **284**(28): p. 18634-18643.

- 192. Little, A.C., et al., *Paradoxical roles of dual oxidases in cancer biology*. Free Radic Biol Med, 2017. **110**: p. 117-132.
- 193. Faria, C.C. and R.S. Fortunato, *The role of dual oxidases in physiology and cancer.* Genet Mol Biol, 2020. **43**(1 suppl. 1): p. e20190096.
- 194. Morand, S.C., et al., *Duox maturation factors form cell surface complexes with Duox affecting the specificity of reactive oxygen species generation.* 2009. **23**: p. 1205 1218.
- 195. Magnani, F., et al., *Crystal structures and atomic model of NADPH oxidase.* 2017. **114**(26): p. 6764-6769.
- 196. Sun, J., Structures of mouse DUOX1-DUOXA1 provide mechanistic insights into enzyme activation and regulation. Nature Structural & Molecular Biology, 2020. **27**(11): p. 1086-1093.
- 197. Gough, D.R. and T.G. Cotter, *Hydrogen peroxide: a Jekyll and Hyde signalling molecule*. Cell Death Dis, 2011. **2**(10): p. e213.
- 198. Burdon, R.H. and C. Rice-Evans, *Free radicals and the regulation of mammalian cell proliferation.* Free Radic Res Commun, 1989. **6**(6): p. 345-58.
- 199. Sundaresan, M., et al., Requirement for generation of H2O2 for platelet-derived growth factor signal transduction. Science, 1995. **270**(5234): p. 296-9.
- 200. Bae, Y.S., et al., Epidermal growth factor (EGF)-induced generation of hydrogen peroxide. Role in EGF receptor-mediated tyrosine phosphorylation. J Biol Chem, 1997. **272**(1): p. 217-21.
- 201. Kim, Y.K., et al., Cooperation of H2O2-mediated ERK activation with Smad pathway in TGF-beta1 induction of p21WAF1/Cip1. Cell Signal, 2006. **18**(2): p. 236-43.
- 202. Milenkovic, M., et al., *Duox expression and related H2O2 measurement in mouse thyroid: onset in embryonic development and regulation by TSH in adult.* J Endocrinol, 2007. **192**(3): p. 615-26.
- 203. Donkó, A., et al., *Urothelial cells produce hydrogen peroxide through the activation of Duox1*. Free Radic Biol Med, 2010. **49**(12): p. 2040-8.
- 204. El Hassani, R.A., et al., *Dual oxidase2 is expressed all along the digestive tract.* Am J Physiol Gastrointest Liver Physiol, 2005. **288**(5): p. G933-42.
- 205. Geiszt, M., et al., *Dual oxidases represent novel hydrogen peroxide sources supporting mucosal surface host defense.* Faseb j, 2003. **17**(11): p. 1502-4.
- 206. Wang, J., et al., *PKCα promotes generation of reactive oxygen species via DUOX2 in hepatocellular carcinoma*. Biochem Biophys Res Commun, 2015. **463**(4): p. 839-45.
- 207. Wu, Y., et al., *Up-regulation and sustained activation of Stat1 are essential for interferon-gamma (IFN-gamma)-induced dual oxidase 2 (Duox2) and dual oxidase A2 (DuoxA2) expression in human pancreatic cancer cell lines.* J Biol Chem, 2011. **286**(14): p. 12245-56.
- 208. Pettigrew, C.A., J.S. Clerkin, and T.G. Cotter, *DUOX enzyme activity promotes AKT signalling in prostate cancer cells.* Anticancer Res, 2012. **32**(12): p. 5175-81.
- 209. Zhang, X., et al., *DUOX2 promotes the progression of colorectal cancer cells by regulating the AKT pathway and interacting with RPL3.* Carcinogenesis, 2021. **42**(1): p. 105-117.
- 210. Kang, K.A., et al., *DUOX2-mediated production of reactive oxygen species induces epithelial mesenchymal transition in 5-fluorouracil resistant human colon cancer cells.* Redox Biol, 2018. **17**: p. 224-235.

- 211. Cho, S.Y., et al., Expression of NOX Family Genes and Their Clinical Significance in Colorectal Cancer. Dig Dis Sci, 2018. **63**(9): p. 2332-2340.
- 212. You, X., et al., *Gene expression and prognosis of NOX family members in gastric cancer*. Onco Targets Ther, 2018. **11**: p. 3065-3074.
- 213. Juhasz, A., et al., Expression of NADPH oxidase homologues and accessory genes in human cancer cell lines, tumours and adjacent normal tissues. Free Radic Res, 2009. **43**(6): p. 523-32.
- 214. Eun, H.S., et al., Gene expression of NOX family members and their clinical significance in hepatocellular carcinoma. Scientific Reports, 2017. **7**(1): p. 11060.
- 215. Corzo, C.A., et al., *Mechanism regulating reactive oxygen species in tumor-induced myeloid-derived suppressor cells.* J Immunol, 2009. **182**(9): p. 5693-701.
- 216. Szewczyk-Golec, K., J. Tyloch, and J. Czuczejko, *Antioxidant defense system in prostate adenocarcinoma and benign prostate hyperplasia of elderly patients.* Neoplasma, 2015. **62**(1): p. 119-23.
- 217. Liguori, I., et al., *Oxidative stress, aging, and diseases.* Clin Interv Aging, 2018. **13**: p. 757-772.
- 218. Shukla, S., et al., Oxidative Stress and Antioxidant Status in High-Risk Prostate Cancer Subjects. Diagnostics (Basel), 2020. **10**(3).
- 219. Fahmy, O., et al., *Updates on Molecular and Biochemical Development and Progression of Prostate Cancer.* J Clin Med, 2021. **10**(21).
- 220. Kalinina, E.V., L.A. Gavriliuk, and V.S. Pokrovsky, *Oxidative Stress and Redox-Dependent Signaling in Prostate Cancer*. Biochemistry (Mosc), 2022. **87**(5): p. 413-424.
- 221. Sekine, H. and H. Motohashi, *Roles of CNC Transcription Factors NRF1 and NRF2 in Cancer.* Cancers (Basel), 2021. **13**(3).
- 222. Wardyn, J.D., A.H. Ponsford, and C.M. Sanderson, *Dissecting molecular cross-talk between Nrf2 and NF-κB response pathways.* Biochem Soc Trans, 2015. **43**(4): p. 621-6.
- 223. Jin, R., et al., *NF-κB gene signature predicts prostate cancer progression.* Cancer Res, 2014. **74**(10): p. 2763-72.
- 224. Papa, S., et al., *Linking JNK signaling to NF-kappaB: a key to survival.* J Cell Sci, 2004. **117**(Pt 22): p. 5197-208.
- 225. Xu, R. and J. Hu, *The role of JNK in prostate cancer progression and therapeutic strategies*. Biomed Pharmacother, 2020. **121**: p. 109679.
- 226. Wang, Y., et al., Self-responsive co-delivery system for remodeling tumor intracellular microenvironment to promote PTEN-mediated anti-tumor therapy. Nanoscale, 2020. **12**(17): p. 9392-9403.
- 227. Chetram, M.A., A.S. Don-Salu-Hewage, and C.V. Hinton, *ROS enhances CXCR4-mediated functions through inactivation of PTEN in prostate cancer cells.* Biochem Biophys Res Commun, 2011. **410**(2): p. 195-200.
- 228. Hahn, A. and S. Zuryn, *Mitochondrial Genome (mtDNA) Mutations that Generate Reactive Oxygen Species.* Antioxidants (Basel), 2019. **8**(9).
- 229. Kalsbeek, A.M.F., et al., *Altered mitochondrial genome content signals worse pathology and prognosis in prostate cancer.* Prostate, 2018. **78**(1): p. 25-31.

- 230. Kalsbeek, A.M.F., et al., *Mitochondrial genome variation and prostate cancer: a review of the mutational landscape and application to clinical management.* Oncotarget, 2017. **8**(41): p. 71342-71357.
- 231. Deep, G., et al., *Graviola inhibits hypoxia-induced NADPH oxidase activity in prostate cancer cells reducing their proliferation and clonogenicity.* Sci Rep, 2016. **6**: p. 23135.
- 232. Tamura, R.E., et al., Induction of Oxidants Distinguishes Susceptibility of Prostate Carcinoma Cell Lines to p53 Gene Transfer Mediated by an Improved Adenoviral Vector. Hum Gene Ther, 2017. **28**(8): p. 639-653.
- 233. Lim, S.D., et al., *Increased Nox1 and hydrogen peroxide in prostate cancer*. Prostate, 2005. **62**(2): p. 200-7.
- 234. Kumar, B., et al., Oxidative stress is inherent in prostate cancer cells and is required for aggressive phenotype. Cancer Res, 2008. **68**(6): p. 1777-85.
- 235. Höll, M., et al., ROS signaling by NADPH oxidase 5 modulates the proliferation and survival of prostate carcinoma cells. Mol Carcinog, 2016. **55**(1): p. 27-39.
- 236. Miyata, Y., et al., A Mini-Review of Reactive Oxygen Species in Urological Cancer: Correlation with NADPH Oxidases, Angiogenesis, and Apoptosis. 2017. **18**(10): p. 2214.
- 237. Wu, Y., et al., Functional activity and tumor-specific expression of dual oxidase 2 in pancreatic cancer cells and human malignancies characterized with a novel monoclonal antibody. Int J Oncol, 2013. **42**(4): p. 1229-38.
- 238. Bertout, J.A., S.A. Patel, and M.C. Simon, *The impact of O2 availability on human cancer*. Nat Rev Cancer, 2008. **8**(12): p. 967-75.
- 239. Keith, B. and M.C. Simon, *Hypoxia-inducible factors, stem cells, and cancer.* Cell, 2007. **129**(3): p. 465-72.
- 240. Vaupel, P., *Tumor microenvironmental physiology and its implications for radiation oncology.* Semin Radiat Oncol, 2004. **14**(3): p. 198-206.
- 241. Graham, K. and E. Unger, *Overcoming tumor hypoxia as a barrier to radiotherapy, chemotherapy and immunotherapy in cancer treatment.* Int J Nanomedicine, 2018. **13**: p. 6049-6058.
- 242. Carnell, D.M., et al., *An immunohistochemical assessment of hypoxia in prostate carcinoma using pimonidazole: implications for radioresistance*. Int J Radiat Oncol Biol Phys, 2006. **65**(1): p. 91-9.
- 243. McKeown, S.R., *Defining normoxia, physoxia and hypoxia in tumours-implications for treatment response.* Br J Radiol, 2014. **87**(1035): p. 20130676.
- 244. Bhandari, V., et al., *Molecular landmarks of tumor hypoxia across cancer types.* Nat Genet, 2019. **51**(2): p. 308-318.
- 245. Bhandari, V., et al., *Divergent mutational processes distinguish hypoxic and normoxic tumours.* Nature Communications, 2020. **11**(1): p. 737.
- 246. Zhang, Q., et al., *Integrative Analysis of Hypoxia-Associated Signature in Pan-Cancer.* iScience, 2020. **23**(9): p. 101460.
- 247. Economopoulou, M., et al., *Histone H2AX is integral to hypoxia-driven neovascularization*. Nat Med, 2009. **15**(5): p. 553-8.
- 248. Han, J., et al., *Hypoxia is a Key Driver of Alternative Splicing in Human Breast Cancer Cells.* Sci Rep, 2017. **7**(1): p. 4108.
- 249. Tang, M., et al., *Tumor Hypoxia Drives Genomic Instability*. Front Cell Dev Biol, 2021. **9**: p. 626229.

- 250. Rose, M., et al., *PARP Inhibitors: Clinical Relevance, Mechanisms of Action and Tumor Resistance.* Front Cell Dev Biol, 2020. **8**: p. 564601.
- 251. Majmundar, A.J., W.J. Wong, and M.C. Simon, *Hypoxia-inducible factors and the response to hypoxic stress.* Mol Cell, 2010. **40**(2): p. 294-309.
- 252. Qing, G. and M.C. Simon, *Hypoxia inducible factor-2alpha: a critical mediator of aggressive tumor phenotypes*. Curr Opin Genet Dev, 2009. **19**(1): p. 60-6.
- 253. Semenza, G.L., *Hypoxia-inducible factors in physiology and medicine*. Cell, 2012. **148**(3): p. 399-408.
- 254. Patel, S.A. and M.C. Simon, *Biology of hypoxia-inducible factor-2alpha in development and disease*. Cell Death Differ, 2008. **15**(4): p. 628-34.
- 255. Mucaj, V., J.E.S. Shay, and M.C. Simon, *Effects of hypoxia and HIFs on cancer metabolism*. International Journal of Hematology, 2012. **95**(5): p. 464-470.
- 256. Krock, B.L., N. Skuli, and M.C. Simon, *Hypoxia-induced angiogenesis: good and evil.* Genes Cancer, 2011. **2**(12): p. 1117-33.
- 257. Jaakkola, P., et al., *Targeting of HIF-alpha to the von Hippel-Lindau ubiquitylation complex by O2-regulated prolyl hydroxylation*. Science, 2001. **292**(5516): p. 468-72.
- 258. Zimna, A. and M. Kurpisz, *Hypoxia-Inducible Factor-1 in Physiological and Pathophysiological Angiogenesis: Applications and Therapies.* Biomed Res Int, 2015. **2015**: p. 549412.
- 259. Jayson, G.C., et al., *Antiangiogenic therapy in oncology: current status and future directions.* Lancet, 2016. **388**(10043): p. 518-29.
- 260. Yatabe, N., et al., *HIF-1-mediated activation of telomerase in cervical cancer cells*. Oncogene, 2004. **23**(20): p. 3708-15.
- 261. Qiang, L., et al., HIF-1α is critical for hypoxia-mediated maintenance of glioblastoma stem cells by activating Notch signaling pathway. Cell Death & Differentiation, 2012. **19**(2): p. 284-294.
- 262. Chen, G., et al., *Hypoxia induces an endometrial cancer stem-like cell phenotype via HIF-dependent demethylation of SOX2 mRNA*. Oncogenesis, 2020. **9**(9): p. 81.
- 263. Maugeri-Saccà, M., P. Vigneri, and R. De Maria, *Cancer stem cells and chemosensitivity*. Clin Cancer Res, 2011. **17**(15): p. 4942-7.
- 264. Chen, J., et al., HIF-1 α inhibition reverses multidrug resistance in colon cancer cells via downregulation of MDR1/P-glycoprotein. PLoS One, 2014. **9**(6): p. e98882.
- 265. Wartenberg, M., et al., Reactive oxygen species-linked regulation of the multidrug resistance transporter P-glycoprotein in Nox-1 overexpressing prostate tumor spheroids. FEBS Lett, 2005. **579**(20): p. 4541-4549.
- 266. Yu, L., et al., *The Glycolytic Switch in Tumors: How Many Players Are Involved?* J Cancer, 2017. **8**(17): p. 3430-3440.
- 267. Semenza, G.L., *HIF-1: upstream and downstream of cancer metabolism.* Curr Opin Genet Dev, 2010. **20**(1): p. 51-6.
- 268. Kim, J.W., et al., HIF-1-mediated expression of pyruvate dehydrogenase kinase: a metabolic switch required for cellular adaptation to hypoxia. Cell Metab, 2006. **3**(3): p. 177-85.
- 269. Fukuda, R., et al., *HIF-1 regulates cytochrome oxidase subunits to optimize efficiency of respiration in hypoxic cells.* Cell, 2007. **129**(1): p. 111-22.

- 270. Grandjean, G., et al., Definition of a Novel Feed-Forward Mechanism for Glycolysis-HIF1 α Signaling in Hypoxic Tumors Highlights Aldolase A as a Therapeutic Target. Cancer Res, 2016. **76**(14): p. 4259-4269.
- 271. Wang, Q.S., et al., Role of mitochondrial reactive oxygen species in hypoxia-dependent increase in intracellular calcium in pulmonary artery myocytes. Free Radic Biol Med, 2007. **42**(5): p. 642-53.
- 272. Hassan Venkatesh, G., et al., *Hypoxia increases mutational load of breast cancer cells through frameshift mutations.* Oncoimmunology, 2020. **9**(1): p. 1750750.
- 273. Pires, I.M., et al., *Effects of acute versus chronic hypoxia on DNA damage responses and genomic instability.* Cancer Res, 2010. **70**(3): p. 925-35.
- 274. Kovac, S., et al., *Nrf2 regulates ROS production by mitochondria and NADPH oxidase.* Biochim Biophys Acta, 2015. **1850**(4): p. 794-801.
- 275. Jiang, F., Y. Zhang, and G.J. Dusting, *NADPH oxidase-mediated redox signaling: roles in cellular stress response, stress tolerance, and tissue repair.* Pharmacol Rev, 2011. **63**(1): p. 218-42.
- 276. Yuan, G., et al., *Hypoxia-inducible factor 1 mediates increased expression of NADPH oxidase-2 in response to intermittent hypoxia*. J Cell Physiol, 2011. **226**(11): p. 2925-33.
- 277. Goyal, P., et al., *Upregulation of NAD(P)H oxidase 1 in hypoxia activates hypoxia-inducible factor 1 via increase in reactive oxygen species.* Free Radic Biol Med, 2004. **36**(10): p. 1279-88.
- 278. Rathore, R., et al., *Hypoxia activates NADPH oxidase to increase [ROS]i and [Ca2+]i through the mitochondrial ROS-PKCepsilon signaling axis in pulmonary artery smooth muscle cells.* Free Radic Biol Med, 2008. **45**(9): p. 1223-31.
- 279. Manuelli, V., et al., Regulation of redox signaling in HIF-1-dependent tumor angiogenesis. Febs j, 2022. **289**(18): p. 5413-5425.
- 280. Cheng, H.H., et al., *Circulating microRNA profiling identifies a subset of metastatic prostate cancer patients with evidence of cancer-associated hypoxia*. PLoS One, 2013. **8**(7): p. e69239.
- 281. Long, Q., et al., Global transcriptome analysis of formalin-fixed prostate cancer specimens identifies biomarkers of disease recurrence. Cancer Res, 2014. **74**(12): p. 3228-37.
- 282. Milosevic, M., et al., *Tumor hypoxia predicts biochemical failure following radiotherapy for clinically localized prostate cancer.* Clin Cancer Res, 2012. **18**(7): p. 2108-14.
- 283. Sampson, N., et al., *In vitro model systems to study androgen receptor signaling in prostate cancer.* Endocr Relat Cancer, 2013. **20**(2): p. R49-64.
- 284. Rana, M., et al., Androgen receptor and its splice variant, AR-V7, differentially induce mRNA splicing in prostate cancer cells. Scientific Reports, 2021. **11**(1): p. 1393.
- 285. Richard, D.E., et al., p42/p44 mitogen-activated protein kinases phosphorylate hypoxia-inducible factor 1alpha (HIF-1alpha) and enhance the transcriptional activity of HIF-1. J Biol Chem, 1999. **274**(46): p. 32631-7.
- 286. Winter, J., et al., caRpools: an R package for exploratory data analysis and documentation of pooled CRISPR/Cas9 screens. Bioinformatics, 2016. **32**(4): p. 632-4.
- 287. Love, M.I., W. Huber, and S. Anders, *Moderated estimation of fold change and dispersion for RNA-seq data with DESeq2*. Genome Biol, 2014. **15**(12): p. 550.

- 288. Kuleshov, M.V., et al., Enrichr: a comprehensive gene set enrichment analysis web server 2016 update. Nucleic Acids Res, 2016. **44**(W1): p. W90-7.
- 289. Subramanian, A., et al., Gene set enrichment analysis: a knowledge-based approach for interpreting genome-wide expression profiles. Proc Natl Acad Sci U S A, 2005. **102**(43): p. 15545-50.
- 290. Abida, W., et al., *Genomic correlates of clinical outcome in advanced prostate cancer.* Proc Natl Acad Sci U S A, 2019. **116**(23): p. 11428-11436.
- 291. Barbie, D.A., et al., *Systematic RNA interference reveals that oncogenic KRAS-driven cancers require TBK1*. Nature, 2009. **462**(7269): p. 108-12.
- 292. Hänzelmann, S., R. Castelo, and J. Guinney, *GSVA: gene set variation analysis for microarray and RNA-Seq data.* BMC Bioinformatics, 2013. **14**(1): p. 7.
- 293. Chuang, Y.Y., et al., Gene expression after treatment with hydrogen peroxide, menadione, or t-butyl hydroperoxide in breast cancer cells. Cancer Res, 2002. **62**(21): p. 6246-54.
- 294. *The Gene Ontology resource: enriching a GOld mine.* Nucleic Acids Res, 2021. **49**(D1): p. D325-d334.
- 295. Haider, S., et al., *BioMart Central Portal--unified access to biological data*. Nucleic Acids Res, 2009. **37**(Web Server issue): p. W23-7.
- 296. Balbas, M.D., et al., *Overcoming mutation-based resistance to antiandrogens with rational drug design.* Elife, 2013. **2**: p. e00499.
- 297. Bolger, A.M., M. Lohse, and B. Usadel, *Trimmomatic: a flexible trimmer for Illumina sequence data*. Bioinformatics, 2014. **30**(15): p. 2114-2120.
- 298. Dobin, A., et al., *STAR: ultrafast universal RNA-seq aligner.* Bioinformatics, 2013. **29**(1): p. 15-21.
- 299. Robinson, M.D., D.J. McCarthy, and G.K. Smyth, edgeR: a Bioconductor package for differential expression analysis of digital gene expression data. Bioinformatics, 2010. **26**(1): p. 139-40.
- 300. Sakharkar, M.K., et al., A systems biology approach towards the identification of candidate therapeutic genes and potential biomarkers for Parkinson's disease. PLoS One, 2019. **14**(9): p. e0220995.
- 301. Upadhyay, A., et al., *Neurocalcin Delta Knockout Impairs Adult Neurogenesis Whereas Half Reduction Is Not Pathological.* Front Mol Neurosci, 2019. **12**: p. 19.
- 302. Li, T., et al., *The Neurexin/N-Ethylmaleimide-sensitive Factor (NSF) Interaction Regulates Short Term Synaptic Depression.* J Biol Chem, 2015. **290**(29): p. 17656-17667.
- 303. Akamatsu, S., et al., *Clinical and molecular features of treatment-related neuroendocrine prostate cancer.* 2018. **25**(4): p. 345-351.
- 304. Beltran, H., et al., *Aggressive variants of castration-resistant prostate cancer*. Clin Cancer Res, 2014. **20**(11): p. 2846-50.
- 305. Merkens, L., et al., Aggressive variants of prostate cancer: underlying mechanisms of neuroendocrine transdifferentiation. Journal of Experimental & Clinical Cancer Research, 2022. **41**(1): p. 46.
- 306. Beltran, H., et al., *Divergent clonal evolution of castration-resistant neuroendocrine prostate cancer.* Nat Med, 2016. **22**(3): p. 298-305.

- 307. Shiota, M., et al., *Antioxidant therapy alleviates oxidative stress by androgen deprivation and prevents conversion from androgen dependent to castration resistant prostate cancer.* J Urol, 2012. **187**(2): p. 707-14.
- 308. Miller, D.R., et al., p66Shc protein through a redox mechanism enhances the progression of prostate cancer cells towards castration-resistance. Free Radic Biol Med, 2019. **139**: p. 24-34.
- 309. Shiota, M., et al., Castration resistance of prostate cancer cells caused by castration-induced oxidative stress through Twist1 and androgen receptor overexpression. Oncogene, 2010. **29**(2): p. 237-50.
- 310. Shiota, M., A. Yokomizo, and S. Naito, *Oxidative stress and androgen receptor signaling in the development and progression of castration-resistant prostate cancer.* Free Radic Biol Med, 2011. **51**(7): p. 1320-8.
- 311. Bell, E.L., et al., *Mitochondrial reactive oxygen species trigger hypoxia-inducible factor-dependent extension of the replicative life span during hypoxia.* Mol Cell Biol, 2007. **27**(16): p. 5737-45.
- 312. Qutub, A.A. and A.S. Popel, *Reactive oxygen species regulate hypoxia-inducible factor 1alpha differentially in cancer and ischemia.* Mol Cell Biol, 2008. **28**(16): p. 5106-19.
- 313. Movafagh, S., S. Crook, and K. Vo, *Regulation of hypoxia-inducible factor-1a by reactive oxygen species: new developments in an old debate.* J Cell Biochem, 2015. **116**(5): p. 696-703.
- 314. Morgan, M.J. and Z.G. Liu, *Crosstalk of reactive oxygen species and NF-κB signaling*. Cell Res, 2011. **21**(1): p. 103-15.
- 315. Tao, L., et al., Reactive oxygen species oxidize STING and suppress interferon production. Elife, 2020. **9**.
- 316. Kopitar-Jerala, N., *The Role of Interferons in Inflammation and Inflammasome Activation.* Front Immunol, 2017. **8**: p. 873.
- 317. Kolamunne, R.T., et al., *Nrf2 activation supports cell survival during hypoxia and hypoxia/reoxygenation in cardiomyoblasts; the roles of reactive oxygen and nitrogen species.* Redox Biol, 2013. **1**(1): p. 418-26.
- 318. Küper, A., et al., Overcoming hypoxia-induced resistance of pancreatic and lung tumor cells by disrupting the PERK-NRF2-HIF-axis. Cell Death & Disease, 2021. **12**(1): p. 82.
- 319. Chacko, Balu K., et al., *The Bioenergetic Health Index: a new concept in mitochondrial translational research.* Clinical Science, 2014. **127**(6): p. 367-373.
- 320. Yu, T., B. Tang, and X. Sun, *Development of Inhibitors Targeting Hypoxia-Inducible Factor 1 and 2 for Cancer Therapy.* Yonsei Med J, 2017. **58**(3): p. 489-496.
- 321. Fallah, J. and B.I. Rini, *HIF Inhibitors: Status of Current Clinical Development*. Curr Oncol Rep, 2019. **21**(1): p. 6.
- 322. Yoshihama, Y., et al., AR-negative prostate cancer is vulnerable to loss of JMJD1C demethylase. Proc Natl Acad Sci U S A, 2021. **118**(36).
- 323. Fei, T., et al., Genome-wide CRISPR screen identifies HNRNPL as a prostate cancer dependency regulating RNA splicing. Proc Natl Acad Sci U S A, 2017. **114**(26): p. E5207-e5215.
- 324. Lei, H., et al., CRISPR screening identifies CDK12 as a conservative vulnerability of prostate cancer. Cell Death Dis, 2021. **12**(8): p. 740.
- 325. Palit, S.A., et al., *TLE3 loss confers AR inhibitor resistance by facilitating GR-mediated human prostate cancer cell growth.* Elife, 2019. **8**.

- 326. Palit, S.A.L., et al., A kinome-centered CRISPR-Cas9 screen identifies activated BRAF to modulate enzalutamide resistance with potential therapeutic implications in BRAF-mutated prostate cancer. Sci Rep, 2021. **11**(1): p. 13683.
- 327. Rodríguez, Y., et al., A Genome-Wide CRISPR Activation Screen Identifies PRRX2 as a Regulator of Enzalutamide Resistance in Prostate Cancer. Cancer Res, 2022. **82**(11): p. 2110-2123.
- 328. Tsujino, T., et al., CRISPR screens reveal genetic determinants of PARP inhibitor sensitivity and resistance in prostate cancer. Nature Communications, 2023. **14**(1): p. 252.
- 329. Wang, C., et al., Genome-wide CRISPR screens reveal synthetic lethality of RNASEH2 deficiency and ATR inhibition. Oncogene, 2019. **38**(14): p. 2451-2463.
- 330. Pinto, F., et al., Mechanisms of Resistance to Second-Generation Antiandrogen Therapy for Prostate Cancer: Actual Knowledge and Perspectives. Med Sci (Basel), 2022. **10**(2).
- 331. Akter, J., et al., Expression of NLRR3 orphan receptor gene is negatively regulated by MYCN and Miz-1, and its downregulation is associated with unfavorable outcome in neuroblastoma. Clin Cancer Res, 2011. **17**(21): p. 6681-92.
- 332. Feng, L.Y. and L. Li, Low expression of NCALD is associated with chemotherapy resistance and poor prognosis in epithelial ovarian cancer. J Ovarian Res, 2020. **13**(1): p. 35.
- 333. Chen, Y., et al., Clinicopathological and prognostic significance of NCALD protein expression in lung adenocarcinoma. Transl Cancer Res, 2019. **8**(3): p. 752-760.
- 334. Song, Y., et al., *High NCALD expression predicts poor prognosis of cytogenetic normal acute myeloid leukemia.* J Transl Med, 2019. **17**(1): p. 166.
- 335. Arman, T. and P.S. Nelson, *Endocrine and paracrine characteristics of neuroendocrine prostate cancer.* Front Endocrinol (Lausanne), 2022. **13**: p. 1012005.
- 336. Okasho, K., O. Ogawa, and S. Akamatsu, *Narrative review of challenges in the management of advanced neuroendocrine prostate cancer*. Transl Androl Urol, 2021. **10**(10): p. 3953-3962.
- 337. Akamatsu, S., et al., *Clinical and molecular features of treatment-related neuroendocrine prostate cancer.* Int J Urol, 2018. **25**(4): p. 345-351.
- 338. Zhang, W., et al., Role of the DNA damage response in prostate cancer formation, progression and treatment. Prostate Cancer and Prostatic Diseases, 2020. **23**(1): p. 24-37.
- 339. Yu, H., et al., *FOXM1 modulates docetaxel resistance in prostate cancer by regulating KIF20A*. Cancer Cell International, 2020. **20**(1): p. 545.
- 340. Faskhoudi, M.A., et al., *Molecular landscape of c-Myc signaling in prostate cancer: A roadmap to clinical translation.* Pathol Res Pract, 2022. **233**: p. 153851.
- 341. Fortunato, R.S., et al., *DUOX1 Silencing in Mammary Cell Alters the Response to Genotoxic Stress*. Oxid Med Cell Longev, 2018. **2018**: p. 3570526.
- 342. Luo, M., et al., *Antioxidant Therapy in Cancer: Rationale and Progress.* Antioxidants (Basel), 2022. **11**(6).
- 343. Ngo, B., et al., *Targeting cancer vulnerabilities with high-dose vitamin C.* Nature Reviews Cancer, 2019. **19**(5): p. 271-282.
- 344. Niki, E., Role of vitamin E as a lipid-soluble peroxyl radical scavenger: in vitro and in vivo evidence. Free Radic Biol Med, 2014. **66**: p. 3-12.

- 345. Li, P., et al., NAC selectively inhibit cancer telomerase activity: A higher redox homeostasis threshold exists in cancer cells. Redox Biol, 2016. **8**: p. 91-7.
- 346. Augsburger, F., et al., *Pharmacological characterization of the seven human NOX isoforms and their inhibitors*. Redox Biol, 2019. **26**: p. 101272.
- 347. Batinic-Haberle, I. and M.E. Tome, *Thiol regulation by Mn porphyrins, commonly known as SOD mimics*. Redox Biol, 2019. **25**: p. 101139.
- 348. Altenhöfer, S., et al., Evolution of NADPH Oxidase Inhibitors: Selectivity and Mechanisms for Target Engagement. Antioxid Redox Signal, 2015. **23**(5): p. 406-27.
- 349. O'Donnell, B.V., et al., Studies on the inhibitory mechanism of iodonium compounds with special reference to neutrophil NADPH oxidase. Biochem J, 1993. **290 (Pt 1)**(Pt 1): p. 41-9.
- 350. Doroshow, J.H., et al., Effects of iodonium-class flavin dehydrogenase inhibitors on growth, reactive oxygen production, cell cycle progression, NADPH oxidase 1 levels, and gene expression in human colon cancer cells and xenografts. Free Radic Biol Med, 2013. **57**: p. 162-75.
- 351. Monzur, S., et al., *Diphenyleneiodonium efficiently inhibits the characteristics of a cancer stem cell model derived from induced pluripotent stem cells.* Cell Biochem Funct, 2022. **40**(3): p. 310-320.
- 352. Schröder, K., *NADPH oxidases: Current aspects and tools.* Redox Biol, 2020. **34**: p. 101512.
- 353. Lu, J., et al., Characterization of potent and selective iodonium-class inhibitors of NADPH oxidases. Biochem Pharmacol, 2017. **143**: p. 25-38.
- 354. Zulato, E., et al., *LKB1 loss is associated with glutathione deficiency under oxidative stress and sensitivity of cancer cells to cytotoxic drugs and γ-irradiation.* Biochem Pharmacol, 2018. **156**: p. 479-490.
- 355. Conklin, K.A., *Chemotherapy-associated oxidative stress: impact on chemotherapeutic effectiveness.* Integr Cancer Ther, 2004. **3**(4): p. 294-300.
- 356. Marullo, R., et al., *Cisplatin induces a mitochondrial-ROS response that contributes to cytotoxicity depending on mitochondrial redox status and bioenergetic functions.* PLoS One, 2013. **8**(11): p. e81162.
- 357. Murphy, M.P., et al., *Guidelines for measuring reactive oxygen species and oxidative damage in cells and in vivo*. Nature Metabolism, 2022. **4**(6): p. 651-662.
- 358. Veal, E.A., A.M. Day, and B.A. Morgan, *Hydrogen peroxide sensing and signaling*. Mol Cell, 2007. **26**(1): p. 1-14.
- 359. Nauseef, W.M., *Detection of superoxide anion and hydrogen peroxide production by cellular NADPH oxidases.* Biochim Biophys Acta, 2014. **1840**(2): p. 757-67.
- 360. Tam, N.N., et al., Androgenic regulation of oxidative stress in the rat prostate: involvement of NAD(P)H oxidases and antioxidant defense machinery during prostatic involution and regrowth. Am J Pathol, 2003. **163**(6): p. 2513-22.
- 361. Pang, S.T., et al., Gene expression profiling of androgen deficiency predicts a pathway of prostate apoptosis that involves genes related to oxidative stress. Endocrinology, 2002. **143**(12): p. 4897-906.
- 362. Samaranayake, G.J., et al., *Thioredoxin-1 protects against androgen receptor-induced redox vulnerability in castration-resistant prostate cancer.* Nature Communications, 2017. **8**(1): p. 1204.

- 363. Shan, W., et al., *Thioredoxin 1 as a subcellular biomarker of redox imbalance in human prostate cancer progression.* Free Radic Biol Med, 2010. **49**(12): p. 2078-87.
- 364. Ripple, M.O., et al., *Prooxidant-antioxidant shift induced by androgen treatment of human prostate carcinoma cells*. J Natl Cancer Inst, 1997. **89**(1): p. 40-8.
- 365. Pathak, S., et al., Androgen manipulation alters oxidative DNA adduct levels in androgen-sensitive prostate cancer cells grown in vitro and in vivo. Cancer Lett, 2008. **261**(1): p. 74-83.
- 366. Lu, J.P., et al., Androgens induce oxidative stress and radiation resistance in prostate cancer cells though NADPH oxidase. Prostate Cancer and Prostatic Diseases, 2010. **13**(1): p. 39-46.
- 367. Pinthus, J.H., et al., Androgen induces adaptation to oxidative stress in prostate cancer: implications for treatment with radiation therapy. Neoplasia, 2007. **9**(1): p. 68-80.
- 368. Woodward, W.A., et al., Effects of androgen suppression and radiation on prostate cancer suggest a role for angiogenesis blockade. Prostate Cancer Prostatic Dis, 2005. **8**(2): p. 127-32.
- 369. Lorenzo, P.I. and F. Saatcioglu, Inhibition of apoptosis in prostate cancer cells by androgens is mediated through downregulation of c-Jun N-terminal kinase activation. Neoplasia, 2008. **10**(5): p. 418-28.
- 370. Fontana, F., et al., Mitochondrial functional and structural impairment is involved in the antitumor activity of δ -tocotrienol in prostate cancer cells. Free Radic Biol Med, 2020. **160**: p. 376-390.
- 371. Wu, W., et al., Phenylbutyl isoselenocyanate induces reactive oxygen species to inhibit androgen receptor and to initiate p53-mediated apoptosis in LNCaP prostate cancer cells. Mol Carcinog, 2018. **57**(8): p. 1055-1066.
- 372. Xu, H., et al., Preclinical Study Using ABT263 to Increase Enzalutamide Sensitivity to Suppress Prostate Cancer Progression Via Targeting BCL2/ROS/USP26 Axis Through Altering ARv7 Protein Degradation. Cancers (Basel), 2020. **12**(4).
- 373. Khurana, N., et al., Bardoxolone-Methyl (CDDO-Me) Suppresses Androgen Receptor and Its Splice-Variant AR-V7 and Enhances Efficacy of Enzalutamide in Prostate Cancer Cells. Antioxidants (Basel), 2020. **9**(1).
- 374. Kumar, R., et al., Supraphysiologic Testosterone Induces Ferroptosis and Activates Immune Pathways through Nucleophagy in Prostate Cancer. Cancer Res, 2021. **81**(23): p. 5948-5962.
- 375. Lam, H.M., et al., Durable Response of Enzalutamide-resistant Prostate Cancer to Supraphysiological Testosterone Is Associated with a Multifaceted Growth Suppression and Impaired DNA Damage Response Transcriptomic Program in Patient-derived Xenografts. Eur Urol, 2020. **77**(2): p. 144-155.
- 376. Schweizer, M.T., et al., Effect of bipolar androgen therapy for asymptomatic men with castration-resistant prostate cancer: results from a pilot clinical study. Sci Transl Med, 2015. **7**(269): p. 269ra2.
- 377. Nyquist, M.D., et al., Selective androgen receptor modulators activate the canonical prostate cancer androgen receptor program and repress cancer growth. J Clin Invest, 2021. **131**(10).
- 378. Qiu, X., et al., Response to supraphysiological testosterone is predicted by a distinct androgen receptor cistrome. JCI Insight, 2022. **7**(10).

- 379. Konaté, M.M., S. Antony, and J.H. Doroshow, *Inhibiting the Activity of NADPH Oxidase in Cancer*. Antioxid Redox Signal, 2020. **33**(6): p. 435-454.
- 380. Hayashi, Y., et al., *Hypoxia/pseudohypoxia-mediated activation of hypoxia-inducible* factor- 1α in cancer. Cancer Sci, 2019. **110**(5): p. 1510-1517.
- 381. Marignol, L., et al., *Hypoxia, notch signalling, and prostate cancer.* Nat Rev Urol, 2013. **10**(7): p. 405-13.
- 382. Jain, R.K., et al., Endothelial cell death, angiogenesis, and microvascular function after castration in an androgen-dependent tumor: role of vascular endothelial growth factor. Proc Natl Acad Sci U S A, 1998. **95**(18): p. 10820-5.
- 383. Shabsigh, A., et al., Rapid reduction in blood flow to the rat ventral prostate gland after castration: preliminary evidence that androgens influence prostate size by regulating blood flow to the prostate gland and prostatic endothelial cell survival. Prostate, 1998. **36**(3): p. 201-6.
- 384. Davis, C.K., et al., *Hypoxia Mimetic Agents for Ischemic Stroke*. Front Cell Dev Biol, 2018. **6**: p. 175.
- 385. Xing, Y., et al., COX2 is involved in hypoxia-induced TNF- α expression in osteoblast. Scientific Reports, 2015. **5**(1): p. 10020.
- 386. Chen, R., M.A. Ahmed, and N.R. Forsyth, *Dimethyloxalylglycine (DMOG), a Hypoxia Mimetic Agent, Does Not Replicate a Rat Pheochromocytoma (PC12) Cell Biological Response to Reduced Oxygen Culture.* Biomolecules, 2022. **12**(4).
- 387. Li, Q., R. Ma, and M. Zhang, *CoCl(2) increases the expression of hypoxic markers HIF-*1α, VEGF and CXCR4 in breast cancer MCF-7 cells. Oncol Lett, 2018. **15**(1): p. 11191124.
- 388. Bae, S., et al., *The hypoxia-mimetic agent cobalt chloride induces cell cycle arrest and alters gene expression in U266 multiple myeloma cells.* Int J Mol Med, 2012. **30**(5): p. 1180-6.
- 389. Park, S.Y., et al., *Hypoxia increases androgen receptor activity in prostate cancer cells.* Cancer Res, 2006. **66**(10): p. 5121-9.
- 390. Butterworth, K.T., et al., *Hypoxia selects for androgen independent LNCaP cells with a more malignant geno- and phenotype.* Int J Cancer, 2008. **123**(4): p. 760-8.
- 391. Mabjeesh, N.J., et al., Androgens stimulate hypoxia-inducible factor 1 activation via autocrine loop of tyrosine kinase receptor/phosphatidylinositol 3'-kinase/protein kinase B in prostate cancer cells. Clin Cancer Res, 2003. **9**(7): p. 2416-25.
- 392. Geng, H., et al., Interplay between hypoxia and androgen controls a metabolic switch conferring resistance to androgen/AR-targeted therapy. Nature Communications, 2018. **9**(1): p. 4972.
- 393. Frohlich, D.A., et al., *The role of Nrf2 in increased reactive oxygen species and DNA damage in prostate tumorigenesis.* Oncogene, 2008. **27**(31): p. 4353-4362.
- 394. Harder, B., et al., *Molecular mechanisms of Nrf2 regulation and how these influence chemical modulation for disease intervention.* Biochem Soc Trans, 2015. **43**(4): p. 680-6.
- 395. Buelna-Chontal, M. and C. Zazueta, *Redox activation of Nrf2 & NF-κB: a double end sword?* Cell Signal, 2013. **25**(12): p. 2548-57.
- 396. Lee, S., et al., Impairment of HIF-1 α -mediated metabolic adaption by NRF2-silencing in breast cancer cells. Redox Biol, 2019. **24**: p. 101210.

- 397. Johansson, K., et al., Cross Talk in HEK293 Cells Between Nrf2, HIF, and NF-κB Activities upon Challenges with Redox Therapeutics Characterized with Single-Cell Resolution. Antioxid Redox Signal, 2017. **26**(6): p. 229-246.
- 398. Azimi, I., et al., *Hypoxia-induced reactive oxygen species mediate N-cadherin and SERPINE1 expression, EGFR signalling and motility in MDA-MB-468 breast cancer cells.* Sci Rep, 2017. **7**(1): p. 15140.
- 399. Clanton, T.L., *Hypoxia-induced reactive oxygen species formation in skeletal muscle.* J Appl Physiol (1985), 2007. **102**(6): p. 2379-88.
- 400. Kondoh, M., et al., *Hypoxia-induced reactive oxygen species cause chromosomal abnormalities in endothelial cells in the tumor microenvironment.* PLoS One, 2013. **8**(11): p. e80349.
- 401. Ishikawa, K., et al., *ROS-generating mitochondrial DNA mutations can regulate tumor cell metastasis*. Science, 2008. **320**(5876): p. 661-4.
- 402. Oberley, T.D., et al., Localization of antioxidant enzymes and oxidative damage products in normal and malignant prostate epithelium. Prostate, 2000. **44**(2): p. 144-55.
- 403. Kierans, S.J. and C.T. Taylor, *Regulation of glycolysis by the hypoxia-inducible factor* (HIF): implications for cellular physiology. J Physiol, 2021. **599**(1): p. 23-37.
- 404. Al Tameemi, W., et al., *Hypoxia-Modified Cancer Cell Metabolism.* Front Cell Dev Biol, 2019. **7**: p. 4.
- 405. Gordan, J.D., et al., *HIF-2alpha promotes hypoxic cell proliferation by enhancing c-myc transcriptional activity.* Cancer Cell, 2007. **11**(4): p. 335-47.
- 406. Chen, C., et al., c-Myc enhances colon cancer cell-mediated angiogenesis through the regulation of HIF-1 α . Biochem Biophys Res Commun, 2013. **430**(2): p. 505-11.
- 407. Li, Y., et al., Molecular Crosstalk Between MYC and HIF in Cancer. 2020. 8.
- 408. Ivashchenko, O., et al., *Intraperoxisomal redox balance in mammalian cells: oxidative stress and interorganellar cross-talk.* Mol Biol Cell, 2011. **22**(9): p. 1440-51.
- 409. Nickens, K.P., et al., A bioenergetic profile of non-transformed fibroblasts uncovers a link between death-resistance and enhanced spare respiratory capacity. Mitochondrion, 2013. **13**(6): p. 662-7.
- 410. Teh, J.T., et al., Respiratory Capacity and Reserve Predict Cell Sensitivity to Mitochondria Inhibitors: Mechanism-Based Markers to Identify Metformin-Responsive Cancers. Mol Cancer Ther, 2019. **18**(3): p. 693-705.
- 411. Marchetti, P., et al., *Mitochondrial spare respiratory capacity: Mechanisms, regulation, and significance in non-transformed and cancer cells.* Faseb j, 2020. **34**(10): p. 13106-13124.
- 412. Oliva, C.R., et al., Acquisition of temozolomide chemoresistance in gliomas leads to remodeling of mitochondrial electron transport chain. J Biol Chem, 2010. **285**(51): p. 39759-67.
- 413. Zhang, Q., et al., Upregulation of MAPK/MCL-1 Maintaining Mitochondrial Oxidative Phosphorylation Confers Acquired Resistance to BCL-2 Inhibitor Venetoclax in AML. Blood, 2016. **128**(22): p. 101.
- 414. Paulus, A., et al., Waldenstrom macroglobulinemia cells devoid of BTK(C481S) or CXCR4(WHIM-like) mutations acquire resistance to ibrutinib through upregulation of Bcl-2 and AKT resulting in vulnerability towards venetoclax or MK2206 treatment. Blood Cancer J, 2017. **7**(5): p. e565.

- 415. Ganapathy-Kanniappan, S. and J.F. Geschwind, *Tumor glycolysis as a target for cancer therapy: progress and prospects.* Mol Cancer, 2013. **12**: p. 152.
- 416. Vali, M., et al., Intraarterial therapy with a new potent inhibitor of tumor metabolism (3-bromopyruvate): identification of therapeutic dose and method of injection in an animal model of liver cancer. J Vasc Interv Radiol, 2007. **18**(1 Pt 1): p. 95-101.
- 417. Vali, M., et al., *Targeting of VX2 rabbit liver tumor by selective delivery of 3-bromopyruvate: a biodistribution and survival study.* J Pharmacol Exp Ther, 2008. **327**(1): p. 32-7.
- 418. Maschek, G., et al., 2-deoxy-D-glucose increases the efficacy of adriamycin and paclitaxel in human osteosarcoma and non-small cell lung cancers in vivo. Cancer Res, 2004. **64**(1): p. 31-4.
- 419. Dwarakanath, B. and V. Jain, *Targeting glucose metabolism with 2-deoxy-D-glucose for improving cancer therapy.* Future Oncol, 2009. **5**(5): p. 581-5.
- 420. Bénéteau, M., et al., *Combination of glycolysis inhibition with chemotherapy results in an antitumor immune response.* Proc Natl Acad Sci U S A, 2012. **109**(49): p. 20071-6.
- 421. Filomeni, G., et al., Metabolic oxidative stress elicited by the copper(II) complex [Cu(isaepy)2] triggers apoptosis in SH-SY5Y cells through the induction of the AMP-activated protein kinase/p38MAPK/p53 signalling axis: evidence for a combined use with 3-bromopyruvate in neuroblastoma treatment. Biochem J, 2011. **437**(3): p. 443-53.
- 422. Kelsey, R., *Glycolysis and AR expression as biomarkers*. Nature Reviews Urology, 2018. **15**(1): p. 2-2.
- 423. Xiao, H., et al., *GLUT1 regulates cell glycolysis and proliferation in prostate cancer.* Prostate, 2018. **78**(2): p. 86-94.
- 424. Li, L., et al., Combined inhibition of glycolysis, the pentose cycle, and thioredoxin metabolism selectively increases cytotoxicity and oxidative stress in human breast and prostate cancer. Redox Biol, 2015. **4**: p. 127-35.
- 425. Rice, M.A., et al., SU086, an inhibitor of HSP90, impairs glycolysis and represents a treatment strategy for advanced prostate cancer. Cell Rep Med, 2022. **3**(2): p. 100502.
- 426. Parczyk, J., et al., Dichloroacetate and PX-478 exhibit strong synergistic effects in a various number of cancer cell lines. BMC Cancer, 2021. **21**(1): p. 481.
- 427. Guo, H., et al., *ONECUT2* is a driver of neuroendocrine prostate cancer. Nat Commun, 2019. **10**(1): p. 278.
- 428. Jayaprakash, P., et al., *Targeted hypoxia reduction restores T cell infiltration and sensitizes prostate cancer to immunotherapy.* J Clin Invest, 2018. **128**(11): p. 5137-5149.
- 429. Li, Y., L. Zhao, and X.F. Li, *The Hypoxia-Activated Prodrug TH-302: Exploiting Hypoxia in Cancer Therapy.* Front Pharmacol, 2021. **12**: p. 636892.
- 430. Koh, M., et al., *Molecular mechanisms for the activity of PX-478, an antitumor inhibitor of the hypoxia-inducible factor-1 alpha.* Molecular cancer therapeutics, 2008. **7**: p. 90-100.
- 431. Jacoby, J.J., et al., *Treatment with HIF-1alpha antagonist PX-478 inhibits progression and spread of orthotopic human small cell lung cancer and lung adenocarcinoma in mice.* J Thorac Oncol, 2010. **5**(7): p. 940-9.

- 432. Palayoor, S.T., et al., *PX-478, an inhibitor of hypoxia-inducible factor-1alpha, enhances radiosensitivity of prostate carcinoma cells.* Int J Cancer, 2008. **123**(10): p. 2430-7.
- 433. Tran, M.G.B., et al., *Independence of HIF1a and androgen signaling pathways in prostate cancer.* BMC Cancer, 2020. **20**(1): p. 469.
- 434. Yang, L., et al., *Development and Validation of a 28-gene Hypoxia-related Prognostic Signature for Localized Prostate Cancer*. EBioMedicine, 2018. **31**: p. 182-189.
- 435. Ashton, J. and R. Bristow, *Bad neighbours: hypoxia and genomic instability in prostate cancer.* Br J Radiol, 2020. **93**(1115): p. 20200087.
- 436. Boutros, P.C., et al., *Spatial genomic heterogeneity within localized, multifocal prostate cancer.* Nat Genet, 2015. **47**(7): p. 736-45.
- 437. Vergis, R., et al., Intrinsic markers of tumour hypoxia and angiogenesis in localised prostate cancer and outcome of radical treatment: a retrospective analysis of two randomised radiotherapy trials and one surgical cohort study. Lancet Oncol, 2008. **9**(4): p. 342-51.
- 438. Moreno Roig, E., et al., *Prognostic Role of Hypoxia-Inducible Factor-2α Tumor Cell Expression in Cancer Patients: A Meta-Analysis.* Front Oncol, 2018. **8**: p. 224.

PUBLICATIONS

BIOCHEMISTRY

A hotspot for posttranslational modifications on the androgen receptor dimer interface drives pathology and anti-androgen resistance

Andrea Alegre-Martí^{1,2}†, Alba Jiménez-Panizo^{1,2}†, Adrián Martínez-Tébar³†, Coralie Poulard⁴, M. Núria Peralta-Moreno⁵, Montserrat Abella^{1,2}, Rosa Antón⁶, Marcos Chiñas^{3,7}, Ulrich Eckhard⁸, Josep M. Piulats³, Ana M. Rojas⁹, Juan Fernández-Recio¹⁰, Jaime Rubio-Martínez⁵, Muriel Le Romancer⁴, Álvaro Aytes³‡*, Pablo Fuentes-Prior⁶‡*, Eva Estébanez-Perpiñá^{1,2}‡*

Mutations of the androgen receptor (AR) associated with prostate cancer and androgen insensitivity syndrome may profoundly influence its structure, protein interaction network, and binding to chromatin, resulting in altered transcription signatures and drug responses. Current structural information fails to explain the effect of pathological mutations on AR structure-function relationship. Here, we have thoroughly studied the effects of selected mutations that span the complete dimer interface of AR ligand-binding domain (AR-LBD) using x-ray crystallography in combination with in vitro, in silico, and cell-based assays. We show that these variants alter AR-dependent transcription and responses to anti-androgens by inducing a previously undescribed allosteric switch in the AR-LBD that increases exposure of a major methylation target, Arg⁷⁶¹. We also corroborate the relevance of residues ${\rm Arg}^{761}$ and ${\rm Tyr}^{764}$ for AR dimerization and function. Together, our results reveal allosteric coupling of AR dimerization and posttranslational modifications as a disease mechanism with implications for precision medicine.



INTRODUCTION

The androgen receptor (AR; AR/NR3C4) is a member of the steroid subfamily of nuclear receptors essential for male development and tissue homeostasis (1-2). The AR protein is composed of an intrinsically disordered N-terminal region (NTD) followed by a "core" that contains the actual DNA- and ligand-binding domains (DBD and LBD, respectively) (Fig. 1A) (2-3). The atomic details of fulllength AR (FL AR) still remain elusive, but a low-resolution structure by cryo-electron microscopy (cryo-EM) complexed to DNA and a coregulator has provided a model of its overall architecture (4). This EM structure features a noncanonical head-to-head dimer (i.e., centered on H5 helices, in contrast to the canonical, H10-centered arrangement [see (3) for a detailed comparison of the dimerization modes], in line with previously reported x-ray structures of dimeric DBD (5) and LBD isolated moieties (6).

¹Structural Biology of Nuclear Receptors, Department of Biochemistry and Molecular Biomedicine, Faculty of Biology, University of Barcelona (UB), 08028 Barcelona, Spain. ²Institute of Biomedicine of the University of Barcelona (IBUB), University of Barcelona (UB), 08028 Barcelona, Spain. ³Programs of Molecular Mechanisms and Experimental Therapeutics in Oncology (ONCOBell) and Cancer Therapeutics Resistance (ProCURE), Catalan Institute of Oncology, Bellvitge Institute for Biomedical Research, 08908 Barcelona, Spain. ⁴Cancer Research Center of Lyon, CNRS UMR5286, Inserm U1502, University of Lyon, 69000 Lyon, France. ⁵Department of Materials Science and Physical Chemistry, Faculty of Chemistry and Institut de Recerca en Química Teorica i Computacional (IQTCUB), 08028 Barcelona, Spain. ⁶Biomedical Research Institute Sant Pau (IIB Sant Pau), 08041 Barcelona, Spain. ⁷Universidad Nacional Autónoma de México, Centro de Ciencias Genómicas, Cuernavaca, 61740 Morelos, Mexico. ⁸Department of Structural and Molecular Biology, Molecular Biology Institute of Barcelona (IBMB-CSIC), 08028 Barcelona, Spain. ⁹Computational Biology and Bioinformatics, Andalusian Center for Developmental Biology (CABD-CSIC), 41013 Sevilla, Spain. ¹⁰Instituto de Ciencias de la Vid y del Vino (ICVV-CSIC), CSIC-UR-Gobierno de La Rioja, 26007 Logroño, Spain. †These authors contributed equally to this work.

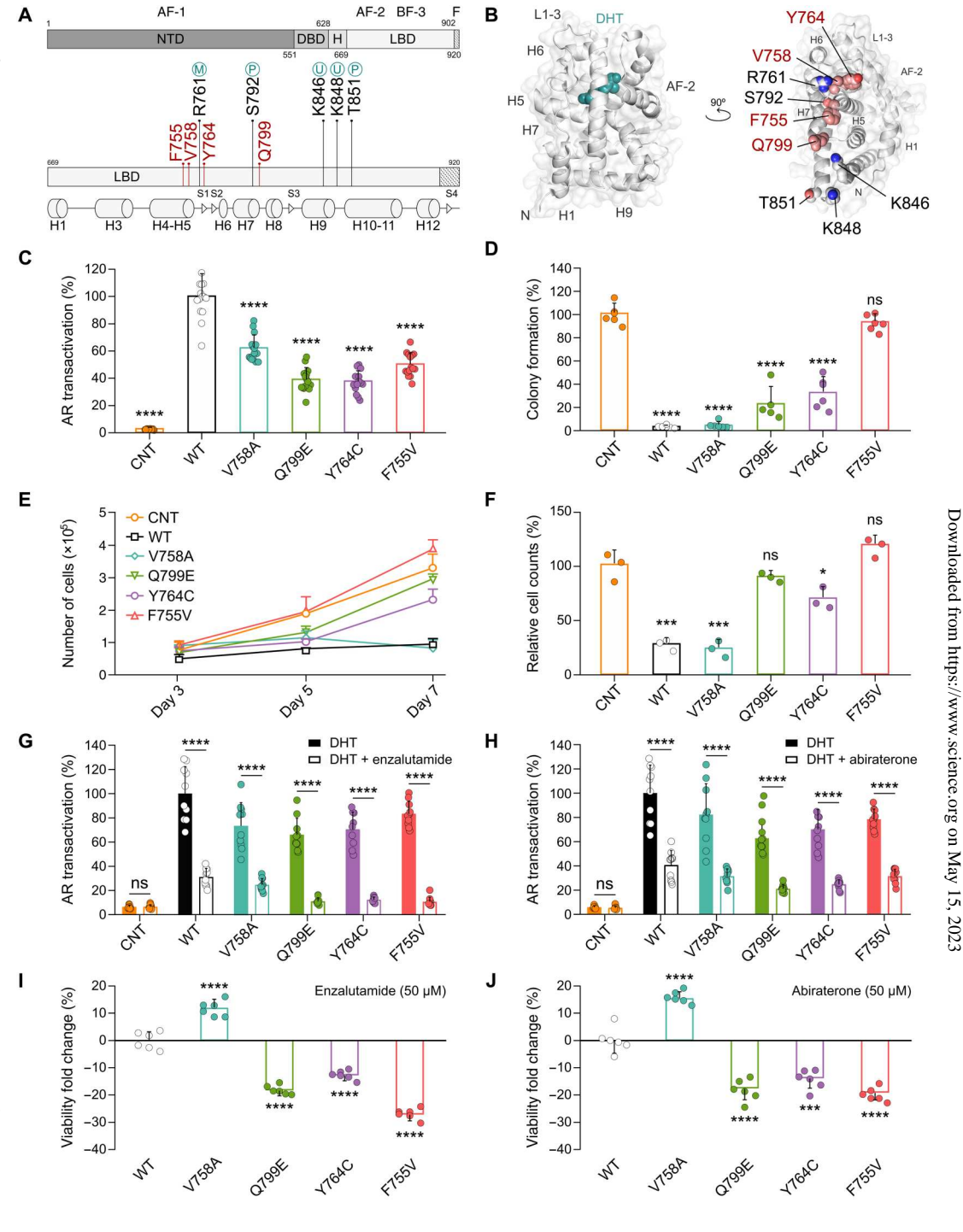
Another EM structure of the AR core has recently been published in three distinctive configurations (7), further corroborating the noncanonical AR-LBD dimerization mode (3). These EM structures evidence that AR is a highly dynamic protein. AR physiological functions are inherently linked to not only the correct folding of DBD and LBD modules but also to their relative orientations (e.g., N-terminal and C-terminal (N/C) interaction), oligomerization, and coregulator binding to control transcription (2, 8). Besides, AR protein structure and function relationship are regulated by posttranslational modifications (PTMs) such as methylation, phosphorylation, ubiquitination, acetylation, and sumoylation, adding an extra level of complexity that has only been scarcely studied (9–19). In particular, no structural data have been reported on the mechanistic consequences of these covalent modifications to date.

Tight spatial and temporal regulation of AR activity is critical for the proper functioning of tissue-specific signaling cascades. Therefore, dysfunctions of the AR-regulated pathways have profound pathophysiological consequences (2, 8, 20–22). Up-regulated receptor activity is the dominant driver in one of the leading cancers in adult men, prostate cancer (PCa; 1-2, 8, 21-22), making AR a central therapeutic target for PCa treatment (2). On the other hand, impaired response to androgens leads to an X chromosome-linked disorder of sex development in genetic males termed androgen insensitivity syndrome (AIS) (23-25). Many point mutations in the AR gene associated with either resistance to PCa therapeutic drugs (anti-androgens; 26-28) and/or with AIS have been reported (29) (table S1 and Fig. 1A). Knowledge of the structure of the wild-type (WT) protein does not allow to predict the structural and functional impact of point mutations and therefore their pathogenicity and clinical implications in patients (3, 6–7). Whereas mutations causing AIS occur in the germ line, PCa-linked mutations are mostly somatic and occur before endocrine treatment or

[‡]These authors contributed equally to this work.

^{*}Corresponding author. Email: evaestebanez@ub.edu (E.E.-P.); fuentespriorpablo@ gmail.com (P.F.-P.); aaytes@idibell.cat (A.A.)

Fig. 1. Mutations at the AR-LBD dimer interface affect cellular phenotypes, transcriptional activity, and response to antiandrogens. (A) Cartoon of AR domain organization. Physiologically relevant interaction sites [top; activation function-1 (AF-1), AF-2 and binding function-3 (BF-3)], mutated AR-LBD residues (red; middle), and secondary structure elements [bottom; helices (H, cylinders) and β strands (S1 to S4, triangles)] are indicated. Neighboring residues of major PTM sites are shown [methylation (M), phosphorylation (P), and ubiquitination (U)]. (B) Three-dimensional structure of AR-LBD (gray). Note that disease-linked residues (red spheres) and PTM sites (gray spheres) highlighted in (A) form an extended path on the AR-LBD dimer interface. (C) Relative AR transcriptional activity in CNT, WT, and mutant AR-transduced PC3 cells (mean \pm SD, n = 3). Differences against WT were calculated using a t test and considered significant at P values <0.1. (#P < 0.1 *P < 0.05, **P < 0.01, ***P < 0.001, and ****P < 0.0001). The same Pvalue guidelines and asterisk significance will be used through this manuscript. (D) Clonogenicity assay quantification in transduced PC3 cells (mean \pm SD, n = 3). Representative crystal violet-stained cultures are shown in fig. S1A. (E) Time course of transduced PC3 cells proliferation (mean \pm SD, n = 3). Proliferation is completely suppressed with WT AR or V785A but no other mutants. (F) Relative cell counts at day 7 after transduction. (G and H) Effect of anti-androgens on the relative AR transcriptional activity of transduced PC3 cells (mean \pm SD, n = 5). (I and J) Viability fold change in response to anti-androgens in transduced cells relative to the CNT cells (mean ± SD, n = 3). Differences against CNT (D and F) between anti-androgen treated and nontreated cells (G and H) or against WT (I and J) were calculated using t tests. ns, not significant.



are induced by the selective pressure of anti-androgen therapies (2–3). While few mutations in PCa have been described as oncogenic or drivers (causative of the disease), most are considered passenger or silent mutations, although a contribution to PCa development and/or progression cannot be excluded (29–32).

To date, only three point mutants of the AR-LBD have been structurally characterized out of the over 350 reported variants

(table S1). These oncogenic mutations (W742L, H875Y, and T878A) map to the internal ligand-binding pocket (LBP) and are responsible for rendering the anti-androgens cyproterone acetate, flutamide, and bicalutamide ineffective, respectively. Comparison of the WT AR-LBD and these mutant structures did not reveal any overall conformational changes. However, these mutations change the volume and shape of the LBP allowing the receptor to

remain active even in the presence of antagonists, thus explaining tumor escape from therapeutic control (2, 26–28). On the other hand, there are a wide variety of phenotypes associated with AR gene mutations in patient with AIS, ranging from mild symptoms (MAIS), to partial (PAIS) or completely feminized phenotypes (CAIS) (23–25, 33–34). Expectedly, about half of the CAIS-linked mutations map to the AR-LBD, but only a few of them can be easily rationalized as directly affecting hormone binding (3, 29).

AR-LBD pathogenic mutations outside the LBP may affect ARdependent gene signatures through modulation of the monomeroligomer equilibrium, accessibility of PTM sites, and/or by altering dynamic interactions with coregulators and chromatin. These processes are likely to be intricately intertwined and coupled via allosteric signaling transmission both within the AR monomer and across its dimerization interface (3-7). Here, we present a multidisciplinary investigation of the impact of several mutations of solventexposed AR-LBD residues identified in patients with PCa and/or AIS (Fig. 1A; see table S2 for major information on the studied mutations). Transcriptomic and in vitro cell-based assays demonstrate that these variants affect PCa proliferation and response to anti-androgens. Biochemical and biophysical investigations including high-resolution x-ray structures of mutant AR-LBD showed reduced thermal stability of the isolated domains as well as changes in the flexibility in functional sites of the receptor distal from the mutation site and unexpectedly revealed a previously unobserved rearrangement of the loop-featuring residue Arg⁷⁶¹. The structural reorganization of this loop increases the degree of Arg⁷⁶¹ exposure, which correlated with an apparent increase in the extent of its methylation in cells. Together, our findings point to an intricate interplay between networks of local structural changes at and around the dimerization interface and global AR tertiary and quaternary structures that are coupled to PTM events. In turn, this network has a definite impact on AR transcriptional activity and gene programs that are affected by specific mutations. Our results may serve to predict the structural and functional impact of AR pathogenic mutations and open unexplored avenues for structure-guided modulation of its function in PCa tumors and patients with AIS.

RESULTS

We previously presented the crystal structure of the transcriptionally active, isolated dimeric AR-LBD (6) also corroborated in the multidomain protein (4, 7). The structural analysis revealed that the dimerization interface is a hotspot for mutations identified in patients with PCa and/or AIS [see (3) and table S1]. There was no clear-cut separation between PCa- and AIS-linked mutations, and some of these variants were linked to both conditions, albeit occurring in different developmental stages. These observations prompted us to perform a thorough characterization of the structural changes and functional impact of AR point mutants at the dimerization interface (Fig. 1B).

Mutations at the AR-LBD dimer interface differently affect cell proliferation and response to anti-androgens

To assess the functional impact of point mutations that affect the AR-LBD dimer interface, we generated AR-null PC3 cell lines (CNT) stably expressing either WT AR or mutants Phe⁷⁵⁵Val (F755V) (35–37), Val⁷⁵⁸Ala (V758A) (38–42), Tyr⁷⁶⁴Cys (Y764C)

(36, 39, 42-48), or Gln⁷⁹⁹Glu (Q799E) (39, 42, 44-45, 48-54) (Fig. 1, A and B). As expected, WT expression resulted in a 24.5fold increase in AR transactivation as measured by luciferase reporter expression under the control of a synthetic AR promoter. All four mutants displayed a significantly lower AR transactivation activity compared to WT (Fig. 1C). Further, expression of WT and V758A resulted in a nearly complete inhibition of colony formation (Fig. 1D and fig. S1A) and proliferation (Fig. 1, E and F) compared to CNT cells that were highly statistically significant. Dihydrotestosterone (DHT) treatment of AR-transduced DU145 (fig. S2, B to D) and of AR-sensitive lymph node carcinoma of the prostate (LNCaP) cells (fig. S2, E to G) resulted in comparable growth-suppressive effects that were not observed in AR-negative parental DU145 cells (fig. S2, B to D), in a castration-resistant PCa cell line, 22rv1 (fig. S2, H to J), or in AR-insensitive, nontumor human prostate epithelial cells, RWPE1 (fig. S2, K to M). These observations confirm previous reports on the growth-suppressive effect of AR stimulation in AR-responsive cells (55, 56). In notable contrast, F755V and Q799E had proliferation rates not significantly different from those of the CNT cells, while proliferation was only modestly impaired by Y764C (Fig. 1, E and F). Similarly, colony forming capacity was unchanged for F755V and partially, albeit significantly, reduced in Glu⁷⁹⁹- and Cys⁷⁶⁴-expressing cells (Fig. 1D and

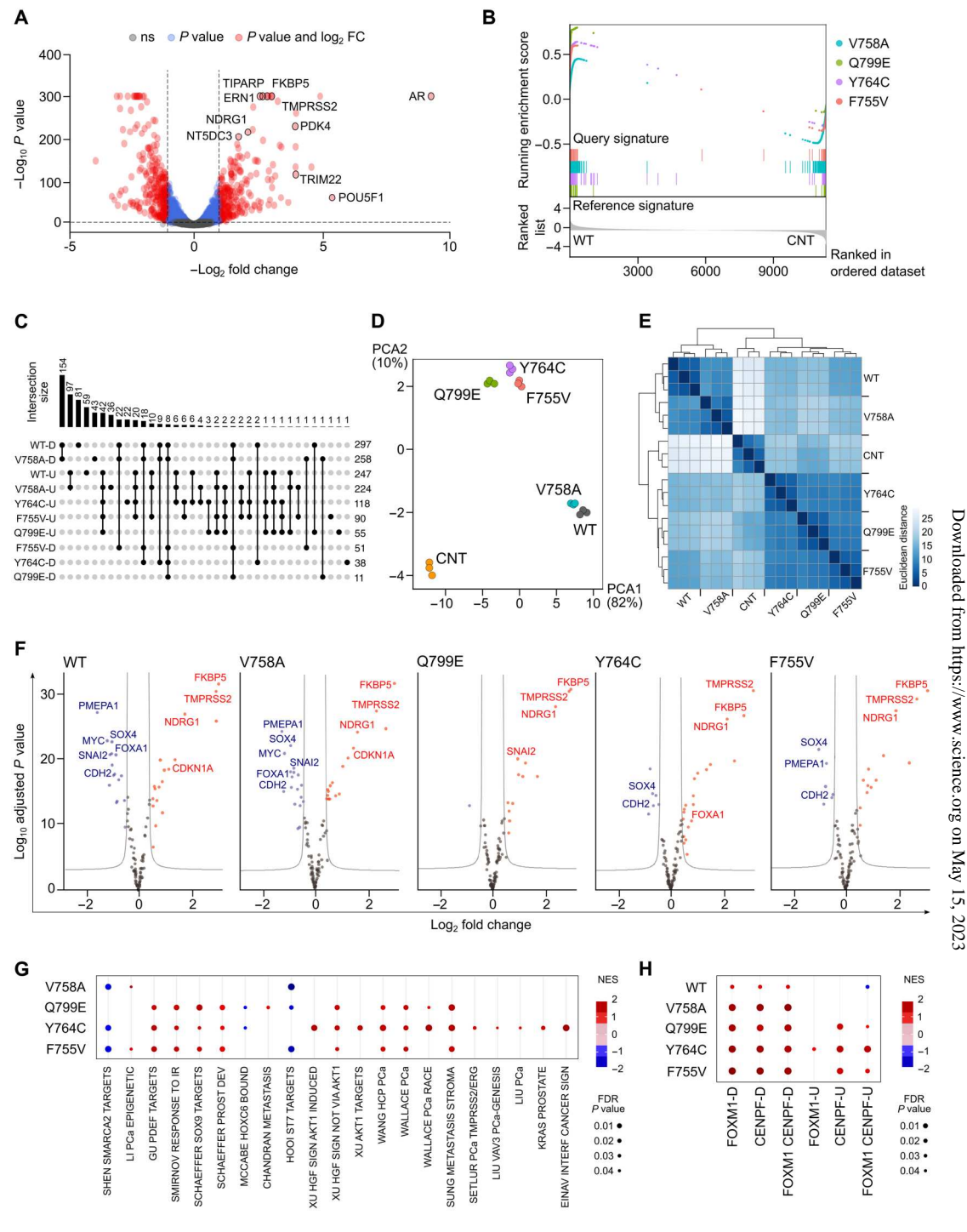
Next, we asked whether the differences in proliferation and clonogenicity displayed by the AR variants would translate into distinct responses to anti-androgenic treatments. WT or mutant AR-expressing cells were treated with enzalutamide (Fig. 1, G and I), abiraterone (Fig. 1, H and J), or apalutamide (fig. S1B), and AR transactivation was measured. Transactivation was significantly inhibited by enzalutamide and abiraterone in both WT and mutant AR cells (Fig. 1, G and H). Reduction in AR transactivation was not a consequence of impaired cell viability upon anti-androgen treatment (Fig. 1, I and J, and fig. S1B). Specifically, V758A cells showed an 11.7, 20.6, and 16.1% increased viability compared to WT when treated with enzalutamide, apalutamide, or abiraterone, respectively. On the contrary, F755V, Y764C, and Q799E mutant cells displayed a significantly increased sensitivity to all three anti-androgens (Fig. 1, I and J, and fig. S1B).

Together, these results indicate that expression of ligand-bound WT AR in AR-null PCa cells induces a quiescent cell phenotype in AR-responsive cells without affecting the response to anti-androgen treatment. The data also demonstrate that, overall, point mutations at the AR dimerization surface negatively impact its ability to suppress proliferation and clonogenicity and mostly sensitize cells to anti-androgens (Fig. 1 and figs. S1, A and B, and S2).

Mutations at the AR-LBD dimer interface profoundly deregulate androgen-dependent transcription programs

Having demonstrated that dimerization surface mutations in the AR-LBD have an important impact on cellular functions, we next investigated whether these mutations alter gene expression patterns (Fig. 2 and fig. S1). Transcriptomic data were generated for WT and each mutant AR and compared to nontransduced cells as control. As expected, AR and canonical AR target genes such as *Transmembrane protease*, serine 2 (TMPRSS2), FK506-binding protein 5 (FKBP5), and TCDD-inducible poly [ADP-ribose] polymerase (TIPARP) were significantly up-regulated in both WT and mutant AR-expressing cells (Fig. 2A and fig. S1C), which was orthogonally

Fig. 2. The transcriptional profiles of AR-LBD dimerization surface mutants differ from that of the WT receptor. The results of RNA-seq experiments conducted in triplicate for each cell line are summarized. (A) Differential expression analysis between CNT and AR-transduced cells. Genes with $|log_2(fold\ change)| \ge 1$ and $P \le 0.05$ are shown in red. (**B**) GSEA demonstrates similar signatures of WT and mutant AR. (C) Differentially expressed genes overlap between WT AR and its mutants. The bar plot (top) indicates the number of genes in the intersection between signatures. Vertical lines (bottom) connect the corresponding overlapping signatures. For each WT and mutant AR, signatures are separately given for up- (U) and down-regulated genes (D), and the size of the gene set is indicated (right). (D and E) Principal component analysis (PCA) and heatmap analysis of transcription profiles identifies three groups: (i) CNT, (ii) V785A and WT, and (iii) F755V, Y764C, and Q799E. (F) Volcano plots of AR target genes for WT and mutant AR. Canonical repressed (blue) and activated (red) AR targets are labeled. Note that repression of genes such as MYC, SOX4, FOXA1, and CDH2 is lost in O799E, Y764C, and F755V but not in V785A. (G) GSEA of the mutant AR signatures against WT AR on prostate cancer gene sets. Note that the V758A signature shows very limited overall enrichment indicating its strong similarity with WT. (H) GSEA of WT and mutant AR against a previously defined PCa malignancy signature (58). Enrichment for up- and down-regulated targets of the malignancy signature drivers forkhead box protein M1 (FOXM1), Centromere Protein F (CENPF), or both are shown separately. Only the F755V, Y764C, and Q799E signatures are enriched in the FOXM1 and/or CENPF regulons. Normal-



ized enrichment score (NES) scale and false discovery rate (FDR) P value thresholds are indicated.

validated in quantitative polymerase chain reaction (qPCR) assays (fig. S1, G and H). In agreement with the functional evidence described above, the V758A mutant displayed AR target gene expression patterns most similar to WT AR (Fig. 2, C to E). Accordingly, gene set enrichment analysis (GSEA) showed that all four mutant AR signatures were similar to the WT signature (Fig. 2B). Although

the AR regulon was conserved in all mutants, there were significant differences between the four variants. V758A showed a dynamic gene expression profile most similar to WT, while the differentially expressed gene (DEG) sets of F755V, Y764C, and Q799E were much smaller and shared fewer target genes compared to WT AR or V758A (Fig. 2C and fig. S1C). Variance assessment and clustering

of expression profiles further confirmed the similarity of WT and V758A transcriptomes, on the one hand, and those of F755V, Y764C, and Q799E, on the other. These two clusters were identified both by a principal components analysis (PCA) (Fig. 2D) and by clustering analysis computing sample-to-sample distances using variance-stabilizing transformation (VST) data (Fig. 2E). Further, gene expression in the AR regulon as defined by the DoRothEA collection of human regulons (57) showed that the set of activated AR target genes in WT and mutants remains largely conserved (Fig. 2F). However, only WT and V758A maintained a repressed gene set that included cancer drivers Forkhead Box A1 (FOXA1) and MYC proto-oncogen (MYC) as well as epithelial-to-mesenchymal transition drivers Snail Family Transcriptional Repressor 2 (SNAI2/SLUG), Cadherin-2 (CDH2, encoding N-cadherin), and SRY-Box Transcription Factor 4 (SOX4) (Fig. 2F and fig. S1I). This is consistent with the important reduction in proliferation and clonogenicity described above (Fig. 1, D to F, and fig. S1A). GSEA analysis of the four AR mutants versus WT signatures evidenced again that V758A was not enriched in any of the PCa signatures in the Molecular Signature Database (MSigDB), as opposed to the significant enrichment demonstrated for F755V, Y764C, and Q799E (Fig. 2G). Accordingly, only these three mutant signatures were found positively enriched in a previously defined up-regulated gene signature strongly associated with poorer outcome in patients with PCa (Fig. 2H) (58).

Last, querying the collection of manually drawn Kyoto Encyclopedia of Genes and Genomes (KEGG) database evidenced an unexpected enrichment for the Y764C mutant in biological pathways associated with pathogen infection and immune response including coronavirus disease 2019 (fig. S1D), which was supported by the significant regulon enrichment in the mediator of type I interferon signaling, STAT2 (fig. S1E), and the activation of the Janus kinase/signal transducers and activators of transcription (JAK/STAT) pathway (fig. S1F) using the DoRothEA and the Pathway RespOnsive GENes (PROGENy) algorithms, respectively. Together, these data suggest that the observed differences in cellular phenotype between the different AR mutants are at least in part the result of a differentially reprogramed transcriptome in which WT and V758A show a less oncogenic and undifferentiated molecular phenotype compared to F755V, Y764C, and Q799E mutants.

AR-LBD interface residue mutations do not compromise domain folding but lead to reduced thermal stability and increased sensitivity to proteolysis

To study the possible structural impact of point mutants located at the AR-LBD dimerization interface, we produced and purified to homogeneity WT AR-LBD and its point mutants F755L, F755V, V758A, Y764C, and Q799E. Next, we characterized these recombinant proteins both biophysically using differential scanning fluorimetry (DSF) and biochemically through limited proteolysis assays (figs. S3 and S4). The results of these experiments demonstrated that all mutants are properly folded but have substantially lower thermal stability compared to the WT protein, as indicated by the reduced melting temperatures ($T_{\rm m}$) (fig. S3, A and B). In line with the RNA sequencing (RNA-seq) results presented above, core dimer interface mutants F755V, F755L, and Y764C exhibited a remarkable drop in $T_{\rm m}$ compared to the WT protein (between 5° and 6°C), the latter being the most thermolabile of all the studied variants. By contrast, the $T_{\rm m}$ of mutants V758A and Q799E was

only 1°C lower than the WT AR-LBD protein, demonstrating WT-like stability (fig. S3, A and B). Energy estimations using FoldX based on previously reported structures of monomeric and dimeric AR-LBD also suggested that the studied missense mutations have an important impact on the domain stability (fig. S3C), both in its monomeric and putative dimeric conformations. Mutations of the core interface, F755V/L and Y764C, are predicted to be particularly deleterious for homodimeric AR-LBD (fig. S3C).

AR-LBD is a highly basic protein domain (isoelectric point: 8.94) with 14 arginines (fig. S4A) and 14 lysines outbalancing 11 negatively charged aspartate or glutamate residues. To assess whether the decrease in thermal stability of AR-LBD point mutants also manifests as an increased sensitivity to proteolysis, we incubated highly purified samples of WT AR-LBD and its point mutants with the endoproteinase, Arg-C, which cleaves peptide bonds at the C-terminus of Arg residues (fig. S4, B to E).

Again, the resulting cleavage pattern of V758A is most similar to that of WT AR-LBD (fig. S4, B, C, E, and F). Although the thermal stabilities of the two mutants are similar (fig. S3, A and B), the proteolytic patterns of V758A and Q799E differ notably (fig. S4, C to F and H). Mutants F755L (fig. S4, B, E, and G), F755V (fig. S4, C, E, and I), and Y764C (fig. S4, D, E, and H) have enhanced proteolytic susceptibility. In summary, point mutations of residues at the AR-LBD homodimerization interface appear to have an unanticipated global impact on the overall domain stability, as evidenced by notably lower $T_{\rm m}$ and enhanced sensitivity to proteolytic attack (figs. S3 and S4).

AR-LBD dimer interface mutants exhibit enhanced flexibility and distinct structural rearrangements both locally and at distant AF-2 and BF-3 sites

The results of the experiments described above demonstrate a large impact of AR-LBD dimer interface mutants on AR transcriptional function, stability, and sensitivity to proteolytic attack. To assess whether these differences are reflected by noticeable structural rearrangements, we expressed crystallized and refined at high resolution the x-ray crystal structures of the V758A, Y764C, F755V, F755L, and Q799E AR-LBD variants (Figs. 3 and 4). All mutant proteins crystallized as monomers in the orthorhombic space group (P212121) (Figs. 3A and 4A and fig. S3D; see fig. S3E and Fig. 4B for comparison; Table 1). The "helical sandwich" fold typical of the nuclear receptor superfamily is conserved (3), and the hormone (DHT) is bound inside the LBP essentially as in WT AR-LBD (Figs. 3A and 4A). The root mean square deviations (RMSDs) for the equivalent Ca atoms between the WT structure [Protein Data Bank (PDB) 1T7T] and the V758A, Y764C, F755V, Q799E, and F755L mutants are 0.29, 0.33, 0.47, 0.52, and 0.54 Å, respectively.

Despite this overall conservation of the global protein fold, superimposition of the current mutant structures on previously solved structures of WT AR-LBD reveals important local structural changes on four specific distant sites of the domain (see Fig. 3A for an overall representation of the domain with these sites highlighted and Fig. 3, B to E for close-ups of these areas): the H5-S1-H7 area (from now on termed "R761 zone," described in detail below) (Fig. 3B), the L1-3 loop, H6, and the C-t end of H11 (Fig. 3C), two major functional sites, the BF-3 pocket comprising H9 and L9-10 (Fig. 3D), and the AF-2 pocket featuring the L3-4 loop and H12 (chaperone and coactivator binding sites, respectively) (Fig. 3E). In particular, several side chains of charged AF-2 residues

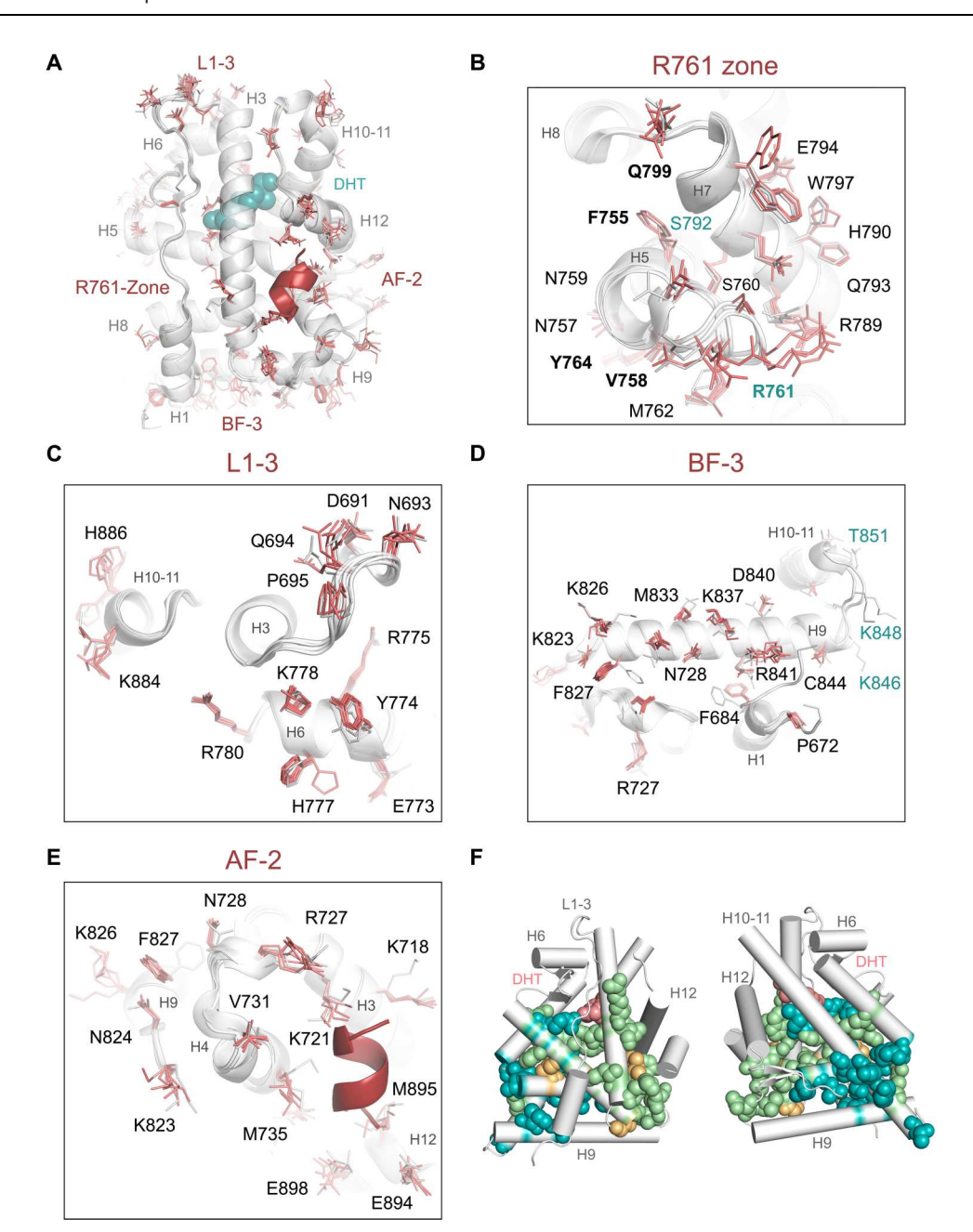


Fig. 3. High-resolution crystal structures of AR-LBD dimer interface mutants reveal local and long-range conformational changes. (**A**) Superimposition of current crystal structures of mutant AR-LBD on WT monomeric (1T7T) and dimeric (5JJM) forms of the domain. Secondary structure elements identical in all structures are depicted as a gray cartoon, with DHT as teal spheres and the AF-2-bound peptide (from 5JJM) in red. Large main- and/or side chain conformational changes cluster in four areas (B to E), highlighted by the major secondary structure elements (coral sticks). (**B**) Dimer interface core lined by H5 and H7, which, in addition to the studied point mutations [Phe⁷⁵⁵ and Val⁷⁵⁸ (H5), Tyr⁷⁶⁴ (S1), and Gln⁷⁹⁹ (H7)] features mostly residues with nonpolar/aromatic side chains, along with the positively charged Arg⁷⁶¹. (**C**) The more distal part of the dimer interface formed by H3 and L1-3 [Tyr⁷⁷⁴ and His⁷⁷⁷ from (B) are shown for orientation]. In this area, several polar residues exhibit noticeable conformational changes. (**D**) BF-3 pocket, where multiple residues exhibit conformational changes, most notably those from H9. (**E**) AF-2 pocket, where in addition to the charge-clamp residues, Lys⁷²¹ and Glu⁸⁹⁴, known to stabilize bound coregulators at this interaction site, the side chains of both charged (Lys⁷¹⁸, Arg⁷²⁷, Lys⁸²³, and Glu⁸⁹⁸) and aliphatic residues (Met⁷³⁵ and Met⁸⁹⁵) display conformational variability. (**F**) Sector 1 (teal) comprises 17 residues in and around H5, H7, H8, H9, and H10-11 (Met⁷⁴³, Phe⁷⁴⁸, Gly⁷⁵¹, Arg⁷⁵³, Leu⁷⁹³, Leu⁷⁹³, Leu⁸⁰⁴, Met⁸⁰⁴, Leu⁸¹¹, Phe⁸¹⁴, Glu⁸³⁸, Ile⁸⁴², Thr⁸⁵¹, Tyr⁸⁵⁸, Thre⁸⁶¹, Lys⁸⁶², and Leu⁸⁶⁴), whereas sector 2 (green) features 20 residues mostly from H3, H5, H7, H8, S3, and H10-11 (Arg⁷¹¹, Leu⁷¹³, Trp⁷¹⁹, Ala⁷²⁰, Lys⁷²¹, Phe⁷²⁶, Leu⁷²⁹, Leu⁸⁰⁵, Leu⁸¹³, Asp⁸²⁰, and Arg⁸⁵⁶). Last, three residues (Gly⁷²⁵ and Ile⁷³⁸ at the AF-2 groove and Phe⁸⁰⁵ at H7) belong to both sectors

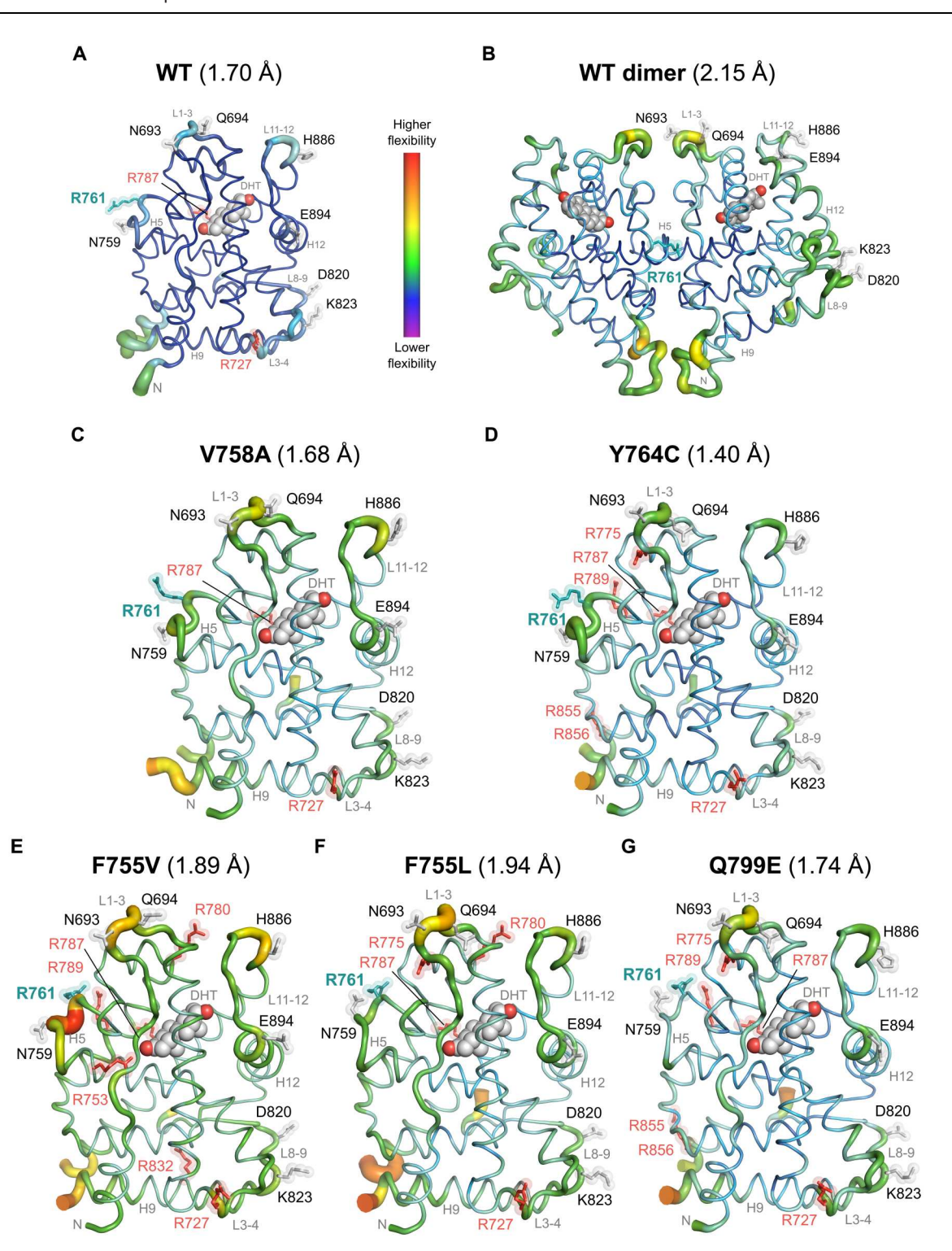


Fig. 4. AR-LBD dimer interface mutants display local flexibility differences. (A to G) Visualization of protein mobility for WT and AR-LBD mutant proteins. Proteins are represented as ribbons sized by temperature factors (B-factors) and colored according to the average B-factors of each residue (i.e., areas with larger atomic displacements appear thicker and are depicted with warmer colors (red, orange, and yellow), whereas those with lower thermal motion are shown thinner and with cold colors (green, blue, and violet). DHT molecules bound inside the LBP pockets are shown as gray spheres with oxygen atoms in red. WT AR-LBD-DHT monomer (A, PDB 1T7T) and dimer (B, PDB 5JJM) are shown for comparison. Note that all mutants exhibit a larger mobility than WT AR-LBD.

	V758A	Y764C	F755V	F755L	Q799E
PDB code	7ZU1	7ZTZ	7ZTX	7ZTV	7ZU2
Wavelength (Å)	0.979	0.979	0.979	0.979	0.979
Resolution range	66.17– 1.68 (1.71–1.68)	65.84– 1.40 (1.42–1.40)	65.82– 1.89 (1.93–1.89)	56.2– 1.94 (1.99–1.94)	44.55– 1.74 (1.77–1.74)
Space group	P2 ₁ 2 ₁ 2 ₁				
Cell constants a, b, c (Å) / α , β , γ (°)	55.62, 66.17, 70.95 / 90, 90, 90	56.39, 65.84, 72.82 / 90, 90, 90	54.57, 65.82, 70.37 / 90, 90, 90	56.18, 65.80, 72.31 / 90, 90, 90	56.51, 66.04, 72.42 / 90, 90, 90
Molecules in the ASU	1	1	1	1	1
Total reflections	176567 (4168)	247697 (9727)	143549 (9454)	84880 (3942)	147708 (8184)
Unique reflections	29533 (1229)	53810 (2576)	20910 (1309)	18026 (1027)	28510 (1559)
Multiplicity	6.0 (3.4)	4.6 (3.8)	6.9 (7.2)	4.7 (3.8)	5.2 (5.2)
Completeness (%)	96.6 (80.4)	99.6 (98.2)	99.9 (100.0)	88.1 (79.8)	100.0 (100.0)
Mean I/sigma(I)	10.3 (0.7)	18.8 (0.5)	8.8 (0.7)	10.4 (2.8)	12.3 (1.5)
Wilson B-factor	27.1	27.0	38.2	22.8	26.1
R-meas	0.084 (2.026)	0.030 (1.692)	0.116 (3.399)	0.093 (0.720)	0.089 (2.398)
R-pim	0.033 (1.015)	0.014 (0.841)	0.045 (1.257)	0.042 (0.363)	0.039 (1.042)
CC1/2	0.998 (0.364)	1.000 (0.395)	0.998 (0.364)	0.989 (0.854)	0.999 (0.337)
Reflections used in refinement	28174	51127	19842	17086	27029
Reflections used for R-free	1235 (4.2)	2619 (4.9)	1020 (4.9)	888 (4.9)	1433 (5.0)
R-work	0.21	0.19	0.20	0.22	0.18
R-free	0.25	0.22	0.25	0.26	0.22
Total number of atoms / Protein / DHT ligand / Water	2135 / 2008 / 21 / 81	2161/2010/21/120	2041 / 1973 / 21 / 32	2066 / 1997 / 21 / 44	2080 / 1985 / 21 / 64
RMS (bonds)	0.007	0.011	0.008	0.007	0.009
RMS (angles)	1.420	1.828	1.606	1.500	1.581
Ramachandran favored (%)	98.76	98.74	98.32	98.33	99.16
Ramachandran allowed (%)	1.24	1.26	1.26	1.25	0.84
Clashscore	5.32	1.23	3.47	2.47	3.7
Average B-factor / Protein (main, side chains) / DHT ligand / Water	40.4 / 40.0 (36.9, 42.8) / 29.1 / 44.4	35.6 / 35.1 (32.0, 38.1) / 25.4 / 42.8	48.2 / 48.1 (44.2, 51.9) / 34.3 / 47.3	37.5 / 37.6 (34.3, 40.8) / 25.3 / 36.3	37.3 / 37.2 (33.3, 40.9) / 26.0 / 41.9

exhibit conformational differences, most notably the so-called charge-clamp residues, Lys⁷²¹ and Glu⁸⁹⁴, which are known to stabilize bound coregulators at this protein-protein interaction site (Fig. 3E). Regarding the BF-3 pocket, and in addition to charged/polar residues such as Arg⁸⁴¹ and Thr⁸⁵¹, also the aromatic Phe⁸²⁷ exhibits a large flexibility (Fig. 3D). Noteworthy, Phe⁸²⁷ and Arg⁸⁴¹ undergo major conformational changes upon small-molecule binding to this surface-exposed pocket (63). Loop L1-3 also exhibits side-chain conformational differences in several residues (Tyr⁷⁷⁴, His⁷⁷⁷, and Lys⁷⁷⁸), which we had previously identified as part of a secondary dimer interface in AR-LBD crystals to generate a tetrameric arrangement of the receptor (Fig. 3C) (6).

These structural variations are also reflected by an overall enhanced flexibility of all mutants compared to WT AR-LBD [average temperature factor (B-factor) of 21.2 for the monomeric AR-LBD; PDB 1T7T], as demonstrated by the higher B-factors of both main and side chain atoms in all variable regions (Fig. 4).

Residues with particularly higher B-factors in the mutants are Asn⁶⁹³ and Gln⁶⁹⁴ (L1-3), Arg⁷²⁷ (L4-5), Asn⁷⁵⁹, and Arg⁷⁶¹, a residue strictly conserved in AR from fish to humans, but not found in other steroidal receptors (H5 and loop H5-S1; fig. S3, F and G), Asp⁸²⁰ and Lys⁸²³ (L9-10), His⁸⁸⁶ (H6), and Glu⁸⁹⁴ (H12) (Fig. 4). Overall, mutants V758A and Y764C are most similar to the WT protein in this regard, while Q799E, F755L, and F755V exhibit increased flexibility in H5, L1-3, and L9-10 (Fig. 4, A to G).

Our previous statistical coupling analysis (SCA) (64) revealed that two groups of correlated residues or "sectors" define the internal circuits linking major interaction sites in the LBD of the related glucocorticoid receptor (GR). To analyze whether the AR-LBD dimerization surface is allosterically coupled to other functional regions, we also performed SCA analysis, which identified 40 residues grouped in two sectors in the upper half of the domain (Fig. 3, F and G). Sector 1 residues cluster around the domain N-terminus (except the DHT ligand, Arg⁷⁵²), while sector 2 comprises LBP and

AF-2 residues. Further, three residues common to both sectors are strategically located to cross-connect the LBP, AF-2, and BF-3 and dimerization interface (Fig. 3, F and G). Together, our results suggest that both sectors link functionally relevant regions thus coupling, e.g., ligand binding to dimerization, coregulator binding, or chaperone docking/release.

To further explore the LBD dynamics and possible allosteric couplings between AR-LBD functional areas, we performed four 1-us-long molecular dynamics (MD) simulations for both WT AR-LBD and all the mutants (Fig. 5). The analysis of the time evolution of the RMSD for all the Ca atoms using the experimental structure of WT AR-LBD as reference confirms that the overall fold of the domain is stable against these point mutations, and all structures show global structural stability. Moreover, global conformations do not vary remarkably for any of the mutants, and their final RMSDs oscillate at around 2 Å (Fig. 5A). To evaluate the flexibility of the mutants in more detail, we analyzed how a given residue fluctuates around a specific position with time. To this end, we quantified the fluctuations for all residues using the averaged root mean square fluctuation (RMSF) value, averaged for the four MD replicas (Fig. 5B). As expected, more flexible regions correspond to those with higher B-factors in the current structures (compare Figs. 4 and 5). To analyze how specific mutations affect the dynamics of the different regions, we calculate the RMSF differences between WT AR and the studied variants (Fig. 5B). The stretch Lys⁸⁸⁴-Val⁸⁸⁸ (H10-H11) presents, for all the mutants, a markedly decreased flexibility compared to WT (Figs. 5B and 3C). On the other hand, the L1-3 loop (residues Cys⁶⁸⁷-Asn⁶⁹³) is notably more flexible in the V758A and F755L mutants. This behavior is also observed in the Q799E mutant, although less pronounced, but neither in Y764C nor in F755V mutants. These two regions are located far from the mutated residues, suggesting that mutations in the AR-LBD dimerization site induce conformational changes in the AF-2 pocket and thus that dimerization and coregulator binding are allosterically coupled.

Next, and to complement the dynamic description of the impact of the different mutations, we quantified local conformational changes by calculating the differences in the average Ca-Ca distances between spatially neighboring residue pairs [extended up to the second coordination shell (SCS); ~9.1 Å]. The results of these $\Delta \overline{R}_{ii}$ analyses are presented in Fig. 5C. Overall, all mutant structures tend to have larger inter-residue distances compared to the WT protein, and some specific groups of residues show remarkable changes in their average pair distances. This is particularly true for residues Lys⁸⁸⁴-His⁸⁸⁶ and Val⁸⁸⁸-Phe⁸⁹² at the C-terminal end of H10-H11 and the L11-12 loop (box A in Fig. 5C). In line with the experimental findings, the R761 zone shows important changes in all the mutants (residues Asn⁷⁵⁹ to Tyr⁷⁶⁴, L5-S1 loop). This region presents two different groups of moving residues, consisting of the stretch from ${\rm Arg}^{789}$ to ${\rm Phe}^{795}$ (H7) and ${\rm Ser}^{754}\text{-Val}^{758}$ of H4-H5 (boxes B1 and B2 in Fig. 5C, respectively). Furthermore, in all mutants, changes in average distances of residues Leu⁷²⁹-Asp⁷³³ (L3-4 loop and N-terminal end of H4-H5) and Gly⁸²¹-Asn⁸²⁴ (S3-9 loop) are coupled (box C in Fig. 5C). However, in this case, changes are negative for mutations Q779E and F755V, both negative and positive for Y764C and V758A mutants, or positive for F755L. Last, residues Cys⁶⁸⁷ to Gln⁶⁹⁴ (L1-3) behave differently in each mutant. For F755L, this region shows negative changes in their average distances to residues ${\rm Ala}^{688}$ - ${\rm Arg}^{711}$ (L1-3 and H3) and the Phe⁷⁶⁵-Leu⁷⁶⁹ stretch (boxes D1 and D2 in Fig. 5C, respectively). Mutant V758A presents fewer changes in the average distances in the same regions, some of which are positive in the first one (box D1 in Fig. 5C). For the Y764C mutant, the first group of distances becomes completely positive, while the second one practically disappears. No noticeable changes were detected for mutants F755V and Q799E. In summary, residue pair distance analysis shows that the different interface mutations induce local conformational changes in AR-LBD. These changes are located far from the mutated residues in line with an allosteric mechanism. Moreover, although some changes are common to all the mutations, markedly different local responses were observed in specific AR regions.

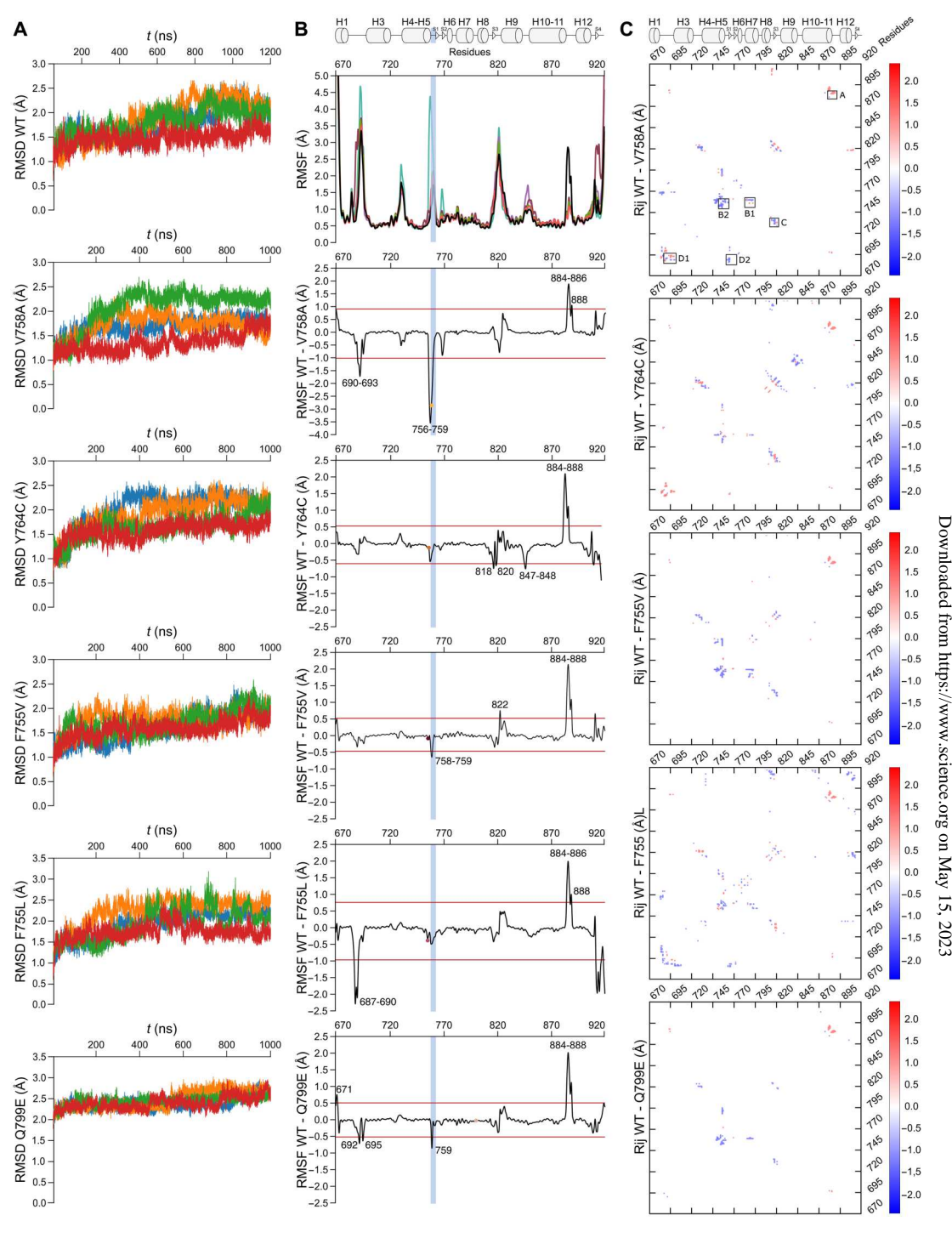
The noncanonical AR-LBD dimerization mode is conserved upon single point mutations of dimer interface residues

Because the studied AR mutations are located at the noncanonical dimerization interface, we next wondered whether they might impair homodimer formation (Fig. 6). We had previously shown that AR-LBD dimerization in solution could be demonstrated with the homo-bifunctional cross-linker, bis(maleimido)ethane (BMOE), which cross-links residue Cys⁶⁸⁷ from two monomers (6). To verify whether mutant proteins are able to dimerize as WT AR-LBD, we incubated purified samples of the recombinant proteins with either BMOE (spacer arm length: 8.0 Å) or a similar cross-linker with a slightly larger spacer arm, 1,4-bis(maleimido)butane (BMB; 10.9 Å) and separated the reaction products by SDS-polyacrylamide gel electrophoresis (SDS-PAGE). The results of these experiments revealed similar patterns of AR-LBD homodimer formation in all cases, indicating that receptor homodimerization is not compromised by point mutations of interface residues (Fig. 6A).

Further, and to assess the possible impact of the studied mutants on the dimerization potential of AR-LBD mutants, we performed docking calculations using normalized interface propensity (NIP) (65) and optimal docking area (ODA) (66) (fig. S5). The computed binding energy of dimeric WT AR-LBD (PDB 5JJM; Fig. 4B; chains B and C, removing residues 845 to 851; Fig. 4B) was similar to that of V758A and Y764C mutants (assuming the same orientation as WT) and more favorable than that of the other mutants. Actually, the electrostatic energy contribution was much larger for WT than for any mutant, while the desolvation energy showed the opposite trend (fig. S5A). The size of the dimer interface as estimated from the buried surface area (BSA) was larger for WT than for the mutants, being V758A the one closest to WT (fig. S5A).

We also built alternative dimer arrangements by docking, based on WT (PDB 5JJM, chain B without residues 845 to 851) and current mutant monomeric structures (fig. S5B). The top ranked model in WT docking matched the x-ray dimer orientation (5.6 Å RMSD), with slightly better binding energy (fig. S5B). For all mutants, we also obtained similar orientations to the experimental dimer (RMSD < 10 Å), although not as the lowest-ranking models (fig. S5B). Binding energies for V758A and Y764C docking dimers were similar to those obtained by superimposition on the x-ray dimer, while in the rest of the mutants, the binding energy of the docking dimer was more favorable (although showing slightly higher RMSD). NIP-based interface hotspot residues predicted from docking (red residues in fig. S5C) were located at the x-ray dimer interface in WT and all mutants (except in F755V, which shows an additional NIP region around Asp 829, Arg 832, and

Fig. 5. Molecular dynamics study of the WT and mutant AR-LBD structures demonstrate overall domain stability coupled with local changes in flexibility. (A) Evolution of the RMSD for WT AR-LBD and the studied mutants along four independent MD runs. All structures converge demonstrating global structural stability. (B) Averaged RMSF of the four MD runs calculated for each structure: WT AR-LBD (black), V758A (blue), Y764C (purple), Q799E (green), F755L (violet), and F755V (red) (top plot). The remaining plots show the differences between the WT and mutant RMSF values. Residues with RMSF values higher than $+2\sigma$ or lower than -2σ (indicating decreased or increased flexibility compared to WT, respectively) are labeled. Only changes with values greater than twice their SDs were considered significant (red lines). Major changes in flexibility around the mutation site were detected only for the V758A mutant. Mutant F755V only shows a small change in this region, while Q799E does not present any changes near the mutated residue but around Asn⁷⁵⁹ instead, in line with the experimental structure. Note that flexibility in the L5-S1 loop is remarkably higher in V758A, F755V, and Q799E compared to WT (blue). On the contrary, the C-terminal end of H10-11 shows lower relative flexibility in all the mutants. (C) Plots of the differences in average pairwise distances $(\Delta \overline{R}_{ii})$, with $\Delta \overline{R}_{ij} = \overline{R}_{ij,WT} - \overline{R}_{ij,mut}$, being $\overline{R}_{ij,\text{WT}}$ and $\overline{R}_{ij,\text{mut}}$ the average distances between $C\alpha$ atoms of residues i and j along the MD trajectories of the WT and mutated structures, respectively. Red and blue represent positive and negative $\Delta \overline{R}_{ii}$ values, corresponding to residue pairs whose average distances decrease or increase due to the mutation, respectively. Only residue pairs with $\Delta \overline{R}_{ii} > 2.50$ or < -1.40, which represent the most significant distance changes, are shown.



Ile⁸³⁶), with residue at position 755 appearing among the highest NIP values in all cases but in F755V. Desolvation areas predicted by ODA surface analysis were mostly located at the x-ray dimer interface in WT and all mutants (fig. S5D), indicating that a large part of the expected dimeric interface has favorable desolvation energy, especially the region around residue position 755. In general,

predicted dimer interfaces from docking experiments and ODA are consistent with the x-ray dimer orientation (6).

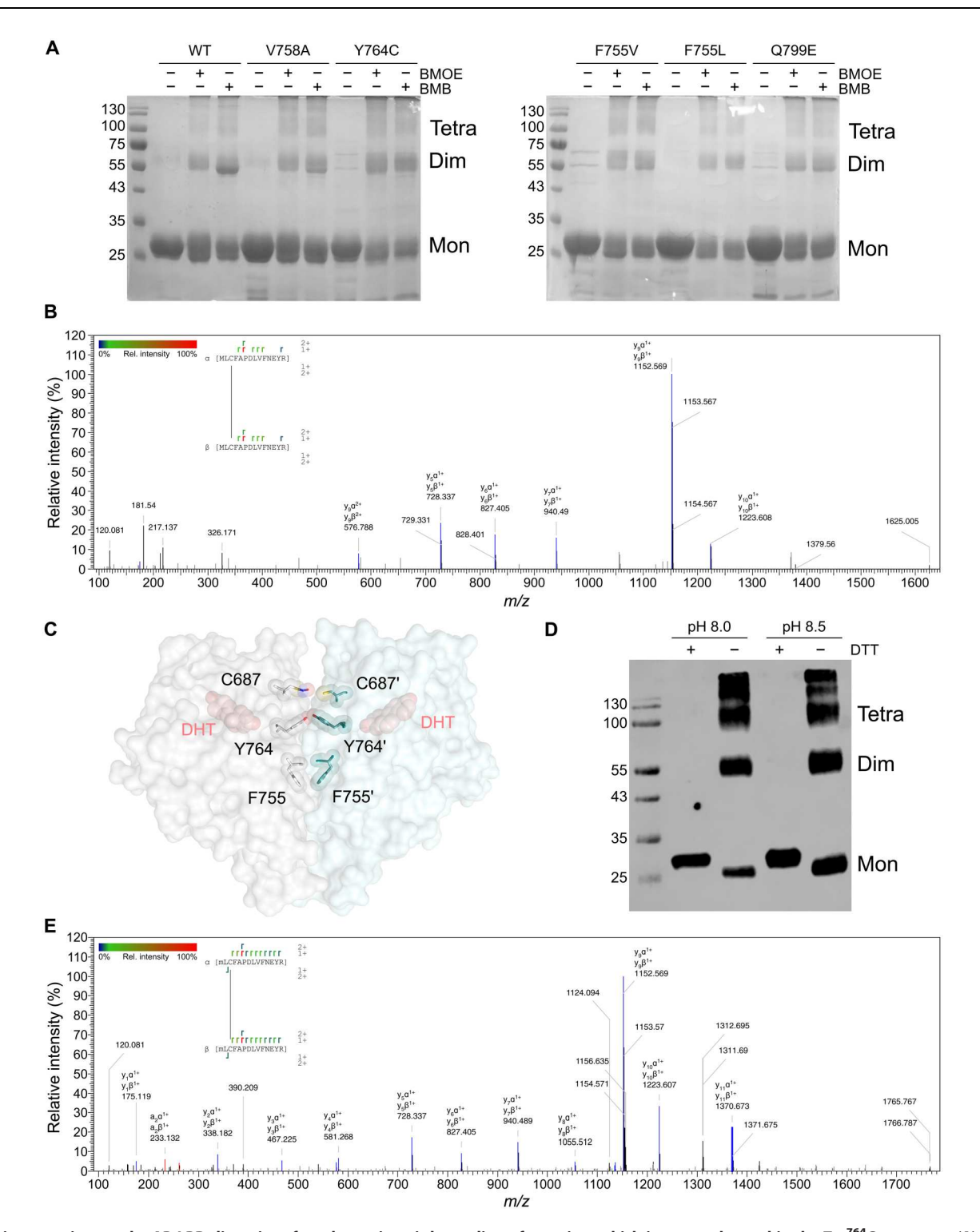


Fig. 6. Point mutations at the AR-LBD dimer interface do not impair homodimer formation, which is even enhanced in the Tyr⁷⁶⁴Cys mutant. (A) SDS-PAGE analysis of WT and mutant AR-LBD samples treated with the bifunctional cross-linkers, BMOE or BMB. Note similar intensities of bands corresponding to dimeric AR-LBD in all cases, indicating that homodimer formation is not compromised by any of the studied point mutants. (B) Representative MS/MS spectra identifying BMB-cross-linked tryptic peptides between Cys⁷⁶⁴ residues from two LBD monomers. (C) Three-dimensional structure of the AR-LBD dimer (PDB 5JJM) in surface representation. Selected interface residues of both monomers [Cys⁶⁸⁷, Tyr⁷⁶⁴, and Phe⁷⁵⁵ (as reference)] are shown as sticks. The DHT molecule is depicted as salmon spheres. (D) SDS-PAGE analysis of AR-LBD(Y764C) behavior under reducing (lanes 2 and 4, +DTT) and nonreducing conditions (lanes 3 and 5, -DTT). Note the spontaneous dimerization in solution when the protein is incubated under nonreducing conditions. (E) Representative MS/MS spectra demonstrating formation of a disulfide bridge between mutant Cys⁷⁶⁴ residues from two LBD monomers. *m/z* stands for mass/charge ratio.

The recurrent point mutation Y764C highlights the ability of AR-LBD dimer interface to adopt different relative orientations in AR homodimers

AR variant Tyr⁷⁶⁴Cys was first identified in a PAIS family and has since been repeatedly reported in AIS and PCa individuals worldwide (36, 39, 42-48). Because this recurrent mutation introduces a solvent-exposed cysteine at the AR-LBD dimerization interface (Fig. 6C), we reasoned that the mutant protein would be more reactive, favoring formation of disulfide-bridged homodimers in solution. Y764C but neither WT AR-LBD nor other mutants tested rapidly forms covalent dimers in solution at basic pH as assessed by nonreducing SDS-PAGE (Fig. 6D). To directly prove that residues Cys⁷⁶⁴/Cys⁷⁶⁴ from each monomer are responsible for disulfide bridge-mediated dimerization in solution, bands corresponding to the AR-LBD(Y764C) dimer were excised from the gel and subjected to enzymatic digestion with endoproteinases trypsin and GluC. Tandem mass spectrometry (MS/MS) analysis of these digests allowed indeed the identification of peaks corresponding to Cys⁷⁶⁴-cross-linked peptides (Fig. 6E and table S3). The dimeric AR-LBD conformation previously identified by x-ray crystallography (Fig. 4B) (6) would not support reaction of neighboring Cys⁷⁶⁴ residues (distance between Cβ atoms: 11 Å; Fig. 5C), but the recent structure of multidomain AR reveals the plasticity of this interface (7). Therefore, and to provide additional evidence of the plasticity of the AR-LBD homodimer, we analyzed by MS/MS the band corresponding to BMB-cross-linked, dimeric AR-LBD(Y764C) (Fig. 6B). The results corroborated the presence of a BMB-mediated linkage between Cys⁷⁶⁴ Sy atoms from two monomers (Fig. 6B and table S4).

The R761 zone undergoes large conformational rearrangements in AR-LBD point mutants

In the AR-LBD homodimer, the major interface is formed by polar and hydrophobic residues from H5, β strand S1, and their connecting loop, with additional contributions made by residues from H1 and H7-H9 and L1-3 (Fig. 7, A and B). The core dimer interface features residues Val^{758} -Arg⁷⁶¹, along with the aromatic residues Trp^{752} , Phe⁷⁵⁵, and Tyr⁷⁶⁴, which are involved in an intricate network of hydrogen bond (H-bond) and van der Waals (VdW) interactions. Most notably, stacked residues Trp⁷⁵² and Phe⁷⁵⁵ rigidify the H5-H5' dimer interface, which is strengthened by strong VdW contacts of the latter with Pro⁸⁰² as well as by H-bonds between the guanidinium group of Arg⁷⁶¹ and the main chain carbonyl oxygen atoms of Glu6⁷⁹, Ala⁶⁸⁰, and/or Glu⁶⁸² from the neighboring monomer (Fig. 7B). Unexpectedly, point mutations F755V/L (Fig. 7, F and G) and Q799E (Fig. 7H) resulted in a fully different conformation of H5-S1 loop residues compared to WT (Fig. 7C). Although residues Val⁷⁵⁵/Leu⁷⁵⁵ occupy essentially the same position as the WT Phe⁷⁵⁵, loss of stabilizing interactions mediated by the Phe⁷⁵⁵ phenol ring ultimately result in the exposure of the downstream Asn⁷⁵⁸-Arg⁷⁶¹ sequence, which deviates by up to 4 Å from the more compact conformation commonly observed in structures of AR-LBD, and in which residue Ser⁷⁶⁰ is essentially buried (Fig. 7, C to H). Most notably, the side chain of Arg^{761} extends into bulk solvent and exhibits various degrees of freedom in the different mutants (Figs. 3B and 7, A to G). These residues are best defined by electron density in the F755L and Q799E crystals, in which the guanidinium group of Arg⁷⁶¹ is sandwiched between the carboxylates of its "own" Glu⁷⁷³ and Asp⁸²⁹ from a crystal neighbor (Fig. 7, G and

H). This extended conformation is stabilized by the side chain of Asn⁷⁵⁹, which accepts an H-bond from the main chain N atom of Arg⁷⁶¹. The proline-like conformation adopted by the preceding residue, Ser⁷⁶⁰, is also noteworthy (Fig. 7G). Important contacts with a crystal neighbor constrain H5-S1 residues from larger displacements (Fig. 7, C to H). We reasoned that, in solution, these rearrangements could lead to even more extensive unfolding of the R761 switch zone. Important residue movements in this region were identified in our current MD simulations, some of which are larger than the deviations between mutant and WT in experimental structures (Fig. 5B and fig. S6).

Full-length AR is preferentially monomethylated in vivo by the methyltransferase, PRMT5, and methylation of Arg⁷⁶¹ is affected by AR-LBD dimer interface disease-linked mutations

Our structural analysis of AR-LBD point mutants that affect the dimer interface revealed important structural rearrangements, which parallel the differences in the transcription profiles of these variants (see above). These observations prompted us to explore possible functional consequences of the studied mutations. Residue Arg⁷⁶¹ adopts a markedly different, more exposed conformation in several mutants (Fig. 8, A to G), and it has been previously reported as a substrate of a major type II arginine methyltransferase with both mono- and symmetrical dimethylation activity, Protein arginine methyltransferase 5 (PRMT5), with important functional implications (18). To assess direct physical interactions between FL AR and endogenous PRMT5 in living cells, we performed proximity-ligation assays (PLA). The results of these experiments demonstrated strong AR-PRMT5 interactions in PC3-WT and PC3-Q799E cells, which were significantly reduced in PRMT5-silenced cells (Fig. 9, A and B; note the 50% loss of AR-PRMT5 interactions for both WT and Q799E). Furthermore, PLA experiments demonstrated arginine monomethylation of FL AR, as well as weaker symmetric dimethylation, which was reduced 50% upon incubation with the PRMT5-specific inhibitor, GSK595 (Fig. 9, D to F). In all PLA experiments, we observed heterogeneous patterns, with some nuclei showing strong AR-PRMT5 or methylation signals while others were practically devoid of these signals (Fig. 9, A and C). We also note that levels of Q799E mutant were remarkably lower in these experiments.

Western blot analysis of immunoprecipitated AR samples verified that Arg residues of both WT and mutant AR proteins were monomethylated in PC3 cells (Fig. 8H). Similar to the results of PLA experiments for the Q799E variant (Fig. 9C), the concentrations of mutant proteins were lower, and comparison of the relative intensities of bands corresponding to total and methylated AR fractions revealed that mutants were methylated to a lower extent. This feature is probably due to enhanced degradation of the mutant proteins, compared to WT AR (figs. S3, A and B, and S4) rather than reduced expression. In this regard, recombinant WT AR-LBD and its mutants are produced at similar levels in a heterologous system (Fig. 8I). In light of the structural information presented above, these findings strongly suggest that residue Arg⁷⁶¹ is preferentially monomethylated by PRMT5 in WT and AR-LBD mutants (Fig. 8H).

In the absence of structural information on the mechanism of recognition and processing of globular, macromolecular substrates by the methylosome (the hetero-octameric PRMT5-MEP50

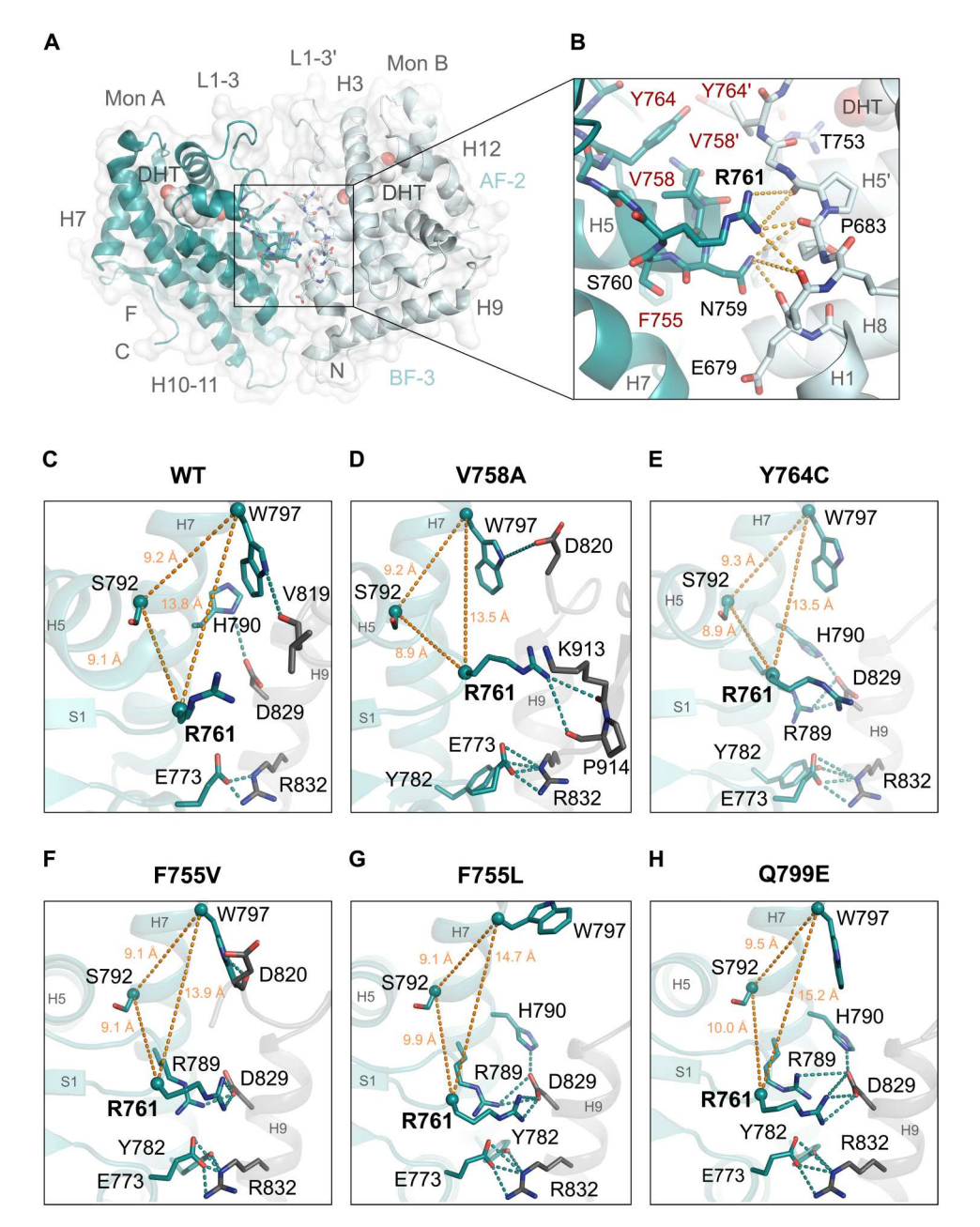


Fig. 7. The R761 zone undergoes large conformational rearrangements in AR-LBD point mutants. (A) Surface and cartoon representation of the AR-LBD-DHT dimer (PDB 5JJM). Residues comprising the core dimer interface are shown as color-coded sticks (oxygen, red; nitrogen, blue; carbon, teal or sky blue). (B) Close-up of the core dimer interface. Interface residues are shown as sticks and labeled. Major interdomain hydrogen bonds are represented as orange dotted lines. (**C** to **H**) Close-ups of the R761 zone in the crystal structures of mutant AR-LBD (teal-colored cartoons). The closest crystal neighbor is also shown in all cases (colored dark gray), to highlight major interactions due to the crystal packing. Residues involved in the crystal contacts are represented as color-coded sticks. Note the tighter contacts involving the Arg⁷⁶¹ side chain in mutants F755V (F), F755L (G), and Q799E (H) compared to WT (C), V758A (D), and Y764C (E), most notably salt bridges with the Asp⁸²⁹ carboxylate from the neighboring monomer. Distances between the posttranslationally modifiable residues, Arg⁷⁶¹ and Ser⁷⁹², and from both of them to the reference residue, Trp⁷⁹⁷, are also given.

complex) and to explore possible binding modes of AR, we performed docking experiments using the current structure of AR-LBD Q799E mutant and previously reported structures of the PRMT5·MEP50 complex (Fig. 9, G and H) (67–70). Similar interactions could be expected for WT AR and other point mutants. The results of these docking experiments suggest how the extended H5-

S1 loop in the AR-LBD would fit into the active site of the methyl-transferase, supported by additional interactions of residues from the neighboring PRMT5 monomer (Fig. 9, G and H). Further, inspection of the docking solutions suggests that the AR-PRMT5 complex might be stabilized by additional interactions of AR-DBD with the N-terminal subunit of the transferase, while the

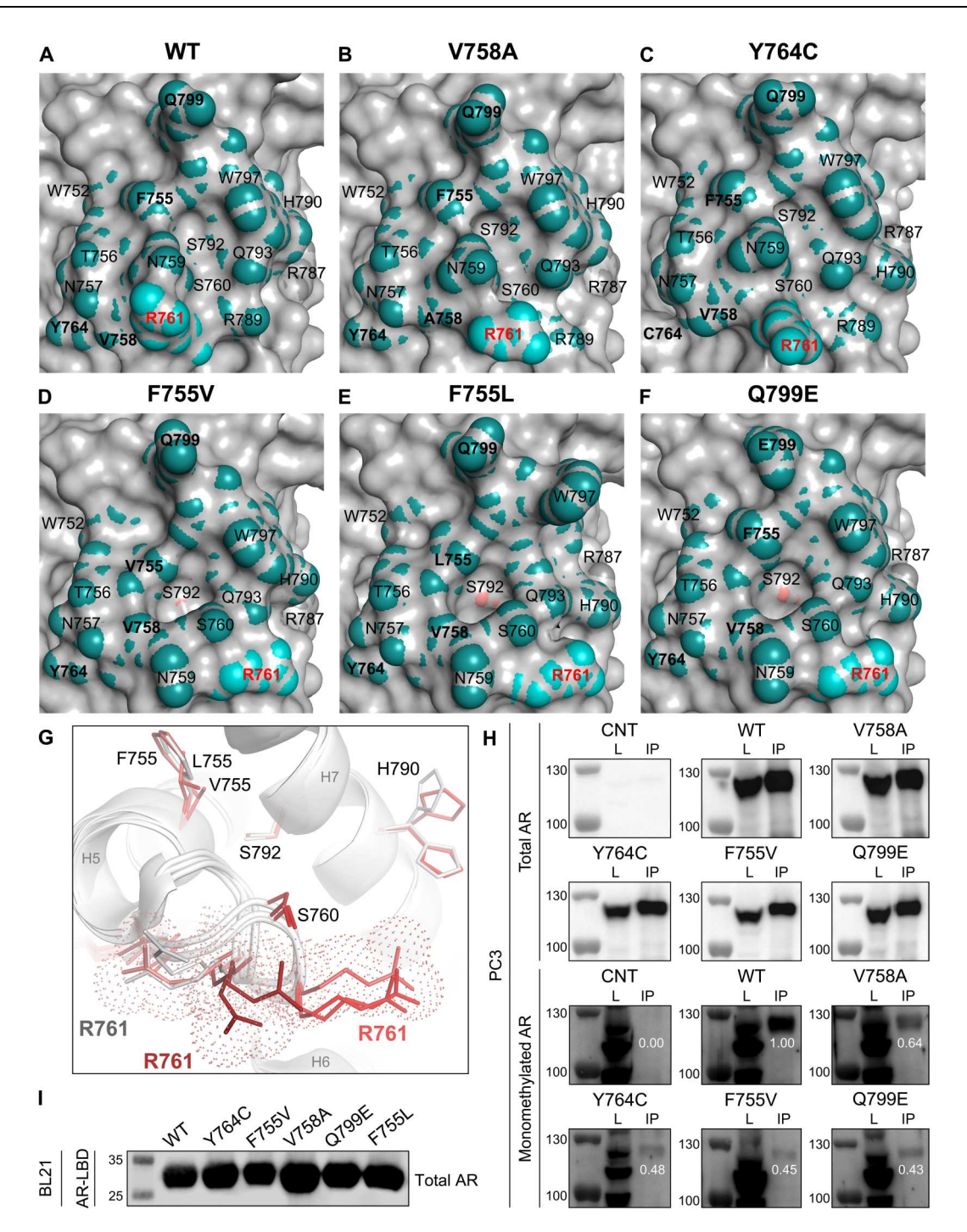
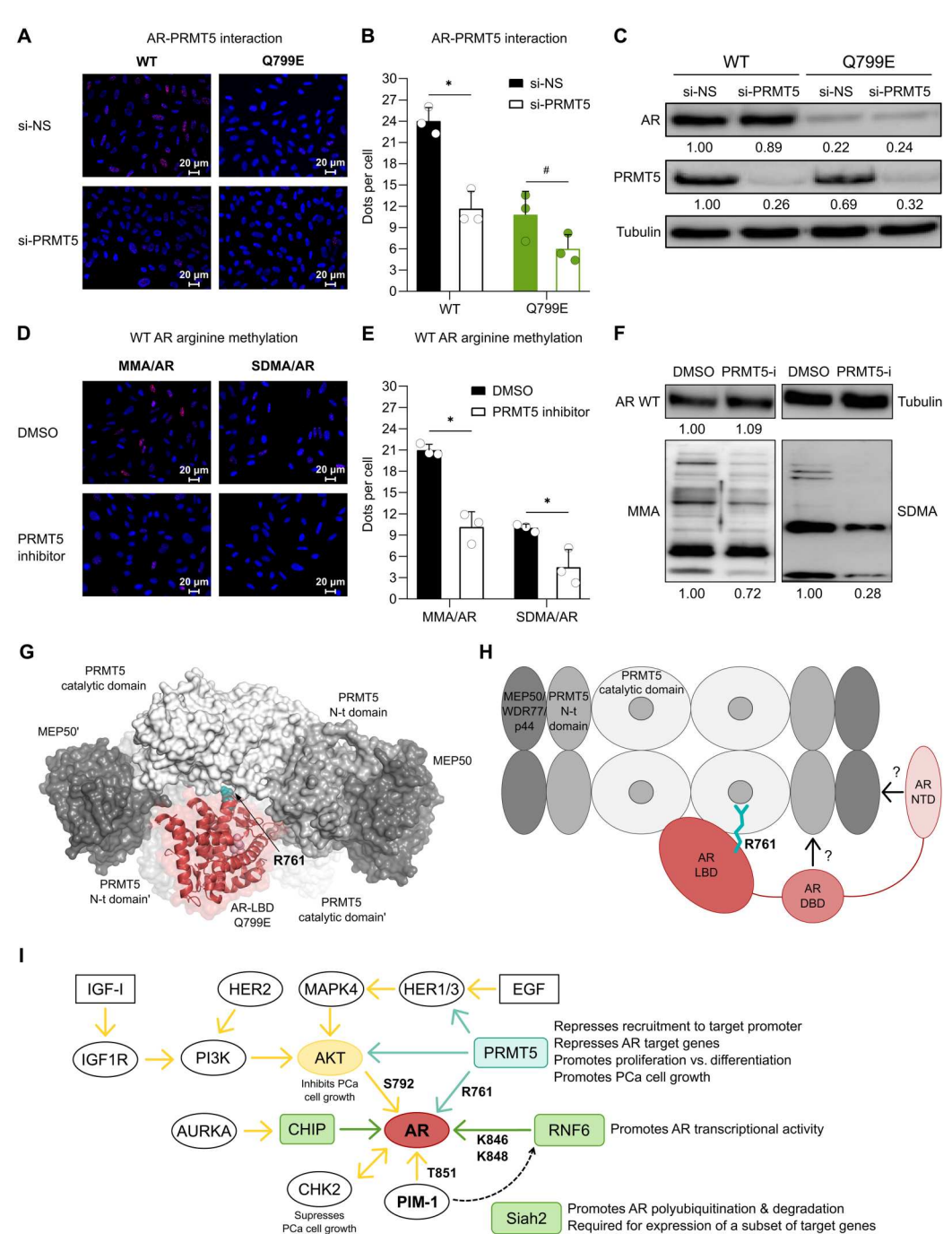


Fig. 8. Arg⁷⁶¹ is more solvent exposed in pathological AR mutations affecting on arginine methylation of the full-length receptor. (A to F) Surface representation of the AR-LBD pocket spanned by residues Trp⁷⁵² and Phe⁷⁵⁵-Val⁷⁵⁸ (H5), Tyr⁷⁶⁴ (S1), Arg⁷⁸⁹-Gln⁷⁹³, Trp⁷⁹⁷, and Gln⁷⁹⁹ (H7) and Asn⁷⁵⁹-Arg⁷⁶¹ (loop H5-S1). All residues are shown as teal spheres superimposed by a gray surface to highlight the pocket topography. Note that conformational changes of Arg⁷⁶¹ (labeled in red) and surrounding residues remodel this pocket thus increasing solvent accessibility of Ser⁷⁹² (salmon), a key phosphorylation site by AKT kinase nested at its bottom. (**G**) Simplified cartoon representation of the Arg⁷⁶¹ zone depicting the major displacement of Arg⁷⁶¹ triggered by the dimerization mutants (different shades of red) relative to the WT position (gray). The pathological mutations induce a dislodgement of loop H5-S1, best appreciated by the different conformations adopted by the Arg⁷⁶¹ side chain: from an intermediate state in V758A and Y764C (dark red, facing the viewer) to a right-oriented, more solvent-exposed position in F755V, F755L and Q799E (in salmon). (**H**) Western blot analysis of total and monomethylated FL AR fractions in PC3 cell lines expressing transduced WT or point mutants of the receptor. L, total lysate; IP, immunoprecipitated fraction. A monoclonal antibody that specifically recognizes monomethylated arginine residues was used for WB. Monomethylated AR bands were double normalized against the total IP AR and against the monomethylated WT AR band (= 1.00), so that monomethylation levels of AR mutants are not biased by the amount of immunoprecipitated proteins. (**I**) Relative expression levels of WT and mutant AR-LBD recombinant domains in BL21 *Escherichia coli* cells.

PRMT5-MEP50 complex. (A) Representative PLA images demonstrating AR-PRMT5 physical interactions (red dots). Nuclei were counterstained with 4',6-diamidino-2-phenylindole (DAPI; blue). PRMT5-silenced cells (si-PRMT5) were compared to nonsilenced cells (si-NS). (B) Quantified PRMT5-AR interactions are shown (mean \pm SEM, n = 3). Differences between si-PRMT5 and si-NS cells were calculated using a t test. (C) Whole-cell extracts from (A) were analyzed and quantified for AR, PRMT5, and tubulin expression by immunoblot. (D) Representative images from AR methylation assessed using PLA with anti-AR and pan-methyl antibodies recognizing mono- (MMA) or symmetrically dimethylated arginine residues (SDMA). Red dots correspond to detected MMA and SDMA WT AR, and nuclei counterstained with DAPI (blue). A PRMT5-specific inhibitor was used to verify that the methylation signal was PRMT5-dependent. (E) The number of detected MMA/ AR and SDMA/AR is shown (mean \pm SEM, n = 3). Differences between catalytically active and inhibited PRMT5 cells were calculated using a t test. (F) Whole-cell extracts from (D) were analyzed and quantified for total AR, MMA-, and SDMA-protein patterns and tubulin expression by immunoblot. Note that, while SDMA can be mediated only by PRMT5 and PRMT9, MMA can be catalyzed by type I and II PRMTs. This explains the larger impact of the PRMT5specific inhibitor on the SDMA fraction. (G) Model of AR-LBD(Q799E) approaching the active site of the PRMT5-MEP50 methylosome. For simplicity, only a heterotetrameric (PRMT5)₂·(MEP50)₂ complex is shown (PDB 4GQB). Note that folded substrates such as AR-LBD would interact with two neighboring catalytic subunits, in addition to NTD-MEP50 and DBD-PRMT5 contacts. (H) Diagram of putative interactions between AR domains and the methylosome. (I) Summary of PTMs affecting the AR-LBD.



Note that PRMT5 regulates the cascade at different levels, including epidermal growth factor receptor (EGFR/HER1), protein kinase B (AKT), and AR. Phosphorylation (yellow), methylation (blue), and ubiquitination (green) pathways are shown: insulin-like growth factor 1 (IGF-I), insulin-like growth factor 1 receptor (IGF-1R), epidermal growth factor (EGF), epidermal growth factor receptor (HER1, 2 or 3), phosphoinositide 3-kinase (PI3K), mitogen-activated protein kinase 4 (MAPK4), aurora kinase A (AURKA), clonal hematopoiesis of indeterminate potential (CHIP), ring finger protein 6 (RNF6), checkpoint kinase 2 (CHK2), proto-oncogene serine/threonine-protein kinase (PIM-1) and E3 ubiquitin-protein ligase (Siah2).

MEP50/WDR77 component could recognize methylated Arg residues within the AR-NTD (Fig. 9, G and H). Synergy between these different interactions would ultimately provide the necessary energy to enforce structural rearrangements required to insert the nonglycine side chains of Ser⁷⁶⁰ and Met⁷⁶² in the corresponding subsites of the enzyme, thus allowing methylation of residue Arg⁷⁶¹.

DISCUSSION

Although missense mutations of the AR gene have repeatedly been associated with conditions such as PCa and AIS (29), the molecular mechanisms of disease causation and the affected pathways remain poorly understood to date. Previous structural analyses of AR point mutants have been limited to internal residues that line the LBP, which are particularly relevant because of their association with resistance to anti-androgen therapy in patients with PCa (e.g., W742L, H875Y, and T878A) (26–28). Here, we present a thorough multidisciplinary analysis of the structural and functional impact of several mutations that are buried at the AR-LBD dimer interface (6) and which have been repeatedly linked to either AIS and/or PCa (F755L/V, V758A, Y764C, and Q799E). Although being essentially solvent-exposed residues in monomeric AR and thus unlikely to compromise the overall folding of the protein, we show that these disease-linked variants have significant structural and functional implications. Most notably, transcriptomic analysis demonstrated that, despite overall conservation of AR programs, notable differences exist at the transcriptional level between WT AR and most mutants, including key drivers of PCa progression such as FOXA1 and MYC. In general, mutations at the AR-LBD dimer interface impaired AR's ability to halt proliferation and colony formation while retaining sensitivity to AR targeting drugs, consistent with a role for the nuclear factor as master regulator of differentiation (58). The growth-suppressive role for ligand-bound AR had previously been shown (55, 56) and has been the basis for the proposed supraphysiologic testosterone treatment in patients with PCa that is being evaluated in clinical settings as part of the bipolar androgen therapy (71). Mechanistically, AR signaling has been shown to be dichotomous, promoting or repressing growth at low or high activity levels, respectively (72), and distinct transcriptional outputs have been identified for patients responding to supraphysiologic testosterone (73).

These large differences in transcriptional programs were paralleled by a largely reduced stability of the mutant AR-LBD modules, as indicated by notably lower T_m of up to 6°C and increased sensitivity to proteolysis in F755L/V and Y764C. Our current high-resolution crystal structures of the mutant domains reveal, in addition to changes in the targeted dimerization interface, an increased propensity to side chain movements of residues that cluster in previously described functional areas of the receptor: the exposed AF-2 and BF-3 pockets but also in the minor dimerization site identified in our previous crystal structure of multimeric AR-LBD and which evokes the tetrameric assemblies identified in living cells (6). Similar movements were also identified in MD simulations of mutant proteins (Fig. 5 and fig. S6). Structural rearrangements are particularly noteworthy in variants F755L/V and Q799E, in which residues of the R761 zone (H5-S1 loop) adopt a previously not observed, much more solvent-exposed conformation, which deviates by up to 4 Å from that observed in all previously reported structures of AR-LBD bound to both agonists and antagonists.

On the other hand, introduction of a cysteine in a solventexposed position at the dimer interface (Y764C) increases the propensity to nonproductive dimer formation, particularly in the crowded nuclear environment and likely further conformational changes in the FL protein. In this regard, the recently presented low-resolution cryo-EM structures of the core AR have revealed, in addition to an "entrenched" arrangement, which would correspond to our previously presented structure of dimeric AR-LBD (6), a more open or "splayed" assembly of AR monomers (7).

Our previous MD simulations of the V758A mutant indicated allosterically transmitted conformational changes in the AR-LBD (41). The current crystal structures of AR-LBD point mutations that affect the dimerization interface confirm and extend these observations. These replacements induce conformational changes at areas located in the diametrically opposed pole of the domain, most notably the AF-2 binding pocket (Figs. 1B and 3E). This is the first time that a mutation in the AR-LBD dimerization site has been linked to conformational changes in the AF-2 pocket, suggesting that dimerization and coregulators binding are allosterically coupled. Careful inspection of the crystal structures supported by MD and SCA analyses suggests allosteric pathways connecting the dimer interface with the LBP and the AF-2 and BF-3 sites in AR-LBD.

Previous investigations have revealed several functional defects in the studied mutants, including a lower affinity for agonists, which, at least in the case of Y764C, was shown to result from a more rapid dissociation of ligands without significant changes in the LBP, a significant to near complete loss of NTD-LBD (N/C) interactions, and a largely reduced transcriptional activity, particularly at physiological DHT concentrations (summarized in table S2). Together, these functional findings are in line with our current structural observations of increased mobility of AR-LBD mutants and have important consequences for the structure-function relationship of the receptor. First, the overall decrease in domain stability together with subtle displacements of AF-2 residues might impair both intra- (N-/C-terminal) and intermolecular interactions (with coactivators and corepressors). Conversely, the presence of the NTD would seem to stabilize the LBD upon N-/C- interactions, as suggested by the lower thermostability of a double mutant with a shortened polyQ stretch in the NTD in addition to the Y764C point mutation (43). This is also in line with the cryo-EM structures of FL AR, which revealed a compact conformation with a central LBD surrounded by the NTD (4, 7), and with our recent identification of NTD-LBD interactions (74-75). Second, even mutations that do not affect the LBP directly can have a profound impact on DHT affinity, by facilitating its dissociation from the internal binding site. In this regard, hormone trafficking in and out the LBP is likely to involve displacements of residues in the H5-S1 loop similar to the ones observed in our current crystal structures or perhaps of a larger magnitude. N/C interactions of the Q799E mutant were normal, however (48), highlighting the unique molecular fingerprint of each mutation.

The PCa-associated transcription factor, estrogen-responsive gene (ERG), was previously shown to recruit protein arginine methyltransferase PRMT5 to AR-target genes (18). PRMT5 then methylates AR at position 761, ultimately down-regulating AR transcriptional activity. Here, we corroborate and extend these findings by showing a direct physical interaction of endogenous PRMT5 with both WT and the Q799E mutant of FL AR in living cells. Further, we verified that AR is both mono- and, to a lesser extent, symmetrically dimethylated in cells in a PRMT5-dependent manner (Fig. 9, A to F). The presence of nonglycine residues both before and after Arg⁷⁶¹ would seem to make its methylation less favorable than canonical Gly-Arg-Gly motifs, in light of current structural evidence for PRMT5 (68-69) and other methylases (76). However, a recent systematic analysis of the human methylome has revealed a large number of substrates with bulky side chains preceding and/or following the modified arginine (77). Our docking experiments suggest that Arg⁷⁶¹ processing by the octameric (PRMT5)₄·(MEP50)₄ heterocomplex known as methylosome would depend on secondary interactions of residues in the immediate vicinity of the methylated arginine, on the one side, and exposed residues of the PRMT5 catalytic domain and the N-terminal subunit of a neighboring molecule in the methylosome, on the other. Substrate recognition might be assisted by additional interactions with the highly acidic noncatalytic subunit of the methylosome, MEP50/WDR77, which have been shown to orient substrate histones toward the buried active site of PRMT5 (78). A summary of predicted AR interactions with the methylosome that might ultimately determine specific recognition and processing of Arg⁷⁶¹ is schematically presented in Fig. 9 (G and H).

Although the more exposed, protruding conformation of Arg⁷⁶¹ in AR-LBD mutants would favor recognition and processing by the methylosome, we have actually observed a decrease in the total and methylated fractions of the studied AR mutants in cells. Point mutants of the AR-LBD are unlikely to affect protein expression, and we have observed similar expression levels of recombinant WT AR-LBD and its mutants. Therefore, this apparent contradiction points to an enhanced degradation of mutant AR protein. AR is polyubiquitinated by several E3 ligases (Fig. 9I), followed by its degradation in the proteasome. The tumor suppressor, C terminus of Hsp70-interacting protein (CHIP), appears to be particularly relevant in this regard, as it couples the chaperone machinery to AR degradation, inducing mitotic arrest (79, 80). Of particular clinical relevance, CHIP has been shown to modulate sensitivity to anti-androgen therapy in advanced PCa (81). These findings are also important with regard to the current development of proteolysis targeting chimeras as pharmacological alternatives for PCa treatment (82, 83).

Multiple additional connections between the PRMT5·MEP50 methylosome, AR pathophysiological activity, and PCa etiology have been reported. PRMT5 functions as an epigenetic activator of AR transcription in PCa (84), while the noncatalytic methylosome component, MEP50 (also termed androgen coactivator p44), has been previously identified as an AR interactor linked to PCa progression, which enhances AR-driven gene expression independently of PRMT5 catalytic activity. Accordingly, MEP50 expression levels are higher in PCa tissue than in adjacent, normal prostate tissue (85), and it has been associated with androgen-independent PCa (86). Further, MEP50 is required for homeostasis of prostate epithelial cells by controlling the proper expression of AR-target genes, and its translocation from the nucleus into the cytoplasm in PCa cells results in exacerbated proliferation of prostate epithelial cells (87). Together, the close relationship between methylosome and AR activity at the light of our current observations provokes a systematic analysis of AR methylation in patients with PCa and suggests avenues for therapeutic intervention, in particular in TMPRSS2:ERG-positive PCa (18).

Another important PRMT5 substrate, AKT kinase, is also methylated at a noncanonical sequence that resembles the AR-LBD modification site (Gln-Arg-Leu) (88). The side chain of the methylated arginine residue, Arg³⁹¹, is fully buried in the AKT protein core, indicating that large conformational changes are not uncommon in PRMT5 substrates. This finding is also relevant because AKT has been shown to phosphorylate AR at two canonical RXRXX(S/T) sites, Ser²¹³ in the NTD and Ser⁷⁹² in the LBD (*12–15*). Noteworthy, Ser⁷⁹² is located close to Arg⁷⁶¹, and it is more exposed in the mutants with an open H5-S1 loop. However, we have not detected significant differences in the degree of phosphorylation between WT and mutant AR.

Inspection of the AR-LBD 3D structure reveals that the dimerization interface comprises, in addition to Arg⁷⁶¹ and the nearby Ser⁷⁹², several residues that have been previously reported as targets of PTMs (Figs. 1A and 9I). This extended patch includes in particular the pair of lysine residues at positions 846 and 848, which are ubiquitinated by RNF6 to modulate coactivator recruitment and AR transcriptional activity (16). Last, residue Thr⁸⁵¹ is phosphorylated by the PIM-1L isoform of this Ser/Thr kinase, which stabilizes AR by recruiting RNF6 (17). The phosphomimetic Thr⁸⁵¹Asp mutation resulted in increased transcriptional activity due to enhanced recruitment of coactivators at AF-2 (89), mirroring the impact of several point mutations at the dimer interface characthe impact of several point mutations at the dimer interface characterized in the current work. Together, this AR surface emerges as a major hotspot for PTMs (a summary of AR-LBD PTMs and their functional consequences is given in Fig. 9I). These findings underscore the realization that PTMs regulating DNA accessibility and transcription not only are not limited to histones but also affect also other elements of the transcription machinery (extended histone code) (90). Future investigations should depend on the cross-talk between PTMs and AR quaternary structure including interdomain motions and allosteric pathways connecting the different functional areas of the reader feature and their invest on its interest. functional areas of the nuclear factor and their impact on its interactions with specific coregulatory proteins and its proteasome-mediated degradation.

In summary, the results of our multidisciplinary approach reveal a complex landscape of structure and function alterations induced by mostly conservative mutations that affect the dimerization interface of the AR-LBD, which opens various avenues for structureguided modulation of AR function. The characterization of AR mutations presented here through a combination of complementary structural (x-ray crystallography coupled with docking experiments and MD simulations) and functional assays including transcriptome analysis could be straightforwardly extended to other pathological AR mutants including other oncogenic forms of the receptor. Early prognosis and precision pharmacology of ARlinked diseases would benefit from this integration of structural and cell biology studies under consideration of the interplay between AR mutations and PTM-driven pathology. Eventually, it might be possible to comprehensibly link all AR mutations to specific PCa subtypes, as has been achieved for the related estrogen receptor in breast cancer (21-22), as an important step toward truly personalized treatment of patients with PCa.

Our results open various avenues for structure-guided modulation of AR function. The future of precision pharmacology to tackle AR-linked diseases and also for the prognosis and treatment of patients with PCa needs to integrate structural biology with studies of cellular effects of mutations and PTM-driven pathology.

MATERIALS AND METHODS

Cell lines and plasmids

PC3, DU145, LNCaP, 22rv1, and RWPE-1 cell lines were purchased from and authenticated by ATCC (American Type Culture Collection). For maintenance, cells were cultured in RPMI 1640 or Dulbecco's modified Eagle's medium (DMEM), respectively, supplemented with 10% fetal bovine serum (FBS). For functional assay, cells were depleted of androgens using 10% charcoal-stripped serum (CSS; Thermo Fisher Scientific). Site-directed mutagenesis of a commercial lentiviral AR plasmid (pLENTI6.3/AR-GC-E2325, plasmid #85128, Addgene) was conducted to generate variants AR-F755V, AR-V758A, AR-Y764C, and AR-Q799E. For lentivirus production, human embryonic kidney 293FT (HEK293-FT) cells were cultured in DMEM (Thermo Fisher Scientific), and the lentiviral packaging vectors psPAX2 and pCMV-VSV-G were cotransfected in polyethylenimine (1 mg/ml) containing Opti-MEM (Thermo Fisher Scientific). After viral transduction using supernatants supplemented with polybrene (8 µg/ml), PC3 cells were incubated for 48 hours and selected with blasticidin (5 µg/ml) to generate control, WT AR, and mutants cell lines.

Luciferase reporter assay

To assess AR transcriptional activity, a luciferase-based assay was performed in PC3 cells, which were seeded (15,000 cells per well) in white with clear flat-bottom 96-well plates (RPMI 1640 media supplemented with 10% CSS). After 24 hours, 50% confluent cells were transfected using a Lipofectamine 2000 transfection reagent (Thermo Fisher Scientific), following the manufacturer's instructions. Renilla luciferase expression is controlled by a constitutive promoter for normalization (pRL-TK Renilla luciferase, Promega). On the other hand, Firefly luciferase plasmid (pARE-4X-Luciferase) contains four androgen response elements (AREs) cloned in tandem into pGL3 (Promega) (91). Transfection was performed using 100 ng of pARE-4X-Luciferase and 10 ng of pRL-TK Renilla luciferase. Both luciferases are monomeric and neither requires posttranslational processing, so they can function as genetic coreporters immediately upon translation.

Transfection mixes were prepared in Opti-MEM I (Thermo Fisher Scientific). Six hours after transfection, the medium was aspirated and replaced with RPMI 1640 media supplemented with 10% CSS. For the assay testing the transactivation level of AR mutants, cells were stimulated 24 hours after transfection for 4 hours with vehicle or 20 nM DHT. For luciferase assay testing AR mutants' resistance to PCa treatment drugs, cells were treated for 30 min with abiraterone (40 or 80 µM) or enzalutamide (50 or 200 µM) before 20-nM DHT stimulation for 4 hours. Luciferase activity was measured after cell incubation with the corresponding compounds with the Dual-Glo Luciferase Assay System (Promega) using an EnSpire Alpha plate reader (PerkinElmer). After background subtraction, the ratio of firefly to Renilla luciferase activity was calculated. Assays were performed in three independent experiments with five internal replicates each. GraphPad Prism 8.0 software was used to perform the statistical analyses using t test, once confirmed the normal distribution of the values.

Functional cell assays Colony formation and proliferation assays

Approximately 30,000 PC3 cells were seeded in six-well plates and grown in RPMI 1640 media supplemented with 10% CSS, in two independent replicates for each experiment. The next day (day 1), cells were stimulated with 20 nM DHT. The stimulation was repeated every 2 days. Colonies were grown until day 9 and stained with crystal violet [0.5% (w/v) in 10% ethanol and 90% formaldehyde]. After 30 min of incubation and several washes with water, colonies were scanned and quantified using ImageJ software (https://imagej. nih.gov/ij/). Colony formation capacity was normalized to control cells. Statistical analysis was performed using t test, showing the differences with respect to PC3 WT AR. For colony formation assays in other cell lines, cells were seeded on the basis of their proliferation rate (DU145: 8000 cells per well; RWPE-1: 20,000 cells per well; 22Rv1: 30,000 cells per well; LNCaP: 80,000 cells per well). While DU145 and RWPE cells were cultured in CSS for this assay, 22Rv1 and LNCaP were cultured in FBS to prevent them from stopping proliferation. In all cases, media were supplemented with increasing concentrations of DHT.

Proliferation assays

Cells were trypsinized and counted (with trypan blue stain to discriminate living cells) every 2 days, starting at day 3 and finishing at day 7, to follow the time course growth. To compare proliferation at

day 7, to follow the time course growth. To compare proliferation at day 7, the number of cells of each PC3 variant was normalized to their corresponding nonstimulated control (without DHT). Statistical analysis was performed using t test, showing the differences with respect to PC3 WT AR. **MTT cell viability assays**Approximately 4000 cells (n = 6) were seeded in 96-well plates in RPMI 1640 media containing 10% CSS. Cells were supplemented the next day with DHT combined with abiraterone acetate (Memorial Sloan Kettering Cancer Center), enzalutamide (MDV3100; Sigma-Aldrich), or applutamide (Jansen) at different concentrations. Sigma-Aldrich), or apalutamide (Janssen) at different concentrations. After 72 hours, cells were treated for 3 hours with 10 µl per well of MTT [3-(4,5-dimethylthiazol-2-yl)-2,5-diphenyltetrazolium bromide; 5 mg/ml], a yellow tetrazole that is reduced to purple formazan crystals by living cells. Formazan crystals were dissolved with 100 µl of solubilization buffer (10% SDS and 10 mM HCl) for 3 hours. Plates were read at optical density = 560 nm in a spectrophotometer, and then the percentage of viable cells compared to the untreated wells was determined. In the case of abiraterone, the inhibitory concentration was calculated using nonlinear regression fit in GraphPad Prism 8.0 software, normalizing to untreated cells. Statistical analysis was performed using parametric paired t test comparing each PC3 AR-mutant regression curve versus PC3 WT AR. Because of drug resistance of PC3 cells against enzalutamide and apalutamide, data did not fit nonlinear regression models. To compare enzalutamide and apalutamide resistance, normalized cell viability (at 50 μM enzalutamide or 100 μM apalutamide) was expressed as a fold change percentage with respect to WT AR. Statistical analysis was performed using a t test, showing the differences between the PC3 WT AR and its mutants. For viability assays of other cell lines, cells were seeded to reach confluence (90%) at the end of the experiment (DU145: 2500 cells per well; LNCaP, 22Rv1, and RWPE-1: 5000 cells per well). While DU145 and RWPE were cultured in CSS for this assay, 22Rv1 and LNCaP were cultured in FBS to prevent them from stopping proliferation. In both cases, media were supplemented with increasing concentrations of DHT.

Immunoprecipitation and Western blotting

For immunoprecipitation (IP) of FL AR, PC3 cells were scraped off the plate and transferred to a microcentrifuge tube using lysis buffer (LyB) containing 50 mM tris, 150 mM NaCl, 0.2% NP-40, and 10% glycerol supplemented with protease inhibitor cocktail (Roche), 1% phosphatase inhibitor cocktail 3 (Sigma-Aldrich), and 0.5% phenylmethylsulfonyl fluoride (Sigma-Aldrich) (in following, inhibitor mix). Samples were sonicated on ice three times for 5 s each, 30% amplitude, and centrifuged. IP of the collected supernatant was performed using magnetic beads (Protein G and Protein A Mag Sepharose beads, Thermo Fisher Scientific). AR XP (1:50; Cell Signaling, 5153) and immunoglobulin G (IgG; 1:50; rabbit IgG polyclonal-isotype control, Abcam) antibodies were preincubated for 1 hour with 25 μl of A + G beads (1:1) at 4°C, and cell lysates (1.6 mg) were precleared with 5 µl of A + G beads (1:1). Beads were removed from the precleared lysates and then transferred into AR or IgG tubes for IP at 4°C overnight in a rotating wheel. Afterward, beads from the negative control (IgG tubes) and the immunoprecipitated samples were washed twice with LyB and five times with LyB lacking NaCl. Last, beads were eluted with 70 µl of Laemmli buffer containing 10% β-mercaptoethanol for 5 min at 98°C, and samples were analyzed by Western blotting.

For Western blot analysis of total protein extracts, PC3 cells were lysed with 1× radioimmunoprecipitation assay (RIPA) buffer [10 mM tris-HCl (pH 7.5), 0.1% SDS, 1% deoxycholate sodium salt, 1% triton X-100, 0.15 M NaCl, and 1 mM EDTA] supplemented with inhibitor mix. Proteins (30 µg per lane) were resolved by SDS-PAGE and transferred onto a polyvinylidene difluoride membrane (GE Healthcare, Amersham), which was blocked with PBS-T (phosphate-buffered saline and 0.1× Tween 20) containing 5% bovine serum albumin (Sigma-Aldrich). Primary antibodies for Western blot were incubated at 4°C overnight: anti-AR (1:500; Abcam), anti-mono methyl arginine (R*GG) (1:500; Cell Signaling), and anti-rabbit IgG horseradish peroxidase-linked antibodies (1:10,000; Cell Signaling). HRP-conjugated secondary antibody was incubated for 1 hour at room temperature. The ECL Plus Western Blotting Detection Kit (Thermo Fisher Scientific) was used for detection in a ChemiDoc MP Imaging System (Bio-Rad).

Transcriptomic analysis

For transcriptomic analysis, approximately 500,000 PC3 cells were seeded in 10-cm plates in RPMI 1640 media supplemented with 10% CSS (hormone depletion conditions) (n = 3). After 48 hours, cells were stimulated with 20 nM DHT for 4 hours and collected. RNA was purified using the Maxwell RSC simplyRNA Tissue Kit (Promega), following the manufacturer's instructions. RNA quality control, library preparation, 2 × 100 bp, >25 M paired-end reads, and stranded mRNA sequencing (RNA-seq) were performed using an Illumina HiSeq2500 platform. RNA-seq lanes were joined and reads were mapped with STAR (92) to the primary assembly of the human reference genome (GRCh38) in conjunction with the complete gene annotation file available in GENCODE (93). The gene read count was performed with the STAR parameter - quant-Mode GeneCounts. Results indicate, on average, 90% of reads uniquely mapped in all samples; around 80% of the reads are overlapping genes.

We used the IDEAmex service (94) to perform differential expression analysis using DESeq2 (95) and limma methods (96). The count matrix was filtered considering 5 counts per million

(CPM). To define DEGs, we considered an absolute \log_2 fold change ≥ 1 and an adjusted P value or false discovery rate (FDR) ≤ 0.05 . The following DE analyses were performed: PC3 control versus WT AR and point mutants F755V, V758A, Y764C, and Q799E, as well as WT AR versus PC3, F755V, V758A, Y764C, and Q799E. To identify the intersection of genes differentially expressed between contrasts, we used the function UpSet from the package Complex heatmaps (97). Volcano plots were generated using the Enhanced Volcano R package on DESeq2. AR targets were recovered from DoRothEA (57).

For PCA, raw counts were filtered to have at least three samples with a CPM \geq 5. Counts were transformed using the VST function (98). The PCA was calculated with the plotPCA function in DESeq2 and visualized with the ggplot2 package. For the VST data, we calculated the Euclidean distances between samples using the R function dist. We plotted the sample distance matrix with the rows/columns arranged by the distances, manually providing sampleDists to the clustering distance argument of the pheatmap function.

Enrichment analysis

GSEA (99) was performed to assess the enrichment of the different mutant AR signatures against a reference signature of DEGs between control versus WT AR ranked according to the log₂ fold change value and the clusterProfiler R package (100) on DESeq2 results. GSEA was also used to ascertain the enrichment in selected gene sets that match against the search for "prostate cancer" in MSigDB or the entire Biological Pathways collection in the KEGG database. We performed GSEA against PCa malignant signatures FOXM1, CENPF, and FOXM1 + CENPF for each DESeq2 result between PC3 control versus WT AR, F755V, V758A, Y764C, or Q799E. Signatures recovered are defined as top 200 up- and down-regulated DEGs (58).

Transcription factor activity was estimated with the DoRothEA R package (*57*) using results from the limma package (*96*) between PC3 versus WT AR or F755V, V758A, Y764C, or Q799E mutants. We estimated activity for pathways involved in cancer with PROGENy (*101*). DEG results between PC3 control versus WT AR, F755V, V758A, Y764C, or Q799E using as input the list of genes ranked by the log₂ fold change.

AR target genes expression analysis by RT-qPCR

For qPCR, approximately 300,000 PC3 cells were seeded in six-well plates in duplicates in RPMI 1640 media supplemented with 10% FBS. After 48 hours, 70% confluent cells were hormone-depleted by using RPMI 1640 media supplemented with 10% CSS. After 24 hours, cells were stimulated with 20 nM DHT for 4 hours and collected. RNA was extracted using a TRIzol reagent according to the manufacturer's instructions. After DNA digestion (deoxyribonuclease, Amplification Grade, Invitrogen), cDNA was obtained using the High-Capacity cDNA Reverse Transcription Kit (Applied Biosystems). Total cDNA was diluted 1:10, qPCR was performed using PowerUp SYBR Green Master Mix (Applied Biosystems), and plates were read with a LightCycler 480 (Roche). The following reverse transcription (RT)-qPCR primers were used to amplify glyceraldehyde phosphate dehydrogenase (GAPDH; 5'-CATCTTCCAGGAGCGAGATC; 5'-GCTGTTGTCATACTTCT-CATGG), TMPRSS2 (5'-CCTGACGCAGGCTTCCAAC; 5'-GGTCAAGGTGATGCACAGTG), FKBP5 (5'-GCGAAGGAGAA-GACCACGACAT; 5'-TAGGCTTCCCTGCCTCTCCAAA), and

FOXA1 (5'-GCAATACTCGCCTTACGGCT; 5'-TACA-CACCTTGGTAGTACGCC). Results were normalized to GADPH expression level, and each sample was quantified in triplicate. Relative quantification considers GAPDH internal standard and control conditions (PC3-CNT without DHT) to normalize and compare samples. GraphPad Prism 8.0 software was used to perform the statistical analyses using t test, which confirmed the normal distribution of the values.

Proximity ligation assay

PLA experiments were performed using reagents from the Naveniflex MR Kit (Navinci) essentially as previously described (102). Briefly, cells were seeded onto coverslips in 12-well plates, fixed in methanol for 2 min, and then washed twice in 1× phosphate-buffered saline. Fixed cells were stored at 4°C for subsequent staining or saturated with the blocking solution for 1 hour at 37°C. All further steps were performed at this temperature. Cells were then incubated with different pairs of primary antibodies: (i) anti-AR (Cell Signaling, #5153) and anti-PRMT5 (Santa Cruz Biotechnology, sc-376937), (ii) anti-AR (Santa Cruz, sc-7305) and anti-MMA (Cell Signaling, #8711), or (iii) anti-AR (Santa Cruz, sc-7305) and anti-SDMA (Cell Signaling, #13222) for 1 hour. After three washes in tris-buffered saline with 0.1% Tween® 20 detergent (TBS-T), mouse and rabbit secondary antibodies conjugated with complementary oligonucleotides ("Navenibodies") were added and incubated for 1 hour. Again, cells were washed three times in TBS-T and subsequently incubated with reaction reagents A, B, and C to activate the oligonucleotides, to allow the interaction of Navenibodies that are in close proximity and the DNA hybridization and amplification of the proximity fluorescent probes (ATTO647), respectively. Last, cells were washed 2 min in 1× tris-buffered saline (TBS) and incubated for 15 min with 0.1× TBS at room temperature. The samples were mounted using Duolink in situ mounting medium containing 4',6-diamidino-2-phenylindole (DAPI; Sigma-Aldrich, #DUO82040). The edges of the coverslips were sealed using nail polish. Slides were then stored in the dark at 4°C for a short term or visualized under a Zeiss fluorescence microscope, and interactions were counted for at least 300 cells using ImageJ software (103). In some experiments, PRMT5 was downregulated using ON-TARGETplus Human SMARTpool small interfering RNA (siRNAs; Dharmacon, #L-015817-00-0005). The unrelated siRNA ON-TARGETplus Non-targeting Control Pool (Dharmacon, #D-001810-10-05) was used as control in these siRNA experiments. Alternatively, PRMT5 activity was blocked by preincubating the cells for 48 hours with the specific inhibitor, GSK595 (0.5 µM; Sigma-Aldrich). Cells incubated with the same volume of dimethyl sulfoxide were used as reference in these experiments.

Cloning and mutagenesis of the hAR-LBD construct

Recombinant human AR-LBD (hAR-LBD; amino acids 641 to 920) was cloned into a modified pGEX vector as previously published (63). The resulting fusion protein consists of a histidine tag sequence followed by a glutathione S-transferase and a Tobacco etch virus (TEV) cleavage site before the corresponding sequence of the hAR-LBD. The pGEX vector template encoding WT hAR-LBD was mutated using the Q5 Site-Directed Mutagenesis Kit (New England Biolabs) to generate AR-LBD mutant vectors with the following primers (Y764C: 5'-CAGGATGCTCTgGCTTCGC, 5'-

GAGTTGACATTGGTGAAGGATCG; V758A: 5'- TTCAC-CAATGcCAACTCCAGGATGCTC, 5'- GGATCGCCAGCC-CATGGC; F755V: 5'- CTGGCGATCCgTCACCAATGT, 5'-CCCATGGCAAACACCATGAGC; F755L: 5'- CTGGCGATCCT-TaACCAATGT, 5'- CCCATGGCAAACACCATGAGC; and Q799E: 5'- TGGATGGCTCgAAATCACCCC, 5'-AACTCTTGAGAGAGGTGC).

Differential scanning fluorimetry

Thermofluor experiments were performed in an iQ5 Multicolor Real-Time PCR Detection System (Bio-Rad) using 96-well plates (Hard-Shell High-Profile Semi-Skirted PCR Plate, Bio-Rad) and a 25-µl total volume for each reaction essentially as described in 104. Melting curves were acquired from eight replicates to determine the average $T_{\rm m}$. AR samples (0.5 mg/ml) were prepared in 20 mM Hepes (pH 8.0), 150 mM Li₂SO₄, 10% glycerol, 50 mM imidazole, 1 mM dithiothreitol (DTT), and 50 µM DHT and centrifuged 5 min at 14,000 rpm. SYPRO Orange dye (Sigma-Aldrich) was first prepared at 80× in the protein buffer, starting from a 5000× commercial dilution. The final concentration of SYPRO Orange dye in each 25-µl reaction was 5×. The plates were sealed with optical quality sealing film (Microseal B Seals, Bio-Rad) and centrifuged at 2000g for 30 s. Samples were equilibrated for 60 s and analyzed using a linear gradient from 16° to 95°C in increments of 1°C/min, recording the SYPRO orange fluorescence throughout the gradient in the iQ5 Optical System Software 2.0. Values were fitted using the online tool JTSA with the Boltzmann four-parameter logistic equation, and the calculated fluorescence shift midpoints were compared via unpaired t test for equal variances in GraphPad Prism 8.

Proteolytic digestion

Samples of recombinant WT AR-LBD and all studied mutants were buffered-exchanged into 25 mM tris (pH 7.6), 10 mM CaCl₂, and 1 mM DTT using a PD-10 column and concentrated to 0.5 mg/ml using a centrifugal filter device. Sequencing-grade Arg-C protease (Clostripain, P5214 Abnova) was added [50/1 (w/w), protein/protease], and mixtures were incubated at 37°C with shaking. Aliquots of the proteolytic reactions were taken at indicated times, immediately mixed with reducing Laemmli buffer, and heated at 95°C for 5 min. Reaction products were separated on SDS-polyacrylamide gels and stained with Coomassie Brilliant Blue.

Crystallization and structure determination

Purified, concentrated DHT-bound AR-LBD mutants (F755L, F755V, V758A, Y764C, and Q799E) were combined with a twofold molar excess of UBA3 peptide and incubated for 1 hour at room temperature. Drops of the AR-LBD mixture were equilibrated against 0.1 M tris-HCl (pH 8.0) containing either 0.2 M sodium chloride, 2.0 M ammonium sulfate, 0.1 M ammonium acetate, or 2.5 M sodium formate using the sitting drop vapor-diffusion method. Diffraction data were collected at 100 K at the XALOC beamline of the ALBA-CELLS synchrotron (www.cells. es/en/beamlines/bl13-xaloc) and processed using MOSFLM (www.mrc-lmb.cam.ac.uk/harry/mosflm/) and CCP4 (www.ccp4. ac.uk/). The crystal structures were solved and refined using MOLREP (www.ccp4.ac.uk/html/molrep.html#references), REFMAC5 (www2.mrc-lmb.cam.ac.uk/groups/murshudov/ content/refmac/refmac.html), and COOT (www2.mrc-lmb.cam.ac.

uk/personal/pemsley/coot/) from the CCP4 package. Crystal packing was analyzed using PISA (www.ebi.ac.uk/), model quality was assessed with MolProbity (http://molprobity.biochem.duke. edu/), and structure figures were prepared with PyMOL (www. pymol.org).

Cross-linking experiments

Purified recombinant WT and mutant AR-LBD proteins were incubated with fourfold molar excess of BMOE or BMB cross-linkers for 2 hours at 37°C following the manufacturer's instructions. Samples of the reaction mixtures were boiled in the presence of reducing Laemmli sample buffer and resolved by SDS-PAGE.

Y764C covalent dimerization in solution

Purified recombinant Y764C (3 mg/ml) was incubated in 20 mM Hepes (pH 8.0), 150 mM Li₂SO₄, 10% glycerol, 50 mM imidazole, 1 mM DTT, 50 μM DHT, or in the same buffer without DTT after desalting using a PD-10 column (GE Healthcare). Y764C samples incubated under reducing and nonreducing conditions were boiled in the presence of reducing Laemmli sample buffer and resolved in a 10% SDS-polyacrylamide gel.

Nano-liquid chromatography-MS/MS experiments

Bands corresponding to dimeric, BMB-cross-linked Y764C were excised from the gels and subjected to in-gel digestion following the standard protocols. Briefly, excised bands were reduced (10 mM DTT) in 50 mM bicarbonate buffer (pH 8.0) for 45 min at 56°C, alkylated (50 mM iodoacetamide in 50 mM ammonium bicarbonate buffer for 30 min at 25°C), and digested with trypsin overnight at 37°C in 100 mM ammonium acetate buffer (pH 8). (Sequencing-grade endoproteases were from Promega).

The following procedures have been performed as previously published (64). Tryptic peptides were diluted in 1% formic acid (FA) and loaded onto a 180 µm by 20 mm C18 Symmetry trap column (Waters) at a flow rate of 15 µl/min using a nanoAcquity Ultra Performance LCTM chromatographic system (Waters). Peptides were separated using a C18 analytical column (BEH130 C18, 75 mm by 25 cm, 1.7 μm; Waters) with a 120-min run, comprising three consecutive linear gradients: from 1 to 35% B in 100 min, from 35 to 50% B in 10 min, and from 50 to 85% B in 10 min (A = 0.1% FA in water, B = 0.1% FA in CH_3CN). The column outlet was directly connected to an Advion TriVersa NanoMate fitted on an Linear trap quadrupole furier transform (LTQ-FT) Ultra mass spectrometer (Thermo Fisher Scientific), which was operated in positive mode using the data-dependent acquisition mode. Survey MS scans were acquired in the Fourier transform ion cyclotron resonance (FT-ICR) cell with the resolution (defined at 400 mass/charge ratio) set to 100,000. Up to six of the most intense ions per scan were fragmented and detected in the linear ion trap. The ion count target value was 1,000,000 for the survey scan and 50,000 for the MS/MS scan. Target ions already selected for MS/MS were dynamically excluded for 30 s. Spray voltage in the NanoMate source was set to 1.70 kV. Capillary voltage and tube lens on the LTQ-FT were tuned to 40 and 120 V, respectively. The minimum signal required to trigger MS to MS/MS switch was set to 1000, and activation Q value was set at 0.25. Singly charged precursors were rejected for fragmentation.

Docking experiments and dimeric interface analysis

The dimerization energy of the AR-LBD dimeric conformation found in the x-ray structure (PDB 5JJM, chains B:C) as well as that of the modeled mutant dimers (built by superimposition of the mutant monomeric structures onto the corresponding subunits of the crystallographic dimer) was computed with the pyDock bindEy module (105) based on energy terms previously optimized for rigid-body docking. The pyDock binding energy is basically composed of Lennard-Jones VdW, Coulombic electrostatics, and implicit desolvation based on accessible surface area (ASA) with atomic solvation parameters optimized for protein-protein interactions (106). To avoid excessive penalization from possible clashes derived from the rigid-body approach, VdW total contribution was weighed by a factor of 0.1. For the same reason, VdW and electrostatic values per intermolecular atom pair were restricted to a maximum of +1.0 kcal/mol or to a range between -1.0 and +1.0kcal/mol, respectively. BSA values of WT and mutant dimers were computed as the difference in ASA between the dimer and the unbound molecules, using ICM-Browser (www.molsoft.com). In addition, homodimeric docking models of WT AR-LBD and its mutants were built using the pyDock docking and scoring method (105). First, protein models were prepared by removing all cofactors and heteroatoms, and missing side chains were modeled with SCWRL 3.0 (105). Then, the fast Fourier transform-based docking programs FTDock (with electrostatics and 0.7 Å grid resolution) (www.sbg.bio.ic.ac.uk/docking/ftdock.html) and ZDOCK 2.1 (https://zdock.umassmed.edu/) were used to generate 10,000 and 2000 rigid-body docking poses, respectively. These were merged in a single pool for subsequent pyDock scoring, as detailed above. From the resulting docking poses, NIP values were obtained for each residue with the built-in patch module of pyDock, implementing the pyDockNIP algorithm (65). An NIP value of 1 indicates that the corresponding residue is involved in all predicted interfaces of the 100 lowest energy docking solutions, while a value of 0 means that it appears as expected by random chance. Last, a negative NIP value implies that the residue appears at the lowenergy docking interfaces less often than random. Usually, residues with NIP \geq 0.2 are considered as hotspot residues. In addition, ODA was obtained by computing surface patches with optimal desolvation energy generated from each surface residue (66). Residues with low ODA values, usually less than −10.0 kcal/mol, indicate regions with favorable desolvation energy upon interaction with a partner protein. Residues from Lys 845 to Ser 851 were removed from WT for all energy and docking calculations, for consistency in the comparative analysis, since these residues are missing in all mutant structures. Additional docking experiments were performed using the LZerD protein docking web server (https://lzerd.kiharalab.org/) with the structure of a hetero-tetrameric (PRMT5)2. (MEP50)2 complex as receptor (PDB 7L1G) and the current structure of AR-LBD(Q799E) as ligand. Solutions that satisfied the constraints (distance of Arg⁷⁶¹-flanking residues to the PRMNT5 catalytic machinery, <6 Å) were visually inspected.

Computational analysis of the estimated energetic impact of AR point mutations

We estimated the impact of the studied mutations on the overall protein stability with the FoldX empirical force (https://foldxsuite. crg.eu/) (107). Ten iterations were conducted for each mutation and later averaged. Computed free energy differences between mutant and WT proteins (estimated $\Delta\Delta G$) < 1 kcal/mol were considered not significant, those between 1 and 2, 2 and 4, and >4 kcal/mol as slightly, mildly, and strongly destabilizing, respectively. (FoldX has an estimated error of ~0.7 kcal/mol).

Statistical coupling analysis

Following previously published protocol [(64), DOI: 10.5281/zenodo.7274365], we identified two different sectors by using the SCA5 8/2011 version (108) and the updated version pySCA (109–110) with an alignment of 880 sequences. The stability of the identified sectors was assessed with a statistical test based on hypergeometric calculations of the groups of residues belonging to given sectors between pairs of alignments. *P* values were adjusted using FDR. Next, specific residues from the significant sectors were extracted and selected according to their rank.

Molecular dynamic simulations System preparation

The crystal structure of monomeric AR-LDB-DHT (PDB 1T7T) was used to represent the WT receptor, while the x-ray mutant structures used were those determined in this work. In a first step, hydrogens were added to all protein residues in their corresponding protonation states at pH 7.0, and side chain orientations were adjusted using the Protein Preparation Wizard workflow included in Maestro v.10.0 software package (www.schrodinger.com/products/ maestro). Missing residues in all the mutant structures (Lys⁸⁴⁵ to Ser⁸⁵¹) were obtained from the WT structure by superposition. The parameters for DHT were obtained using the general amber force field (gaff2) (111), and charges were generated with the restrained electrostatic potential (112) at the HF/6-31G(d,p) level using the Antechamber module of AMBER18 (https://ambermd. org/). Next, each system was placed in a cubic periodic box filled with Optimal Point Charge water molecules (113), setting a minimum distance of 15 Å between the solute and the box walls. Water molecules closer than 1.0 Å to any complex atom were removed. Then, counter ions were added to neutralize the system following a grid-shaped procedure for mapping the electrostatic potential surface. All calculations were done using the ff19SB force field (114) with a cutoff of 10 Å for noncovalent interactions, applying the PME (Particle Mesh Ewald) method (115) for the treatment of the electrostatic interactions.

Molecular dynamics

Before starting the MD calculations, the structures were first relaxed to eliminate possible steric clashes with a 5000-step minimization procedure using the steepest descent method. Then, the systems were stepwise heated to 300 K at a rate of 30 K every 20 ps, fixing the main atoms of the proteins with a harmonic positional restriction of 5 kcal/mol Å⁻², using the Langevin thermostat algorithm with a collision frequency of 3 ps⁻¹ under the NVT ensemble (heating). Subsequently, 100-ps simulations were performed at constant pressure (NPT ensemble) keeping fixed the main atoms with the same harmonic positional restrictions for density equilibration (density equilibration). Last, conventional MD of 1 µs for all the mutants and 1.2 µs for the WT protein were carried out within the NVT ensemble in quadruplicate to increase the conformational sampling of the system (116). The ParmEd program (https://parmed.github.io/ParmEd/html/index.html) was used to introduce hydrogen mass repartitioning to allow integration times

of 4 fs (117), and the SHAKE algorithm (118) was used to constrain the bonds involving the hydrogen atoms.

RMSD and RMSF

RMSD along the simulation time was computed using the CPPTRAJ module from AMBER18 (https://amber-md.github.io/cpptraj/CPPTRAJ.xhtml) for all the MD trajectories to assess the structural stability of the systems along time. RMSD was computed with respect to all the C α atoms, using the not minimized x-ray structure of the WT as reference for all the systems. The resulting superimposed trajectories were used to calculate the RMSF for each of the residues of the protein to obtain information about their conformational flexibility.

Residue pair distance

To quantify the effect of the different mutations on the distances between AR residue pairs, we implemented the algorithm described by Vatansever and coworkers (119). This algorithm is based on the concept of first coordination shell defined in the Gaussian network model but extended to a SCS with a radius of ~9.1 Å to better account for the contribution of nonbonded pairs (120). Briefly, for each Cα,i atom, the time-averaged distance to any other Cα,j atom that belongs to its SCS was obtained for the WT ($\overline{R}_{ij,WT}$) and the studied mutants $(\overline{R}_{ij,\text{mut}})$. Then, the difference $(\Delta \overline{R}_{ij})$ between $\overline{R}_{ij,\mathrm{WT}}$ and $\overline{R}_{ij,\mathrm{mut}}$ was calculated, $\Delta \overline{R}_{ij} = \overline{R}_{ij,WT} - \overline{R}_{ij,mut}$. To this end, we first calculated for all residues the changes in the time-averaged distance between residue iand all j residues that belong to its SCS for the WT structure $(\overline{R}_{ij,WT})$ and for all mutants $(\overline{R}_{ij,mut})$. The obtained $\Delta \overline{R}_{ij}$ differences indicate the degree of distortion introduced by a specific mutation. Residue pairs (*i* and *j*) that have the largest positive ($\Delta \overline{R}_{ij} > 2.50 \text{ Å}$) and negative distances ($\Delta \overline{R}_{ii} < -1.40 \text{ Å}$) between WT and each mutant were highlighted.

Supplementary Materials

This PDF file includes:

Figs. S1 to S6 Tables S1 to S4 References

View/request a protocol for this paper from Bio-protocol.

References and Notes

- W. D. Tilley, C. M. Wilson, M. Marcelli, M. J. McPhaul, Androgen receptor gene expression in human prostate carcinoma cell lines. *Cancer Res.* 17, 5382–5386 (1990).
- E. Estébanez-Perpiñá, C. L. Bevan, I. J. McEwan, Eighty years of targeting androgen receptor activity in prostate cancer: The fight goes on. Cancers 13, 509 (2021).
- A. Jiménez-Panizo, P. Pérez, A. M. Rojas, P. Fuentes-Prior, E. Estébanez-Perpiñá, Non-canonical dimerization of the androgen receptor and other nuclear receptors: Implications for human disease. *Endocr. Relat. Cancer* 26, R479–R497 (2019).
- X. Yu, P. Yi, R. A. Hamilton, H. Shen, M. Chen, C. E. Foulds, M. A. Mancini, S. J. Ludtke, Z. Wang, B. W. O'Malley, Structural insights of transcriptionally active, full-length androgen receptor coactivator complexes. *Mol. Cell.* 79, 812–823.e4 (2020).
- P. L. Shaffer, A. Jivan, D. E. Dollins, F. Claessens, D. T. Gewirth, Structural basis of androgen receptor binding to selective androgen response elements. *Proc. Natl. Acad. Sci. U.S.A.* 101. 4758–4763 (2004).
- M. Nadal, S. Prekovic, N. Gallastegui, C. Helsen, M. Abella, K. Zielinska, M. Gay, M. Vilaseca, M. Taulès, A. B. Houtsmuller, M. E. van Royen, F. Claessens, P. Fuentes-Prior, E. Estébanez-Perpiñá, Structure of the homodimeric androgen receptor ligand-binding domain. *Nat. Commun.* 8, 14388 (2017).

SCIENCE ADVANCES | RESEARCH ARTICLE

- E. V. Wasmuth, A. Vanden Broeck, J. R. LaClair, E. A. Hoover, K. E. Lawrence, N. Paknejad, K. Pappas, D. Matthies, B. Wang, W. Feng, P. A. Watson, J. C. Zinder, W. R. Karthaus, M. J. de la Cruz, R. K. Hite, K. Manova-Todorova, Z. Yu, S. T. Weintraub, S. Klinge, C. L. Sawyers, Allosteric interactions prime androgen receptor dimerization and activation. *Mol. Cell.* 82, 2021–2031 (2022)
- K. E. Knudsen, T. M. Penning, Partners in crime: Deregulation of AR activity and androgen synthesis in prostate cancer. *Trends Endocrinol. Metab.* 21, 315–324 (2010).
- Y. Wen, M. C.-T. Hu, K. Makino, B. Spohn, G. Bartholomeusz, D. H. Yan, M. C. Hung, HER-2/ neu promotes androgen-independent survival and growth of prostate cancer cells through the Akt pathway. *Cancer Res.* 60, 6841–6845 (2000).
- H. K. Lin, S. Yeh, H. Y. Kang, C. Chang, Akt suppresses androgen-induced apoptosis by phosphorylating and inhibiting androgen receptor. *Proc. Natl. Acad. Sci. U.S.A.* 98, 7200–7205 (2001)
- H. K. Lin, Y. C. Hu, L. Yang, S. Altuwaijri, Y. T. Chen, H. Y. Kang, C. Chang, Suppression versus induction of androgen receptor functions by the phosphatidylinositol 3-Kinase/Akt pathway in prostate cancer LNCaP cells with different passage numbers. *J. Biol. Chem.* 278, 50902–50907 (2003).
- S. S. Taneja, S. Ha, N. K. Swenson, H. Y. Huang, P. Lee, J. Melamed, E. Shapiro, M. J. Garabedian, S. K. Logan, Cell-specific regulation of androgen receptor phosphorylation in vivo. *J. Biol. Chem.* 280, 40916–40924 (2005).
- K. Xu, H. Shimelis, D. E. Linn, R. Jiang, X. Yang, F. Sun, Z. Guo, H. Chen, W. Li, H. Chen, X. Kong, J. Melamed, S. Fang, Z. Xiao, T. D. Veenstra, Y. Qiu, Regulation of androgen receptor transcriptional activity and specificity by RNF6-induced ubiquitination. *Cancer Cell* 15. 270–282 (2009).
- D. E. Linn, X. Yang, Y. Xie, A. Alfano, D. Deshmukh, X. Wang, H. Shimelis, H. Chen, W. Li, K. Xu, M. Chen, Y. Qiu, Differential regulation of androgen receptor by PIM-1 kinases via phosphorylation-dependent recruitment of distinct ubiquitin E3 ligases. *J. Biol. Chem.* 287, 22959–22968 (2012).
- D. Gioeli, B. M. Paschal, Post-translational modification of the androgen receptor. Mol. Cell. Endocrinol. 352, 70–78 (2012).
- T. van der Steen, D. J. Tindall, H. Huang, Posttranslational modification of the androgen receptor in prostate cancer. Int. J. Mol. Sci. 14, 14833–14859 (2013).
- Y. Koryakina, H. Q. Ta, D. Gioeli, Androgen receptor phosphorylation: Biological context and functional consequences. *Endocr. Relat. Cancer* 21, T131–T145 (2014).
- Z. Mounir, J. M. Korn, T. Westerling, F. Lin, C. A. Kirby, M. Schirle, G. McAllister, G. Hoffman, N. Ramadan, A. Hartung, Y. Feng, D. R. Kipp, C. Quinn, M. Fodor, J. Baird, M. Schoumacher, R. Meyer, J. Deeds, G. Buchwalter, T. Stams, N. Keen, W. R. Sellers, M. Brown, R. A. Pagliarini, ERG signaling in prostate cancer is driven through PRMT5-dependent methylation of the androgen receptor. *eLife* 5, e13964 (2016).
- L. Malbeteau, H. T. Pham, L. Eve, M. R. Stallcup, C. Poulard, M. Le Romancer, How protein methylation regulates steroid receptor function. *Endocr. Rev.* 43, 160–197 (2022).
- Q. Wang, W. Li, X. S. Liu, J. S. Carroll, O. A. Jänne, E. K. Keeton, A. M. Chinnaiyan, K. J. Pienta, M. Brown, A hierarchical network of transcription factors governs androgen receptordependent prostate cancer growth. *Mol. Cell* 27, 380–392 (2007).
- D. Robinson, E. M. Van Allen, Y. M. Wu, N. Schultz, R. J. Lonigro, J. M. Mosquera, B. Montgomery, M. E. Taplin, C. C. Pritchard, G. Attard, H. Beltran, W. Abida, R. K. Bradley, J. Vinson, X. Cao, P. Vats, L. P. Kunju, M. Hussain, F. Y. Feng, S. A. Tomlins, K. A. Cooney, D. C. Smith, C. Brennan, J. Siddiqui, R. Mehra, Y. Chen, D. E. Rathkopf, M. J. Morris, S. B. Solomon, J. C. Durack, V. E. Reuter, A. Gopalan, J. Gao, M. Loda, R. T. Lis, M. Bowden, S. P. Balk, G. Gaviola, C. Sougnez, M. Gupta, E. Y. Yu, E. A. Mostaghel, H. H. Cheng, H. Mulcahy, L. D. True, S. R. Plymate, H. Dvinge, R. Ferraldeschi, P. Flohr, S. Miranda, Z. Zafeiriou, N. Tunariu, J. Mateo, R. Perez-Lopez, F. Demichelis, B. D. Robinson, M. Schiffman, D. M. Nanus, S. T. Tagawa, A. Sigaras, K. W. Eng, O. Elemento, A. Sboner, E. I. Heath, H. I. Scher, K. J. Pienta, P. Kantoff, J. S. De Bono, M. A. Rubin, P. S. Nelson, L. A. Garraway, C. L. Sawyers, A. M. Chinnaiyan, Integrative clinical genomics of advanced prostate cancer. Cell 161, 1215–1228 (2015).
- D. A. Quigley, H. X. Dang, S. G. Zhao, P. Lloyd, R. Aggarwal, J. J. Alumkal, A. Foye, V. Kothari, M. D. Perry, A. M. Bailey, D. Playdle, T. J. Barnard, L. Zhang, J. Zhang, J. F. Youngren, M. P. Cieslik, A. Parolia, T. M. Beer, G. Thomas, K. N. Chi, M. Gleave, N. A. Lack, A. Zoubeidi, R. E. Reiter, M. B. Rettig, O. Witte, C. J. Ryan, L. Fong, W. Kim, T. Friedlander, J. Chou, H. Li, R. Das, H. Li, R. Moussavi-Baygi, H. Goodarzi, L. A. Gilbert, P. N. Lara, C. P. Evans, T. C. Goldstein, J. M. Stuart, S. A. Tomlins, D. E. Spratt, R. K. Cheetham, D. T. Cheng, K. Farh, J. S. Gehring, J. Hakenberg, A. Liao, P. G. Febbo, Genomic hallmarks and structural variation in metastatic prostate cancer. Cell 174, 758–769.e9 (2018).
- D. B. Lubahn, T. R. Brown, J. A. Simental, H. N. Higgs, C. J. Migeon, E. M. Wilson, F. S. French, Sequence of the intron/exon junctions of the coding region of the human androgen receptor gene and identification of a point mutation in a family with complete androgen insensitivity. Proc. Natl. Acad. Sci. U.S.A. 86, 9534–9538 (1989).
- O. Hiort, G. H. Sinnecker, P. M. Holterhus, E. M. Nitsche, K. Kruse, The clinical and molecular spectrum of androgen insensitivity syndromes. Am. J. Med. Genet. 63, 218–222 (1996).

- I. A. Hughes, J. D. Davies, T. I. Bunch, V. Pasterski, K. Mastroyannopoulou, J. Macdougall, Androgen insensitivity syndrome. *Lancet* 380, 1419–1428 (2012).
- C. E. Bohl, W. Gao, D. D. Miller, C. E. Bell, J. T. Dalton, Structural basis for antagonism and resistance of bicalutamide in prostate cancer. *Proc. Natl. Acad. Sci. U.S.A.* 102, 6201–6206 (2005).
- C. E. Bohl, Z. Wu, D. D. Miller, C. E. Bell, J. T. Dalton, Crystal structure of the T877A human androgen receptor ligand-binding domain complexed to cyproterone acetate provides insight for ligand-induced conformational changes and structure-based drug design. *J. Biol. Chem.* 282, 13648–13655 (2007).
- J. S. Sack, K. F. Kish, C. Wang, R. M. Attar, S. E. Kiefer, Y. An, G. Y. Wu, J. E. Scheffler, M. E. Salvati, J. Krystek, R. Weinmann, H. M. Einspahr, Crystallographic structures of the ligand-binding domains of the androgen receptor and its T877A mutant complexed with the natural agonist dihydrotestosterone. *Proc. Natl. Acad. Sci. U.S.A.* 98, 4904–4909 (2001).
- B. Gottlieb, L. K. Beitel, A. Nadarajah, M. Paliouras, M. Trifiro, The androgen receptor gene mutations database: 2012 update. *Hum. Mutat.* 33, 887–894 (2012).
- Z. Culig, A. Hobisch, M. Erdel, G. Bartsch, H. Klocker, Studies on androgen receptor mutations and amplification in human prostate cancer. *Methods Mol. Med.* 81, 267–275 (2003).
- E. R. Hyytinen, K. Haapala, J. Thompson, I. Lappalainen, M. Roiha, I. Rantala, H. J. Helin, O. A. Jänne, M. Vihinen, J. J. Palvimo, P. A. Koivisto, Pattern of somatic androgen receptor gene mutations in patients with hormone-refractory prostate cancer. *Lab. Invest.* 82, 1591–1598 (2002).
- 32. M. J. McPhaul, M. Marcelli, S. Zoppi, C. M. Wilson, J. E. Griffin, J. D. Wilson, Mutations in the ligand-binding domain of theandrogen receptor gene cluster in two regions of the gene. *J. Clin. Invest.* **90**, 2097–2101 (1992).
- C. Radmayr, Z. Culig, A. Hobisch, S. Corvin, G. Bartsch, H. Klocker, Analysis of a mutant androgen receptor offers a treatment modality in a patient with partial androgen insensitivity syndrome. *Eur. Urol.* 33, 222–226 (1998).
- T. R. Brown, D. B. Lubahn, E. M. Wilson, F. S. French, C. J. Migeon, J. L. Corden, Functional characterization of naturally occurring mutant androgen receptors from subjects with complete androgen insensitivity. *Mol. Endocrinol.* 4, 1759–1772 (1990).
- J. M. Lobaccaro, S. Lumbroso, R. Ktari, R. Dumas, C. Sultan, An exonic point mutation creates a *Maelll* site in the androgen receptor gene of a family with complete androgen insensitivity syndrome. *Hum. Mol. Genet.* 2, 1041–1043 (1993).
- Y.-H. Liu, C. Li, S.-F. Zhou, Prediction of deleterious functional effects of non-synonymous single nucleotide polymorphisms in human nuclear receptor genes using a bioinformatics approach. *Drug Metab. Lett.* 3, 242–286 (2009).
- R. Tadokoro-Cuccaro, T. I. Bunch, J. W. Schwabe, I. A. Hughes, J. C. Murphy, Comparison of the molecular consequences of different mutations at residue 754 and 690 of the androgen receptor (AR) and androgen insensitivity syndrome (AIS) phenotype. Clin. Endocrinol. 71. 253–260 (2009).
- M. Marcelli, M. Ittmann, S. Mariani, R. Sutherland, R. Nigam, L. Murthy, Y. Zhao,
 D. Diconcini, E. Puxeddu, A. Esen, J. Eastham, N. L. Weigel, D. J. Lamb, Androgen receptor mutations in prostate cancer. *Cancer Res.* 60, 944–949 (2000).
- X. B. Shi, A. H. Ma, L. Xia, H. J. Kung, R. W. De Vere White, Functional analysis of 44 mutant androgen receptors from human prostate cancer. Cancer Res. 62, 1496–1502 (2002).
- X. E. Zhou, K. M. Suino-Powell, J. Li, Y. He, J. P. MacKeigan, K. Melcher, E. L. Yong, H. E. Xu, Identification of SRC3/AIB1 as a preferred coactivator for hormone-activated androgen receptor. *J. Biol. Chem.* 285, 9161–9171 (2010).
- S. Grosdidier, L. R. Carbó, V. Buzón, G. Brooke, P. Nguyen, J. D. Baxter, C. L. Bevan, P. Webb,
 E. Estébanez-Perpiñá, J. Fernández-Recio, Allosteric conversation in the androgen receptor ligand-binding domain surfaces. *Mol. Endocrinol.* 26, 1078–1090 (2012).
- C. W. Hay, I. J. McEwan, The impact of point mutations in the human androgen receptor: Classification of mutations on the basis of transcriptional activity. PLOS ONE 7, e32514 (2012)
- M. J. McPhaul, M. Marcelli, W. D. Tilley, J. E. Griffin, R. F. Isidro-Gutierrez, J. D. Wilson, Molecular basis of androgen resistance in a family with a qualitative abnormality of the androgen receptor and responsive to high-dose androgen therapy. J. Clin. Invest. 87, 1413–1421 (1991).
- I. Murono, B. B. Mendonca, I. J. Arnhold, A. C. Rigon, C. J. Migeon, T. R. Brown, Human androgen insensitivity due to point mutations encoding amino acid substitutions in the androgen receptor steroid-binding domain. *Hum. Mutat.* 6, 152–162 (1995).
- C. A. Quigley, A. De Bellis, K. B. Marschke, M. K. El-Awady, E. M. Wilson, F. S. French, Androgen receptor defects: Historical, clinical, and molecular perspectives. *Endocr. Rev.* 16, 271–321 (1995).
- E. Langley, J. A. Kemppainen, E. M. Wilson, Intermolecular NH2—/carboxyl-terminal interactions in androgen receptor dimerization revealed by mutations that cause androgen insensitivity. *J. Biol. Chem.* 273, 92–101 (1998).

SCIENCE ADVANCES | RESEARCH ARTICLE

- K. F. Melo, B. B. Mendonca, A. E. C. Billerbeck, E. M. Costa, M. Inácio, F. A. Silva, A. M. Leal, A. C. Latronico, I. J. Arnhold, Clinical, hormonal, behavioral, and genetic characteristics of androgen insensitivity syndrome in a Brazilian cohort: Five novel mutations in the androgen receptor gene. J. Clin. Endocrinol. Metab. 88, 3241–3250 (2003).
- I. Jääskeläinen, A. Deeb, J. W. Schwabe, N. P. Mongan, H. Martin, I. A. Hughes, Human androgen receptor gene ligand-binding-domain mutations leading to disrupted interaction between the N- and C-terminal domains. J. Mol. Endocrinol. 36, 361–368 (2006).
- J. Batch, D. Williams, H. Davies, B. Brown, B. A. Evans, I. A. Hughes, M. Patterson, Androgen receptor gene mutations identified by SSCP in fourteen subjects with androgen insensitivity syndrome. *Hum. Mol. Genet.* 1, 497–503 (1992).
- C. L. Bevan, B. B. Brown, H. R. Davies, B. A. Evans, I. A. Hughes, M. N. Patterson, Functional analysis of six androgen receptor mutations identified in patients with partial androgen insensitivity syndrome. *Hum. Mol. Genet.* 5, 265–273 (1996).
- Q. Wang, F. J. Ghadessy, A. Trounson, D. de Kretser, R. McLachlan, S. Ng, E. Yong, Azoospermia associated with a mutation in the ligand-binding domain of an androgen receptor displaying normal ligand binding, but defective trans-activation. *J. Clin. Endocrinol. Metab.* 83, 4303–4309 (1998).
- O. Hiort, P.-M. Holterhus, T. Horter, W. Schulze, B. Kremke, M. Bals-Pratsch, G. H. G. Sinnecker, K. Kruse, Significance of Mutations in the Androgen Receptor Gene in Males with Idiopathic infertility. *J. Clin. Endocrinol. Metab.* 85, 2810–2815 (2000).
- N. Kalfa, P. Philibert, R. Werner, F. Audran, A. Bashamboo, H. Lehors, M. Haddad, J. M. Guys, R. Reynaud, P. Alessandrini, K. Wagner, J. Y. Kurzenne, F. Bastiani, J. Bréaud, J. S. Valla, G. M. Lacombe, M. Orsini, J. P. Daures, O. Hiort, F. Paris, K. McElreavey, C. Sultan, Minor hypospadias: The "Tip of the Iceberg" of the partial androgen insensitivity syndrome. PLOS ONE 8, e61824 (2013).
- J. Qi, M. Tripathi, R. Mishra, N. Sahgal, L. Fazil, S. Ettinger, W. J. Placzek, G. Claps, L. W. Chung, D. Bowtell, M. Gleave, N. Bhowmick, Z. A. Ronai, The E3 ubiquitin ligase siah2 contributes to castration-resistant prostate cancer by regulation of androgen receptor transcriptional activity. *Cancer Cell* 23, 332–346 (2013).
- 55. R. Kumar, J. Mendonca, O. Owoyemi, K. Boyapati, N. Thomas, S. Kanacharoen, M. Coffey, D. Topiwala, C. Gomes, B. Ozbek, T. Jones, M. Rosen, L. Dong, S. Wiens, W. N. Brennen, J. T. Isaacs, A. M. D. Marzo, M. C. Markowski, E. S. Antonarakis, D. Z. Qian, K. J. Pienta, D. M. Pardoll, M. A. Carducci, S. R. Denmeade, S. K. Kachhap, Supraphysiologic testosterone induces ferroptosis and activates immune pathways through nucleophagy in prostate cancer. Cancer Res. 81, 5948–5962 (2021).
- 56. H. M. Lam, H. M. Nguyen, M. P. Labrecque, L. G. Brown, I. M. Coleman, R. Gulati, B. Lakely, D. Sondheim, P. Chatterjee, B. T. Marck, A. M. Matsumoto, E. A. Mostaghel, M. T. Schweizer, P. S. Nelson, E. Corey, Durable response of enzalutamide-resistant prostate cancer to supraphysiological testosterone is associated with a multifaceted growth suppression and impaired DNA damage response transcriptomic program in patient-derived xenografits. Eur. Urol. 77, 144–155 (2020).
- L. Garcia-Alonso, C. H. Holland, M. M. Ibrahim, D. Turei, J. Saez-Rodriguez, Benchmark and integration of resources for the estimation of human transcription factor activities. *Genome Res.* 29, 1363–1375 (2019).
- A. Aytes, A. Mitrofanova, C. Lefebvre, M. J. Alvarez, M. Castillo-Martin, T. Zheng,
 J. A. Eastham, A. Gopalan, K. J. Pienta, M. M. Shen, A. Califano, C. Abate-Shen, Cross-species regulatory Network Analysis identifies a synergistic interaction between FOXM1 and CENPF that drives prostate cancer malignancy. *Cancer Cell* 25, 638–651 (2014).
- H. Takahashi, M. Furusato, W. C. Allsbrook, H. Nishii, S. Wakui, J. C. Barrett, J. Boyd, Prevalence of androgen receptor gene mutations in latent prostatic carcinomas from japanese men. *Cancer Res.* 55, 1621–1624 (1995).
- W. Weidemann, B. Linck, H. Haupt, B. Mentrup, G. Romalo, K. Stockklauser,
 A. O. Brinkmann, H. U. Schweikert, K. D. Spindler, Clinical and biochemical investigations and molecular analysis of subjects with mutations in the androgen receptor gene. *Clin. Endocrinol.* 45, 733–739 (1996).
- J. Thompson, F. Saatcioglu, O. A. Jänne, J. J. Palvimo, Disrupted amino- and carboxylterminal interactions of the androgen receptor are linked to androgen insensitivity. *Mol. Endocrinol.* 15, 923–935 (2001).
- O. A. O'Mahony, M. P. Steinkamp, M. A. Albertelli, M. Brogley, H. Rehman, D. M. Robins, Profiling human androgen receptor mutations reveals treatment effects in a mouse model of prostate cancer. *Mol. Cancer Res.* 6, 1691–1701 (2008).
- E. Estébanez-Perpiñá, L. A. Arnold, P. Nguyen, E. D. Rodrigues, E. Mar, R. Bateman, P. Pallai, K. M. Shokat, J. D. Baxter, R. K. Guy, P. Webb, R. J. Fletterick, A surface on the androgen receptor that allosterically regulates coactivator binding. *Proc. Natl. Acad. Sci. U.S.A.* 104, 16074–16079 (2007).
- 64. A. Jiménez-Panizo, A. Alegre-Martí, T. T. Tettey, G. Fettweis, M. Abella, R. Antón, T. A. Johnson, S. Kim, R. L. Schiltz, I. Núñez-Barrios, J. Font-Díaz, C. Caelles, A. F. Valledor, P. Pérez, A. M. Rojas, J. Fernández-Recio, D. M. Presman, G. L. Hager, P. Fuentes-Prior, E. Estébanez-Perpiñá, The multivalency of the glucocorticoid receptor ligand-binding

- domain explains its manifold physiological activities. *Nucleic Acids Res.* **50**, gkac1119 (2022).
- S. Grosdidier, J. Fernández-Recio, Identification of hot-spot residues in protein-protein interactions by computational docking. BMC Bioinformatics 9, 447 (2008).
- J. Fernandez-Recio, M. Totrov, C. Skorodumov, R. Abagyan, Optimal docking area: A new method for predicting protein-protein interaction sites. *Proteins* 58, 134–143 (2005).
- L. Sun, M. Wang, Z. Lv, N. Yang, Y. Liu, S. Bao, W. Gong, R. M. Xu, Structural insights into protein arginine symmetric dimethylation by PRMT5. *Proc. Natl. Acad. Sci. U.S.A.* 108, 20538–20543 (2011).
- S. Antonysamy, Z. Bonday, R. M. Campbell, B. Doyle, Z. Druzina, T. Gheyi, B. Han,
 L. N. Jungheim, Y. Qian, C. Rauch, M. Russell, J. M. Sauder, S. R. Wasserman, K. Weichert,
 F. S. Willard, A. Zhang, S. Emtage, Crystal structure of the human PRMT5:MEP50 complex.
 Proc. Natl. Acad. Sci. U.S.A. 109, 17960–17965 (2012).
- M. C. Ho, C. Wilczek, J. B. Bonanno, L. Xing, J. Seznec, T. Matsui, L. G. Carter, T. Onikubo, P. R. Kumar, M. K. Chan, M. Brenowitz, R. H. Cheng, U. Reimer, S. C. Almo, D. Shechter, Structure of the arginine methyltransferase PRMT5-MEP50 reveals a mechanism for substrate specificity. PLOS ONE 8, e57008 (2013).
- K. M. Mulvaney, C. Blomquist, N. Acharya, R. Li, M. J. Ranaghan, M. O'Keefe, D. J. Rodriguez, M. J. Young, D. Kesar, D. Pal, M. Stokes, A. J. Nelson, S. S. Jain, A. Yang, Z. Mullin-Bernstein, J. Columbus, F. K. Bozal, A. Skepner, D. Raymond, S. LaRussa, D. C. McKinney, Y. Freyzon, Y. Baidi, D. Porter, A. J. Aguirre, A. Ianari, B. McMillan, W. R. Sellers, Molecular basis for substrate recruitment to the PRMT5 methylosome. *Mol. Cell* 81, 3481–3495.e7 (2021).
- M. T. Schweizer, E. S. Antonarakis, H. Wang, A. Seun Ajiboye, A. Spitz, H. Cao, J. Luo, M. C. Haffner, S. Yegnasubramanian, M. A. Carducci, M. A. Eisenberger, J. T. Isaacs, S. R. Denmeade, Effect of bipolar androgen therapy for asymptomatic men with castration-resistant prostate cancer: Results from a pilot clinical study. Sci. Transl. Med. 7, 269ra2 (2015).
- M. D. Nyquist, L. S. Ang, A. Corella, I. M. Coleman, M. P. Meers, A. J. Christiani, C. Pierce, D. H. Janssens, H. E. Meade, A. Bose, L. Brady, T. Howard, N. De Sarkar, S. B. Frank, R. F. Dumpit, J. T. Dalton, E. Corey, S. R. Plymate, M. C. Haffner, E. A. Mostaghel, P. S. Nelson, Selective androgen receptor modulators activate the canonical prostate cancer androgen receptor program and repress cancer growth. J. Clin. Invest. 131, e146777 (2021).
- X. Qiu, L. G. Brown, J. L. Conner, H. M. Nguyen, N. Boufaied, S. A. Alaiwi, J. H. Seo, T. El Zarif, C. Bell, E. O'Connor, B. Hanratty, M. Pomerantz, M. L. Freedman, M. Brown, M. C. Haffner, P. S. Nelson, F. Y. Feng, D. P. Labbé, H. W. Long, E. Corey, Response to supraphysiological testosterone is predicted by a distinct androgen receptor cistrome. *JCl Insight* 7, e157164 (2022).
- V. Sheikhhassani, B. Scalvini, J. Ng, L. W. H. J. Heling, Y. Ayache, T. M. J. Evers, E. Estébanez-Perpiñá, I. J. McEwan, A. Mashaghi, Topological dynamics of an intrinsically disordered Nterminal domain of the human androgen receptor. *Protein Sci.* 31, e4334 (2022).
- S. A. Mosure, P. Munoz-Tello, K.-T. Kuo, B. M. Tavish, X. Yu, D. Scholl, C. C. Williams, T. S. Strutzenberg, J. Bass, R. Brust, A. A. Deniz, P. R. Griffin, D. J. Kojetin, Structural basis of interdomain communication in PPARγ (2022); www.biorxiv.org/content/10.1101/2022. 07.13.499031v1.abstract.
- X. Zhang, X. Cheng, Structure of the predominant protein arginine methyltransferase PRMT1 and analysis of its binding to substrate Peptides. Structure 11, 509–520 (2003).
- D. Musiani, J. Bok, E. Massignani, L. Wu, T. Tabaglio, M. R. Ippolito, A. Cuomo, U. Ozbek, H. Zorgati, U. Ghoshdastider, R. C. Robinson, E. Guccione, T. Bonaldi, Proteomics profiling of arginine methylation defines PRMT5 substrate specificity. Sci. Signal. 12, eaat8388 (2019).
- E. S. Burgos, C. Wilczek, T. Onikubo, J. B. Bonanno, J. Jansong, U. Reimer, D. Shechter, Histone H2A and H4 N-terminal tails are positioned by the MEP50 WD repeat protein for efficient methylation by the PRMT5 arginine methyltransferase. *J. Biol. Chem.* 290, 9674–9689 (2015).
- P. Chymkowitch, N. Le May, P. Charneau, E. Compe, J. M. Egly, The phosphorylation of the androgen receptor by TFIIH directs the ubiquitin/proteasome process. *EMBO J.* 30, 468–479 (2011).
- S. Sarkar, D. L. Brautigan, S. J. Parsons, J. M. Larner, Androgen receptor degradation by the E3 ligase CHIP modulates mitotic arrest in prostate cancer cells. *Oncogene* 33, 26–33 (2014).
- C. Liu, W. Lou, J. C. Yang, L. Liu, C. M. Armstrong, A. P. Lombard, R. Zhao, O. D. V. Noel, C. G. Tepper, H. W. Chen, M. Dall'Era, C. P. Evans, A. C. Gao, Proteostasis by STUB1/HSP70 complex controls sensitivity to androgen receptor targeted therapy in advanced prostate cancer. *Nat. Commun.* 9, 4700 (2018).
- M. L. Mohler, A. Sikdar, S. Ponnusamy, D. J. Hwang, Y. He, D. D. Miller, R. Narayanan, An overview of next-generation androgen receptor-targeted therapeutics in development for the treatment of prostate cancer. *Int. J. Mol. Sci.* 22, 2124 (2021).
- S. Ha, G. Luo, H. Xiang, A comprehensive overview of small-molecule androgen receptor degraders: Recent progress and future perspectives. J. Med. Chem. 65, 16128–16154 (2022).

- X. Deng, G. Shao, H. T. Zhang, C. Li, D. Zhang, L. Cheng, B. D. Elzey, R. Pili, T. L. Ratliff, J. Huang, C. D. Hu, Protein arginine methyltransferase 5 functions as an epigenetic activator of the androgen receptor to promote prostate cancer cell growth. *Oncogene* 36, 1223–1231 (2017).
- K. Hosohata, P. Li, Y. Hosohata, J. Qin, R. G. Roeder, Z. Wang, Purification and identification of a novel complex which is involved in androgen receptor-dependent transcription. *Mol. Cell. Biol.* 23, 7019–7029 (2003).
- Y. Peng, F. Chen, J. Melamed, L. Chiriboga, J. Wei, X. Kong, M. Mcleod, Y. Li, C. X. Li, A. Feng, M. J. Garabedian, Z. Wang, R. G. Roeder, P. Lee, Distinct nuclear and cytoplasmic functions of androgen receptor cofactor p44 and association with androgen-independent prostate cancer. *Proc. Natl. Acad. Sci. U.S.A.* 105, 5236–5241 (2008).
- 87. L. Zhou, H. Wu, P. Lee, Z. Wang, Roles of the androgen receptor cofactor p44 in the growth of prostate epithelial cells. *J. Mol. Endocrinol.* **37**, 283–300 (2006).
- S. Yin, L. Liu, C. Brobbey, V. Palanisamy, LE. Ball, S. K. Olsen, M. C. Ostrowski, W. Gan, PRMT5-mediated arginine methylation activates AKT kinase to govern tumorigenesis. *Nat. Commun* 12, 1–13 (2021).
- C. Helsen, T. Nguyen, T. Vercruysse, S. Wouters, D. Daelemans, A. Voet, F. Claessens, The T850D phosphomimetic mutation in the androgen receptor ligand binding domain enhances recruitment at activation function 2. Int. J. Mol. Sci. 23, 1557 (2022).
- I. Maksimovic, Y. David, Non-enzymatic covalent modifications as a new chapter in the histone code. *Trends Biochem. Sci.* 46, 718–730 (2021).
- H. S. Soifer, N. Souleimanian, S. Wu, A. M. Voskresenskiy, F. K. Collak, B. Cinar, C. A. Stein, Direct regulation of androgen receptor activity by potent CYP17 inhibitors in prostate cancer cells. *J. Biol. Chem.* 287, 3777–3787 (2012).
- A. Dobin, C. A. Davis, F. Schlesinger, J. Drenkow, C. Zaleski, S. Jha, P. Batut, M. Chaisson, T. R. Gingeras, STAR: Ultrafast universal RNA-seq aligner. *Bioinformatics* 29, 15–21 (2013).
- A. Frankish, M. Diekhans, A. M. Ferreira, R. Johnson, I. Jungreis, J. Loveland, J. M. Mudge, C. Sisu, J. Wright, J. Armstrong, I. Barnes, A. Berry, A. Bignell, S. Carbonell Sala, J. Chrast, F. Cunningham, T. Di Domenico, S. Donaldson, I. T. Fiddes, C. García Girón, J. M. Gonzalez, T. Grego, M. Hardy, T. Hourlier, T. Hunt, O. G. Izuogu, J. Lagarde, F. J. Martin, L. Martínez, S. Mohanan, P. Muir, F. C. P. Navarro, A. Parker, B. Pei, F. Pozo, M. Ruffier, B. M. Schmitt, E. Stapleton, M. M. Suner, I. Sycheva, B. Uszczynska-Ratajczak, J. Xu, A. Yates, D. Zerbino, Y. Zhang, B. Aken, J. S. Choudhary, M. Gerstein, R. Guigó, T. J. P. Hubbard, M. Kellis, B. Paten, A. Reymond, M. L. Tress, P. Flicek, GENCODE reference annotation for the human and mouse genomes. *Nucleic Acids Res.* 47, D766–D773 (2019).
- V. Jimenez-Jacinto, A. Sanchez-Flores, L. Vega-Alvarado, Integrative differential expression analysis for multiple experiments (IDEAMEX): a web server tool for integrated RNA-seq data analysis. Front. Genet. 10, 279 (2019).
- M. I. Love, W. Huber, S. Anders, Moderated estimation of fold change and dispersion for RNA-seq data with DESeq2. Genome Biol. 15, 550 (2014).
- M. E. Ritchie, B. Phipson, D. Wu, Y. Hu, C. W. Law, W. Shi, G. K. Smyth, *limma* powers differential expression analyses for RNA-sequencing and microarray studies. *Nucleic Acids Res.* 43. e47 (2015).
- Z. Gu, R. Eils, M. Schlesner, Complex heatmaps reveal patterns and correlations in multidimensional genomic data. *Bioinformatics* 32, 2847–2849 (2016).
- 98. S. Anders, W. Huber, Differential expression analysis for sequence count data. *Genome Biol.* **11**, R106 (2010).
- A. Subramanian, P. Tamayo, V. K. Mootha, S. Mukherjee, B. L. Ebert, M. A. Gillette, A. Paulovich, S. L. Pomeroy, T. R. Golub, E. S. Lander, J. P. Mesirov, Gene set enrichment analysis: A knowledge-based approach for interpreting genome-wide expression profiles. *Proc. Natl. Acad. Sci. U.S.A.* 102, 15545–15550 (2005).
- T. Wu, E. Hu, S. Xu, M. Chen, P. Guo, Z. Dai, T. Feng, L. Zhou, W. Tang, L. Zhan, X. Fu, S. Liu,
 X. Bo, G. Yu, clusterProfiler 4.0: A universal enrichment tool for interpreting omics data.
 Innovation 2, 100141 (2021).
- M. Schubert, B. Klinger, M. Klünemann, A. Sieber, F. Uhlitz, S. Sauer, M. J. Garnett,
 N. Blüthgen, J. Saez-Rodriguez, Perturbation-response genes reveal signaling footprints in cancer gene expression. *Nat. Commun.* 9, 20 (2018).
- C. Poulard, J. Jacquemetton, T. H. Pham, M. Le Romancer, Using proximity ligation assay to detect protein arginine methylation. *Methods* 175, 66–71 (2020).
- J. Schindelin, I. Arganda-Carreras, E. Frise, V. Kaynig, M. Longair, T. Pietzsch, S. Preibisch, C. Rueden, S. Saalfeld, B. Schmid, J. Y. Tinevez, D. J. White, V. Hartenstein, K. Eliceiri, P. Tomancak, A. Cardona, Fiji: An open-source platform for biological-image analysis. *Nat. Methods* 9, 676–682 (2012).
- R. Gustafsson, U. Eckhard, W. Ye, E. D. Enbody, M. Pettersson, P. Jemth, L. Andersson, M. Selmer, Structure and characterization of phosphoglucomutase 5 from atlantic and baltic herring—An inactive enzyme with intact substrate binding. *Biomolecules.* 10, 1631 (2020).

- T. M. K. Cheng, T. L. Blundell, J. Fernandez-Recio, PyDock: Electrostatics and desolvation for effective scoring of rigid-body protein-protein docking. *Proteins Struct. Funct. Genet.* 68, 503–515 (2007).
- J. Fernández-Recio, M. Totrov, R. Abagyan, Identification of protein-protein interaction sites from docking energy landscapes. J. Mol. Biol. 335, 843–865 (2004).
- R. Guerois, J. E. Nielsen, L. Serrano, Predicting changes in the stability of proteins and protein complexes: A study of more than 1000 mutations. *J. Mol. Biol.* 320, 369–387 (2002).
- N. Halabi, O. Rivoire, S. Leibler, R. Ranganathan, Protein sectors: evolutionary units of three-dimensional structure. Cell 138, 774–786 (2009).
- S. W. Lockless, R. Ranganathan, Evolutionarily conserved pathways of energetic connectivity in protein families. Science 286, 295–299 (1999).
- O. Rivoire, K. A. Reynolds, R. Ranganathan, Evolution-based functional decomposition of proteins. PLOS Comput. Biol. 12, e1004817 (2016).
- J. Wang, R. M. Wolf, J. W. Caldwell, P. A. Kollman, D. A. Case, Development and testing of a general Amber force field. J. Comput. Chem. 25, 1157–1174 (2004).
- C. I. Bayly, P. Cieplak, W. D. Cornell, P. A. Kollman, A well-behaved electrostatic potential based method using charge restraints for deriving atomic charges: The RESP model. *J. Phys. Chem.* 97, 10269–10280 (1993).
- S. Izadi, R. Anandakrishnan, A. V. Onufriev, Building water models: A different approach. J. Phys. Chem. Lett. 5, 3863–3871 (2014).
- 114. C. Tian, K. Kasavajhala, K. A. A. Belfon, L. Raguette, H. Huang, A. N. Migues, J. Bickel, Y. Wang, J. Pincay, Q. Wu, C. Simmerling, Ff19SB: Amino-acid-specific protein backbone parameters trained against quantum mechanics energy surfaces in solution. *J. Chem. Theory Comput.* 16, 528–552 (2020).
- T. Darden, D. York, L. Pedersen, Particle mesh Ewald: An N·log(N) method for Ewald sums in large systems. J. Chem. Phys. 98, 10089–10092 (1993).
- J. J. Perez, M. S. Tomas, J. Rubio-Martinez, Assessment of the sampling performance of multiple-copy dynamics versus a unique trajectory. J. Chem. Inf. Model. 56, 1950–1962 (2016).
- C. W. Hopkins, S. Le Grand, R. C. Walker, A. E. Roitberg, Long-time-step molecular dynamics through hydrogen mass repartitioning. *J. Chem. Theory Comput.* 11, 1864–1874 (2015).
- J. P. Ryckaert, G. Ciccotti, H. J. C. Berendsen, Numerical integration of the cartesian equations of motion of a system with constraints: Molecular dynamics of n-alkanes. J. Comput. Phys. 23, 327–341 (1977).
- S. Vatansever, B. Erman, Z. H. Gümüş, Oncogenic G12D mutation alters local conformations and dynamics of K-Ras. Sci. Rep. 9, 11730 (2019).
- A. R. Atilgan, P. Akan, C. Baysal, Small-world communication of residues and significance for protein dynamics. *Biophys. J.* 86, 85–91 (2004).
- Y. C. Yang, C. A. Banuelos, N. R. Mawji, J. Wang, M. Kato, S. Haile, I. J. McEwan, S. Plymate, M. D. Sadar, Targeting androgen receptor activation function-1 with EPI to overcome resistance mechanisms in castration-resistant prostate cancer. *Clin. Cancer Res.* 22, 4466–4477 (2016).
- N. G. R. D. Elshan, M. B. Rettig, M. E. Jung, Molecules targeting the androgen receptor (AR) signaling axis beyond the AR-Ligand binding domain. Med. Res. Rev. 39, 910–960 (2019).

Acknowledgments: We thank J. Lüders (IRB) for critical comments and suggestions on the manuscript. We thank M. Taulès (CCiTUB), M. Vilaseca (MS facility), R. El Bizri, L. Franco (Idibell), and K. Kahlem (CNAG) for technical support. We thank ALBA-Cells synchrotron Xaloc team for beamline support, Funding: E.E.-P. thanks G. E. Carretero and A. T. Hagler for sponsorships. Caixalmpulse 2018-00018 La Caixa, and 2018-Llavor with 2017SGR1089 (to P.F.-P.; Generalitat de Catalunya). E.E.-P. thanks 2021SGR01433, BFU-Retos2017-86906-R, PDC2021-121688-100, and SAF2017-71878-REDT (Red Nacional de Receptores Nucleares, NurCaMeIn) with SAF2019-REDT-Uroncomol (to A.A.; Red Nacional de Mecanismos Moleculares del Cáncer Urológico, Uroncomol), RTI2018-101500-B-I00 (to P.F.-P.), PID2019-110167RB-I00/AEI/10.13039/ 501100011033 (to J.F.-R.), and RTI2018-096735-B-100 (to A.R.; MINECO). A.A. thanks PI19/00342 and CPII20/00024 (Instituto de Salud Carlos III), W81XWH-18-1-0193 (Department of Defense), and 2017SGR448 (Generalitat de Catalunya). U.E. acknowledges support from the Spanish Ministry of Science and Innovation (RYC2020-029773-I and PID2021-128682OA-I00). M.N.P.-M. thanks Predocs-UB2020 5760700, J.R.-M. thanks grants 2021SGR00350 and CEX2021-001202-M. C.P. and M.L.R. were supported by financial support from ITMO Cancer of Aviesan within the framework of the 2021-2030 Cancer Control Strategy, on funds administered by Inserm. Author contributions: E.E.-P., P.F.-P., and A.A conceived and designed the initial project and supervised its overall execution, provided financial support, and share overall responsibility for the presented results and final approval of the article. A.A.-M., A.J.-P., M.A., and R.A. expressed and purified recombinant proteins. A.A.-M., A.J.-P., and M.A. performed crystallization trials. A.A.-M., A.J.-P., R.A., and E.E.-P. performed site-directed mutagenesis and protein analyses, A.A.-M. and U.E. conducted and analyzed DSF experiments. A.M.R. performed sequence and SCA analyses with A.J.-P. P.F.-P. and E.E.-P. interpreted sequence and SCA analyses. J.F.-R. performed docking,

SCIENCE ADVANCES | RESEARCH ARTICLE

NIP, and ODA calculations. J.F.-R., A.A.-M., P.F.-P., and E.E.-P. interpreted docking, NIP, and ODA calculations. A.A.-M., A.J.-P., R.A., P.F.-P., and E.E.-P. performed MS experiments and interpreted results. A.A.-M., A.J.-P., P.F.-P., and E.E.-P. collected x-ray crystallography diffraction data, P.F.-P. interpreted diffraction data and solved and refined 3D structures. P.F.-P., A.A.-M., A.J.-P., and E.E.-P. analyzed and interpreted the structures. A.A.-M., A.M.-T., M.C., and A.A. performed and supervised RNA-seq experiments with created stable PCa cell lines and performed transcription activity, anti-androgens, and cell proliferation assays. C.P. and M.L.R. performed analysis of AR-PRMT5 interactions and AR methylation in living cells using PLA assays. A.A. and J.M.P. advised on anti-androgen treatments and discussions on prostate cancer implications. J.R.-M. and M.N.P.-M. performed MD simulations and interpreted results with A.A.-M., J.F.-R., E.E.-P., and P.F.-P. E.P.-P., P.F.-P., and A.A. drafted the article. A.A.-M., A.J.-P., A.A., P.F.-P., and E.E.-P. critically reviewed the manuscript. All authors discussed the results and commented on the manuscript. Competing interests: The authors declare that they have no competing interests. Data and materials availability: All data needed to evaluate the conclusions in the paper are present in

the paper and/or the Supplementary Materials. The atomic coordinates and structure factors reported here have been deposited in the PDB with the accession codes 7ZTZ (Y764C), 7ZU2 (Q799E), 7ZU1 (V758A), 7ZTX (F755V), and 7ZTV (F755L). The PDB accessibility has been designed "for immediate release on publication." The MS proteomics data have been deposited to the ProteomeXchange Consortium via the PRIDE partner repository with the dataset identifier PXD028039. The transcriptomic data have been deposited at the NCBI Gene Expression Omnibus (GEO) repository under the accession code GSE210393. Bioinformatics data and code for the clustering and sector analyses are available at Zenodo (DOI: 10.5281/zenodo.7274365).

Submitted 2 August 2022 Accepted 15 February 2023 Published 15 March 2023 10.1126/sciadv.ade2175

Science Advances

A hotspot for posttranslational modifications on the androgen receptor dimer interface drives pathology and anti-androgen resistance

Andrea Alegre-Mart, Alba Jimnez-Panizo, Adrin Martnez-Tbar, Coralie Poulard, M. Nria Peralta-Moreno, Montserrat Abella, Rosa Antn, Marcos Chias, Ulrich Eckhard, Josep M. Piulats, Ana M. Rojas, Juan Fernndez-Recio, Jaime Rubio-Martnez, Muriel Le Romancer, Ivaro Aytes, Pablo Fuentes-Prior, and Eva Estbanez-Perpi

Sci. Adv., **9** (11), eade2175. DOI: 10.1126/sciadv.ade2175

View the article online

https://www.science.org/doi/10.1126/sciadv.ade2175

Permissions

https://www.science.org/help/reprints-and-permissions

Use of this article is subject to the Terms of service

to original U.S. Government Works. Distributed under a Creative Commons Attribution NonCommercial License 4.0 (CC BY-NC).

MOLECULAR BIOLOGY OF PROSTATE CANCER (M KRUITHOF-DE JULIO, SECTION EDITOR)



Epigenetic Regulation in Prostate Cancer Progression

Katia Ruggero 1 · Sonia Farran-Matas 1 · Adrian Martinez-Tebar 1 · Alvaro Aytes 1,2

Published online: 18 April 2018

© The Author(s) 2018, corrected publication May/2018

Abstract

Purpose of Review An important number of newly identified molecular alterations in prostate cancer affect gene encoding master regulators of chromatin biology epigenetic regulation. This review will provide an updated view of the key epigenetic mechanisms underlying prostate cancer progression, therapy resistance, and potential actionable mechanisms and biomarkers.

Recent Findings Key players in chromatin biology and epigenetic master regulators has been recently described to be crucially altered in metastatic CRPC and tumors that progress to AR independency. As such, epigenetic dysregulation represents a driving mechanism in the reprograming of prostate cancer cells as they lose AR-imposed identity.

Summary Chromatin integrity and accessibility for transcriptional regulation are key features altered in cancer progression, and particularly relevant in nuclear hormone receptor-driven tumors like prostate cancer. Understanding how chromatin remodeling dictates prostate development and how its deregulation contributes to prostate cancer onset and progression may improve risk stratification and treatment selection for prostate cancer patients.

Keywords Prostate cancer · Epigenetics · Transcriptional regulation · Chromatin biology · Androgen receptor · Drug targets

Introduction

Prostate cancer has traditionally been seen as an aging-associated, low mutational load tumor with a tendency for genomic rearrangements and a particular dependency on the activity of the androgen receptor (AR). As such, treatment strategies have been focused on targeting the AR axis, either through inhibiting steroidogenic pathways and the production of testosterone, or by antagonizing the AR itself to prevent its nuclear translocation and the activation of its transcriptional network. While these strategies have doubtlessly improved survival for prostate cancer patients, they are not curative in many cases, and resistance eventually occurs in about 30% of

This article is part of the Topical Collection on Molecular Biology of Prostate Cancer

- Alvaro Aytes aaytes@idibell.cat
- Programs of Molecular Mechanisms and Experimental Therapeutics in Oncology (ONCOBell), Catalan Institute of Oncology, Bellvitge Institute for Biomedical Research, Granvia de l'Hopitalet, 199 08908, L'Hospitalet de Llobregat, 08907 Barcelona, Spain
- Programs of Cancer Therapeutics Resistance (ProCURE), Catalan Institute of Oncology, Bellvitge Institute for Biomedical Research, L'Hospitalet de Llobregat, 08907 Barcelona, Spain

patients, who develop castration-resistant prostate tumors (CRPC) for which limited treatment options exist. Moreover, under the CRPC definition, a pool of diverse disease presentations with variable outcomes exists, including neuroendocrine tumors.

Massive parallel sequencing of hundreds of tumor specimens from prostate cancer patients at different stages of cancer progression has provided an accurate picture of the landscape of genetic alterations that accompany cancer evolution in the prostate. Yet, despite several molecular classification systems for prostate tumors have been proposed, clear association with risk stratification remains to be provided. On the other hand, whether these genetic classifiers predict treatment outcome and to what extent genetic alterations in prostate cancer can be exploited for personalized therapies is yet to be proven. Interestingly, together with well-known drivers of cancer progression, an important number of new alterations have been described, with an intriguing enrichment of those affecting key players in chromatin biology and epigenetic master regulators (see a summary in Table 1). This is particularly relevant in metastatic CRPC and tumors that have transitioned to ARindependent phenotypes after progressing on the newest antiandrogen drugs.

Here, we introduce key concepts to understand how epigenetic dysregulation is a plausible driving mechanism in the



 Table 1
 Summary of epigenetic
 master regulators implicated in prostate cancer

Gene name	Function in prostate cancer	References
Methyltransferases		
NSD2	H3K36 di-methyltransferase. Promotes prostate cancer tumorigenesis and progression. It is overexpressed in metastatic stage and associated with biochemical recurrence	[1••, 2, 3]
EZH2	H3K27 di- and tri-methyltransferase. Member of the polycomb repressive complex 2, crucial driver of prostate oncogenesis	[4, 5]
SUV39H1 (KMT1A) SETDB1 (KMT1E)	H3K9 tri methyltransferase. Enhance prostate cancer cell migration and invasion	[6, 7]
SUV39H2 (KMT1B)	H3K9 tri methyltransferase increases androgen-dependent tran- scriptional activity by interacting with the AR	[8]
SMYD3	H3K4 di- and methyltransferase, promotes cell proliferation and migration	[9, 10].
PRMT5	Drives prostate cancer cell growth through epigenetic inactivation of several tumor suppressors through histone arginine methylation at H4R3. Enhances AR-targeted gene expression	[11, 12•, 13]
Demethylases	•	
LSD1	H3K9 and H3K4 demethylase involved in prostate cancer recurrence, CRPC, and poor survival. Regulates AR	[14••, 15, 16•]
JARID1B (KDM5B)	transcriptional activity in a context-dependent manner H3K4 mono, di-, and tri-demethylase. AR coactivator regulating its transcriptional activity. Upregulated in prostate cancer tissues	[17, 18],
JARID1C (KDM5C)	H3K4 di- and tri-demethylase overexpressed in prostate cancer. Proposed as a predictive marker for therapy failure in patients after prostatectomy	[19].
JARID1D (KMD5D)	H3K4 di- and tri-demethylase. Suppress invasion and progression of prostate cancer. Low levels were associated with poor prognosis and resistance to docetaxel	[20, 21]
PHF8	H3K9, H3K27, and H4K20 demethylase. Transcriptional coactivator of AR. Promotes prostate cancer cell proliferation, migration, invasion, and neuroendocrine differentiation. Its expression highly correlated with poor prognosis and is induced by hypoxia	[22–29]
JMJD2A (KDM4A) JMJD2C (KDM4C)	H3K9 and H3K36 tri demethylases. Modulates AR transcriptional activity stimulating ligand-independent gene	[30, 31]
JMJD1A (KDM3A)	transcription via H3K9 demethylation H3K9 mono- and di-demethylase. Regulates AR activity by re- cruitment to target genes only in the presence of androgens	[32, 33]
JMJD2B (KDM4B),	H3K9 tri-demethylase, AR coactivator. Regulates AR transcriptional activity via demethylation activity and via	[34]
JMJD3 (KDM6B)	inhibition of ubiquitination and increased AR stability H3K27 di- and tri-demethylase overexpressed in metastatic prostate cancer	[35].
DNA methylation	•	
DNMTs	Control of transcriptional program during prostate cancer and CRPC progression	[36]
GSTP1	Silencing of GSP1 upon promoter hypermethylation is a potential prognostic biomarker and occurs early during prostate carcinogenesis	[37–39]
Histone acetylation		
P300	Histone acetyltransferase. Besides canonical histone acetylation activity, it acetylates the AR and enhances its transcriptional activity (coactivator) and drives prostate cancer growth	[40, 41]
SIRT1	Histone deacetylase; regulates cellular growth through AR deacetylation	[42, 43].
SIRT2	Histone deacetylase; its downregulation has been associated with increased acetylated H3K18 and poorer outcome and decreased sensitivity to androgen deprivation therapy	[44]
BET bromodomain epigene		

BRD4



 Table 1 (continued)

Gene name	Function in prostate cancer	References
	Bromodomain and extra-terminal protein, interacts with AR and promote its activity and antiandrogen resistance	[45•, 46–48]
TRIM24	Epigenetic reader and transcription co-regulator, overexpressed in CRPC and associated to disease recurrence. Required for prostate cancer cell proliferation in CRPC	[49].
CHD1	H3K4me2-3 epigenetic reader whose loss is related with prostate cancer aggressiveness and DNA repair defects, thus sensitizing tumor cells to PARP inhibitors	[50, 51]
Pioneer transcription fa	· ·	
FOXA1	FOXA1 activity on chromatin results in increased accessibility and increased chromatin-bound AR. High FOXA1 expression leads to a restricted AR cistrome regulation. FOXA1 also has the potential to reprogram GATA2	[52, 53]
GATA2	GATA2 activity in human prostate cancer is strongly associated to AR levels and is hence considered a prostate cancer oncogene	[53–55]
Epigenetic regulators o	e	
SOX2	Overexpressed TF in prostate cancer, regulating CRPC proliferation, and evasion of apoptosis. Promotes tumor metastasis by inducing EMT. Associated to NEPC emergence	[56–61, 62••, 63••]
MYC	Master regulator of prostate cancer transcriptional program. Associated with prostate cancer recurrence and poor prognosis	[64, 65]
MYCN	Driver of NEPC by inducing an EZH2-mediated transcriptional program	[64, 66]
Oncogenic pathways		
Hsp90	Initiates ERK signaling and leads to the recruitment of EZH2 to the E-cadherin promoter and repression of E-cadherin expression, driving EMT and invasion in prostate cancer cells	[67].
DAB2IP	Tumor suppressor Ras-GAP. Negatively controls Ras-dependent mitogenic signals and modulates TNFα/NF-κB, WNT/β-catenin, PI3K/AKT, and androgen receptors pathways	[68–70].
RB1	This tumor suppressor gene is commonly loss in metastatic and antiandrogen resistant prostate cancer and NEPC. Directly repress the expression of Sox2 and Ezh2	[71, 72, 63••]
ACK1	Tyrosine kinase correlated with poor prognosis and interacts with AR to drive ADT resistance and CRPC growth. Regulates transcription of AR and AR-v7 via epigenetic regulation	[72–74]

reprograming of prostate cancer cells as they lose ARimposed identity. Beyond reviewing the current status of epigenetic biomarkers and classifiers and their clinical impact, we will discuss the scientific basis for therapeutic targeting master regulators of chromatin remodeling and integrity and the current state of epigenetic drugs for prostate cancer.

DNA Methylation and Histone Modifications in Prostate Carcinogenesis

Perturbed DNA methylation patterns have long been reported during prostate cancer progression [75]. Among the most well-described alterations is the GSTP1 promoter hypermethylation and subsequent silencing [37], which is thought to occur early during prostate carcinogenesis [38] and has thus been proposed as a potential prognostic biomarker [39]. Yet,

numerous other key genes have been implicated in DNA methylation changes. In fact, the promoter of the Androgen Receptor (AR) itself appears to be hypermethylated in up to 30% of CRPCs, resulting in the loss of AR expression [76]. Moreover, PTEN silencing is often a consequence of promoter CpG islands hypermethylation [77], while hypermethylation of the p16 tumor suppressor gene is associated with a proliferative advantage, thus contributing to carcinogenesis and disease progression [78]. Similarly, the hypomethylation and consequent upregulation of genes like heparanase and urokinase plasminogen activator (uPA) was reported to contribute to tumor cell invasion and metastasis [79]. More globally, DNA methylation signatures have been identified and proposed as molecular biomarkers of prostate cancer progression and treatment response [80].

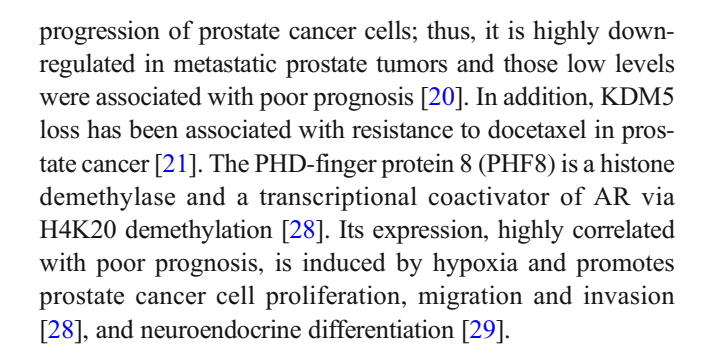
Histone modifications also play an important role in the progression of many tumor types including prostate cancer.



Lysine methyltransferases (KMT) and demethylases (KDM) are important epigenetic histone modifiers implicated in the control of gene transcriptional regulation as well as in nonhistone protein posttranslational modifications and activity modulation [81]. More specifically, SUV39H1 (KMT1A) and SETDB1 (KMT1E) have been shown to enhance prostate cancer cell migration and invasion and to be upregulated in human prostate cancer specimens, and hence suggested as potential therapeutic targets [6], while SUV39H2 (KMT1B) interacts with the AR to increase androgen-dependent transcriptional activity [8]. Furthermore, levels of SETDB1 have been recently associated with prognosis and the development of bone metastases from prostate cancer [7]. Similarly, SET and MYND domain-containing protein 3 (SMYD3) has also been identified as an upregulated H3 and H4 lysine methyltransferase promoting cell proliferation and migration, thus emerging as a predictive marker of prostate cancer [10]. Alternatively, protein arginine methyltransferase 5 (PRMT5) was described as a prostate cancer oncogene driving cancer cell growth through epigenetic inactivation of several tumor suppressors [11] through histone arginine methylation at H4R3. PRMT5 has also recently been shown to enhance AR-targeted gene expression by arginine methylation and interaction with the transcription factor Sp1 [13].

Demethylases also play an important role in prostate cancer development. Lysine-specific demethylase 1 (LSD1/KDM1A) has been proposed as an oncogene whose overexpression has been positively correlated with the malignancy of many cancer types, including prostate [14., 82], promoting carcinogenesis by multiple mechanisms. Increased LSD1 expression is associated with prostate cancer recurrence and poor survival and appears to have distinct functions in androgen-dependent [14., 83] and refractory prostate cancer [15]. Recently, it was discovered that LSD1 is a co-regulator of vitamin D receptor activity in prostate cancer and its expression is correlated with shorter progression-free survival in primary and metastatic patients [84]. In a recent study, it was found that LSD1-mediated epigenetic reprogramming drives CRPC and was associated with the activation of CENPE, which was regulated by the cobinding of LSD1 and AR to its promoter region, which was associated with loss of RB1 [16•].

The overexpression of other histone demethylases (HDMs) has also been observed in prostate cancer. An exhaustive functional screen [27] identified 32 enzymes belonging to the family of JmjC domain-containing histone demethylases as critical for prostate cancer proliferation and survival. KDM5 family members are H3K4 demethylases; JARID1B (KDM5B) is upregulated in prostate cancer tissues and acts as an AR coactivator [17], while JARID1C (KDM5C), overexpressed in prostate cancer, emerged as a predictive marker for therapy failure in patients after prostatectomy [19]. JARID1D (KMD5D) was found to suppress the invasion and



The Histone Methyltransferase NSD2

NSD2 (nuclear receptor binding SET domain protein 2), also known as WHSC1 (Wolf-Hirschhorn syndrome candidate 1) and MMSET (multiple myeloma SET domain), is a member of the histone methyltransferase NSD family of proteins also including NSD1 and NSD3. NSD2 catalyzes the dimethylation of histone H3 at lysine 36 (H3K36me2), a permissive mark associated with open chromation conformation and active gene transcription [85]. NSD2 was first linked to oncogenesis by the involvement in the t(4; 14) translocation identified in up to 20% of multiple myeloma patients [86]. In the past years, NSD2 has been shown to be overexpressed in a variety of solid tumors including prostate cancer, where it has been found overexpressed in metastatic PCa compared to primary tumors and is associated with biochemical recurrence [1••]. Further In vitro studies strengthened the role of NSD2 in prostate cancer tumorigenesis; it has been shown that NSD2 modulates Twist family bHLH transcription factor 1 (TWIST1) to promote epithelial to mesenchymal transition and invasiveness in prostate cancer cell lines [2]. Moreover, Asangani and colleagues had reported that EZH2 mediates the overexpression of NSD2 and that the oncogenic properties of EZH2 are NSD2 dependent [3]. Interestingly, transcriptional targets of NSD2 in prostate cancer cells are highly enriched for components of the NF-kB-network, including IL-6, IL-8, survivin/Birc5, and VEGFA. In fact, NSD2 has been linked to constitutive activation of NF-kB signaling in CRPC, promoting cancer cell proliferation and survival via an autocrine positive loop in which NSD2 expression is in turn stimulated by inflammatory cytokines, such as TNF α and IL-6, via NF-kB [87].

Very recently, work from Li and collaborators showed that NSD2 is activated in PTEN null tumors by the AKT pathway and that its expression is required for metastatic progression. Mechanistically, AKT-mediated phosphorylation of NSD2 prevents its degradation by CRL4^{Cdt2} E3 ligase leading to NSD2 stabilization and overexpression. By directly inducing RICTOR expression, NSD2 mediates a positive feedback loop sustaining AKT signaling [1••].

Finally, NSD2 has been shown to physically interact with the AR DNA-binding domain and to be recruited to the



enhancer region of the PSA gene and enhance AR transcriptional activity [88], suggesting that NSD2 might be implicated in resistant to ADT or androgen signaling inhibition. Of note is the recent identification of NSD2 as a candidate gene promoting androgen independence through an unbiased insertional mutagenesis screen [89]. In fact, unpublished data and data from our laboratory currently under peer-review for publication strongly suggest that NSD2 is an actionable mechanism in CRPC.

Epigenetic Control of Androgen Receptor Activity

Histone modifying enzymes, and LSD1 in particular, are among the best-known modulators of AR transcriptional activity. LSD1 is an important enzyme involved in AR regulation and prostate cancer that interacts with AR and can stimulate [14••] or suppress [15] the transcriptional expression depending on promoter/enhancer context. This interaction promotes ligand-dependent transcription of AR target genes, resulting in enhanced tumor cell growth. Its coactivator activity seems to be associated with H3K9me1,2 demethylation leading to transcriptional de-repression of AR target genes [14••]. Intriguingly, LSD1 also plays a role as co-repressor, via H3K4me1,2 demethylation [90] and the recruitment of corepressor complexes. This highlights the dual role of many chromatin remodelers and may explain why translating them to new therapeutics has so far been limited. A possible way forward may be to define the context specificities for this duality. For example, it has been shown that in high androgen levels, AR recruits LSD1 to mediate AR gene silencing [15]; however, this negative feedback loop is apparently disrupted in CRPC, where low androgen levels promote AR overexpression. Additionally, post-transcriptional modifications can regulate LSD1 activity and may become better targets; LSD1 phosphorylation [91] results in a switch of substrate from H3K4me1,2 to H3K9me1,2, and the promotion of its coactivator activity. Jumonji C domain-containing trimethyl lysine demethylases JMJD2A (KDM4A) and JMJD2C (KDM4C) also play a significant role in modulating AR transcriptional activity [30, 31], stimulating ligand-independent gene transcription via H3K9 demethylation. On the contrary, JMJD1A (KDM3A) recruitment to target genes only occurs in the presence of androgens, regulating AR activity and identifying KDM3A-dependent genes involved in androgen response, hypoxia, glycolysis, and lipid metabolism [33], again evidencing the complex balance between chromatin modifying enzymes in controlling different but interconnected cellular processes. Of note is the case of JMJD2B (KDM4B), which is an AR coactivator, emerging as a suitable therapeutic target for the treatment of prostate cancer. JMJD2B controls AR transcriptional activity via demethylation and inhibition of ubiquitination and increased AR stability [34]. Finally, JMJD3 (KDM6B) is progressively overexpressed in metastatic prostate cancer [35].

Histone Acetylation and AR

Acetylated chromatin is generally associated to active transcription and the enzymes regulating this process are histone acetyltransferases (HAT) and deacetylases (HDAC). Accordingly, acetylated histone H3 in the vicinity of ARbound chromatin has been shown to reduce androgen dependence in castration resistance models [92, 93]. That is the case for canonical HAT like p300 and CREB-binding protein, which, besides canonical histone acetylation activities, have been shown to acetylate the AR and enhance its transcriptional activity [40]. Importantly, two groups have recently independently developed small molecule inhibitors targeting p300/CBP. Lasko and colleagues reported a selective catalytic p300/CBP inhibitor able to downregulate the AR transcriptional program both in castration-sensitive and castrationresistant prostate tumors and to inhibit tumor growth in CRPC xenograft models [94], while Jin and colleagues found that targeting the p300/CBP bromodomain had remarkably similar effetcs [41]. More broadly, a recent study highlights the important role of histone acetylation in prostate cancer beyond active promoters via activation of AR associated enhancers and the increase in chromatin accessibility [95•].

Conversely, a variety of HDACs are also capable of deacetylating the AR and inhibit its activity, for example via regulation of heat-shock protein 90 (Hsp90), a chaperone controlling AR nuclear localization and activation through its acetylation/deacetylation, or sirtuin 1 (SIRT1), which regulates cellular growth through AR deacetylation [42, 43]. In fact, acetylation of H3K18, putatively via downregulation of SIRT2 deacetylase, has been associated to poorer outcome and decreased sensitivity to androgen deprivation therapy (ADT). Finally, at the mechanistic level, the Wu lab has recently demonstrated that HDAC inhibitors can suppress HMGA-driven EMT, reduce tumor growth and metastasis and, importantly, resensitize prostate cancer cells to [96].

The Role of EZH2/Polycomb Repressive Complex in Prostate Cancer

The enhancer of zeste homolog 2 (EZH2) is a critical member of the Polycomb Repressive Complex 2 (PRC2) that regulates histone methylation mainly via lysine 27 at histone H3 (H3K27), a modification associated to transcriptional silencing [97] that is found upregulated in many tumor types. In prostate cancer, its elevated expression associates with poorer outcomes and has therefore been proposed as an oncogene [4, 98]. A major function of EZH2 is to repress lineage-



specifying factors, thereby promoting stemness features [99], epithelial-mesenchymal transition (EMT), and ultimately metastatic progression [100]. A wealth of recent evidence has confirmed these previous observation in the prostate cancer field. Back-to-back recent articles in *Science* by the Sawyers and Goodrich groups demonstrated that lineage plasticity and neuroendocrine differentiation in androgen independence is partly driven by Ezh2 and Sox2 in prostate cancer mouse models carrying loss of function alleles for p53 and Rb tumor suppressors [62••, 63••]. This came to confirm two previous reports by Dardenne and colleagues [64] and by Xu and colleagues [101] showing that N-myc induces EZH2-driven neuroendocrine prostate cancer [64] and it cooperates with E2F1 in castration resistance [101].

Yet, EZH2 has also PRC2-independent roles as coactivator of transcription factors, including an AKT-dependent methylation of the AR, via PI3K/AKT phosphorylation of EZH2 at serine 21 [102], and modulation of AR recruitment to its target sites [103••]. Not surprisingly, EZH2 inhibitors are the focus of intensive development and have been widely tested in vivo [5] and in clinical trials (see Table 2 for details). Beyond a promising drug target, EZH2 and TOP2A have been proposed as prognostic as well as predictive biomarkers of treatment response against EZH2 inhibitors [104].

Bromodomain-Containing Proteins in Prostate Cancer

Bromodomain-containing proteins are chromatin readers that recognized mono-acetylated histones and trigger chromatin remodeling to initiate transcription. Mutations and deregulation of BRD-containing proteins is a common feature of a variety of cancers. More than 50% of primary and metastatic prostate tumors and more than 70% of neuroendocrine prostate cancer present genomic alterations in any of the 42 known BRD-containing proteins [105]. Further, BRD-containing proteins have a diversity of catalytic and scaffolding functions and may act as transcription factors, transcriptional co-factors recruiting other proteins in the transcriptional complex, methyltransferases, HATs, Helicases, and ATP-dependent chromatin remodelers, therefore playing a central role in gene expression regulation [106].

The subgroup of BET proteins (bromodomain and extraterminal), and in particular BRD4, have been the best characterized in prostate cancer, and several inhibitors of BET bromodomains have been developed and are currently in clinical trial (see Table 2). The conserved BET family includes BRD4, BRD2, BRD3, expressed ubiquitously, and BRDT, specifically expressed in the testis. BRD4 recognizes acetylated lysines at enhancers/superenhancer [107••, 108••] and recruits the elongation factor P-TEFb and stimulates RNA polymerase II-dependent transcription [109]. A provocative new

finding by Zuber and colleagues with implications in risk assessment shows that tissue-specific SNPs in superenhancer sequence bound by BRD4 are significantly associated with increased prostate cancer risk and show better enrichment for risk loci than AR [110].

BRD4 physically interacts with high-affinity with the N-terminal domain of AR leading to AR translocation into the nucleus and AR recruitment to target loci, promoting AR activity and expression of AR target genes in CRPC [45•]. A recent study showed that the small molecule BET inhibitor ABBV-075 could disrupt the recruitment of BRD4 at enhancer of AR target genes and repress their expression, whithout affecting AR protein levels [111]. Moreover, BET proteins have a role in resistance to antiandrogens and BET inhibitors can effectively resensitize resistant tumors to enzalutamide [112]. One of these mechanisms of resistance to antiandrogens is the upregulation of the glucocorticoid receptor (GR), and the co-option of the AR regulon, thus favoring CRPC progression by overcoming AR dependency [46, 47, 113].

Beyond AR signaling, BRD4 has been shown to bind to the truncated ERG (ERG Δ 39) encoded by the TMPRSS2-ERG fusion, co-regulating the expression of ERG target genes in CRPC, thereby stimulating cell growth and invasion [114]. Additionally, SPOP, an E3 ligase substrate binding protein frequently mutated in prostate cancer, was also reported to target BET proteins for ubiquitination-mediated degradation. Interestingly, SPOP mutants fail to ubiquitinate BET proteins, leading to their stabilization and to resistance to BET inhibitors [48, 115]. This mechanism of resistance causes activation of AKT-mTORC1 signaling and consequently resistance to BET inhibitors can be overcome by combination with AKT inhibitors [116].

It is well known that one of the major aging-associated drivers of prostate carcinogenesis is oxidative stress and its impact on DNA [117]. Interestingly, Hussong and colleagues have recently established a link between BRD4 and oxidative stress response genes in prostate cancer, such as the KEAP1/NRF2 axis and HMOX1, and reactive oxygen species (ROS) production [118].

Other than BET, several BRD-containing proteins have been associated to prostate cancer progression and are at different validation stages for therapeutic targets in mCRPC. TRIM24, tripartite motif-containing protein 24, is an epigenetic reader and transcription co-regulator overexpressed in CRPC and associated to disease recurrence. Recurrent SPOP mutants stabilize TRIM24 [119], enhancing AR signaling and promoting tumor growth via binding with the proteins TIP60 and BRD7 [120], which has led to the proposition of TRIM24 as an essential gene for prostate cancer cell proliferation in CRPC [49].

Finally, the role of chromodomain proteins, and in particular chromodomain helicase DNA-binding protein 1 (CHD1), has in the recent years been elucidated in the context of



 Table 2
 Clinical trials for epigenetic drugs including prostate cancer patients

Trial ID	Drug	Phase	Conditions	Patients	Status
BET bromodomain	n inhibitors				
NCT02259114	OTX015/MK-8628	I	NUT midline carcinoma, triple negative breast cancer, non-small cell lung cancer (rearranged ALK or mut KRAS), CPRC, pancreatic ductal adenocarcinoma	47	Completed
NCT02698176		I	NUT midline carcinoma, triple negative breast cancer, non-small cell lung cancer, CRPC	13	Terminated
NCT01987362		I	Solid Tumors	120	Active
NCT02711956	ZEN003694	I	Metastatic CRPC (+enzalutamide)	58	Recruiting
NCT02705469		I	Metastatic CRPC	44	Active
NCT03266159	GSK525762	II	Solid tumors	150	Not recruiting
NCT02419417	BMS-986158	I/II	Advanced solid tumors	150	Recruiting
NCT02391480	ABBV-075	I	Advanced cancer, breast cancer, non-small, ell lung cancer, acute myeloid leukemia, multiple myeloma, prostate cancer, small-cell lung cancer, non-Hodgkins lymphoma	150	Recruiting
NCT02630251	GSK2820151	I	Advanced or recurrent solid tumors	60	Recruiting
NCT02369029	BAY 1238097	I	Neoplasms	8	Terminated
NCT02431260	INCB054329	I/II	Advanced cancer	69	Active, not recruiting
NCT02711137	INCB057643	I/II	Advanced cancer	230	Recruiting
NCT02607228	GS-5829	I/II	Metastatic CRPC (+enzalutamide)	132	Recruiting
NCT02711137	INCB057643	I/II	Advanced solid tumors and hematologic malignancy (+abiraterone)	420	Recruiting
EZH2 and PRC1/2				40	
NCT03213665	Tazemetostat	II	Advanced solid tumors, non-Hodgkin lymphoma, or histiocytic (EZH2, SMARCB1, or SMARCA4 mutations)	49	Recruiting
NCT01897571		I/II	Advanced solid tumors	420	Recruiting
NCT02875548		II	Advanced solid tumors	300	Recruiting
NCT03217253		I	Metastatic malignant solid neoplasm	48	Not recruiting
PRMT5 inhibitor					
NCT02900651	MAK683	I/II	Diffuse large B cell lymphoma, advanced solid tumors	113	Recruiting
LSD1/KDM1A inl					
NCT02712905 DNMT inhibitors	INCB059872	I/II	Advanced cancer	180	Recruiting
NCT01118741	Disulfiram		Prostate cancer	19	Completed
NCT00503984	Azacitidine	I/II	Metastatic CRPC (+docetaxel, prednisone)	22	Terminated
NCT00384839		II	CRPC	53	Completed
NCT02998567	Guadecitabine	I	Non-small cell lung cancer, CRPC (+pembrolizumab)	35	Not yet recruiting
HDAC inhibitors					
NCT01075308	Pracinostat (SB939)	II	Metastatic CRPC	32	Completed
NCT00670553		I	Prostate cancer, head and neck cancer, esophageal cancer	7	Completed
NCT00878436	Panobinostat (LBH589)	I/II	CRPC (+bicalutamide)	52	Completed
NCT00667862		II	Metastatic CRPC	35	Completed
NCT00663832		I	CRPC (+docetaxel and prednisone)	44	Completed
NCT00493766		I	CRPC (+docetaxel and prednisone)	16	Terminated
NCT00419536		I	CRPC (+docetaxel and prednisone)	108	Terminated
NCT00330161	Vorinostat (SAHA, MK0683)	II	Metastatic CRPC	29	Completed
NCT01174199		I	Metastatic CRPC	13	Terminated
NCT00589472		II	Primary prostate cancer (+bicalutamide.)	19	Completed



Table 2 (continued)

Trial ID	Drug	Phase	Conditions	Patients	Status
NCT00565227		I	Non-small-cell lung carcinoma, prostate cancer, bladder cancer, urothelial carcinoma	12	Terminated
NCT00511576	Mocetinostat (MGCD0103)	Ι	Breast cancer, lung cancer, prostate cancer, gastric cancer (+docetaxel)	54	Terminated
NCT00020579	Entinostat (MS-275)	I	Advanced solid tumors, lymphoma	75	Completed
NCT00413075	Belinostat (PXD101)	I	Advanced solid tumors, lymphoma	121	Completed
NCT00413322		I	Advanced solid tumors (+5-fluorouracil)	35	Completed

prostate cancer progression. This H3K4me2-3 epigenetic reader has been reported mutated in 43% of Gleason 7 or higher prostate cancer tumors, associated with ETS gene fusion negative status [121] and its loss related with prostate cancer aggressiveness [50] and DNA repair defects, hence sensitizing tumor cells to PARP inhibitors [51]. More recently, Zhao and colleagues at the DePinho laboratory have demonstrated in PTEN null prostate tumors that CHD1 depletion dramatically suppressed cell proliferation, survival, and tumorigenic potential by activating the pro-tumorigenic TNF-NF-κB gene network [122].

Pioneer Factors in Prostate Cancer Progression

Different from other DNA bound proteins and transcription factors, pioneer factors can access their targets in nucleosomes and in highly compacted chromatin regions, facilitating chromatin accessibility and the recruitment of additional TFs and co-TF and the transcriptional machinery [123]. Among paradigmatic pioneering factors are some of the members of the GATA and FoxA gene families, known mainly for their key role as chromatin-factors during early development [124–127].

The best-known pioneering factor for its role in prostate cancer is FOXA1. Through the interaction and recruitment of AR to chromatin site, FoxA1 defines and controls the AR cistrome resulting in context-dependent positive or negative regulation [52, 55, 128, 129]. In particular, because FOXA1 activity on chromatin results in increased accessibility [52] and increased chromatin-bound AR, high FOXA1 expression leads to a restricted AR cistrome regulation [53].

GATA genes, and GATA2 in particular, have proved to be crucial for prostate development via modulating AR function [54, 55]. However, despite the role is comparable to that of FoxA1, the mechanisms have shown

to be quite different. GATA2 depletion did not seem to have a reprogramming effect on AR binding sites and in fact correlated with a downregulation in AR expression. Accordingly, GATA2 activity in human prostate cancer is strongly associated to AR levels and is hence considered a prostate cancer oncogene. Provocatively, it was found that FOXA1 also has the potential to reprogram GATA2 and act as a pioneering effect for both AR and GATA2, suggesting that FOXA1 regulates a transcriptional network that controls AR-mediated gene expression in prostate cancer [53].

Lineage Plasticity in Prostate Cancer Stem Cells

Aside from their ability to induce pluripotency, the Yamanaka factors (OCT4, SOX2, KLF4, and c-MYC) [130], and other reprograming factors like NANOG or LIN28, have been widely implicated in tumorigenesis in various cancers including the prostate.

SOX2 is required for survival, pluripotency, clonogenicity, and self-renewal of ESCs. A relationship between SOX2 overexpression in tumorigenesis has been established in different types of cancer, including prostate [56] and its expression linked to tumor grade [58]. SOX2 is an epigenetic reprogramming factor and oncogene shown to regulate androgen-independent CRPC proliferation and evasion of apoptosis [57, 58] and to promote tumor metastasis by inducing EMT [59]. Further evidence suggests that SOX2 promotes self-renewal of the CSCs population by acting downstream of EGFR [131]. Importantly, in the recent years, SOX2 activity has been tightly associated to neuroendocrine transdifferentiation from prostate adenocarcinoma cells and the subsequent androgen independence of neuroendocrine prostate cancer phenotypes (NEPC). While the exact mechanisms remain unclear, substantial progress was made over the last couple of years. In particular, Russo and colleagues showed that SOX2



was expressed in NEPC murine models [60] whereas others found its expression restricted to NEPC areas of advanced human prostate cancer [61]. Recent studies by Bishop and collaborators at the Zoubeidi laboratory have shown that SOX2 is transcriptionally regulated by neural transcription factor BRN2 [132••], which in turn is negatively suppressed by the AR, hence revealing an AR-dependent suppression of cell differentiation toward a neuroendocrine AR-independent phenotype. Additional support to the central role of SOX2 in the emergence of NEPC and AR-independence after Enzalutamide treatment came from studies at the Ku and Mu and collaborators at the Sawyers and Goodrich laboratories [62••, 63••].

c-MYC (MYC) is a well-known oncogene proposed as a marker of disease progression in prostate cancer [133] and associated with prostate cancer recurrence and poor prognosis [134]. MYC activation cooperates with loss of PTEN to drive prostate cancer progression [135] and metastasis [136]. MYC proteins also drive epigenetic activation of gene expression in prostate cancer; the PRC2 member EZH2 is directly upregulated by MYC [137] and MYCN, which was shown to be a driver of NEPC [66] by inducing an EZH2-mediated transcriptional program [64]. Additionally, MYC expression was found to be regulated by the histone demethylase JMJD1A, controlling proliferation and survival of prostate cancer cells [138]. MYC also regulates the expression of histone demethylases PHF8 and KDMA3 in NEPC and CRPC [29]. Interestingly, while AR signaling in the normal prostate represses MYC expression, its expression is stimulated by AR during tumorigenesis, [139, 140]. It was also recently reported that MYC overexpression deregulates the AR transcriptional program by altering AR chromatin occupancy and H3K4me1 and H3K27me3 marks distribution, antagonizing clinically relevant AR target genes such as PSA [65].

Oncogenic Pathways Involved in Epigenetic Regulations

Together with the AR, the oncogenic pathways most frequently altered in prostate cancer onset and progression are the RB, PI3K/AKT, and Ras/Raf pathways due to mutations in several members [72]. While the Ras/Raf pathway is activated in 43% of primary and 90% of metastatic prostate cancer, the triggering mechanisms remain to be fully understood. The Whitte laboratory demonstrated a synergistic interaction between Ras pathway activation and AR signaling that leads to elevated EZH2 expression and expand prostate cancer progenitor cells in vivo. It has been long suggested that this pathway is a major

contributor of aggressiveness via the activation of EMT transcriptional programs. Nolan and colleagues proposed a model in which the secreted extracellular protein Hsp90 initiates ERK signaling and leads to the recruitment of EZH2 to the E-cadherin promoter and repression of E-cadherin expression, driving epithelial to mesenchymal transition (EMT) and invasion in prostate cancer cells [67]. Additionally, DAB2IP (disabled homolog 2 interacting protein) is a tumor suppressor Ras-GAP that negatively controls Ras-dependent mitogenic signals and modulates TNFα/NF-κB, WNT/β-catenin, PI3K/AKT, and androgen receptors pathways [68–70]. EZH2-induced DAB2IP silencing activates Ras and NFkappaB and triggers metastasis [141, 142]. Data from our laboratory showed that concomitant activation of the PI3K and MAPk pathways in mice results in highly aggressive and fully metastatic tumors that are inherently castration resistant [143, 144]. Interestingly, by targeting the PI3K/MAPk pathways with small molecules in vivo, we demonstrated that the drug response network was highly enriched in epigenetic modulators, including SUV39H1, WHSC1, TOP2A, or UHRF1 [145], suggesting that epigenetic control of gene expression plays a central role in the aggressive phenotype imposed by the activation of Ras signaling. Accordingly, we have found that a core signature of chromatin modifiers and DNMTs drive the cancer cell intrinsic mechanisms of metastasis and CRPC (unpublished).

The retinoblastoma tumor suppressor gene RB1 is more commonly loss in metastatic and antiandrogen resistant prostate cancer (74% of cases) and NEPC (90% of cases) [71] than it is in primary tumors (34% of cases) [72]. It has been recently described an activity of Rb1 in the epigenetic regulation of expression, since RB1 directly repress the expression of Sox2 and Ezh2. Consequently, Rb1 loss in prostate cancer lead to EZH2 and Sox2 increase and gene expression widespread changes that leads toward a stem cell-like state that would facilitate the onset of metastasis, neuroendocrine transdifferentiation, and the acquisition of ADT resistance. The authors show that Ezh2 inhibition restores enzalutamide sensitivity in NEPC variants and recurrent prostate cancer cells by opposing lineage transformation [63...]. Furthermore, mutations in TP53 and RB1 tumor suppressor genes can promote a cellular plasticity state mediated by increased expression of SOX2 that, when it is compromised with antiandrogen therapy promotes resistance through lineage switching [62...]. It has also recently been shown that the Hedgehog (HH) signaling pathway and SOX2 co-operate in androgen-independent prostate cancer to promote carcinogenesis [146].

The PTEN/PI3K/AKT pathway is altered in 42% of primary and 100% of metastatic cases; loss of PTEN and activation of the PI3K/AKT signaling pathway are hallmarks of prostate cancer, and cooperate with the activation of the RAS/MAPK pathway to promote EMT and metastatic CRPC development.



Epigenetically, it has also been shown that PTEN depletion contributes to a switch from a global H3K27 acetylatilation to H3K27 trimethylation, resulting in increased expression of EZH2 and decrease of the target genes DAB2PI together with negative regulator of cell growth p27^{KIP1} and p21^{CIP1} [147]. As mentioned above, increased AKT activity phosphorylates NSD2 at S172, preventing its degradation by CRL4^{Cdt2} E3 ligase, hence leading to its stabilization, which in turn upregulates RICTOR (mTORC2). This results in further enhancement of AKT signaling in a AKT/NSD2/mTORC2 positive feedback loop that sustains AKT signaling [1••].

Constitutive activation of TGF-\beta signaling is a wellrecognized mechanism for induction of EMT and prostate cancer metastasis development. TGF-\(\beta\)1-induced EMT in prostate cancer is mediated by the histone methyltransferase RbBP5. RbBP5 is a conserved component of the COMPASS/-like complex, which catalyzes the trimethylation of histone H3 lysine 4 that is considered an epigenetic mark of actively transcribed genes. RbBP5 activity is in turn modulated by the binding of SMAD2/3, a downstream signaling factor to the TGF-beta pathway, to the Snail promoter [148]. Snail activates the EMT process by inhibiting transcription of E-cadherin via the recruitment to its promoter of the polycomb repressive complex 2 (PRC2) and the histone methylstranferase G9a, leading to repressive H3K27 and H3K9 methylation [149, 150]. An interesting new perspective was provided recently linking ERG signaling with TGF-\(\beta\). Data suggest that ERG regulates the transcription of the transcription factor SOX4 and together they cooperate in TGF-β1-induced EMT of prostate cancer cells [151]. This is not surprising taking into account that the oncogenic role of SOX4 has been proposed in several other tumor types. In particular, SOX4 regulates EZH2 expression and chromating remodeling, and is a key component of the PI3K/AKT pathway in prostate cancer. In fact, SOX4 inhibition reduces AKT and β-catenin pathways activation and decreases prostate cancer invasiveness through positive feedback loop between SOX4 and PI3K-AKT-mTOR [152].

Finally, a tyrosine kinase, namely ACK1, has been found to link oncogenic signaling with epigenetic regulation. ACK1 was found upregulated in primary PCa and CRPC [72, 73], correlated with poor prognosis and reported to interact with AR to drive ADT resistance and CRPC growth [74]. A recent study demostrates that ACK1 regulates transcription of AR and AR-v7 via epigenetic regulation. In particular, ACK1 would phosphorylate histone H4 upstream of the AR transcription start site, recruiting the WRD5/MLL2 complex, therefore mediating H3K4 trymethylation and transcriptional activation. Inhibition of ACK1 with a small molecule inhibitor confirms that this epigenetic activity is required to maintain AR transcription and CRPC tumor growth [153].



Drug Development on Epigenetic Regulators as Therapeutic Targets

Mounting evidence from basic and preclinical investigations suggest that targeting key components of the epigenetic machinery will have clinical benefit for cancer patients including prostate cancer ones. Yet, clinical development for those therapies is still very limited. On the one hand, this may be partly due to the inherent difficulty in targeting nuclear effector mechanisms. On the other hand, the fact that most epigenetic master regulators exert their functions over an extensive transcriptional network in a context-dependent manner makes it particularly challenging to achieve cancer cell specificity, thus resulting in significant toxicity. Despite these limitations, a number of drugs are currently in clinical trials at different phases, being BET bromodomain inhibitors, HMT/HDMT inhibitors, DNMT inhibitors, and HDAC inhibitors the focus of most intense drug development efforts. Table 2 summarizes the most relevant ongoing or recently completed clinical trials involving epigenetic drugs.

Conclusion

In view of the accumulated evidenced supporting the key role of the dysregulated epigenome to prostate cancer onset and progression, three mechanisms emerge as the most significant contributors. First, a number of alterations in epigenetic master regulators result in enhanced transcriptional activity and pro-oncogenic role of the Androgen Receptor signaling. This is largely mediated by either remodeling of the chromatin to facilitate AR binding and assembly of the transcriptional complex and posttranslational modifications in the AR itself or essential co-factors resulting in gain of function features. Secondly, the aberrant activation of transcriptional programs tightly associated to developmental pathways and stem features, either via alterations in pioneering factors or pluripotency master regulators, contributes to the acquisition of treatment-resistant phenotypes that are highly aggressive. Finally, a significant number of alterations in epigenetic master regulators also result in the activation of oncogenic signaling pathways that contribute to the aggressiveness and androgen independence in advanced prostate tumors. In summary, the epigenome is emerging as an attractive and plausible target for anticancer therapy in general and prostate cancer in particular. While drug development is still limited, and faces inherent challenges associated with the unique nature of these targets, it seems evident that efficacy of such treatments will be maximized in combination with standard of care treatments for which most lethal prostate cancer ultimately develop resistant mechanism.

Acknowledgements This research is supported by funding from the Spanish Ministry of Economy, Industry and Competitiveness (MINECO), which is part of the State Research Agency, through the projects PI16/01070 and CP15/00090. We also acknowledge the support from the European Association of Urology Research Foundation (EAURF/407003/XH), and the Fundacion BBVA-Young Investigator Award. We thank CERCA Program / Generalitat de Catalunya for the institutional support.

Compliance with Ethical Standards

Conflict of Interest Katia Ruggero, Sonia Farran-Matas, Adrian Martinez-Tebar, and Alvaro Aytes declare no conflicts of interest.

Human and Animal Rights and Informed Consent This article does not contain any studies with human or animal subjects performed by any of the authors.

Open Access This article is distributed under the terms of the Creative Commons Attribution 4.0 International License (http://creativecommons.org/licenses/by/4.0/), which permits unrestricted use, distribution, and reproduction in any medium, provided you give appropriate credit to the original author(s) and the source, provide a link to the Creative Commons license, and indicate if changes were made.

References

Papers of particular interest, published recently, have been highlighted as:

- Of importance
- Of major importance
 - 1.•• Li N, Xue W, Yuan H, Dong B, Ding Y, Liu Y, et al. AKT-mediated stabilization of histone methyltransferase WHSC1 promotes prostate cancer metastasis. J Clin Invest. 2017;127(4): 1284–302. This work demonstrates that NSD2 is activated in PTEN null tumors by the AKT pathway and that its expression is required for metastatic progression.
 - Ezponda T, Popovic R, Shah MY, Martinez-Garcia E, Zheng Y, Min DJ, et al. The histone methyltransferase MMSET/WHSC1 activates TWIST1 to promote an epithelial-mesenchymal transition and invasive properties of prostate cancer. Oncogene. 2013;32(23):2882–90.
 - Asangani IA, Ateeq B, Cao Q, Dodson L, Pandhi M, Kunju LP, et al. Characterization of the EZH2-MMSET histone methyltransferase regulatory axis in cancer. Mol Cell. 2013;49(1):80–93.
 - Yang YA, Yu J. EZH2, an epigenetic driver of prostate cancer. Protein Cell. 2013;4(5):331–41.
 - Wu C, Jin X, Yang J, Yang Y, He Y, Ding L, et al. Inhibition of EZH2 by chemo- and radiotherapy agents and small molecule inhibitors induces cell death in castration-resistant prostate cancer. Oncotarget. 2016;7(3):3440–52.
 - Yu T, Wang C, Yang J, Guo Y, Wu Y, Li X. Metformin inhibits SUV39H1-mediated migration of prostate cancer cells. Oncogene. 2017;6(5):):28.
 - Li Q, Li Y, Wang Y, Cui Z, Gong L, Qu Z, et al. Quantitative proteomic study of human prostate cancer cells with different metastatic potentials. Int J Oncol. 2016;48(4):1437–46.
 - Askew EB, Bai S, Parris AB, Minges JT, Wilson EM. Androgen receptor regulation by histone methyltransferase suppressor of variegation 3-9 homolog 2 and melanoma antigen-A11. Mol Cell Endocrinol. 2017;443:42–51.

- Vieira FQ, Costa-Pinheiro P, Almeida-Rios D, Graca I, Monteiro-Reis S, Simoes-Sousa S, et al. SMYD3 contributes to a more aggressive phenotype of prostate cancer and targets cyclin D2 through H4K20me3. Oncotarget. 2015;6(15):13644–57.
- Huang L, Xu AM. SET and MYND domain containing protein 3 in cancer. Am J Transl Res. 2017:9(1):1–14.
- Stopa N, Krebs JE, Shechter D. The PRMT5 arginine methyltransferase: many roles in development, cancer and beyond. Cell Mol Life Sci. 2015;72(11):2041–59.
- 12.• Mounir Z, Korn JM, Westerling T, Lin F, Kirby CA, Schirle M, et al. ERG signaling in prostate cancer is driven through PRMT5-dependent methylation of the Androgen Receptor. Elife. 2016;16(5):13964. This paper links for the first time epigenetically driven posttranslational modifications in the AR and ERG transcriptional expression.
- Deng X, Shao G, Zhang HT, Li C, Zhang D, Cheng L, et al. Protein arginine methyltransferase 5 functions as an epigenetic activator of the androgen receptor to promote prostate cancer cell growth. Oncogene. 2017;36(9):1223–31.
- 14.•• Metzger E, Wissmann M, Yin N, Muller JM, Schneider R, Peters AH, et al. LSD1 demethylates repressive histone marks to promote androgen-receptor-dependent transcription. Nature. 2005;437(7057):436–9. This paper links demethylation of a repressive histone mark with androgen-receptor-dependent gene activation.
- Cai C, He HH, Chen S, Coleman I, Wang H, Fang Z, et al. Androgen receptor gene expression in prostate cancer is directly suppressed by the androgen receptor through recruitment of lysine-specific demethylase 1. Cancer Cell. 2011;20(4):457–71.
- 16.• Liang Y, Ahmed M, Guo H, Soares F, Hua JT, Gao S, et al. LSD1-mediated epigenetic reprogramming drives CENPE expression and prostate cancer progression. Cancer Res. 2017;77(20):5479–90. This study shows that LSD1-mediated epigenetic reprogramming drives CRPC and was associated with the activation of CENPE and other cell-cycle genes.
- Xiang Y, Zhu Z, Han G, Ye X, Xu B, Peng Z, et al. JARID1B is a histone H3 lysine 4 demethylase up-regulated in prostate cancer. Proc Natl Acad Sci U S A. 2007;104(49):19226–31.
- Lu W, Liu S, Li B, Xie Y, Adhiambo C, Yang Q, et al. SKP2 inactivation suppresses prostate tumorigenesis by mediating JARID1B ubiquitination. Oncotarget. 2015;6(2):771–88.
- Stein J, Majores M, Rohde M, Lim S, Schneider S, Krappe E, et al. KDM5C is overexpressed in prostate cancer and is a prognostic marker for prostate-specific antigen-relapse following radical prostatectomy. Am J Pathol. 2014;184(9):2430–7.
- Li N, Dhar SS, Chen TY, Kan PY, Wei Y, Kim JH, et al. JARID1D is a suppressor and prognostic marker of prostate cancer invasion and metastasis. Cancer Res. 2016;76(4):831–43.
- Komura K, Jeong SH, Hinohara K, Qu F, Wang X, Hiraki M, et al. Resistance to docetaxel in prostate cancer is associated with androgen receptor activation and loss of KDM5D expression. Proc Natl Acad Sci U S A. 2016;113(22):6259–64.
- Yu L, Wang Y, Huang S, Wang J, Deng Z, Zhang Q, et al. Structural insights into a novel histone demethylase PHF8. Cell Res. 2010;20(2):166–73.
- Qi HH, Sarkissian M, Hu G-Q, Wang Z, Bhattacharjee A, Gordon DB, et al. Histone H4K20/H3K9 demethylase PHF8 regulates zebrafish brain and craniofacial development. Nature. 2010;466: 503-7
- Qiu J, Shi G, Jia Y, Li J, Wu M, Li J, et al. The X-linked mental retardation gene PHF8 is a histone demethylase involved in neuronal differentiation. Cell Res. 2010;20:908–18.
- Liu W, Tanasa B, Tyurina OV, Zhou TY, Gassmann R, Liu WT, et al. PHF8 mediates histone H4 lysine 20 demethylation events involved in cell cycle progression. Nature. 2010;466(7305):508– 12.



- Horton JR, Upadhyay AK, Qi HH, Zhang X, Shi Y, Cheng X. Enzymatic and structural insights for substrate specificity of a family of jumonji histone lysine demethylases. Nat Struct Amp Mol Biol. 2009;17:38.
- 27. Bjorkman M, Ostling P, Harma V, Virtanen J, Mpindi JP, Rantala J, et al. Systematic knockdown of epigenetic enzymes identifies a novel histone demethylase PHF8 overexpressed in prostate cancer with an impact on cell proliferation, migration and invasion. Oncogene. 2012;31(29):3444–56.
- Tong D, Liu Q, Liu G, Yuan W, Wang L, Guo Y, et al. The HIF/ PHF8/AR axis promotes prostate cancer progression. Oncogene. 2016;5(12):e283.
- Maina PK, Shao P, Liu Q, Fazli L, Tyler S, Nasir M, et al. c-MYC drives histone demethylase PHF8 during neuroendocrine differentiation and in castration-resistant prostate cancer. Oncotarget. 2016;7(46):75585–602.
- Shin S, Janknecht R. Activation of androgen receptor by histone demethylases JMJD2A and JMJD2D. Biochem Biophys Res Commun. 2007;359(3):742–6.
- Wissmann M, Yin N, Muller JM, Greschik H, Fodor BD, Jenuwein T, et al. Cooperative demethylation by JMJD2C and LSD1 promotes androgen receptor-dependent gene expression. Nat Cell Biol. 2007;9(3):347–53.
- Yamane K, Toumazou C, Tsukada Y, Erdjument-Bromage H, Tempst P, Wong J, et al. JHDM2A, a JmjC-containing H3K9 demethylase, facilitates transcription activation by androgen receptor. Cell. 2006;125(3):483–95.
- Wilson S, Fan L, Sahgal N, Qi J, Filipp FV. The histone demethylase KDM3A regulates the transcriptional program of the androgen receptor in prostate cancer cells. Oncotarget. 2017;8(18):30328–43.
- Coffey K, Rogerson L, Ryan-Munden C, Alkharaif D, Stockley J, Heer R, et al. The lysine demethylase, KDM4B, is a key molecule in androgen receptor signalling and turnover. Nucleic Acids Res. 2013;41(8):4433–46.
- 35. Xiang Y, Zhu Z, Han G, Lin H, Xu L, Chen CD. JMJD3 is a histone H3K27 demethylase. Cell Res. 2007;17(10):850–7.
- Chin SP, Dickinson JL, Holloway AF. Epigenetic regulation of prostate cancer. Clin Epigenetics. 2011;2(2):151–69.
- Lin PC, Giannopoulou EG, Park K, Mosquera JM, Sboner A, Tewari AK, et al. Epigenomic alterations in localized and advanced prostate cancer. Neoplasia. 2013;15(4):373–83.
- Kang GH, Lee S, Lee HJ, Hwang KS. Aberrant CpG island hypermethylation of multiple genes in prostate cancer and prostatic intraepithelial neoplasia. J Pathol. 2004;202(2):233–40.
- Mahon KL, Qu W, Devaney J, Paul C, Castillo L, Wykes RJ, et al. Methylated glutathione S-transferase 1 (mGSTP1) is a potential plasma free DNA epigenetic marker of prognosis and response to chemotherapy in castrate-resistant prostate cancer. Br J Cancer. 2014;111(9):1802–9.
- Fu M, Wang C, Reutens AT, Wang J, Angeletti RH, Siconolfi-Baez L, et al. p300 and p300/cAMP-response element-binding protein-associated factor acetylate the androgen receptor at sites governing hormone-dependent transactivation. J Biol Chem. 2000;275(27):20853–60.
- 41. Jin L, Garcia J, Chan E, de la Cruz C, Segal E, Merchant M, et al. Therapeutic targeting of the CBP/p300 bromodomain blocks the growth of castration-resistant prostate cancer. Cancer Res. 2017;77(20):5564–75.
- Fu M, Liu M, Sauve AA, Jiao X, Zhang X, Wu X, et al. Hormonal control of androgen receptor function through SIRT1. Mol Cell Biol. 2006;26(21):8122–35.
- Lavery DN, Bevan CL. Androgen receptor signalling in prostate cancer: the functional consequences of acetylation. J Biomed Biotechnol. 2011;862125(10):28.

- Damodaran S, Damaschke N, Gawdzik J, Yang B, Shi C, Allen GO, et al. Dysregulation of Sirtuin 2 (SIRT2) and histone H3K18 acetylation pathways associates with adverse prostate cancer outcomes. BMC Cancer. 2017;17(1):874.
- 45.• Asangani IA, Dommeti VL, Wang X, Malik R, Cieslik M, Yang R, et al. Therapeutic targeting of BET bromodomain proteins in castration-resistant prostate cancer. Nature. 2014;510(7504):278–82. This study reports that BRD4 physically interacts with high-affinity with the N-terminal domain of AR leading to AR translocation into the nucleus and AR recruitment to target loci, promoting AR activity and expression of AR target genes in CRPC.
- Shah N, Wang P, Wongvipat J, Karthaus WR, Abida W, Armenia J, et al. Regulation of the glucocorticoid receptor via a BETdependent enhancer drives antiandrogen resistance in prostate cancer. elife. 2017;6
- Li J, Alyamani M, Zhang A, Chang KH, Berk M, Li Z, et al. Aberrant corticosteroid metabolism in tumor cells enables GR takeover in enzalutamide resistant prostate cancer. elife. 2017;6
- Dai X, Gan W, Li X, Wang S, Zhang W, Huang L, et al. Prostate cancer-associated SPOP mutations confer resistance to BET inhibitors through stabilization of BRD4. Nat Med. 2017;23(9):1063– 71.
- Groner AC, Cato L, de Tribolet-Hardy J, Bernasocchi T, Janouskova H, Melchers D, et al. TRIM24 is an oncogenic transcriptional activator in prostate cancer. Cancer Cell. 2016;29(6): 846–58.
- Rodrigues LU, Rider L, Nieto C, Romero L, Karimpour-Fard A, Loda M, et al. Coordinate loss of MAP3K7 and CHD1 promotes aggressive prostate cancer. Cancer Res. 2015;75(6):1021–34.
- Kari V, Mansour WY, Raul SK, Baumgart SJ, Mund A, Grade M, et al. Loss of CHD1 causes DNA repair defects and enhances prostate cancer therapeutic responsiveness. EMBO Rep. 2016;17(11):1609–23.
- Jin HJ, Zhao JC, Wu L, Kim J, Yu J. Cooperativity and equilibrium with FOXA1 define the androgen receptor transcriptional program. Nat Commun. 2014;5(3972)
- Zhao JC, Fong KW, Jin HJ, Yang YA, Kim J, Yu J. FOXA1 acts upstream of GATA2 and AR in hormonal regulation of gene expression. Oncogene. 2016;35(33):4335–44.
- Lupien M, Eeckhoute J, Meyer CA, Wang Q, Zhang Y, Li W, et al. Fox A1 translates epigenetic signatures into enhancer-driven lineage-specific transcription. Cell. 2008;132(6):958–70.
- Wang Q, Li W, Liu XS, Carroll JS, Jänne OA, Keeton EK, et al. A hierarchical network of transcription factors governs androgen receptor-dependent prostate cancer growth. Mol Cell. 2007;27(3):380–92.
- Wong OG, Huo Z, Siu MK, Zhang H, Jiang L, Wong ES, et al. Hypermethylation of SOX2 promoter in endometrial carcinogenesis. Obstet Gynecol Int. 2010;10(682504):9.
- Lin F, Lin P, Zhao D, Chen Y, Xiao L, Qin W, et al. Sox 2 targets cyclinE, p 27 and survivin to regulate androgen-independent human prostate cancer cell proliferation and apoptosis. Cell Prolif. 2012;45(3):207–16.
- Kregel S, Kiriluk KJ, Rosen AM, Cai Y, Reyes EE, Otto KB, et al. Sox2 is an androgen receptor-repressed gene that promotes castration-resistant prostate cancer. PLoS One. 2013;8(1):11.
- Li X, Xu Y, Chen Y, Chen S, Jia X, Sun T, et al. SOX2 promotes tumor metastasis by stimulating epithelial-to-mesenchymal transition via regulation of WNT/beta-catenin signal network. Cancer Lett. 2013;336(2):379–89.
- Russo MV, Esposito S, Tupone MG, Manzoli L, Airoldi I, Pompa P, et al. SOX2 boosts major tumor progression genes in prostate cancer and is a functional biomarker of lymph node metastasis. Oncotarget. 2016;7(11):12372–85.



- Esposito S, Russo MV, Airoldi I, Tupone MG, Sorrentino C, Barbarito G, et al. SNAI2/Slug gene is silenced in prostate cancer and regulates neuroendocrine differentiation, metastasissuppressor and pluripotency gene expression. Oncotarget. 2015;6(19):17121–34.
- 62.•• Mu P, Zhang Z, Benelli M, Karthaus WR, Hoover E, Chen CC, et al. SOX2 promotes lineage plasticity and antiandrogen resistance in TP53- and RB1-deficient prostate cancer. Science. 2017;355(6320):84–8. This work demonstrates that lineage plasticity and neuroendocrine differentiation in androgen independence is partly driven by Sox2 in prostate cancer mouse models carrying loss of function alleles for p53 and Rb tumor suppressors.
- 63. •• Ku SY, Rosario S, Wang Y, Mu P, Seshadri M, Goodrich ZW, et al. Rb1 and Trp53 cooperate to suppress prostate cancer lineage plasticity, metastasis, and antiandrogen resistance. Science. 2017;355(6320):78–83. This work shows that Sox2 and Ezh2 mediates suppression of prostate cancer lineage plasticity in Rb1 and p53 null tumours. Ezh2 inhibition restores enzalutamide sensitivity in NEPC variants and recurrent prostate cancer cells by opposing lineage transformation.
- Dardenne E, Beltran H, Benelli M, Gayvert K, Berger A, Puca L, et al. N-Myc induces an EZH2-mediated transcriptional program driving neuroendocrine prostate Cancer. Cancer Cell. 2016;30(4): 563–77.
- Barfeld SJ, Urbanucci A, Itkonen HM, Fazli L, Hicks JL, Thiede B, et al. C-Myc Antagonises the transcriptional activity of the androgen receptor in prostate cancer affecting key gene networks. EBioMedicine. 2017;18:83–93.
- Lee JK, Phillips JW, Smith BA, Park JW, Stoyanova T, McCaffrey EF, et al. N-Myc drives neuroendocrine prostate cancer initiated from human prostate epithelial cells. Cancer Cell. 2016;29(4): 536–47.
- Nolan KD, Franco OE, Hance MW, Hayward SW, Isaacs JS. Tumor-secreted Hsp90 subverts polycomb function to drive prostate tumor growth and invasion. J Biol Chem. 2015;290(13): 8271–82.
- Bellazzo A, Di Minin G, Collavin L. Block one, unleash a hundred. Mechanisms of DAB2IP inactivation in cancer. Cell Death Differ. 2017;24(1):15–25.
- Wu K, Liu J, Tseng SF, Gore C, Ning Z, Sharifi N, et al. The role of DAB2IP in androgen receptor activation during prostate cancer progression. Oncogene. 2014;33(15):1954

 –63.
- Tsai YS, Lai CL, Lai CH, Chang KH, Wu K, Tseng SF, et al. The role of homeostatic regulation between tumor suppressor DAB2IP and oncogenic Skp2 in prostate cancer growth. Oncotarget. 2014;5(15):6425–36.
- Tan HL, Sood A, Rahimi HA, Wang W, Gupta N, Hicks J, et al. Rb loss is characteristic of prostatic small cell neuroendocrine carcinoma. Clin Cancer Res. 2014;20(4):890–903.
- Taylor BS, Schultz N, Hieronymus H, Gopalan A, Xiao Y, Carver BS, et al. Integrative genomic profiling of human prostate cancer. Cancer Cell. 2010;18(1):11–22.
- van der Horst EH, Degenhardt YY, Strelow A, Slavin A, Chinn L, Orf J, et al. Metastatic properties and genomic amplification of the tyrosine kinase gene ACK1. Proc Natl Acad Sci U S A. 2005;102(44):15901–6.
- Mahajan NP, Liu Y, Majumder S, Warren MR, Parker CE, Mohler JL, et al. Activated Cdc42-associated kinase Ack1 promotes prostate cancer progression via androgen receptor tyrosine phosphorylation. Proc Natl Acad Sci U S A. 2007;104(20):8438–43.
- Nelson WG, De Marzo AM, Yegnasubramanian S. Epigenetic alterations in human prostate cancers. Endocrinology. 2009;150(9):3991–4002.

- Suzuki H, Ueda T, Ichikawa T, Ito H. Androgen receptor involvement in the progression of prostate cancer. Endocr Relat Cancer. 2003;10(2):209–16.
- Suzuki H, Freije D, Nusskern DR, Okami K, Cairns P, Sidransky D, et al. Interfocal heterogeneity of PTEN/MMAC1 gene alterations in multiple metastatic prostate cancer tissues. Cancer Res. 1998;58(2):204–9.
- Jarrard DF, Bova GS, Ewing CM, Pin SS, Nguyen SH, Baylin SB, et al. Deletional, mutational, and methylation analyses of CDKN2 (p16/MTS1) in primary and metastatic prostate cancer. Genes Chromosomes Cancer. 1997;19(2):90–6.
- Pakneshan P, Xing RH, Rabbani SA. Methylation status of uPA promoter as a molecular mechanism regulating prostate cancer invasion and growth in vitro and in vivo. FASEB J. 2003;17(9): 1081–8
- Ashour N, Angulo JC, Andres G, Alelu R, Gonzalez-Corpas A, Toledo MV, et al. A DNA hypermethylation profile reveals new potential biomarkers for prostate cancer diagnosis and prognosis. Prostate. 2014;74(12):1171–82.
- Coffey K, Rogerson L, Ryan-Munden C, Alkharaif D, Stockley J, Heer R, et al. The lysine demethylase, KDM4B, is a key molecule in androgen receptor signalling and turnover. Nucleic Acids Res. 2013;41(8):4433–46.
- Hayami S, Kelly JD, Cho HS, Yoshimatsu M, Unoki M, Tsunoda T, et al. Overexpression of LSD1 contributes to human carcinogenesis through chromatin regulation in various cancers. Int J Cancer. 2011;128(3):574–86.
- 83. Kahl P, Gullotti L, Heukamp LC, Wolf S, Friedrichs N, Vorreuther R, et al. Androgen receptor coactivators lysine-specific histone demethylase 1 and four and a half LIM domain protein 2 predict risk of prostate cancer recurrence. Cancer Res. 2006;66(23): 11341–7.
- Battaglia S, Karasik E, Gillard B, Williams J, Winchester T, Moser MT, et al. LSD1 dual function in mediating epigenetic corruption of the vitamin D signaling in prostate cancer. Clin Epigenetics. 2017;9(82):017–0382.
- Li Y, Trojer P, Xu CF, Cheung P, Kuo A, Drury WJ, 3rd, et al. The target of the NSD family of histone lysine methyltransferases depends on the nature of the substrate. J Biol Chem 2009; 284(49): 34283–34295.
- Keats JJ, Maxwell CA, Taylor BJ, Hendzel MJ, Chesi M, Bergsagel PL, et al. Overexpression of transcripts originating from the MMSET locus characterizes all t(4;14)(p16;q32)-positive multiple myeloma patients. Blood. 2005;105(10):4060–9.
- 87. Yang P, Guo L, Duan ZJ, Tepper CG, Xue L, Chen X, et al. Histone methyltransferase NSD2/MMSET mediates constitutive NF-kappaB signaling for cancer cell proliferation, survival, and tumor growth via a feed-forward loop. Mol Cell Biol. 2012;32(15):3121–31.
- Kang HB, Choi Y, Lee JM, Choi KC, Kim HC, Yoo JY, et al. The histone methyltransferase, NSD2, enhances androgen receptormediated transcription. FEBS Lett. 2009;583(12):1880–6.
- Nalla AK, Williams TF, Collins CP, Rae DT, Trobridge GD. Lentiviral vector-mediated insertional mutagenesis screen identifies genes that influence androgen independent prostate cancer progression and predict clinical outcome. Mol Carcinog. 2016;55(11):1761–71.
- Shi Y, Lan F, Matson C, Mulligan P, Whetstine JR, Cole PA, et al. Histone demethylation mediated by the nuclear amine oxidase homolog LSD1. Cell. 2004;119(7):941–53.
- Metzger E, Yin N, Wissmann M, Kunowska N, Fischer K, Friedrichs N, et al. Phosphorylation of histone H3 at threonine 11 establishes a novel chromatin mark for transcriptional regulation. Nat Cell Biol. 2008;10(1):53–60.
- Jia L, Berman BP, Jariwala U, Yan X, Cogan JP, Walters A, et al. Genomic androgen receptor-occupied regions with different



- functions, defined by histone acetylation, coregulators and transcriptional capacity. PLoS One. 2008;3(11):10.
- Jia L, Shen HC, Wantroba M, Khalid O, Liang G, Wang Q, et al. Locus-wide chromatin remodeling and enhanced androgen receptor-mediated transcription in recurrent prostate tumor cells. Mol Cell Biol. 2006;26(19):7331–41.
- Lasko LM, Jakob CG, Edalji RP, Qiu W, Montgomery D, Digiammarino EL, et al. Discovery of a selective catalytic p300/ CBP inhibitor that targets lineage-specific tumours. Nature. 2017;550(7674):128–32.
- 95.• Valdes-Mora F, Gould CM, Colino-Sanguino Y, Qu W, Song JZ, Taylor KM, et al. Acetylated histone variant H2A.Z is involved in the activation of neo-enhancers in prostate cancer. Nat Commun. 2017;8(1):1346. This study highlights the important role of histone acetylation in prostate cancer beyond active promoters via activation of AR associated enhancers and the increase in chromatin accessibility
- Ruscetti M, Dadashian EL, Guo W, Quach B, Mulholland DJ, Park JW, et al. HDAC inhibition impedes epithelialmesenchymal plasticity and suppresses metastatic, castrationresistant prostate cancer. Oncogene. 2016;35(29):3781–95.
- Di Croce L, Helin K. Transcriptional regulation by polycomb group proteins. Nat Struct Mol Biol. 2013;20(10):1147–55.
- Melling N, Thomsen E, Tsourlakis MC, Kluth M, Hube-Magg C, Minner S, et al. Overexpression of enhancer of zeste homolog 2 (EZH2) characterizes an aggressive subset of prostate cancers and predicts patient prognosis independently from pre- and postoperatively assessed clinicopathological parameters. Carcinogenesis. 2015;36(11):1333-40.
- Lee TI, Jenner RG, Boyer LA, Guenther MG, Levine SS, Kumar RM, et al. Control of developmental regulators by Polycomb in human embryonic stem cells. Cell. 2006;125(2):301–13.
- Liu L, Xu Z, Zhong L, Wang H, Jiang S, Long Q, et al. Enhancer of zeste homolog 2 (EZH2) promotes tumour cell migration and invasion via epigenetic repression of E-cadherin in renal cell carcinoma. BJU Int. 2016;117(2):351–62.
- Xu H, Xu K, He HH, Zang C, Chen CH, Chen Y, et al. Integrative analysis reveals the transcriptional collaboration between EZH2 and E2F1 in the regulation of cancer-related gene expression. Mol Cancer Res. 2016;14(2):163–72.
- Cha TL, Zhou BP, Xia W, Wu Y, Yang CC, Chen CT, et al. Akt-mediated phosphorylation of EZH2 suppresses methylation of lysine 27 in histone H3. Science. 2005;310(5746):306–10.
- 103.•• Xu K, Wu ZJ, Groner AC, He HH, Cai C, Lis RT, et al. EZH2 oncogenic activity in castration-resistant prostate cancer cells is Polycomb-independent. Science. 2012;338(6113):1465-9. This paper provides compelling evidence that the oncogenic role of Ezh2 in CRPC is partly independent of its repressive function and acts via coactivator functions with key transcription factors including AR
- 104. Labbe DP, Sweeney CJ, Brown M, Galbo P, Rosario S, Wadosky KM, et al. TOP2A and EZH2 provide early detection of an aggressive prostate cancer subgroup. Clin Cancer Res. 2017;23(22): 7072–83.
- Urbanucci A, Mills IG. Bromodomain-containing proteins in prostate cancer. Mol Cell Endocrinol. 2017;
- Fujisawa T, Filippakopoulos P. Functions of bromodomaincontaining proteins and their roles in homeostasis and cancer. Nat Rev Mol Cell Biol. 2017;18(4):246–62.
- 107.•• Loven J, Hoke HA, Lin CY, Lau A, Orlando DA, Vakoc CR, et al. Selective inhibition of tumor oncogenes by disruption of superenhancers. Cell 2013; 153(2):320–334.
- 108.•• Whyte WA, Orlando DA, Hnisz D, Abraham BJ, Lin CY, Kagey MH, et al. Master transcription factors and mediator establish super-enhancers at key cell identity genes. Cell. 2013;153(2): 307–19. This two papers provide evidence that disruption of

- enhancers and superenhancers through BET bromodomain inhibition is a promising therapeutic option in cancer and highlight the key role of this epigenetic master regulator in cancer progression
- 109. Jang MK, Mochizuki K, Zhou M, Jeong HS, Brady JN, Ozato K. The bromodomain protein Brd4 is a positive regulatory component of P-TEFb and stimulates RNA polymerase II-dependent transcription. Mol Cell. 2005;19(4):523–34.
- Zuber V, Bettella F, Witoelar A, Andreassen OA, Mills IG, Urbanucci A. Bromodomain protein 4 discriminates tissuespecific super-enhancers containing disease-specific susceptibility loci in prostate and breast cancer. BMC Genomics. 2017;18(1): 270
- Faivre EJ, Wilcox D, Lin X, Hessler P, Torrent M, He W, et al. Exploitation of castration-resistant prostate cancer transcription factor dependencies by the novel BET inhibitor ABBV-075. Mol Cancer Res. 2017;15(1):35–44.
- Asangani IA, Wilder-Romans K, Dommeti VL, Krishnamurthy PM, Apel IJ, Escara-Wilke J, et al. BET Bromodomain inhibitors enhance efficacy and disrupt resistance to AR antagonists in the treatment of prostate cancer. Mol Cancer Res. 2016;14(4):324–31.
- Arora VK, Schenkein E, Murali R, Subudhi SK, Wongvipat J, Balbas MD, et al. Glucocorticoid receptor confers resistance to antiandrogens by bypassing androgen receptor blockade. Cell. 2013;155(6):1309–22.
- Blee AM, Liu S, Wang L, Huang H. BET bromodomain-mediated interaction between ERG and BRD4 promotes prostate cancer cell invasion. Oncotarget. 2016;7(25):38319–32.
- Janouskova H, El Tekle G, Bellini E, Udeshi ND, Rinaldi A, Ulbricht A, et al. Opposing effects of cancer-type-specific SPOP mutants on BET protein degradation and sensitivity to BET inhibitors. Nat Med. 2017;23(9):1046–54.
- Zhang P, Wang D, Zhao Y, Ren S, Gao K, Ye Z, et al. Intrinsic BET inhibitor resistance in SPOP-mutated prostate cancer is mediated by BET protein stabilization and AKT-mTORC1 activation. Nat Med. 2017;23(9):1055–62.
- Gupta-Elera G, Garrett AR, Robison RA, O'Neill KL. The role of oxidative stress in prostate cancer. Eur J Cancer Prev. 2012;21(2): 155–62.
- Hussong M, Borno ST, Kerick M, Wunderlich A, Franz A, Sultmann H, et al. The bromodomain protein BRD4 regulates the KEAP1/NRF2-dependent oxidative stress response. Cell Death Dis. 2014;5:e1195.
- Theurillat JP, Udeshi ND, Errington WJ, Svinkina T, Baca SC, Pop M, et al. Prostate cancer. Ubiquitylome analysis identifies dysregulation of effector substrates in SPOP-mutant prostate cancer. Science. 2014;346(6205):85–9.
- Kikuchi M, Okumura F, Tsukiyama T, Watanabe M, Miyajima N, Tanaka J, et al. TRIM24 mediates ligand-dependent activation of androgen receptor and is repressed by a bromodomain-containing protein, BRD7, in prostate cancer cells. Biochim Biophys Acta. 2009;1793(12):1828–36.
- Grasso CS, Wu YM, Robinson DR, Cao X, Dhanasekaran SM, Khan AP, et al. The mutational landscape of lethal castrationresistant prostate cancer. Nature. 2012;487(7406):239–43.
- Zhao D, Lu X, Wang G, Lan Z, Liao W, Li J, et al. Synthetic essentiality of chromatin remodelling factor CHD1 in PTENdeficient cancer. Nature. 2017;542(7642):484–8.
- Zaret KS, Carroll JS. Pioneer transcription factors: establishing competence for gene expression. Genes Dev. 2011;25(21):2227– 41
- Lee CS, Friedman JR, Fulmer JT, Kaestner KH. The initiation of liver development is dependent on Foxa transcription factors. Nature. 2005;435(7044):944–7.



- Watt AJ, Zhao R, Li J, Duncan SA. Development of the mammalian liver and ventral pancreas is dependent on GATA4. BMC Dev Biol. 2007;7(1):37.
- Zhao R, Watt AJ, Li J, Luebke-Wheeler J, Morrisey EE, Duncan SA. GATA6 is essential for embryonic development of the liver but dispensable for early heart formation. Mol Cell Biol. 2005;25(7):2622–31.
- Holtzinger A, Evans T. Gata4 regulates the formation of multiple organs. Development. 2005;132(17):4005–14.
- Wang Q, Li W, Zhang Y, Yuan X, Xu K, Yu J, et al. Androgen receptor regulates a distinct transcription program in androgenindependent prostate cancer. Cell. 2009;138(2):245–56.
- Wang D, Garcia-Bassets I, Benner C, Li W, Su X, Zhou Y, et al. Reprogramming transcription by distinct classes of enhancers functionally defined by eRNA. Nature. 2011;474(7351):390–4.
- Takahashi K, Tanabe K, Ohnuki M, Narita M, Ichisaka T, Tomoda K, et al. Induction of pluripotent stem cells from adult human fibroblasts by defined factors. Cell. 2007;131(5):861–72.
- Rybak AP, Tang D. SOX2 plays a critical role in EGFR-mediated self-renewal of human prostate cancer stem-like cells. Cell Signal. 2013;25(12):2734–42.
- 132.•• Bishop JL, Thaper D, Vahid S, Davies A, Ketola K, Kuruma H, et al. The master neural transcription factor BRN2 is an androgen receptor-suppressed driver of neuroendocrine differentiation in prostate cancer. Cancer Discov. 2017;7(1):54–71. This works provides a mechanistic model for neuroendocrine differentiation after AR signaling blockade using patiend-derived models
- 133. Zeng W, Sun H, Meng F, Liu Z, Xiong J, Zhou S, et al. Nuclear C-MYC expression level is associated with disease progression and potentially predictive of two year overall survival in prostate cancer. Int J Clin Exp Pathol. 2015;8(2):1878–88.
- 134. Rye M, Bertilsson H, Drabløs F, Angelsen A, Bathen T, Tessem M-B. Gene signatures ESC, MYC and ERG-fusion are early markers of a potentially dangerous subtype of prostate cancer2014. 50 p.
- Kim J, Roh M, Doubinskaia I, Algarroba GN, Eltoum IE, Abdulkadir SA. A mouse model of heterogeneous, c-MYCinitiated prostate cancer with loss of Pten and p53. Oncogene. 2012;31(3):322–32.
- 136. Hubbard GK, Mutton LN, Khalili M, McMullin RP, Hicks JL, Bianchi-Frias D, et al. Combined MYC activation and Pten loss are sufficient to create genomic instability and lethal metastatic prostate cancer. Cancer Res. 2016;76(2):283–92.
- Koh CM, Iwata T, Zheng Q, Bethel C, Yegnasubramanian S, De Marzo AM. Myc enforces overexpression of EZH2 in early prostatic neoplasia via transcriptional and post-transcriptional mechanisms. Oncotarget. 2011;2(9):669–83.
- 138. Fan L, Peng G, Sahgal N, Fazli L, Gleave M, Zhang Y, et al. Regulation of c-Myc expression by the histone demethylase JMJD1A is essential for prostate cancer cell growth and survival. Oncogene. 2016;35(19):2441–52.
- 139. Vander Griend DJ, Litvinov IV, Isaacs JT. Conversion of androgen receptor signaling from a growth suppressor in normal prostate epithelial cells to an oncogene in prostate cancer cells involves a gain of function in c-Myc regulation. Int J Biol Sci. 2014;10(6): 627–42.

- Antony L, van der Schoor F, Dalrymple SL, Isaacs JT. Androgen receptor (AR) suppresses normal human prostate epithelial cell proliferation via AR/beta-catenin/TCF-4 complex inhibition of c-MYC transcription. Prostate. 2014;74(11):1118–31.
- Chen H, Tu SW, Hsieh JT. Down-regulation of human DAB2IP gene expression mediated by polycomb Ezh2 complex and histone deacetylase in prostate cancer. J Biol Chem. 2005;280(23): 22437–44.
- 142. Min J, Zaslavsky A, Fedele G, McLaughlin SK, Reczek EE, De Raedt T, et al. An oncogene-tumor suppressor cascade drives metastatic prostate cancer by coordinately activating Ras and nuclear factor-kappaB. Nat Med. 2010;16(3):286–94.
- 143. Aytes A, Mitrofanova A, Lefebvre C, Alvarez MJ, Castillo-Martin M, Zheng T, et al. Cross-species regulatory network analysis identifies a synergistic interaction between FOXM1 and CENPF that drives prostate cancer malignancy. Cancer Cell. 2014;25(5):638–51.
- 144. Aytes A, Mitrofanova A, Kinkade CW, Lefebvre C, Lei M, Phelan V, et al. ETV4 promotes metastasis in response to activation of PI3-kinase and Ras signaling in a mouse model of advanced prostate cancer. Proc Natl Acad Sci U S A. 2013;110(37):E3506–15.
- Mitrofanova A, Aytes A, Zou M, Shen MM, Abate-Shen C, Califano A. Predicting drug response in human prostate cancer from preclinical analysis of in vivo mouse models. Cell Rep. 2015;12(12):2060–71.
- Kar S, Sengupta D, Deb M, Pradhan N, Patra SK. SOX2 function and Hedgehog signaling pathway are co-conspirators in promoting androgen independent prostate cancer. Biochim Biophys Acta. 2017;1863(1):253–65.
- Ding L, Chen S, Liu P, Pan Y, Zhong J, Regan KM, et al. CBP loss cooperates with PTEN haploinsufficiency to drive prostate cancer: implications for epigenetic therapy. Cancer Res. 2014;74(7): 2050–61.
- 148. Li D, Sun H, Sun WJ, Bao HB, Si SH, Fan JL, et al. Role of RbBP5 and H3K4me3 in the vicinity of Snail transcription start site during epithelial-mesenchymal transition in prostate cancer cell. Oncotarget. 2016;7(40):65553–67.
- Dong C, Wu Y, Yao J, Wang Y, Yu Y, Rychahou PG, et al. G9a interacts with Snail and is critical for Snail-mediated E-cadherin repression in human breast cancer. J Clin Invest. 2012;122(4): 1469–86.
- 150. Liu S, Ye D, Guo W, Yu W, He Y, Hu J, et al. G9a is essential for EMT-mediated metastasis and maintenance of cancer stem celllike characters in head and neck squamous cell carcinoma. Oncotarget. 2015;6(9):6887–901.
- Liu Y, Zeng S, Jiang X, Lai D, Su Z. SOX4 induces tumor invasion by targeting EMT-related pathway in prostate cancer. Tumour Biol. 2017;39(5):1010428317694539.
- 152. Bilir B, Osunkoya AO, WGt W, Sannigrahi S, Lefebvre V, Metzger D, et al. SOX4 is essential for prostate tumorigenesis initiated by PTEN ablation. Cancer Res. 2016;76(5):1112–21.
- 153. Mahajan K, Malla P, Lawrence HR, Chen Z, Kumar-Sinha C, Malik R, et al. ACK1/TNK2 regulates histone H4 Tyr88phosphorylation and AR gene expression in castration-resistant prostate cancer. Cancer Cell. 2017;31(6):790–803.e8.

